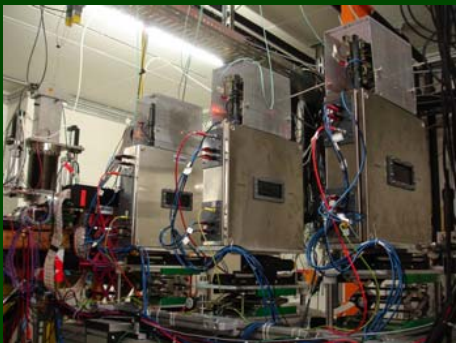
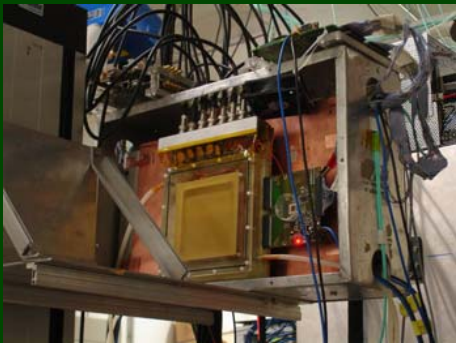
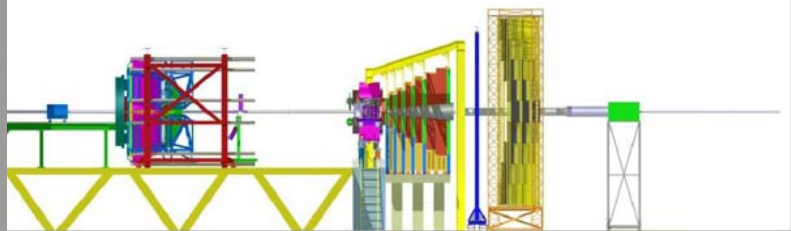
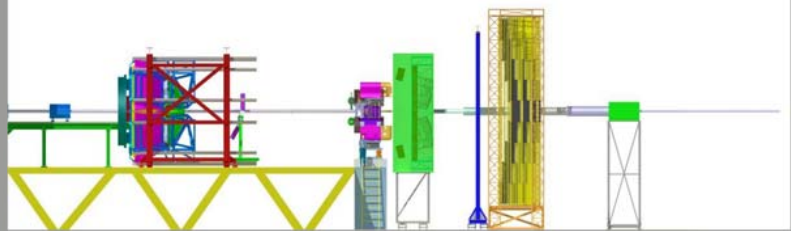
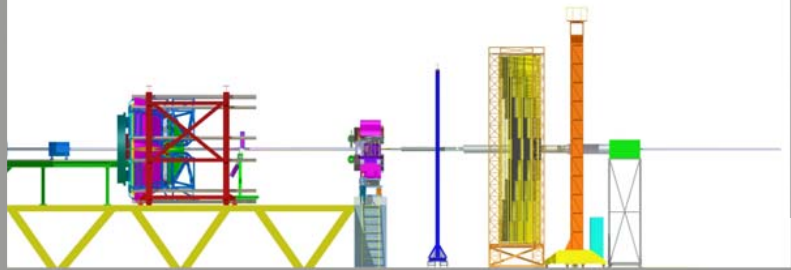


# 2011



# CBM PROGRESS REPORT





# CBM Progress Report 2011

ISBN 978-3-9811298-9-2

Editors: Volker Friese and Christian Sturm  
[v.friese@gsi.de](mailto:v.friese@gsi.de)      [c.sturm@gsi.de](mailto:c.sturm@gsi.de)

©2012 GSI Darmstadt, D-64291 Darmstadt, Germany  
<http://www.gsi.de>

Printed in Darmstadt by GSI Darmstadt

This work was supported by the China Scholarship Council, the Seventh Framework Programme (FP7) of the European Commission through projects HadronPhysics2, AIDA, ULISI and MC-PAD, the Bundesministerium für Wirtschaft und Technologie, Germany, through INNO-KOM-Ost, the Bundesministerium für Bildung und Forschung, Germany, through grants 06WU9195I, 06FY9099I, 06HD9117I, 06HD9121I and 06DR9059D, the Hessian LOEWE initiative through the Helmholtz International Center for FAIR, the Helmholtz Graduate School HIRe for FAIR, the Helmholtz Research School H-QM, the GSI Helmholtzzentrum für Schwerionenforschung GmbH, Germany, through its F&E programme and project WKAMPE1012, the GSI Summer Student programme, the International Science & Technology Center (ISTC) Project No. 3540, the Pusan National University Research Grant, the Federal Purpose-oriented Program "Scientific and Scientific-Pedagogical Cadres of Innovative Russia" for 2009–2013, the Federal agency of Russia for atomic energy (Rosatom), the Romanian NASR/CAPACITATI-Modul III contract nr. 42, and the NASR/NUCLEU Project.

Front cover: (Left) Installations for in-beam tests of CBM prototype detectors. From top to bottom: TRD at the CERN-PS, GEM at COSY, STS at COSY, RICH at the CERN-PS. (Right) Schematic view of the CBM setups at SIS-100 (see page 1 for details).

Dear Colleagues,

After more than 10 years of discussions and planning the starting signal for the construction of the FAIR project finally has been given: in December 2011 the first trees were cut. Below you see the FAIR construction site as of March 7, 2012. The photos show the northern (upper picture where the CBM cave will be located) and the southern part of the FAIR experimental area. According to the official planning the CBM buildings will be completed in May 2017, and we should then be ready to move in with the magnet and the detectors.

Peter Senger



Photos: W. Niebur, GSI

# Contents

<b>Preface</b>	<b>i</b>
<b>General Aspects</b>	<b>1</b>
P. Senger and the CBM Collaboration: <i>The CBM experiment at SIS-100</i> . . . . .	1
K. K. Gudima, Yu. A. Murin and E. I. Litvinenko: <i>The HYPQGSMEvent generator for the simulation of hypernuclei production in central collisions of heavy ions for NICA/MPD and FAIR/CBM</i> . . . . .	3
C. Bergmann et al.: <i>Common CBM beam test of the RICH, TRD and TOF subsystems at the CERN PS T9 beam line</i> . . . . .	4
A. Senger: <i>Radiation dose calculations for the CBM detectors with FLUKA</i> . . . . .	5
<b>Micro-Vertex Detector</b>	<b>6</b>
M. Winter for the IPHC team: <i>Development of high-precision pixel sensors for the CBM vertex detector</i> . . . . .	6
M. Koziel et al.: <i>A latch-up protected power supply for the CBM-MVD</i> . . . . .	7
C. Schrader et al.: <i>Status of the CBM-MVD prototype readout</i> . . . . .	8
B. Milanovic et al.: <i>The CBM-MVD prototype readout network</i> . . . . .	9
D. Doering et al.: <i>Radiation tolerance studies on a CMOS Monolithic Active Pixel Sensor with high-resistivity epitaxial layer</i> . . . . .	10
M. Domachowski et al.: <i>A simulation model for irradiated and partially depleted Monolithic Active Pixel Sensors</i> . . . . .	11
T. Tischler et al.: <i>Simulation of the material budget of the CBM-MVD for SIS-100</i> . . . . .	12
C. Trageser et al.: <i>Studies on the tracking efficiency of the CBM Micro-Vertex Detector (MVD)</i> . . . . .	13
<b>Silicon Tracking System</b>	<b>14</b>
A. Kotynia and J. M. Heuser: <i>Performance simulations of the CBM Silicon Tracking System</i> . . . . .	14
V. Friese: <i>Radiation environment of the CBM Silicon Tracking System</i> . . . . .	15
S. Chatterji et al.: <i>Radiation damage modelling for the development of microstrip detectors for the CBM Silicon Tracking System</i> . . . . .	16
J. M. Heuser et al.: <i>Optimization of microstrip detectors for the CBM Silicon Tracking System</i> . . . . .	17
H. Shang et al.: <i>Performance of prototype Silicon Tracking Detectors for the CBM experiment</i> . . . . .	18
Yu. A. Murin et al.: <i>First experience in prototyping detector modules for the CBM STS</i> . . . . .	19
S. N. Igolkin, Yu. A. Murin and S. N. Vinogradov : <i>Pre-production of ultra-light carbon fiber support frames for the CBM-STS</i> . . . . .	20
V. M. Borshchov et al.: <i>A study of heat simulators of front-end information processing boards for the CBM-STS</i> . . . . .	21
Yi. Bocharov et al.: <i>Element of protection circuitry for high-voltage detectors in the CBM experiment</i> . . . . .	22
M. Singla et al.: <i>3D simulations of low-mass, low-noise analog readout cables for the CBM Silicon Tracking System</i> . . . . .	23
T. Balog and A. Lymanets: <i>Calibration of the n-XYTER front-end chip</i> . . . . .	24
J. Heuser et al.: <i>Performance of the n-XYTER chip with external triggering</i> . . . . .	25
I. Sorokin, W. F. J. Müller and C. J. Schmidt: <i>Rice formula applicability for noise rate estimation in the CBM and other experiments with self-triggered electronics: comparing the calculation to a measurement on example of the n-XYTER chip</i> . . . . .	26
O. Torheim et al.: <i>Development of a 512-channel front-end board with 4 n-XYTER2 chips</i> . . . . .	27
T. Balog, W. F. J. Müller and C. J. Schmidt: <i>Comparison of the SPADIC and n-XYTER self-triggered front-end chips</i> . . . . .	28
V. Kleipa: <i>Radiation-tolerant operation of a commercial micro controller for applications in front-end electronics</i> . . . . .	29

R. Nath, S. Chatterji and J. M. Heuser: <i>Database development for the CBM Silicon Tracking System</i> . . . .	30
<b>Ring Imaging Cherenkov Detector</b>	<b>31</b>
C. Pauly et al.: <i>Fiber hodoscopes for beam diagnostic and particle tracking</i> . . . . .	31
J. Kopfer et al.: <i>In-beam test of a real-size CBM-RICH prototype at the CERN PS</i> . . . . .	32
T. Mahmoud et al.: <i>Construction of the CBM-RICH prototype detector</i> . . . . .	34
C. Pauly et al.: <i>The photon detection system of the CBM-RICH prototype detector</i> . . . . .	35
I. Galm et al.: <i>Wavelength-shifting films for use on MAPMTs with UV-extended windows</i> . . . . .	36
E. Lebedeva et al.: <i>Measurements of the surface homogeneity for the prototype mirrors of the CBM-RICH detector</i> . . . . .	37
S. Reinecke et al.: <i>Reflectivity measurements of various prototype mirrors for the RICH detector</i> . . . . .	38
V. Dobyryn et al.: <i>Development of a mirror mount system for the CBM-RICH prototype detector</i> . . . . .	39
L. Kochenda et al.: <i>Beamtest results of the RICH prototype gas system</i> . . . . .	40
J. Song, C. Son and I.-K. Yoo: <i>Detector control system for the RICH Prototype</i> . . . . .	41
<b>Muon System</b>	<b>43</b>
S. Chattopadhyay et al.: <i>Sector layout of Muon Chambers (MUCH): First results</i> . . . . .	43
S. Biswas et al.: <i>Study of the characteristics of GEM for the FAIR experiment CBM</i> . . . . .	44
<b>Transition Radiation Detectors</b>	<b>45</b>
D. Emschermann and C. Bergmann: <i>Update of the TRD geometry to version v12a</i> . . . . .	45
M. Petriş et al.: <i>Single sided TRD prototype</i> . . . . .	46
M. Petriş et al.: <i>High granularity single sided TRD prototype</i> . . . . .	47
M. Petriş et al.: <i><math>e/\pi</math> Identification and position resolution of double sided TRDs</i> . . . . .	48
D. Emschermann, J. Adamczewski-Musch and B. W. Kolb: <i>Development of an EPICS controlled, Mpod based, mixed HV and LV system for the Münster CBM TRD prototypes</i> . . . . .	49
C. Bergmann et al.: <i>Test of Münster CBM TRD prototypes at the CERN PS/T9 beam line</i> . . . . .	50
A. Arend et al.: <i>Test of the Frankfurt CBM TRD prototypes at the CERN-PS</i> . . . . .	51
A. Abuhoza et al.: <i>Optimization of a setup for ageing studies of gaseous detectors</i> . . . . .	52
F. Constantin and M. Petcu: <i>Free running mode acquisition for a high counting rate TRD</i> . . . . .	53
<b>Time-of-Flight Detectors</b>	<b>54</b>
B. Kämpfer et al.: <i>Development of ceramics RPC for high rate capability timing detector application</i> . . . . .	54
M. Petriş et al.: <i>Time and position resolution for high granularity, multigap, symmetric, differential readout - timing RPC</i> . . . . .	55
M. Petriş et al.: <i>Towards a real size RPC cell for CBM RPC-TOF</i> . . . . .	56
I. Deppner et al.: <i>Performance of large area MMRPC prototype</i> . . . . .	57
Y. Wang et al.: <i>Ageing Test of High Rate MRPC</i> . . . . .	58
P.-A. Loizeau et al.: <i>In beam test of CBM-TOF electronics chain</i> . . . . .	59
C. Xiang et al.: <i>FPGA based control and monitor for CBM-TOF readout</i> . . . . .	60
<b>DAQ and Online Event Selection</b>	<b>61</b>
F. Lemke, S. Schenk and U. Brüning: <i>The adapted CBM network structure design and CBMnet V2.0 implementation</i> . . . . .	61
T. K. Bhattacharyya et al.: <i>Radiation tolerant 2.5GHz clock multiplier unit in UMC 0.18<math>\mu</math>m technology</i> . . . . .	62
N. Abel et al.: <i>SysCore3 — a new board for the Universal ROC</i> . . . . .	63
J. Gebelein and U. Kebschull: <i>FPGA fault tolerance in radiation susceptible environments</i> . . . . .	64
J. de Cuveland, D. Hutter and V. Lindenstruth: <i>CBM First-level Event Selector dataflow architecture and microslice concept</i> . . . . .	65
H. Engel and U. Kebschull: <i>ALICE CRORC as CBM FLES interface board prototype</i> . . . . .	66
S. Linev, J. Adamczewski-Musch and P. Zumbbruch: <i>Status of data acquisition software DABC</i> . . . . .	67
J. Adamczewski-Musch and S. Linev: <i>A Go4-based online-analysis framework for CBM beam tests</i> . . . . .	68

<b>Software and Algorithms</b>	<b>69</b>
G. Kozlov: <i>Study of clustering algorithms for detectors with a pad structure</i>	69
I. Kisel, I. Kulakov and H. Pabst: <i>Numerical stability of the KF track fit in single precision</i>	70
I. Rostovtseva et al.: <i>Study of the L1 CA track finder efficiency in the STS for <math>\Lambda^0</math>, <math>K_s^0</math> and <math>\phi</math> signals</i>	71
S. Jarp et al.: <i>Optimization of the CA-based track finder for CBM</i>	72
S. Lebedev et al.: <i>Status of event reconstruction for the RICH detector in the CBM experiment</i>	73
A. Lebedev, S. Lebedev and G. Ososkov: <i>Status of global track reconstruction in the CBM experiment</i>	74
I. Kisel, I. Vassiliev and M. Zyzak: <i>A SIMDized particle finder for the CBM experiment</i>	75
A. Lebedev, S. Lebedev and G. Ososkov: <i>Towards automatization of software quality monitoring in CBM</i>	76
<b>Physics Performance</b>	<b>77</b>
V. P. Ladygin, A. I. Malakhov and T. A. Vasiliev: <i>Identification of high-momentum pions with RICH</i>	77
I. Vassiliev and V. Akishina: <i><math>K_s^0</math>, <math>\Lambda</math> and <math>\Xi^-</math> reconstruction in Au+Au collisions at NICA energies</i>	78
Yu. A. Murin et al.: <i>On a study of sub-threshold production of heavy hyperons with the CBM STS</i>	79
A. I. Zinchenko et al.: <i>Feasibility study of light hypernuclei reconstruction with the CBM detector</i>	80
S. M. Kiselev: <i>Reconstruction of <math>\pi^0</math> and <math>\eta</math> with a light ECAL</i>	81
S. M. Kiselev: <i>Reconstruction of <math>\omega \rightarrow \pi^0\gamma</math> with a light ECAL in p+C collisions at SIS-100</i>	82
I. Vassiliev, I. Kisel and V. Vovchenko: <i><math>D^{*+}</math> decay reconstruction in C+C collisions at 25A GeV in the CBM experiment</i>	83
E. Lebedeva et al.: <i>Status of low-mass di-electron simulations in the CBM experiment</i>	84
O. Yu. Derenovskaya and I. O. Vassiliev: <i>Reconstruction of <math>J/\psi \rightarrow e^+e^-</math> in Au+Au collisions at SIS-300 energies</i>	85
O. Yu. Derenovskaya and I. O. Vassiliev: <i><math>J/\psi</math> reconstruction in p + Au collisions at 30 GeV</i>	86
V. P. Ladygin, A. I. Malakhov and T. A. Vasiliev: <i>High <math>p_T</math> pion production in central Au+Au collisions at SIS-100/300 energies with CBM</i>	87
I. S. Kulakov et al.: <i>Performance analysis of the Cellular Automaton algorithm on a many-core server at LIT JINR</i>	88
<b>Publications</b>	<b>89</b>
<b>Activities</b>	<b>91</b>
<b>Collaboration</b>	<b>97</b>



## The CBM experiment at SIS-100

*P. Senger<sup>1</sup> and the CBM Collaboration*

<sup>1</sup>GSI, Darmstadt, Germany

### Introduction

The mission of high-energy nucleus-nucleus collision experiments worldwide is to investigate the properties of strongly interacting matter under extreme conditions. At very high collision energies as available at RHIC and LHC, the measurements concentrate on the study of the properties of deconfined QCD matter at very high temperatures and almost zero net baryon densities. The goal of the Compressed Baryonic Matter (CBM) experiment at the FAIR SIS100/300 accelerator system is to explore the QCD phase diagram in the region of very high baryon densities. In particular, the experiments will focus on the search for the phase transition between hadronic and quark-gluon matter, the QCD critical endpoint, new forms of strange matter, in-medium modifications of hadrons and the onset of chiral symmetry restoration. A detailed discussion of the physics of compressed baryonic matter can be found in the CBM Physics Book [1].

The research on compressed baryonic matter will start already with beams from the SIS-100 accelerator as an integral part of the physics programme of the FAIR modularized start version as presented in the FAIR Green Paper [2]. In the SIS-100 energy range, the physics topics of dilepton and strangeness production will be addressed by two collaborations, HADES and CBM, sharing the same experimental area. The layouts and acceptances of both experiments are optimized for different beam energy regimes but provide sufficient overlap in beam energy to ensure two independent evaluations of these challenging measurements and to allow experimental crosschecks for the lighter collision systems. The investigation of dilepton-, strangeness-, and charm production over the full range of beam nuclei and energies will be conducted with a basis version of the CBM setup. The various observables and the corresponding experimental requirements will be discussed in the following.

### The CBM research programme at SIS-100

The SIS-100 accelerator will deliver beams of heavy ions (Au) up to  $11A$  GeV ( $\sqrt{s_{NN}} = 4.7$  GeV), light ions (e.g. Ca) up to  $14A$  GeV ( $\sqrt{s_{NN}} = 5.3$  GeV) and protons up to  $29$  GeV ( $\sqrt{s_{NN}} = 7.5$  GeV). The research programme based on these beams will address the following fundamental questions:

- What is the equation of state of nuclear matter at neutron star densities (up to 6 times saturation density  $\rho_0$ ), and what are the relevant degrees of freedom at these densities? Are there new phases of QCD matter like quarkyonic matter?

- How far can we extend the chart of nuclei towards the third (strange) dimension by producing single and double hypernuclei? Does strange matter exist in the form of heavy multi-strange objects?
- To what extent are the properties of hadrons modified in dense baryonic matter, and are there signatures for chiral symmetry restoration?
- How is charm produced at threshold beam energies, how does charm propagate in nuclear matter, and what are the in-medium properties of charmed particles?

### Experimental setup

The measurement of bulk hadrons, multi-strange hyperons, hypernuclei, lepton pairs and charmed particles in nuclear collisions at SIS-100 energies requires a large-acceptance, high-rate detector system. The Compressed

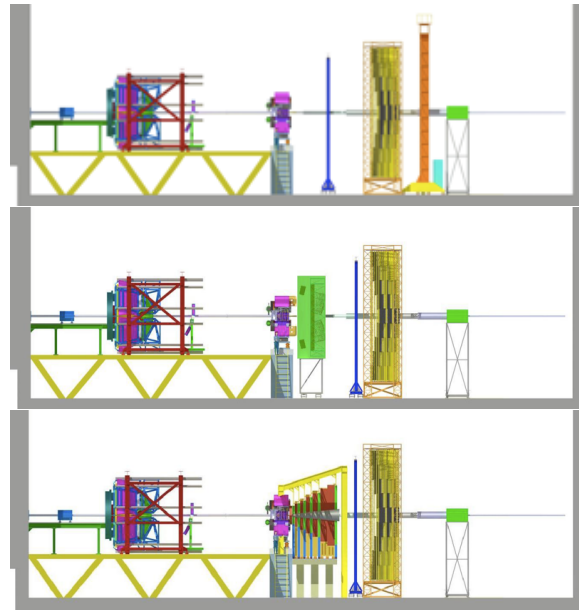


Figure 1: Three flavours of the CBM basis version with the HADES detector in front. Upper panel: CBM setup for the measurements of bulk hadrons, multi-strange hyperons and open charm consisting of the magnet, MVD (open charm only), STS, one TRD station as tracker, TOF, ECAL, PSD, and DAQ/FLES. Centre panel: CBM setup for the measurements of di-electrons with an additional RICH detector. Bottom panel: CBM setup for measurements of charmonium with a MUCH start version replacing the RICH.

Table 1: Observables and detector combinations at SIS-100

Observables	Collisions systems	Detectors
Hadrons, hyperons $e^+e^-$ from low-mass vector mesons	up to Ni+Ni at 8.4 GeV	HADES
Hadrons, hyperons, hypernuclei, photonic decay of low-mass vector mesons	up to Au+Au at 11.4 GeV	Magnet, STS, TRD, TOF, ECAL, PSD, DAQ/FLES
$e^+e^-$ from low-mass vector mesons	up to Au+Au at 11.4 GeV	Magnet, MVD, STS, RICH, TRD, TOF, PSD, DAQ/FLES
$D$ mesons	p+A up to 30 GeV Ca+Ca up to 14.4 GeV	Magnet, MVD, STS, TRD, TOF, PSD, DAQ/FLES
Charmonium	p+A up to 30 GeV Ca+Ca up to 14.4 GeV Au+Au up to 11.4 GeV	Magnet, MVD, STS, MUCH, TRD, TOF, PSD, DAQ/FLES
Photons	Au+Au up to 11.4 GeV	Magnet, STS, ECAL, PSD, DAQ/FLES

Baryonic Matter (CBM) experimental setup is being designed to fulfill these requirements (see Fig. 1 and Tab. 1). The setup comprises:

- A spectrometer with a silicon tracking system (STS) inside a superconducting magnet with large aperture (polar angle acceptance  $2.5^\circ - 25^\circ$  for all azimuth angles). The STS will measure the trajectories of the produced particles in the magnetic dipole field, determine their momenta and reconstruct hyperons by their decay topology.
- A micro-vertex detector (MVD) for the high-precision measurement of the decay vertices of charmed hadrons.
- A large-area time-of-flight detector (TOF) consisting of multi-gap resistive plate chambers for the time-of-flight measurement.
- A RICH detector for the identification of electron-positron pairs from the decay of low-mass vector mesons.
- An intermediate tracking detector with three to four TRD layers allowing to match tracks reconstructed in the STS to the TOF measurement. This TRD constitutes the start version of the full TRD to be used at SIS-300, which will consist of about ten detector layers for the identification of high-momentum electrons.
- A muon detection system (MUCH) for the measurement of charmonium via its decay into muon pairs. This MUCH start version, consisting of two detector triplets, will be upgraded to the full system with seven triplets for deployment at SIS-300. Both the MUCH and the RICH detectors will be movable in order to be used alternatively for muon or electron measurements.
- An electromagnetic calorimeter (ECAL) for the measurement of photons from light vector meson decays.

- A forward calorimeter (PSD) for the determination of the collision centrality and the reaction plane by the measurement of projectile spectators.
- An ultra-fast data acquisition (DAQ) and first level event selection (FLES) performed on a computer farm consisting of many-core CPUs accelerated with graphics cards.

In conclusion, the combination of the HADES detector with the basis version of the CBM set-up is very well suited to start an internationally competitive nuclear-matter research programme with a substantial discovery potential using beams from SIS-100. A world-wide unique experimental search for quark-gluon matter at ultra-high baryon densities will become possible with the full version of the CBM detector system using high-energy and high-intensity beams from SIS-300.

## References

- [1] The CBM Physics Book, Eds. B. Friman et al., Springer Series: Lecture Notes in Physics, Vol. 814, 2011, ISBN: 978-3-642-13292-6, Electronic author's version: <http://www.gsi.de/documents/DOC-2009-Sep-120-1.pdf>
- [2] FAIR Green Paper - The Modularized Start Version, Darmstadt 2009, <http://www.gsi.de/documents/DOC-2009-Nov-124-1.pdf>

# The HYPQGSM event generator for the simulation of hypernuclei production in central collisions of heavy ions for NICA/MPD and FAIR/CBM

K. K. Gudima<sup>1</sup>, Yu. A. Murin<sup>2</sup>, and E. I. Litvinenko<sup>2</sup>

<sup>1</sup>Institute of Applied Physics, AS, Chisinau, Moldova; <sup>2</sup>JINR, Dubna, Russia

We propose an event generator for relativistic hadron-nucleus and nucleus-nucleus collisions to study the production of light hypernuclei in central collisions of heavy ions in the energy regime of the future FAIR and NICA facilities. The generator is an extension of the latest modification of the LAQGSM code [1], which in turn is an improvement of the Quark-Gluon String Model (QGSM) [2]. It describes the reactions induced by both particles and nuclei as a three-stage process: i) Intra-Nuclear Cascade (INC), ii) pre-equilibrium emission of particles during the equilibration of the excited residual nuclei formed after the INC, and iii) evaporation of particles from the remnant compound nuclei or fission of these nuclei. The main products of the INC are generated in the time-evolution model of hadron-hadron (h-h) collisions based on the experimental data on elastic and inelastic (h-h) interactions at energies  $\sqrt{s} < 4.5$  GeV and on the theoretical prescriptions of QGSM for soft elementary h-h inelastic interactions at higher energies. For light nuclei with  $A < 12$ , instead of evaporation the model also considers the Fermi breakup to follow the INC. It is assumed that the high-energy d, t,  $^3\text{He}$ , and  $^4\text{He}$  are produced through coalescence from the nucleons emitted during the cascade [2].

The physics of hyperfragment production in central collisions differs from the mechanism governed by the capture of the  $\Lambda$  particle by the projectile or target remnants [3]. One might assume that in this case, coalescence alone is responsible for production of not only light secondary nuclei d, t,  $^3\text{He}$ , and  $^4\text{He}$ , but also for the light hypernuclei

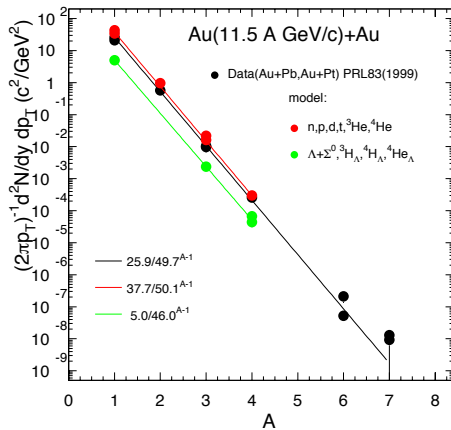


Figure 1: Invariant yields of the fragments produced in central collisions of gold nuclei at 11.5A GeV/c

$^3_{\Lambda}\text{H}$ ,  $^4_{\Lambda}\text{H}$ ,  $^4_{\Lambda}\text{He}$ ,  $^5_{\Lambda}\text{He}$ ,  $^4_{\Lambda\Lambda}\text{H}$ ,  $^5_{\Lambda\Lambda}\text{H}$ ,  $^5_{\Lambda\Lambda}\text{He}$ ,  $^6_{\Lambda\Lambda}\text{He}$ , and even for the production of the hypothetical dibaryons  $\Lambda\Lambda$ ,  $\Lambda\text{N}$ ,  $\Xi\text{N}$ , and  $\Xi\Xi$ . In considering this case, we arrived, however, at the conclusion that to fit the experimental data, the coalescence criterion of the proximity of nucleons in momentum space [4] has to be supplemented by the additional condition of their proximity in configuration space, with the coalescence parameters related through the condition  $r_c = \frac{1}{p_c}$  with the same values of  $p_c$  as used in [4].

An example of the calculated invariant yields of the fragments produced in Au + Au collisions at 11.5A GeV/c together with the experimental data is shown in Fig. 1. Our approach uses the same coalescence parameters both for conventional fragments and for hyperfragments. The prescriptions for the multiplicity of hyperfragments generated in central ( $b \leq 3.5$  fm) Au + Au collisions at projectile energies up to 20A GeV are presented in Fig. 2.

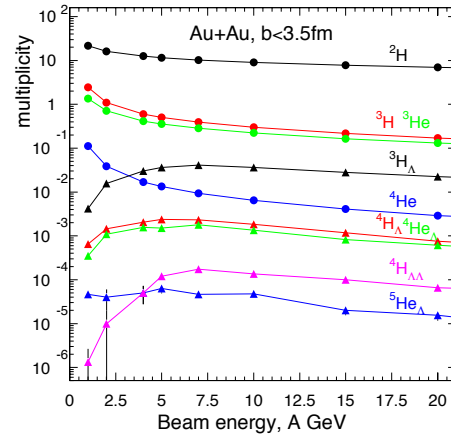


Figure 2: Multiplicity of the reaction species produced through coalescence in central gold-gold collisions

## References

- [1] K. K. Gudima, S. G. Mashnik and A. J. Sierk, *User Manual for the Code LAQGSM*, LANL Report LA-UR-01-6804 (2001)
- [2] N. S. Amelin, K. K. Gudima and V. D. Toneev, *Sov. J. Nucl. Phys.* **51** (1990) 327 and references therein
- [3] A. S. Botvina *et al.*, *Phys. Rev. C* **84** (2011) 064904
- [4] V. D. Toneev and K. K. Gudima, *Nucl. Phys. A* **400** (1983) 173c

## Common CBM beam test of the RICH, TRD and TOF subsystems at the CERN PS T9 beam line

C. Bergmann<sup>1</sup>, A. Andronic<sup>1</sup>, D. Emschermann<sup>1</sup>, D. Vernekohl<sup>1</sup>, J. P. Wessels<sup>1</sup>, C. Pauly<sup>2</sup>, M. Petriş<sup>3</sup>, M. Petrovici<sup>3</sup>, J. Adamczewski-Musch<sup>4</sup>, S. Linev<sup>4</sup>, W. F. J. Müller<sup>4</sup>, A. Arend<sup>5</sup>, and M. Hartig<sup>5</sup>

<sup>1</sup>Westfälische Wilhelms-Universität, Münster, Germany; <sup>2</sup>Bergische Universität, Wuppertal, Germany; <sup>3</sup>NIPNE, Bucharest, Romania; <sup>4</sup>GSI, Darmstadt, Germany; <sup>5</sup>Goethe-Universität, Frankfurt, Germany

A common beam test of the CBM Ring Imaging CHerenkov (RICH), Time Of Flight (TOF) and various Transition Radiation Detector (TRD) prototypes was performed at the CERN Proton Synchrotron (PS) accelerator in October 2011. The measurements were carried out at the T9 beam line in a mixed beam of electrons and pions with momenta from 2 to 10 GeV/c. In addition to the above mentioned subsystems the setup consisted of: a fiber-hodoscope, beam trigger scintillators, two Cherenkov detectors and a Pb-glass calorimeter for  $e/\pi$  identification (shown in Fig. 2). Upstream, at the beginning of the setup the fiber-hodoscope was mounted, followed by a large volume RICH prototype [1], 12 TRD prototypes from the four laboratories in Bucharest, Münster [2], Dubna and Frankfurt [3] and finally the TOF detector, see Figure 1.

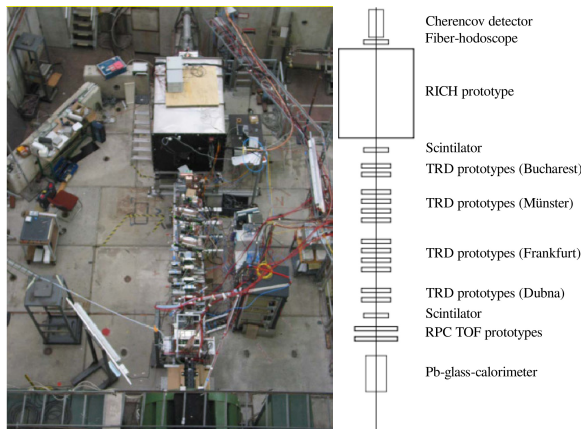


Figure 1: Setup of the PS/T9 beam line for CBM in 2011

The RICH was based on a mirror focusing setup with CO<sub>2</sub> gas as radiator and 16 Hamamatsu MAPMTs, arranged in a 4 × 4 array. The readout of the RICH subsystem was based on the triggerless nXYTER [4] front-end. For the TRD, various MWPC geometries with and without a small drift section and with various wire/pad geometries were under test. Complementary approaches for the signal processing were investigated: The TRDs from Münster and Frankfurt were read out with the custom Self-triggered Pulse Amplification and Digitization asIC (SPADIC) [5], which is a sampling ADC, while the detectors from Bucharest and Dubna used the Fast Analog Signal Processor (FASP) ASIC or the MAD32, a VME-based

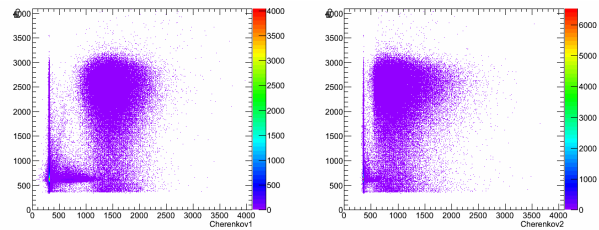


Figure 2: Pb-glass vs. Cherenkov 1 (left) and Pb-glass vs. Cherenkov 2 (right) at 4 GeV/c particle momentum

peak sensing ADC. Part of the TRD test program were systematic high voltage scans, operation with different gas mixtures Ar(80%)+CO<sub>2</sub>(20%) and Xe(80%)+CO<sub>2</sub>(20%), variation of the incident beam angle and beam momentum, and tests of different radiator prototypes. Two RPC TOF prototypes from Bucharest were tested using a C<sub>2</sub>F<sub>4</sub>H<sub>2</sub>(90%)+SF<sub>6</sub>(5%)+C<sub>4</sub>H<sub>10</sub>(5%) gas mixture.

A hybrid data acquisition based on the DABC/MBS system was prepared to read the beam monitoring detectors and all triggered and self-triggered prototypes in a common system. The Go4 framework [6] was configured to provide a detailed online monitoring, including information from part of the slow control system [7], which helped to fine-tune and monitor the detectors during data taking.

### References

- [1] J. Kopfer *et al.*, *In-beam test of a real-size CBM-RICH prototype at CERN PS*, this report
- [2] C. Bergmann *et al.*, *Test of Münster CBM TRD prototypes at the CERN PS/T9 beam line*, this report
- [3] A. Arend *et al.*, *In beam test of the Frankfurt TRD prototypes for the CBM experiment*, this report
- [4] C. J. Schmidt *et al.*, *Development of the n-XYTER front end board FEB-D for CBM*, GSI Scientific Report 2010, p. 227
- [5] T. Armbruster, P. Fischer and I. Perić, CBM Progress Report 2010, Darmstadt 2011, p. 45
- [6] J. Adamczewski-Musch and S. Linev, *A Go4-based online-analysis framework for CBM testbeams*, this report
- [7] D. Emschermann, J. Adamczewski-Musch and B. W. Kolb, *Development of an EPICS controlled, MPOD based, mixed HV and LV system for the Münster CBM TRD prototypes*, this report

## Radiation dose calculations for the CBM detectors with FLUKA

A. Senger

GSI, Darmstadt, Germany

Radiation dose calculations for the CBM detectors were carried out with the FLUKA code [1, 2] for a gold beam with an energy of 35A GeV and an intensity of  $10^9$  ions/s. The gold target had a thickness of 250  $\mu\text{m}$  resulting in an interaction rate of about 1%. The calculations were performed for the two CBM detector setups with the MUCH detector and the RICH detector (see Fig. 1).

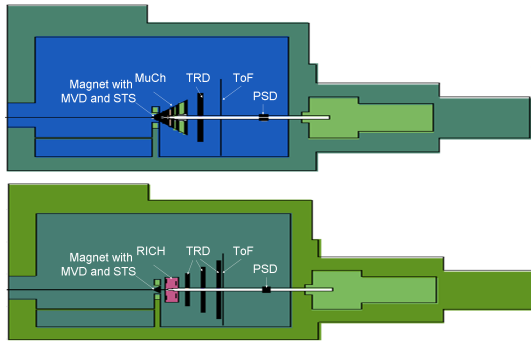


Figure 1: FLUKA geometry of CBM. Top panel: muon setup with MUCH, bottom panel: electron setup with RICH.

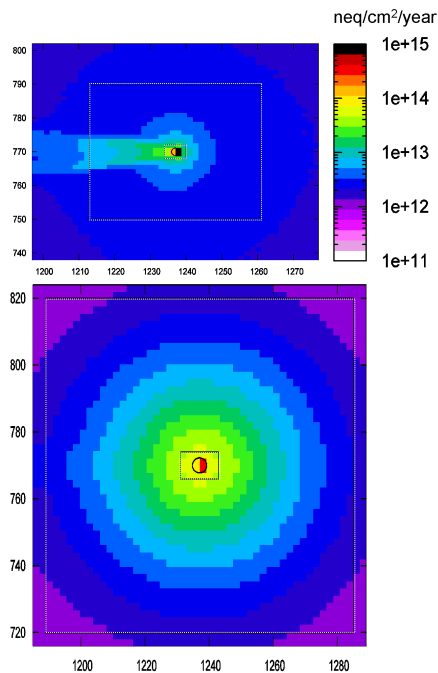


Figure 2: Non-ionising dose in the first (top) and last (bottom) STS station. The inner and outer dashed lines correspond to the detector acceptance

The results of the calculations are shown in Fig. 2 and listed in Tab. 1. Figure 2 depicts the non-ionising energy loss (NIEL) in units of 1 MeV neutrons per  $\text{cm}^2$  and per year for the first (top) and the last (bottom) STS layer. In the first STS layer the effect of delta-electrons is clearly seen. The ionizing dose and the NIEL are listed in Tab. 1 for all CBM detector systems. The results refer to an integral number of  $5 \times 10^{13}$  gold beam particles for the MVD and to  $5 \times 10^{15}$  gold beam particles for the other detector systems.

Table 1: Ionising dose and non-ionising energy loss in the CBM detector systems calculated for a 35A GeV Au beam impinging on a 1% interaction Au target. A CBM year corresponds to  $5 \times 10^{13}$  beam ions for the MVD and to  $5 \times 10^{15}$  beam ions for the other detector systems.

detector	Dose (Gy/year)		NIEL ( $n_{\text{eq}}/\text{cm}^2/\text{year}$ )		
	max	min	max	min	
MVD	5 cm	$10^4$	100	$2 \times 10^{13}$	$5 \times 10^{10}$
	10 cm	$5 \times 10^3$	10	$7 \times 10^{12}$	$5 \times 10^{10}$
	15 cm	$10^3$	5	$2 \times 10^{12}$	$5 \times 10^{10}$
STS	30 cm	$8 \times 10^4$	200	$2 \times 10^{13}$	$5 \times 10^{12}$
	40 cm	$3 \times 10^4$	50	$2 \times 10^{13}$	$5 \times 10^{12}$
	50 cm	$3 \times 10^4$	50	$10^{13}$	$5 \times 10^{12}$
	60 cm	$10^4$	50	$10^{13}$	$5 \times 10^{12}$
	70 cm	$7 \times 10^3$	50	$10^{13}$	$5 \times 10^{12}$
	80 cm	$7 \times 10^3$	50	$10^{13}$	$5 \times 10^{12}$
	90 cm	$5 \times 10^3$	50	$4 \times 10^{13}$	$2 \times 10^{12}$
100 cm	$4 \times 10^3$	50	$6 \times 10^{13}$	$10^{12}$	
MuCh	1	$10^3$	50	$8 \times 10^{13}$	$5 \times 10^{12}$
	2	100	5	$8 \times 10^{12}$	$5 \times 10^{11}$
	3	80	1	$10^{12}$	$10^{11}$
RICH	1000	0.1	$2 \times 10^{12}$	$2 \times 10^9$	
TRD	100	0.5	$5 \times 10^{11}$	$8 \times 10^8$	
ToF	100	1	$10^{11}$	$10^{10}$	
PSD	$10^4$	8	$10^{14}$	$5 \times 10^{12}$	
electronics cave	0.2		$2 \times 10^9$	$10^8$	

### References

- [1] G. Battistoni *et al.*, *The FLUKA code: Description and benchmarking*, Proc. of Hadronic Shower Simulation Workshop 2006, AIP Conf. Proc. **896** (2007) 31
- [2] A. Fasso *et al.*, *FLUKA: a multi-particle transport code*, CERN-2005-10, INFN/TC 05/11, SLAC-R-773 (2005)

## Development of high-precision pixel sensors for the CBM vertex detector

*M. Winter for the IPHC team*

IPHC, Strasbourg, France

CMOS Pixel Sensors (CPS) are developed since many years for the Micro-Vertex Detector (MVD) of the CBM experiment. While the sensor requirements governing the vertexing precision present no difficulty per se, those imposed by the running conditions are much more demanding because of the high particle rate foreseen.

The intrinsic potential of the CPS technology should, in principle, allow matching all the MVD requirements. However, commercially available technologies tend to feature fabrication parameters (e. g. sensitive volume characteristics, feature size, number of metal layers) which are relatively far from being optimal for charged particle detection. Over the last couple of years, however, several CMOS producers have started to offer manufacturing processes for imaging applications, which are based on a high-resistivity (typically 1 k $\Omega$ -cm), about 15  $\mu$ m thick, epitaxial layer. The development of CPS in the last few years was based on such a, 0.35  $\mu$ m feature size, CMOS process. It resulted in the fabrication of the MIMOSA-28 sensor for the vertex detector of the STAR experiment, constructed within the framework of its inner tracker upgrade [1].

This outcome is a major step in the development of the sensor needed for the MVD, but the 0.35  $\mu$ m technology used is not adequate, in particular because of its limited ionising radiation tolerance. In 2011, a 0.18  $\mu$ m process recently made available was addressed, which seems to offer much more favourable parameters. Besides improving intrinsically the ionising radiation tolerance, the process also allows using 6 – 7 metal layers and features deep p-wells in which PMOS transistors can be implemented without generating parasitic charge collection. Moreover, the process is also of interest for other projects, including the upgrade of the ALICE Inner Tracking System (ITS), which makes the development benefit from combined resources.

The first step of the development consists in exploring the technology characteristics impacting most the sensor detection performances. This is the goal of the chip called MIMOSA-32, fabricated end of 2011. It is composed of two main sub-arrays (see Fig. 1) and peripheral test structures. One of the sub-arrays is composed of pixels with various dimensions and different amplification designs, some of them with PMOS transistors implemented in deep p-wells, with and without enclosed layout designs. The other sub-array is made of 128 columns of pixels, each column being ended with a discriminator. One of the test structures is a matrix of about 1000 elongated, 20 $\times$ 80  $\mu$ m<sup>2</sup> large pixels, each equipped with an integrated, low-power discriminator adapted to a rolling-shutter read-out.

The sensor tests, scheduled for spring and summer 2012, will determine the radiation tolerance of the technology.

Meanwhile, the next step of the development is being prepared. It consists in realising two complementary chips, one prototyping the upstream part of the final sensor architecture, while the other addresses its downstream part.

The upstream prototype, called MIMOSA-22THR, features 128 columns of 576 (22 $\times$ 22  $\mu$ m<sup>2</sup>) pixels. Each column is ended with a discriminator. It will essentially reproduce the MIMOSA-22 prototype [2], fabricated in 2008 in the 0.35  $\mu$ m technology used up to now. Two smaller, more advanced versions will also be fabricated. One of them features a more advantageous row sequencer implementation, while the other will allow reading two rows at once, with two discriminators ending each column. The latter design is intended to double the read-out speed.

The downstream prototype contains the zero-suppression micro-circuits. Called SUZE-02, it is an evolved version of the zero-suppression micro-circuit SUZE-01 fabricated in 2007 in the 0.35  $\mu$ m technology mentioned earlier [3]. It differs from it in three aspects: a larger number of hits to process per frame, a 4 times faster frame read-out and the possibility to rely on an external trigger signal to activate the zero-suppression circuitry. This latter modification aims at reducing the power consumption and the data stream delivered by the sensor.

All these prototypes are foreseen for fabrication in summer 2012. Assuming satisfactory test results, the two architectures will be merged in a sensor containing the full chain and featuring a sensitive area of 1 cm<sup>2</sup>. Its manufacturing is foreseen in summer 2013. It will act as a forerunner of the prototype suited to the MVD, to be fabricated in 2014/15.

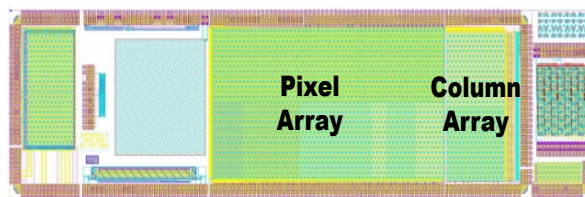


Figure 1: MIMOSA-32 layout and its main sub-arrays

### References

- [1] A. Dorokhov *et al.*, Nucl. Instrum. Methods **A 650** (2011) 174
- [2] M Gelin *et al.*, IEEE Trans. Nucl. Sci. **56** (2009) 1677
- [3] A. Himmi *et al.*, *A Zero Suppression Micro-Circuit for Binary Readout CMOS Pixel Sensors*, in: Proc. of TWEPP-09, CERN-2009-006, p. 426

## A latch-up protected power supply for the CBM-MVD

*M. Koziel, N. Bialas, C. Schrader, S. Schreiber, and J. Stroth for the CBM-MVD collaboration*

Goethe-Universität, Frankfurt, Germany

This report summarizes the implementation of a latch-up protected power supply for the CBM Micro Vertex Detector.

In the CBM experiment, the CMOS sensors equipping the Micro Vertex Detector (MVD) will be constantly exposed to a high flux of a variety of particles. Latch-up will occur regularly, and therefore a protection system is needed. Latch-up is a term used to describe a particular type of short circuit related to the creation of a low-impedance path between the power supply rails of a MOS-FET circuit. This path is created due to parasitic PNP thyristor structures formed by nearby NMOS and PMOS transistors. During normal operation the parasitic thyristor is off. Spikes of the bias voltages or the charge carrier injections caused by impinging particles may switch on and latch the thyristor. If so, the structure can start to conduct high currents which can lead to permanent damage of devices.

Since the latch-up can be cured with power cycling, an option to handle it is to bias the sensors with a dedicated and protected low-voltage power supply. This power supply should detect the over-current caused by latch-up states, quickly switch off the power after detecting the latch-up, and bias the device again when the latch-up state is cured.

Figure 1 depicts the simplified schematic view of the latch-up protection system for the CBM-MVD sensors. The latch-up detection is realized by means of the so-called “shunt resistor” ( $R_{SHUNT}$ ). During normal operation, the sensor consumes a current of about 150 mA at 3.3 V bias voltage. This leads to a voltage drop on the  $R_{SHUNT}$  of 0.6 V. During the latch-up/over-current state, this voltage drop increases, reflecting an increase of the current consumption. The voltage from the shunt resistor is compared with the reference one by means of the LT1711 comparator. If the voltage across the  $R_{SHUNT}$  is higher than the reference, the switches S1 and S2 are opened, and the linear regulators become disconnected from the power lines. Consequently, the sensor is switched off. The measured switch-off time between the over-current state and 0 A consumption is 2  $\mu$ s for a capacitive load of 1.2  $\mu$ F. After a user-defined time interval, a timer switches the power supply on again. Both the analog (VDA) and the digital power (VDD) supply channels are protected.

The main elements of the protection circuit are:

- A shunt resistor  $R_{SHUNT} = 4 \Omega$ . It is located upstream of the voltage regulator in order to allow using larger resistances and determining a larger voltage drop of 0.6 V across this resistor. Such a high  $V_{SHUNT}$

reduces the sensitivity of the latch-up detection system to pick-up noise and allows using this voltage without amplification for a comparison with the reference one.

- A fast comparator (4 ns propagation time) with output latch (LT1711).
- A CMOS linear regulator. It features 3.3 V / 500 mA fixed output voltage, 5.5 V input voltage and a low quiescent current. The sense input of this device is used to compensate for the voltage drop along the cables and to achieve 3.3 V at the destination point. The regulator features a ramping output voltage ( $V_{out}$  rises to its nominal value within 500  $\mu$ s) which allows reducing the current consumption when switching on the sensors. Consequently, lower threshold values for the over-current states may be applied.
- A timer LTC6993-1.
- A fast MOS switch IRF7410 (S1 and S2).

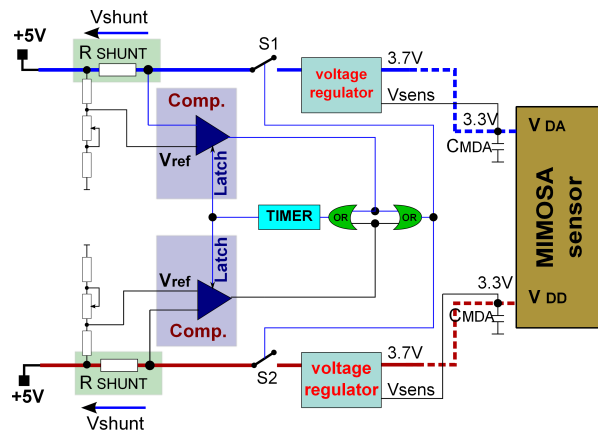


Figure 1: Schematic view of the latch-up protected power supply for the CBM-MVD sensors

The latch-up detection system discussed above was implemented in the front-end board for the read-out system of the CBM-MVD prototype. It allows to detect over-current states and react on them by switching the sensors off within 2  $\mu$ s.

## Status of the CBM-MVD prototype readout

*C. Schrader, S. Amar-Youcef, N. Bialas, M. Deveaux, M. Koziel, J. Michel, B. Milanovic, C. Müntz, B. Neumann, S. Schreiber, T. Tischler, M. Wiebusch, and J. Stroth for the CBM-MVD Collaboration*

Goethe-Universität, Frankfurt, Germany

The readout system of the prototype of the CBM-MVD is intended to provide the bandwidth (of several GByte/s [1]) and scalability needed in the final MVD for SIS-100. It was developed based on the state-of-the-art sensor MIMOSA-26 [2].

The concept of the readout system of the MVD prototype is shown in Fig. 1. Two sensors are bonded on a single-layer flex-print cable (FPC) which transfers the data to a full passive radiation-tolerant front-end board (FEB). The current FPC is based on copper traces and has a material budget of 0.08%  $X_0$  assuming 100% fill factor (0.03%  $X_0$  for aluminum traces).

Additional single-layer FPCs arrange the FEBs in a queue for a JTAG boundary scan, which allows access to the internal registers of the individual sensors. An FPGA-based sensor slow-control board writes the registers and reports errors to a user interface. The operation frequency of the JTAG interface (TTL signals) can be adjusted between 100 kHz and 10 MHz. Hence, the sensors of the MVD for SIS-100 can be programmed within  $< 0.5$  s (300  $\mu$ s per sensor), optionally during one beam spill break. For error-free JTAG chain operation, the signal behavior, signal shape and the crosstalk between the lines of the single-layer FPC were extensively studied and simulated. Currently, the crosstalk is reduced to 150 mV, owing to a moderate signal rise time and serial signal termination [3].

In order to characterize the internal digital-to-analog-converters of the MIMOSA-26 sensor as needed for threshold setting, a highly integrated voltage measurement instrument was developed. This device directly monitors the reference voltage outputs of the sensor and can be read out via a serial interface. A complete integration into the existing FPGA-based MVD slow control is under development. The slow control provides also latch-up handling and on-line monitoring of temperature and current.

In the current set-up the digital data stream of the sensors is transferred via LVDS cables to a converter board. However, to read out the successor MAPS sensor (MIMOSIS-1 with up to 0.8 Gbps data output), an optical high-speed readout system is needed. Here, the challenge is to realize the optical interface without any switchable logic to reduce the bit error rate due to radiation influences. To test several versions of optical high-speed interfaces, an optical demonstrator converter board was developed based on a standalone transceiver TLK3101 (1.5 Gbps to 2.5 Gbps) and TLK6002 (0.47 Gbps to 6.25 Gbps). The transceiver provides the data for one optical link with 8bit/10bit encoding. Hence, one optical link will be used to transfer the data from one sensor module to the Read-Out Controller (ROC).

Such a sensor module comprises up to five MIMOSIS-1 sensors needed for the first and second station of the MVD for SIS-100.

The read-out protocol of the ROC is a modified version of the HADES readout network suited for the required triggerless data acquisition of the MVD prototype. The TrbNet protocol is highly scalable and provides secure data acquisition, monitoring and slow-control [4]. The actual set-up is able to handle several Gbps and consists of three ROCs. A Central Control Unit (CCU) is responsible for synchronization of the sensor data within few nanoseconds. The data are multiplexed via TrbNet hubs and transported to readout PCs via Ethernet. Each hub can handle 100 MByte/s.

A dedicated ROOT-based offline analysis software is used to evaluate the data. The software is designed to allow using major functionalities of *cbmroot* including reconstruction and analysis.

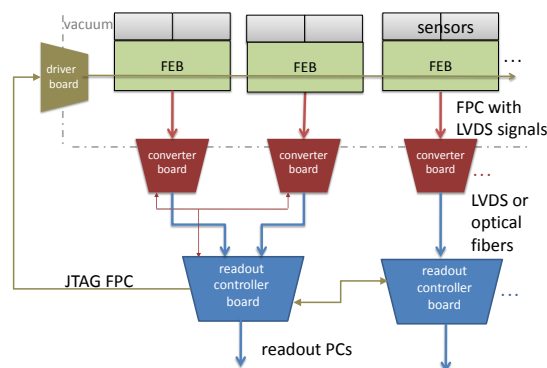


Figure 1: The prototype read-out chain. The LVDS readout cables will be replaced by optical fibres in the next prototype iteration.

## References

- [1] S. Seddiki, *Data rates of the CBM-MVD expected at SIS-100*, CBM Collaboration Meeting, Mamaia, Romania, October 2010
- [2] C. Hu-Guo *et al.*, Nucl. Instrum. Methods **A 623** (2010) 480
- [3] B. Neumann, *Frequency dependent transmission in flex-print-cables*, MVD internal note, October 2011
- [4] B. Milanovic *et al.*, *The CBM-MVD prototype readout network*, this report



## The CBM-MVD prototype readout network

*B. Milanovic, M. Deveaux, I. Fröhlich, J. Michel, B. Neumann, J. Stroth, and C. Schrader for the CBM-MVD Collaboration*

Goethe-Universität, Frankfurt, Germany

Currently, the prototype of the CBM Micro Vertex Detector is under development. In order to be prepared for the upcoming in-beam studies and to elaborate a first approach to the DAQ, a flexible readout network was implemented.

The Micro Vertex Detector (MVD) for the CBM experiment is based on Monolithic Active Pixel Sensors (MAPS) built in silicon CMOS technology. Here, MIMOSA26 (Mi26) was chosen as the sensor version used for the MVD prototype. This chip digitizes the analogue signal directly on the chip and thereby simplifies readout and analysis. The resulting pattern is read out row-wise and encoded on-the-fly into a continuous data stream with a constant readout cycle time (“frames”).

The aim of the readout network presented in this work is to support the control and readout of Mi26 and also of all following MAPS families (e. g. MIMOSIS-1). The data stream of the sensors is read out using Readout Controllers (ROCs), where one ROC is connected to multiple MAPS. The data are either extracted directly on the ROC or over network hubs to the nearby PC farm. As mentioned above, the cycle time of the sensors is constant, but in order to combine the individual frames into “Masterframes” which have the same time stamp, the network has to maintain the synchronization of all MAPS during runtime. The optimal solution for this task makes use of one centralized controller for clock distribution, synchronization and control named Central Control Unit (CCU). Moreover, the network must have a large throughput of several GByte/s and should allow to connect the JTAG interface of the sensors for programming [1].

For the first version presented in this paper, the HADES TrbNet [2] was chosen as a framework for the network. One of the main reasons for the decision towards TrbNet was the large toolset already present from the HADES Experiment. For instance, the EPICS input-output controller, DAQ scripts and various monitoring features are already tested and fully operational. The current ROC implementation uses the HADES-TRBv2 [3] with a MAPS-specific add-on board [4]. Moreover, the CCU was implemented on the FPGA of the TRBv2 board from the HADES experiment. The CCU distributes ROC-controlling messages over three prioritized channels, multiplexed with prioritized Round Robin on one optical fibre. Clock distribution and network synchronization are performed using designated, equally long LVDS lines. In order to maintain the synchronization of all front-ends, the CCU transmits deterministic SYNC pulses to all ROCs over the LVDS ca-

bles. After the SYNC, a frame request is sent to acquire the frame simultaneously on all ROCs. Therefore, if one sensor runs out of sync or experiences a major error, the problem is immediately recognized and the frame can be discarded from the ROCs keeping the data consistent.

The current configuration supports up to four Mi26 sensors per Trbv2. A setup consisting of two ROCs, each connected to two Mi26, is currently being tested (see Fig. 1). The network operates fully synchronous without any measurable deviations. The CCU performs well, and the data are extracted via TrbNet Hubs with up to 50 MByte/s to the PC. This setup can be further extended. The network is highly scalable and will be further improved with newer ROC versions, using for instance the recently developed TRBv3 board. With appropriate add-on boards, such ROCs could handle up to 40 Mi26 sensors. This new setup is planned to be tested under in-beam conditions soon.

In the final version of the MVD, the data format will be kept, and parts of the TrbNet protocol, namely the monitoring and slow-control, can be incorporated into CBMnet.

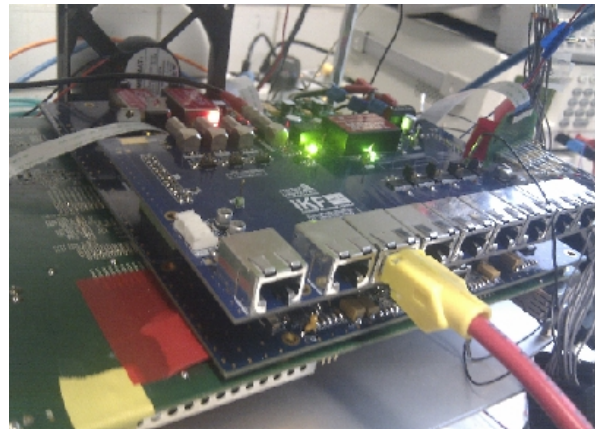


Figure 1: The tested MVD prototype readout chain

### References

- [1] C Schrader *et al.*, *Status of the CBM-MVD prototype readout*, this report
- [2] J. Michel *et al.*, *J. Instrum.* **6** (2011) C12056
- [3] I. Fröhlich *et al.*, *IEEE Trans. Nucl. Sci.* **55** (2008) 59
- [4] C. Schrader *et al.*, *PoS(Bormio2010)017* (2010)

## Radiation tolerance studies on a CMOS Monolithic Active Pixel Sensor with high-resistivity epitaxial layer

*D. Doering, M. Deveaux, M. Domachowski, I. Fröhlich, M. Koziel, C. Müntz, P. Scharrer, and J. Stroth*

Goethe-Universität, Frankfurt, Germany

Nowadays CMOS active pixel sensors (MAPS) match the requirements of CBM in terms of spatial resolution and material budget. For several years, their radiation tolerance has been adapted to the needs of this experiment. Manufacturing MAPS in a CMOS process with a high-resistivity epitaxial layer improved their tolerance to non-ionizing radiation by more than one order of magnitude [1, 2]. A novel sensor, MIMOSA-18AHR, was hoped to provide further improvement.

MIMOSA-18AHR was designed by the PICSEL group of IPHC Strasbourg and manufactured in a 0.35  $\mu\text{m}$  CMOS technology featuring a 15  $\mu\text{m}$  thick epitaxial layer with 400  $\Omega\cdot\text{cm}$  resistivity. It hosts pixels with a pitch of 10, 12.5 and 25  $\mu\text{m}$ . Some samples were irradiated with  $3 \cdot 10^{14}$   $n_{\text{eq}}/\text{cm}^2$  reactor neutrons and tested with  $^{55}\text{Fe}$  and  $^{106}\text{Ru}$  sources. They were operated at  $T = -35^\circ\text{C}$  chip temperature to suppress their (shot-) noise to  $\approx 16$  e ENC ( $\approx 9$  e ENC before irradiation).

Figure 1 shows the amplitude spectrum of the 10  $\mu\text{m}$  pixels of a non-irradiated and an irradiated sensor, which were illuminated with the 5.9 keV X-rays of a  $^{55}\text{Fe}$  source. Its  $x$  axis represents the charge collection efficiency (CCE) of a certain sub-volume of the active volume and the  $y$  axis the relative size of this sub-volume. The unusually large depleted part of the pixel records the  $K_\alpha$  and  $K_\beta$  lines of the source and defines our 100% CCE. The peak marked with an arrow represents the average CCE of the undepleted part of the active volume. Differently than known from conventional chips, the CCE of this volume (35%) is not modified by radiation damage. However, the irradiated chip senses  $\approx 15\%$  less photons, which hints to a loss of active volume. Loosing active volume may cause blind spots in the pixels, which were feared to deteriorate the detection efficiency of the sensor for MIPs. This was however not observed when testing the sensors with the  $^{106}\text{Ru}$  source: The number of  $\beta$  particles recorded by the irradiated sensor remains at  $\gtrsim 99\%$  of the initial value (see Fig. 2). The most probable signal charge is reduced by  $\approx 15\%$  after irradiation. This coincides with the loss of active volume indicated by the  $^{55}\text{Fe}$  measurements. Both effects may be explained with a shrinking of the effective thickness of the active volume. In this case, the signal charge created by the  $\beta$  rays is reduced because of shorter trajectories in the active volume.

The remaining  $S/N = 31$  ( $S/N = 70$  before irradiation) corresponds to the numbers known from non-irradiated MAPS with standard epitaxial layer. This study therefore provides strong evidence that MIMOSA-18AHR can with-

stand a non-ionizing dose of  $\gtrsim 10^{14}$   $n_{\text{eq}}/\text{cm}^2$ , which goes substantially beyond the CBM requirements. However, this conclusion remains to be confirmed by a beam test scheduled for late 2012.

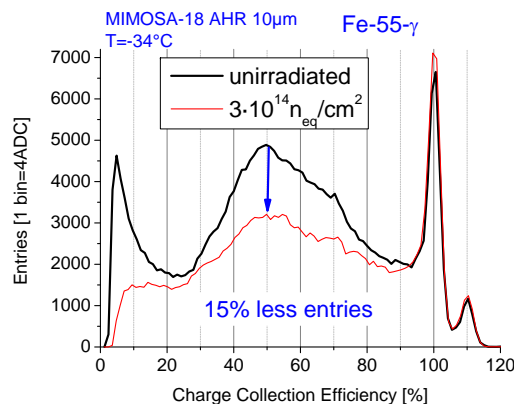


Figure 1: Response of MIMOSA-18AHR to X-rays from a  $^{55}\text{Fe}$  source (see text)

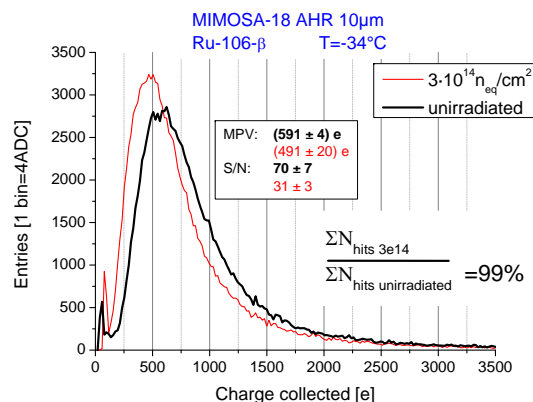


Figure 2: Response of MIMOSA-18AHR to  $\beta$  rays of a  $^{106}\text{Ru}$  source

### References

- [1] A. Dorokhov *et al.*, Nucl. Instrum. Methods **A 642** (2010) 432
- [2] M. Deveaux *et al.*, Nucl. Instrum. Methods **A 583** (2010) 134

## A simulation model for irradiated and partially depleted Monolithic Active Pixel Sensors

*M. Domachowski<sup>1</sup>, M. Deveaux<sup>1</sup>, D. Doering<sup>1</sup>, C. Dritsa<sup>1,2</sup>, C. Müntz<sup>1</sup>, C. Trageser<sup>1</sup>, and J. Stroth<sup>1,3</sup>*

<sup>1</sup>Goethe-Universität, Frankfurt, Germany; <sup>2</sup>Justus-Liebig-Universität, Gießen, Germany; <sup>3</sup>GSI, Darmstadt, Germany

The radiation tolerance of Monolithic Active Pixel Sensors (MAPS) has been significantly improved during the last few years. This was achieved by using a dedicated high-resistivity epitaxial layer, which allows for a partial depletion of this active volume. The resulting acceleration of the charge collection counteracts the lower lifetime of charge carriers which is found in silicon with radiation-induced bulk damage. Moreover, the signal charge is concentrated in the central pixels of the hit clusters, resulting in smaller clusters and a higher  $S/N$ .

In the simulation framework of the CBM experiment (cbmroot), the response of MAPS is simulated with a dedicated digitizer [1]. This response model is based on a parametrization of data obtained from MAPS with a standard epitaxial layer. We tested whether the existing digitizer can be adopted to the response of the novel sensor generation.

The study was based on experimental data taken from MIMOSA-18AHR prototypes [2] delivered by the PICSEL group of IPHC Strasbourg. MIMOSA-18AHR is based on a  $0.35 \mu\text{m}$  CMOS process and hosts four types of pixels with a pitch of  $10 \mu\text{m}$ ,  $12.5 \mu\text{m}$  and  $25 \mu\text{m}$ . The epitaxial layer of the chip has a resistivity of  $400 \Omega\cdot\text{cm}$  and a thickness of  $15 \mu\text{m}$ . First, the sensors were irradiated with up to  $3 \cdot 10^{14} \text{ n}_{\text{eq}}/\text{cm}^2$ . In a second step they were evaluated with  $\beta$  rays from a  $^{106}\text{Ru}$  source. The data obtained were used to measure the pulse height of the pixels in hit clusters, which provided the necessary input for tuning the digitizer.

The accuracy of the simulation model is benchmarked with the so-called “accumulated charge plot” shown in Fig. 1. This plot is provided by ordering the signals of the 25 pixels of a hit cluster according to their  $S/N$ . In a next step, the charge for the ( $1 \leq N \leq 25$ ) pixels with highest  $S/N$  is summed up for the individual clusters. Afterwards, the sum is filled into the  $N^{\text{th}}$  of 25 histograms and the procedure is repeated for the next cluster. The 25 histograms obtained in this way exhibit a Landau distribution which is fitted subsequently. The “accumulated charge plot” shows the most probable value (MPV) of the charge obtained from the fit of the  $N^{\text{th}}$  histogram as function of  $N$ .

The plot illustrates information about the distribution of the charge over the pixels of the cluster. For instance, Fig. 1 provides the information that roughly 45 % of the cluster charge is collected by the seed pixel ( $N = 1$ ), while a group of three pixels already collect almost the total charge of the cluster. Decreasing charge ( $N > 15$ ) is an artefact caused by noise and the ordering with regard to  $S/N$ .

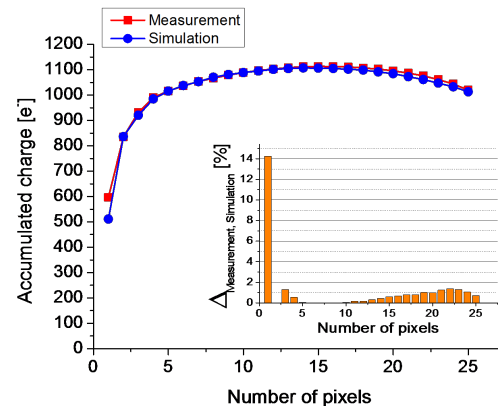


Figure 1: “Accumulated charge plot” (see text) for the  $10 \mu\text{m}$  pixels of a MIMOSA 18-AHR irradiated with  $10^{13} \text{ n}_{\text{eq}}/\text{cm}^2$ . The measured and the simulated sensor response is compared.

The plot was generated with measured and simulated data after tuning the model parameters of the digitizer. Figure 1 shows a representative example for a pixel irradiated with  $10^{13} \text{ n}_{\text{eq}}/\text{cm}^2$  and with  $10 \mu\text{m}$  pixel pitch. One observes that all pixels except of the seed pixel are accurately described. For the seed pixel, the simulation underestimates the signal charge by  $\approx 14\%$ . This effect remains to be understood in detail. However, it is not expected to have a significant impact on potential simulation results.

We conclude that the digitizer is suited for describing sensors with a high-resistivity epitaxial layer. This applies for non-irradiated sensors as well as for sensors irradiated with non-ionizing doses.

The updated sensor models will be part of the upcoming novel version of the MVD digitizer software.

## References

- [1] C. Dritsa, PoS(BORMIO2010)015 (2010)
- [2] IPHC, Strasbourg University, <http://www.iphc.cnrs.fr/List-of-MIMOSA-chips.html>

## Simulation of the material budget of the CBM-MVD for SIS-100

*T. Tischler, S. Amar-Youcef, M. Deveaux, M. Koziel, C. Müntz, C. Schrader, and J. Stroth for the CBM-MVD Collaboration*

Goethe-Universität, Frankfurt, Germany

For the CBM Micro Vertex Detector (MVD) to be installed at SIS-100, improved geometries of the detector were studied within the `cbmroot` framework. To do so, a simplified model of the MVD including sensors (MAPS [1]), their support in the active area (CVD diamond) and copper heat sinks was worked out [2]. To allow using the CAD model within the `cbmroot` framework, it was transformed into a ROOT geometry by a customized converter provided by the Panda Collaboration [3].

Taking advantage of existing FairRoot classes, a new MVD-specific class was implemented to estimate the material budget. The test particles, e. g. neutrinos, are transported through the detector geometry. If they cross a given detector component, the position and the material of this component are stored in order to estimate the total material budget. The material budget is described by the percentage of the radiation length for a given polar angle  $\theta$  in a given range of azimuth  $\phi$ . The estimation of the material budget is currently performed for two cases: for the prototype of the MVD and for the MVD for SIS-100 (see Figs. 1 and 2, respectively).

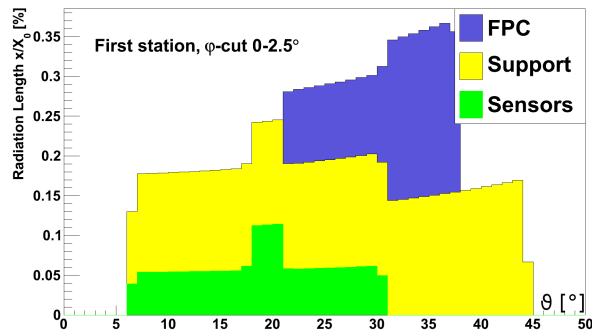


Figure 1: Material budget of the MVD prototype including sensors (50  $\mu\text{m}$  thin MIMOSA-26, double-sided arrangement), sensor support (150  $\mu\text{m}$  thin CVD diamond) and a dedicated FlexPrint cable (FPC, 0.0861%  $X_0$  [4]) for the sensor readout (one FPC in the active area only)

The MIMOSIS-1 sensors are currently under development. Nevertheless, a first implementation was done in order to test the compatibility of the preliminary geometrical layout of this sensor with respect to the acceptance coverage required by the CBM experiment. The heat sinks, which are placed outside of the acceptance, are made of copper (to be replaced by aluminum). The aluminum frame

is needed to mount the heat sinks for the sensors and to support the read-out electronics.

In summary, a successful implementation of the geometry of the MVD prototype as well as of the MVD for SIS-100 in `cbmroot` is presented, starting from realistic CAD models. This allows estimating the material budget by considering the main detector building blocks based on realistic geometries and sensor integration. It is shown that a material budget of few 0.1%  $X_0$ , as required by the CBM experiment, is within reach.

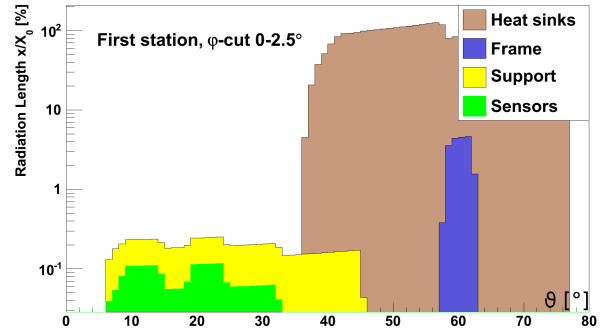


Figure 2: Material budget of the MVD for SIS-100 including sensors (50  $\mu\text{m}$  thin MIMOSIS-1, double-sided arrangement), sensor support (150  $\mu\text{m}$  thin CVD diamond), an aluminum frame and heat sinks

## References

- [1] C. Hu-Guo *et al.*, Nucl. Instrum. Methods A **623** (2010) 480
- [2] T. Tischler *et al.*, CBM Progress Report 2010, Darmstadt 2011, p. 4
- [3] [panda-wiki.gsi.de](http://panda-wiki.gsi.de)
- [4] C. Schrader, *Status of the FEE of the MVD*, 18th CBM Collaboration Meeting, September 2011, Beijing, China

## Studies on the tracking efficiency of the CBM Micro-Vertex Detector (MVD)

*C. Trageser<sup>1</sup>, M. Deveaux<sup>1</sup>, C. Drita<sup>1,2</sup>, and J. Stroth<sup>1</sup>*

<sup>1</sup>Goethe-Universität, Frankfurt, Germany; <sup>2</sup>Justus-Liebig-Universität, Gießen, Germany

The CBM MVD is to provide good sensitivity together with reasonably low device complexity and costs. To find a good compromise, we studied the STS to MVD track matching for different design options.

The cost-efficient standard geometry of the MVD for SIS-300 bases on two stations located 5 cm and 10 cm downstream the target. Tracks found in the Silicon Tracking System (STS) of CBM are extrapolated and extended to this MVD. This is complicated by the large gap (20 cm) between both detectors and the high hit density (up to few 10/mm<sup>2</sup>) caused by a pile-up of several collisions in the MVD. Mismatches in tracking, as caused by wrongly attached hits, were feared to deteriorate the impact parameter (IP) resolution of the MVD and to generate false decay vertex indications.

We studied the MVD geometries listed in Tab. 1 with 25A GeV Au+Au collisions, including  $\delta$  electrons. The collision rates ranged from  $\approx 3 \times 10^4/s$  (pile-up = 0) to  $\approx 3 \times 10^5/s$  (pile up = 10). The default STS geometry and the L1 tracking package of the *cbmroot* release April 2011 were used. They might show better performance after parameter tuning. Only “long”, primary tracks with  $> 4$  hits in the STS were considered and defined as “good” (“bad”) if all related MVD hits were correctly (falsely) assigned. Sub-classes account for hits missing because of the limited geometrical acceptance or inefficiencies of the MVD (see Tab. 2).

Table 1: MVD geometries studied

Station number	1	2	3	4
Distance to target [cm]	5	10	15	20
Inner radius [mm]	5.5	5.5	8.3	11
Outer radius [mm]	25	50	75	100
Thickness [ $\mu m$ ]	300	500	500	600
MVD2	X	X		
MVD3	X	X	X	
MVD4	X	X	X	X

Most background tracks in the open charm reconstruction are emitted from the main vertex of the Au+Au collision (PV), which turns into  $IP = 0$ . True signal tracks originate from a secondary decay vertex (SV) and have a finite true IP. If the uncertainty of the IP measurement is smaller than the width of the IP distribution of the signal, rejecting tracks with small IP forms a powerful cut. However, this accuracy is observed for tracks classified as “Good-1” and “Good-2” only. Cutting on  $IP/\sigma_{IP}$  may compensate, but  $\sigma_{IP}$  is regularly underestimated for tracks with wrong hits.

Figure 1 shows the background-rejection capability of

the major single-track cuts used in open charm analysis. We required  $p > 1$  GeV/c,  $p_t > 0.3$  GeV/c and  $IP/\sigma_{IP} > 6$ . The number of accepted background tracks per frame (or event) are shown as function of MVD geometry and collision pile-up. The color represents the classification of the tracks. The background is formed almost exclusively by tracks with missing or falsely attached hits and gets more pronounced with increasing pile-up. It is substantially reduced by adding one or two stations to the MVD-2.

Table 2: Definition of track classes: Hits correctly assigned ( $\circ$ ), falsely assigned ( $\times$ ), not accepted ( $\square$ ), not detected ( $\blacksquare$ )

name	case	$\circ$	$\times$	$\square$	$\blacksquare$	Colorcode	
Good Tracks	1		X				
	2		X		X		
	3		X			X	
	4		X		X	X	
Mixed Tracks	1		X	X			
	2		X	X	X		
	3		X	X		X	
	4		X	X	X	X	
Ghost Tracks	1			X			
	2			X	X		
	3			X		X	
	4			X	X	X	

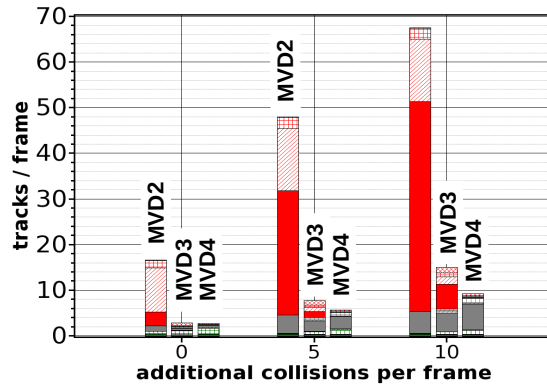


Figure 1: Falsely accepted background tracks per central Au-Au collision. For the color code see Tab. 2.

Our results suggest that an almost perfect track finding is needed to exploit the sensitivity of the MVD. Accounting for this fact, it has to be ensured that the detector provides a reliable and sufficient input for the tracking algorithms. Adding one or two tracking stations between MVD and STS might help to match this requirement.

## Performance simulations of the CBM Silicon Tracking System

A. Kotynia<sup>1</sup> and J. M. Heuser<sup>2</sup>

<sup>1</sup>Goethe-Universität, Frankfurt, Germany; <sup>2</sup>GSI, Darmstadt, Germany

The layout of the Silicon Tracking System (STS) has been the object of extensive studies during the last years: the optimization of its performance has driven several choices concerning soft geometry parameters, such as detector pitch, number of tracking stations and their placement within the magnet volume. The STS performance studies presented in this report show the progress made with optimization of the stations and sensors layout, based on the increasing knowledge of the hardware involved in the detector. Relevant parameters such as the hit and the track reconstruction efficiencies and track parameters were monitored.

The STS consists of eight tracking layers located 30, 40, 50, 60, 70, 80, 90, 100 cm downstream of the target. Each layer is an array of vertical modules containing 300  $\mu\text{m}$  thick double-sided strip sensors. The strip pitch is 58  $\mu\text{m}$  on both sides. Two variations of sensor arrangement in a ladder were studied (Fig. 1):

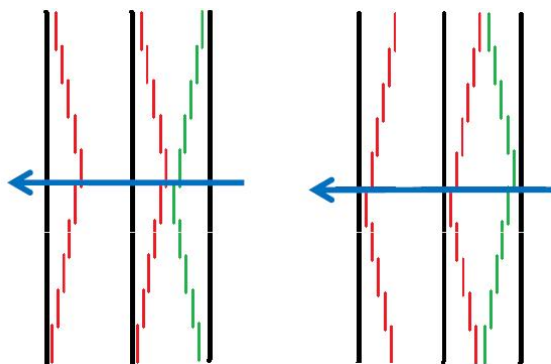


Figure 1: Side view of two neighboring STS ladders: left corresponds to description number 1, right to description number 2

1. The outer sensors on the top and bottom are mounted closest to the support ladder. This creates a gap of approximately 2 cm along the beam in the inner part of the station (close to the beam pipe).
2. The innermost sensors in the ladder are mounted closer to the support structure. In this setup, the gap between neighboring ladders is on the top and on the bottom of the station.

Both setups were tested, and no significant difference in the yields of reconstructed  $K_s$  and  $\Lambda$  was found (Tab. 1). In addition, the possibility of different strip orientation in the sensors was investigated. Because of difficulties with

the production of double-metalization on double-sided sensors, it was proposed to decrease the stereo angle from  $15^\circ$  with double-metalization [1] to  $8^\circ$  without double-metalization in order to decrease the size of the inactive corners in each sensor. The results from STS tracking performance as well as from  $K_s$  and  $\Lambda$  reconstruction for the two stereo angles are summarized in Tab. 2.

Table 1: Simulation results with different sensor arrangements on the STS ladder

Sensor arrangement	Tracking efficiency	$K_s$ S/B	$\Lambda$ S/B	$K_s/\text{ev}$	$\Lambda/\text{ev}$
1	75.6%	0.40	1.17	2.54	2.95
2	75.4%	0.39	0.93	2.41	3.01

Table 2: Simulation results with different stereo angles in the STS sensors

Front side	Back side	Tracking efficiency	Fake/Real hits	$K_s$ S/B	$\Lambda$ S/B
$-7.5^\circ$	$+7.5^\circ$	0.40	4.11	0.40	1.17
$-8.0^\circ$	$0^\circ$	0.39	2.53	0.42	1.26

The layout presented above was used to implement the STS in the CBM simulation framework. This implementation includes the complete chain of physical processes caused by a charged particle traversing the detector, from charge creation in the silicon to the digital output signals. Signal sharing between strips together with charge collection inefficiency and Lorentz shift due to the presence of the magnetic field, channel dead time, and single-channel inefficiency are present in the simulations. Applications of realistic detector response functions together with a Cellular Automaton for track finding and a Kalman Filter for track fitting results in a track finding efficiency of 97% for fast primary tracks and 75% for secondary tracks, with a momentum resolution of 1.2%.

In order to compare the simulation results with those obtained from in-beam experiments, a special geometry was prepared and implemented in the simulation framework with the possibility of changing the detector response parameters. However, such parameters are not yet defined or measured and consequently the full comparison of simulations with experimental data will be the subject of studies in the near future.

## References

- [1] R. Karabowicz, A. Kotynia and J. M. Heuser, CBM Progress Report 2008, Darmstadt 2009, p. 8

## Radiation environment of the CBM Silicon Tracking System

V. Friese

GSI, Darmstadt, Germany

Among the detector systems of the CBM experiment, the Silicon Tracking System (STS), being located in close proximity to the target, will have to face the harshest environment in terms of both ionising and non-ionising radiation. Of particular importance is the latter, causing damage effects in the bulk material which lead to an increased leakage current and, consequently, to an increase of the power dissipation of the sensors.

The standard tool to calculate the non-ionising irradiation is the FLUKA package, which is believed to provide the best physics description in particular for low-energy neutrons. Such calculations, however, are quite expensive in terms of CPU time and require expert knowledge of the FLUKA program. In this report, we present results derived from transport simulations with the standard CBM software `cbmroot`, using the GEANT3 transport engine with the GEISHA model for hadronic interactions, with an energy threshold of 1 keV for neutron production. The calculations were performed for the CBM setup comprising the STS and the muon system, i. e. with a heavy absorber directly behind the last STS station. Input events are minimum bias Au+Au collisions at 25A GeV generated with UrQMD. The results are scaled to  $5 \cdot 10^{13}$  collisions, corresponding to a typical CBM run year of two effective months at 10 MHz interaction rate.

The non-ionising dose was calculated by counting the particles traversing the sensitive area of the silicon stations, giving each particle a weight (NIEL factor) according to its type and energy. The relative damage functions for neutrons, protons, pions and electrons were taken from the tabulations in [1]; the effect of other particle types was neglected. Figure 1 shows the results of this calculation for the first and last station, respectively. The maximal fluence is seen closest to the beam; it ranges from  $4.5 \cdot 10^{13} \text{ n}_{\text{eq}}/\text{cm}^2$  (station 1) to  $1.8 \cdot 10^{13} \text{ n}_{\text{eq}}/\text{cm}^2$  (station 8). In these inner parts, pions are the dominating source in the first stations, while the relative neutron contribution increases with distance from the target and reaches that of pions for the last station. In all stations, the radial profile of the neutron fluence is less steep than that of the charged hadrons; consequently, they dominate the total radiation at the periphery of the stations.

The leakage current is directly proportional to the non-ionising fluence [2]:  $I_{\text{leak}} = \alpha V \Phi$ , with the damage constant  $\alpha = 4.73 \cdot 10^{-4} \text{ eV/K}$  at room temperature. Since it is a strong function of the temperature [3], the STS will be operated in a thermal enclosure. Here, we assume an operating temperature of  $-10^\circ\text{C}$ , at which the leakage current is reduced to 6.3% of its value at room temperature. Under this assumption, we obtain a maximal cur-

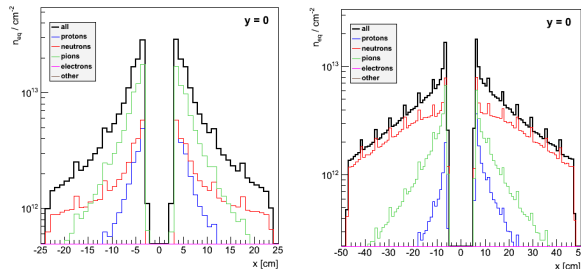


Figure 1: Non-ionising fluence in the bending plane for station 1 (left) and station 8 (right). The spikes are an artefact of the calculation, resulting from overlapping sensors.

rent of  $3.4 \mu\text{A}/\text{cm}^2$  for station 1 and  $1.4 \mu\text{A}/\text{cm}^2$  for station 8. Assuming further an operating voltage of 120 V, corresponding to twice the full depletion voltage for non-irradiated sensors, the maximal power dissipation on the sensor is  $4.1 \text{ mW}/\text{cm}^2$  for station 1 and  $1.6 \text{ mW}/\text{cm}^2$  for station 8.

The ionising dose was calculated by summing up the energy losses of the charged particles traversing the sensitive area as delivered by the GEANT calculation. We obtain maximal values of 23.7 kGy for station 1 and 7.2 kGy for station 8, respectively (see Fig. 2). It should be noted that these values need not coincide with the energy deposited in the material, since secondary electrons might leave the sensitive volume in particular when created close to the surface. Thus, the values presented here can be regarded as upper limits.

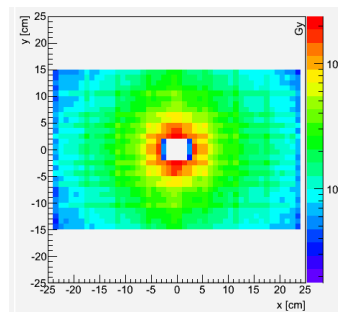


Figure 2: Total ionising dose for station 1

### References

- [1] A. Vasilescu and G. Lindstroem, *Displacement damage in silicon*, on-line compilation [<http://sesam.desy.de/members/gunnar/Si-dfuncs.html>]
- [2] M. Moll *et al.*, Nucl. Instrum. Methods **A 426** (1999) 87
- [3] H. J. Ziock *et al.*, IEEE Trans. Nucl. Sci. **40** (1993) 344

## Radiation damage modelling for the development of microstrip detectors for the CBM Silicon Tracking System

S. Chatterji<sup>1</sup>, M. Singla<sup>2</sup>, A. Lymanets<sup>2,3</sup>, M. Merkin<sup>4</sup>, and J. M. Heuser<sup>1</sup>

<sup>1</sup>GSI, Darmstadt, Germany; <sup>2</sup>Goethe-Univ., Frankfurt, Germany; <sup>3</sup>KINR, Kiev, Ukraine; <sup>4</sup>Moscow State Univ., Russia

The Silicon Tracking System (STS) of the CBM experiment requires radiation-hard microstrip detectors standing neutron fluences up to  $10^{14}$  n<sub>eq</sub>cm<sup>-2</sup>. We have implemented a radiation damage model (Perugia trap model) [1] into the SYNOPSIS TCAD simulation package and compared the results for double-sided silicon strip detectors (DSSDs) with measurements of irradiated prototypes. This validated the applicability of the simulation tool towards optimizing the design and operating scenario of forthcoming full-size prototype detectors.

Synopsys [2], a finite-element semiconductor simulation package, was used to determine the electrical behaviour of these devices. The effective doping concentration ( $N_{\text{eff}}$ ) is parameterized using the Hamburg model, while the minority carrier lifetime  $\tau$  was changed in our simulation package using the definition of Kraner's as follows:

$$1/\tau = 1/\tau_0 + \beta \phi_{\text{eq}},$$

where  $\tau_0$  is the minority carrier lifetime of the initial wafer,  $\phi_{\text{eq}}$  the integrated fluence and  $\beta$  the trapping time. The value of  $\tau_0$  was set to 1 ms for electrons and 0.3 ms for holes as is expected for detector grade silicon.

Some of the CBM02 prototype DSSDs were irradiated at the KRI cyclotron facility in St. Petersburg, Russia. These detectors were measured just after irradiation without any periods of annealing. The variation of leakage current and interstrip resistance with neutron fluence was measured. The TCAD simulation is able to reproduce the measured observations as can be seen from Figs. 1 and 2. The full depletion voltage  $V_{\text{fd}}$  indicates that type inversion occurs at around  $11.2 \times 10^{12}$  n<sub>eq</sub>cm<sup>-2</sup>. In order to investigate the life time of DSSDs, it is imperative to extract the charge collection efficiency as a function of fluence. For this one has to understand strip isolation in particular on the ohmic side. The strip isolation in turn can be understood by studying the interstrip resistance  $R_{\text{int}}$ . It was found that for fluences up to type inversion,  $R_{\text{int}}$  is very low below full depletion, increases steeply at full depletion and continues to increase slightly thereafter. However, for type-inverted sensors, the interstrip resistance is of the order of tens of M $\Omega$  even below full depletion and saturates at around 100 M $\Omega$  after the operating voltage is reached. One can observe that the operating voltage is much higher than  $V_{\text{fd}}$  especially in case of high fluences.

Figure 3 shows the variation of collected charge and cross talk versus  $V_{\text{bias}}$  for the same fluences as used for irradiation. The charge collection follows the same variation as the measured  $R_{\text{int}}$  does with  $V_{\text{bias}}$ . The crosstalk initially increases until  $V_{\text{fd}}$  is reached since the charge sharing between neighbouring strips increases. After  $V_{\text{fd}}$  is

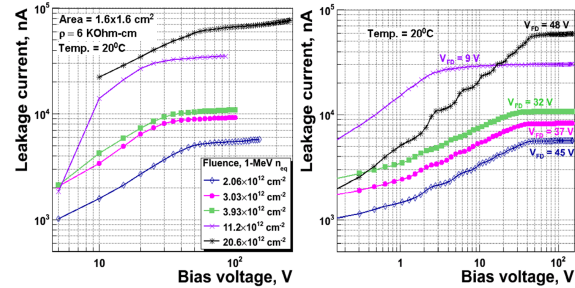


Figure 1: Comparison of measured and simulated leakage current for irradiated DSSDs

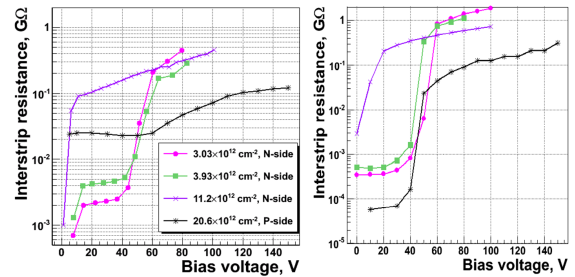


Figure 2: Comparison of measured and simulated interstrip resistance for irradiated DSSDs

reached, the crosstalk decreases since the bias also improves the drift velocity, which tends to reduce charge sharing. The interstrip capacitance  $C_{\text{int}}$  was also measured and simulated since it is the dominant contributor to the capacitive noise. Its value was found to be around 2.09 pF/cm on the ohmic side and 1.6 pF/cm on the junction side. In addition, we have noted that  $C_{\text{int}}$  does not change appreciably with irradiation.

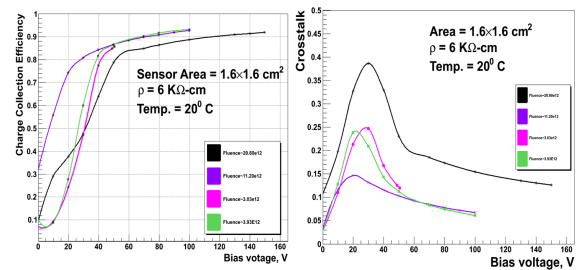


Figure 3: Expected charge collection efficiency and crosstalk for the irradiated DSSDs as a function of  $V_{\text{bias}}$

## References

- [1] M. Petasecca *et al.*, IEEE Trans. Nucl. Sci. **53** (2006) 2971
- [2] <http://www.synopsys.com>



## Optimization of microstrip detectors for the CBM Silicon Tracking System

*J. M. Heuser<sup>1</sup>, S. Chatterji<sup>1</sup>, C. J. Schmidt<sup>1</sup>, V. Kleipa<sup>1</sup>, C. Simons<sup>1</sup>, W. Niebur<sup>1</sup>, J. Eschke<sup>1</sup>, T. Balog<sup>1,2</sup>, L. Long<sup>3</sup>, H. G. Ortlepp<sup>3</sup>, O. Brodersen<sup>3</sup>, A. Lymanets<sup>4,5</sup>, I. Sorokin<sup>4,5</sup>, H. Malygina<sup>4,5</sup>, M. Singla<sup>4</sup>, P. Ghosh<sup>4</sup>, Y. Bansal<sup>6</sup>, N. Joshi<sup>6</sup>, N. Sharma<sup>6</sup>, and N. Tiwari<sup>6</sup>*

<sup>1</sup>GSI, Darmstadt, Germany; <sup>2</sup>Comenius University, Bratislava, Slovakia; <sup>3</sup>CiS Forschungsinstitut für Mikrosensorik und Photovoltaik GmbH, Erfurt, Germany; <sup>4</sup>Goethe-Universität, Frankfurt, Germany; <sup>5</sup>Kiev Institute for Nuclear Research, Kiev, Ukraine; <sup>6</sup>Mody Institute of Technology and Science, Lakshmanagarh, India

A novel radiation-tolerant structure that is expected to improve the application of double-sided silicon microstrip detectors in harsh radiation environments as with the CBM experiment was developed by CiS [1]. A sample of small prototype detectors produced at CiS was exposed to several neutron fluences and subsequently characterized at GSI. The structure could be integrated in a forthcoming full-size prototype detector for the CBM Silicon Tracking System. Meanwhile the third prototype of a full-size microstrip detector for the CBM Silicon Tracking Detector System is being designed in cooperation of GSI and CiS. Based on the evaluation of the second prototype [2, 3], several design optimizations are being applied and processing variations explored.

A new radiation-tolerant structure (“Shottky barrier”) was designed by CiS in a BMWI-supported project and produced on small double-sided microstrip detector prototypes of 256 by 256 orthogonal strips of 50  $\mu\text{m}$  pitch. The Shottky barriers are expected to increase the charge collection on the ohmic sides of double-sided strip detectors after irradiation. GSI is research partner of CiS for the evaluation of the detectors in in-beam experiments with multi-channel front-end electronics. The detectors were checked in the GSI detector laboratory for the quality of their integrated AC coupling capacitors, the bulk currents and bulk capacitances as a function of the bias voltage applied. For some of the detectors, comprising a suitable biasing structure, the interstrip resistances and capacitances were directly measured. Precision equipment like a semi-automatic wafer probe station, source-measure units and LCR meters were utilized, and custom-specific programs for their automated control and readout were developed. Out of the available 45 detectors, a sub-set of 20 was selected and grouped into four irradiation samples. They were sent to Institute Jozef Stefan, Ljubljana, Slovenia, and exposed to 1 MeV equivalent neutron fluences of  $1 \times 10^{12}$ ,  $1 \times 10^{13}$ ,  $3 \times 10^{13}$  and  $1 \times 10^{14} \text{ cm}^{-2}$  within the EU-FP7 Project AIDA. An additional sample without radiation exposure is available for reference. The irradiated detectors were kept at temperatures of around  $-20^\circ \text{C}$ . During testing they were handled at room temperature. The temperatures are logged to take into account annealing effects. The detectors were finally installed into circuit boards and complemented with front-end electronics. They will be

operated in a beam test with 2.4 GeV protons scheduled for January 2012 at COSY, Research Center Jülich, Germany. A tracking telescope will be set up consisting of three stations of silicon microstrip detectors read out with self-triggering front-end electronics based on the *n*-XYTER chip. Two stations were already operated there in 2010 [4]. The third station will comprise the FSD-CBM04 detectors under test. The measurement programme aims at the determination of the charge collection efficiency and charge distribution onto neighbouring strips as a function of the detectors’ neutron exposure and operating conditions.

In preparation of the next full-size prototype microstrip detector CBM05, we investigated the short circuits in the AC coupling layer of the current full-size prototype CBM03 [2, 3]. The thin oxide layer was identified to be shorted in certain areas. This may be due to the quite complex structure of the detector. The processing steps for 19 masks, including the two metal layers per side, may have introduced stress there. A more sturdy layout including a slightly increased thickness of some of the layers was proposed for the next prototype. Several technological tests are in preparation, reusing the masks of layout CBM03 for the production of a single-sided prototype CBM03’. After having evaluated this intermediate prototype in the beginning of 2012, we will launch the production of a batch of the next double-sided full-size prototype CBM05. Like the previous prototype it comprises  $2 \times 1024$  strips of 58  $\mu\text{m}$  pitch arranged under a stereo angle of  $\pm 7.5^\circ$  on an area of 62 mm by 62 mm. The detector is laid out for readout connections at its top and bottom edge, involving double-metal interconnections of the corner strips so that sectors of daisy-chained detectors can be built and arranged on the Silicon Tracker’s ladders.

### References

- [1] <http://www.cismst.de>
- [2] J. M. Heuser *et al.*, CBM Progress Report 2009, Darmstadt 2010, p. 10
- [3] J. M. Heuser *et al.*, CBM Progress Report 2010, Darmstadt 2011, p. 8
- [4] J. M. Heuser *et al.*, CBM Progress Report 2010, Darmstadt 2011, p. 19

## Performance of prototype Silicon Tracking Detectors for the CBM experiment

*H. Shang<sup>1</sup>, I. Sorokin<sup>2,3</sup>, J. M. Heuser<sup>4</sup>, and T. Balog<sup>4,5</sup>*

<sup>1</sup>Tsinghua University, Beijing, China; <sup>2</sup>FIAS, Goethe-Universität, Frankfurt, Germany; <sup>3</sup>KINR, Kiev, Ukraine; <sup>4</sup>GSI, Darmstadt, Germany; <sup>5</sup>Comenius University, Bratislava, Slovakia

Four demonstrator boards (named *2b-4 N001 ... N004*) were produced by SE SRTIIE in Kharkiv, Ukraine. Each of the boards integrated a double-sided CBM02-SPID detector with 256 strips on each side. The demonstrators were intended to be used in the upcoming beamtimes as reference tracking detectors and were tested in the laboratory therefore.

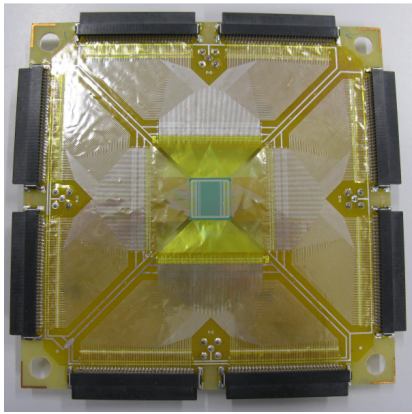


Figure 1: Demonstrator board *2b-4 N001*, n-side view

First, the detectors were checked for defects in the DC-decoupling capacitors. Only one strip with a defect was found among the four boards.

Then, current-voltage characteristics were measured. The full depletion kink, when observed, appeared around 80 V, as expected. The leakage current did not exceed  $1 \mu\text{A}$  at 100 V (the operating voltage), which is normal.

One of the boards, the *2b-4 N003*, was installed into a detector station with n-XYTER-based readout [1] and tested with a  $\beta$ -source ( $^{90}\text{Sr}$ ). After subtracting the slow shaper DC offsets (i. e. pedestals), clusters of various sizes (1 to 5) were reconstructed and the total signal amplitude was determined. The recent n-XYTER calibration [2] was applied. The measurement was repeated for a range of bias voltages (Fig. 3).

The signal amplitude after full depletion is compatible with the expected value of about  $21.7 \text{ ke}^-$  (assuming 95% charge collection efficiency). The operating voltage of 100 V is proven to be a suitable value. The noise level in the assembled system was below  $150 \text{ e}^-$  in most of the channels, which is much better than required.

The prepared detector system is going to be used as a reference tracking station in the upcoming beam tests.

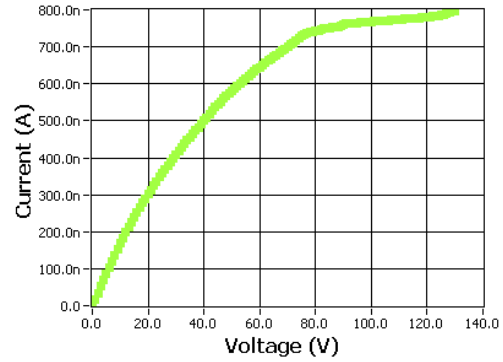


Figure 2: Current-voltage characteristic of *2b-4 N003*

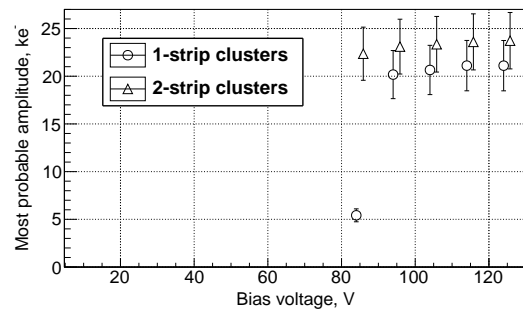
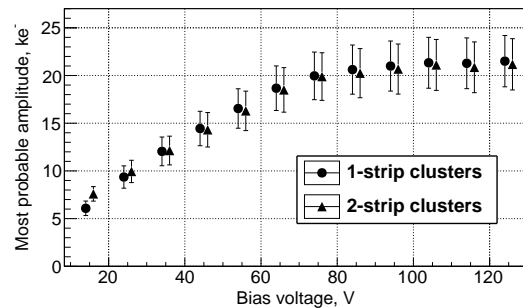


Figure 3: Signal amplitude vs. bias voltage on p- (top) and n-side (bottom) of demonstrator *2b-4 N003*. The points are shifted by  $\pm 1 \text{ V}$  from the original positions (15, 25, ... 125) for readability. Only the calibration uncertainty is shown.

### References

- [1] A. S. Brogna *et al.*, Nucl. Instrum. Methods **A 568** (2006) 301
- [2] T. Balog and A. Lymanets, *Calibration of the n-XYTER front-end chip*, this report

## First experience in prototyping detector modules for the CBM STS

Yu. A. Murin<sup>1</sup>, V. A. Vasendina<sup>1</sup>, V. A. Budilov<sup>1</sup>, S. N. Igolkin<sup>2</sup>, D. E. Karmanov<sup>3</sup>, V. Lenok<sup>1,3</sup>, M. M. Merkin<sup>3</sup>, N. N. Egorov<sup>4</sup>, S. A. Golubkov<sup>4</sup>, V. M. Borshchov<sup>5</sup>, M. A. Protsenko<sup>5</sup>, I. T. Tymchuk<sup>5</sup>, and J. Heuser<sup>6</sup>

<sup>1</sup>JINR, Dubna, Russia; <sup>2</sup>St. Petersburg State University, St. Petersburg, Russia; <sup>3</sup>SINP, Moscow State University, Moscow, Russia; <sup>4</sup>RIMST, Zelenograd, Russia; <sup>5</sup>SE SRTIIE, Kharkov, Ukraine; <sup>6</sup>GSI, Darmstadt, Germany

In 2011, the partners of the CBM-MPD STS Consortium assembled the first electromechanical prototypes of sensitive modules for the CBM and MPD Silicon Tracking Systems [1]. The prototypes were composed of double-sided silicon strip detectors manufactured by RIMST (Russia), ultra thin flat aluminium cables manufactured by SE SRTIIE (Ukraine) and contained elements of ultra-lightweight support structures designed and fabricated at SPbSU (Russia). The work was patronized and coordinated by JINR. The prototypes were assembled at SE SRTIIE and certified at SINP MSU. Several assembled prototypes are depicted in Fig. 1.

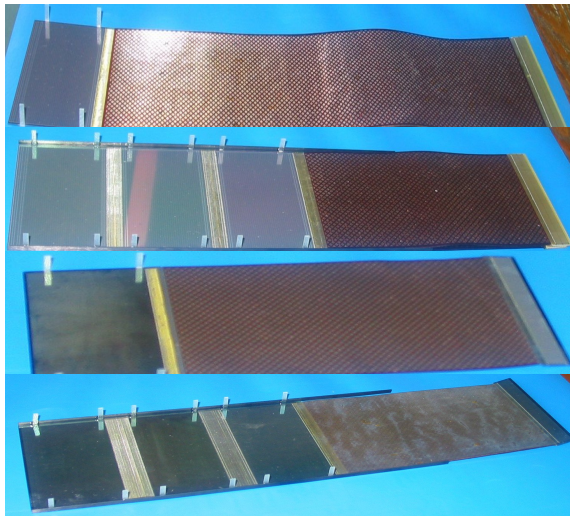


Figure 1: Prototypes of CBM STS modules

The sensors are fixed on carbon fiber support ladders [2] with glass-fiber L-like miniature fixtures as shown in Fig. 2.

All components and the assembled prototypes underwent electric testing, which made it possible to evaluate the quality of the parts and of the assembly as well as to coordinate the test procedures. The tests of the cables showed their high quality: the defect ratio due to wire breaks or shorts was below 1%. The broken-through channels ratio in the detector prototypes was below 1% as well. The tests also revealed a considerable number of breaks and punctures in the double metallization layers of the silicon detectors as well as the poor quality of metallization of con-

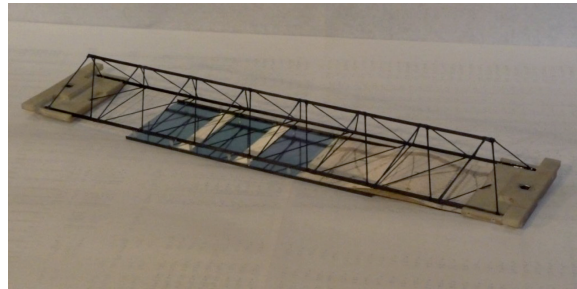


Figure 2: Prototype of a CBM-STS ladder, or super module, with one detector module comprising a daisy chain of three sensors

tact pads of the strips. The three kinds of defects: broken-through channels, loose connections to the strips and inter-strip shorts caused a significant increase in the yield of faulty ladder prototypes (up to 10% through each kind of defect). We consider the inter-channel shorts as caused by the double metallization punctures on the sensor since the number of shorts in the cables before assembling was less than 1%. The experience gained during the tests of the sensors, ribbon cables and ladder assemblies showed that the optimum procedure for testing the assembled ladders should be as follows:

- Measurement of the capacitance of the strips' coupling capacitors without bias voltage to an accuracy of better than 1 pF.
- Measurement of the leakage currents of the coupling capacitors at bias voltage with a picoammeter to an accuracy of better than 100 pA.
- In testing ribbon cables, one may only use a capacitance meter. The breaks and shorts of the lines are detected by the decreased or increased capacitances.
- The detector testing procedure should include testing of double metallization, which was underrated for the detector samples used.

## References

- [1] <http://sts-crimea11.jinr.ru/> and links therein
- [2] S. N. Igolkin, Yu. A. Murin and S. N. Vinogradov, *Pre-production of ultra-light carbon fiber support frames for the CBM-STs*, this report

## Pre-production of ultra-light carbon fiber support frames for the CBM-STS

*S. N. Igolkin<sup>1</sup>, Yu. A. Murin<sup>2</sup>, and S. N. Vinogradov<sup>3</sup>*

<sup>1</sup>St. Petersburg State University, St. Petersburg, Russia; <sup>2</sup>JINR, Dubna, Russia; <sup>3</sup>Meson Ltd., St. Petersburg, Russia

The fabrication technique for the production of light-weight carbon fiber supports was developed and tested in a pre-production of twelve frames specifically designed for the CBM Silicon Tracking System. The technology inherited from the previous experience with ALICE ITS frames [1] is based on a one-cycle polymerization process at 125°C in a metallic mold and enables the fabrication of space frames of irregular shapes. The M55J carbon fiber and the HM45J115REC prepreg from Toray Industries Inc. [2] was used in the process.

A set of fabrication tools is shown in Fig. 1. The sequence of the space frame fabrication is as follows:

- the surfaces of the mold contacting with the compound are coated with an antiblocking agent;
- the carbon fiber impregnated with an epoxy compound is laid in the grooves of the female mold;
- the carbon prepreg, ground contact pads, and the nameplates with frame numbers are laid on the tips of the male parts of the mold;
- the molds are assembled; the processor and the thermocouple are connected to the mold, and the electrical heaters located on the mould walls are switched on;
- the mold is heated to 50°C over 15 min. At this stage the male parts of the mold are pressed against the female ones with the pressure tube;
- the carbon fiber is polymerized at 120-125°C over 1.5 hours;
- the mold is disassembled with the heaters switched on and the frame is picked off;
- after pre-examination, the frame is cleared of the remains of the binder agent;
- the frame is tested and certified.

An optimized version of the frame is shown in Fig. 2. The edges of the frames fabricated with the use of the precision molds are linear within 100 μm, their base sides are flat within 50 μm. Such a 1000 mm long frame weights 14 g.

### References

- [1] Russian Federation Patent No. 2008132135 (27.12.2008); Russian Federation Patent No. 2396168 (10.09.2010)
- [2] <http://www.torayca.com>

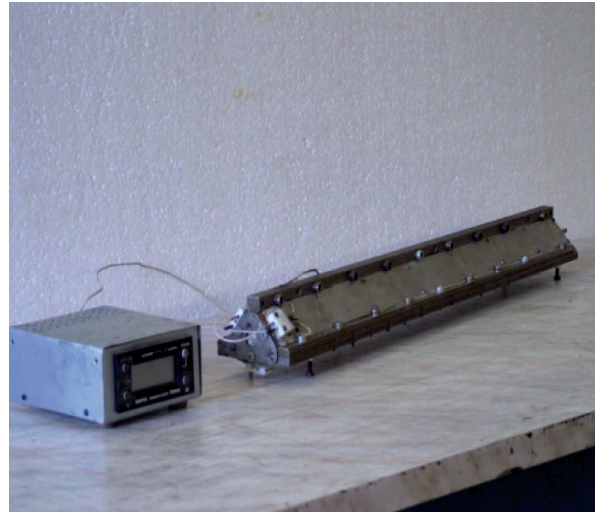


Figure 1: Assembled mold and processor

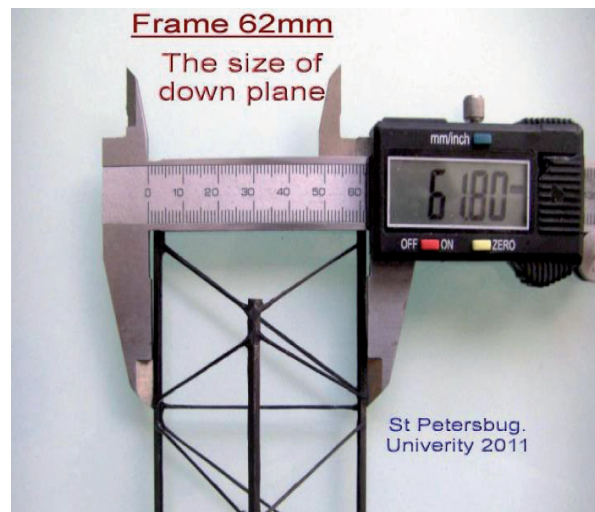


Figure 2: Measuring the critical dimensions of the first optimized STS space frame

## A study of heat simulators of front-end information processing boards for the CBM-STS

V. M. Borshchov<sup>1</sup>, M. A. Protsenko<sup>1</sup>, I. T. Tymchuk<sup>1</sup>, A. V. Tsenner<sup>1</sup>, Yu. A. Murin<sup>2</sup>, and V. A. Vasendina<sup>2</sup>

<sup>1</sup>SE SRTIIE, Kharkov, Ukraine; <sup>2</sup>JINR, Dubna, Russia

The spatial arrangement of the components of the front-end electronics boards and their thermal conditions were prototyped to develop an effective method of heat removal from the chips. The work undertaken within the work plan of the CBM-MPD STS Consortium [1] was patronized and coordinated by JINR (Russia). The heat simulators were designed, assembled and tested at SE SRTIIE (Ukraine). The overall dimensions of the boards shown in Fig. 1 were  $65 \times 30 \text{ mm}^2$ .

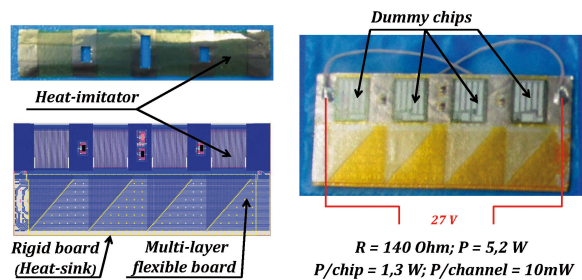


Figure 1: Layout and photograph of the simulator

The heat simulators were manufactured from the following components:

- a multilayer flexible board assembled with the use of ultrasonic welding and gluing;
- dummy chips (0.4 mm thick silicon);
- a 0.3 mm thick rigid base board (heat sink) made either from aluminum or from carbon plastic;
- a  $140 \Omega$  resistive board with a power dissipation of 5.2 W at 27 V (1.3 W per chip, 10 mW per channel).

The temperatures measured on the surfaces of the dummy chips as a function of time are shown in Figs. 1 and 2. The conditions of heat removing in these measurements were as follows: Ch No1 – carbon plastic heat sink and Ch No2 – aluminium heat sink. D1 – measurements for the two dummy chips situated near the board's edges with an additional heating from only one neighbor chip; D2 – measurements for the two central chips with an additional heating from two neighbor chips. The top panel of Fig. 2 presents results for simulators without any additional heat sink, the bottom panel for simulators with an additional heat sink (2 mm thick copper plate) attached to the simulator.

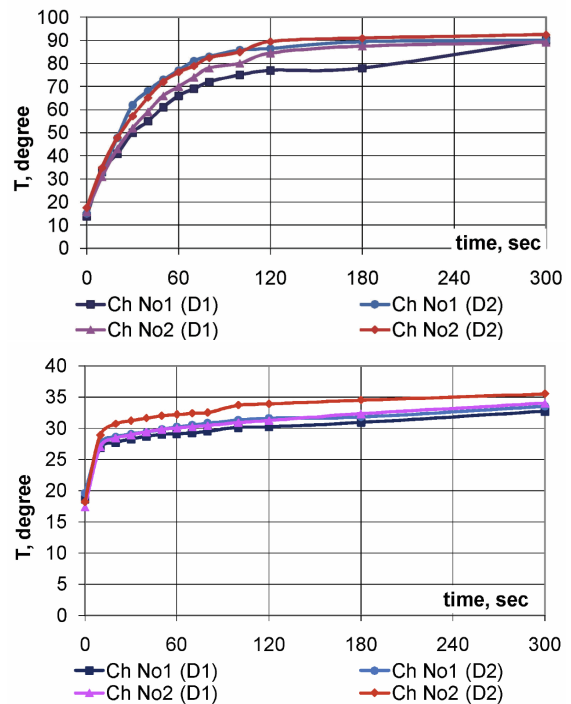


Figure 2: Temperature response of simulators without (top) and with heat sinks (bottom)

The temperature measurements performed with the manufactured simulators demonstrated the feasibility of the polyamide multilayer technology for the production of front-end readout boards with a level of heat release from the read-out chips as expected for the CBM-STS front-end electronics. Both aluminium or carbon fiber rigid plates may be used as primary heat sinks (bridges) for heat evacuation from the ASIC chips to the cooled-off elements of the liquid cooling system of the CBM-STS.

### References

- [1] <http://sts-crimea11.jinr.ru/> and links therein

## Element of protection circuitry for high-voltage detectors in the CBM experiment

*Yu. Bocharov, V. Butuzov, D. Osipov, and A. Simakov*

National Research Nuclear University MEPhI, Moscow, Russia

The design team from National Research Nuclear University MEPhI takes part in the development of front-end ASICs for the CBM Silicon Tracking System [1, 2, 3, 4]. High-voltage protective devices were developed and manufactured at NRNU MEPhI. More than 60,000 of these fuses are successfully used at CERN. These unique devices play a key role ensuring a safe operation of the TRT detector in the ATLAS experiment. Figure 1 shows the cross section of the developed fuse.

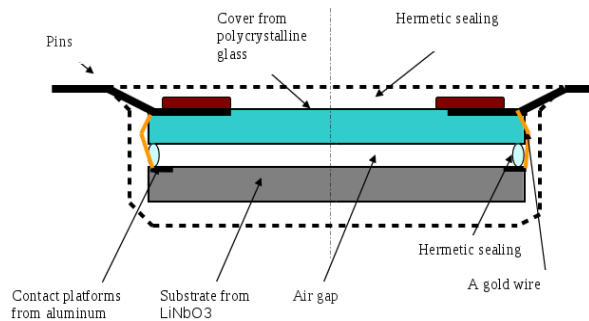


Figure 1: Cross section of the developed fuse

The thin-film fuse uses a  $\text{LiNbO}_3$  substrate of  $5 \text{ mm} \times 3 \text{ mm} \times 1 \text{ mm}$ . The active element is a specially shaped titanium strip of  $9 \mu\text{m}$  width and  $9.5 \text{ mm}$  length with aluminum contacts manufactured by a thermal deposition and a photolithography.

The cover from polycrystalline glass provides both mechanical durability of the fuse and an air gap for the removal of thermal explosion products from the surface of the substrate. The fuse has a double hermetic sealing. This

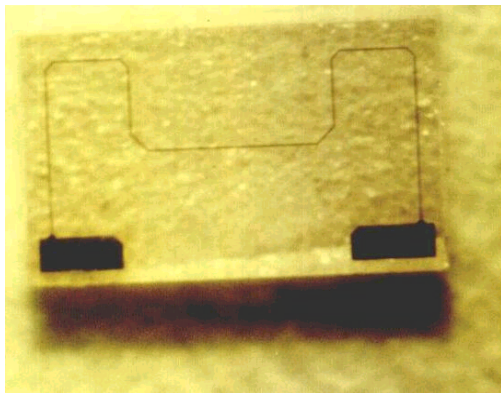


Figure 2: Micro photo of the die

provides an extremely high resistance of more than  $10^{12} \Omega$  and a very low leakage current of less than  $1 \text{ nA}$  at a operational voltage of  $1.5 \text{ kV}$ . Figure 2 shows a micro photo of the die. The fuses after packaging are shown in Fig. 3.



Figure 3: The fuses after packaging

The fuses have the following features:

- A wide range of resistance (up to  $100 \text{ k}\Omega$ ),
- high initial accuracy and long-term stability of the resistance,
- small overall dimensions – less than  $5.8 \text{ mm} \times 3.8 \text{ mm} \times 2 \text{ mm}$ ,
- short reaction time.

The developed device can be efficiently used in protection circuitry of the CBM experiment. Large-volume production of the developed high-voltage fuses is started at NRNU MEPhI.

### References

- [1] E. Atkin *et al.*, CBM Progress Report 2010, Darmstadt 2011, p. 23
- [2] E. Atkin *et al.*, Instrum. Exp. Tech. **53** (2010) 524
- [3] Yu. Bocharov *et al.*, *A Low-Power 9-bit Pipelined CMOS ADC with Amplifier and Comparator Sharing Technique*, 37th Solid-State Circuits Conference (ESSCIRC 2011), 12–16 September 2011, Helsinki, Finland  
<http://www.esscirc2011.org/fringe.php>
- [4] Yu. Bocharov *et al.*, *A Low-Power 9-bit Pipelined CMOS ADC for the front-end electronics of the Silicon Tracking System*, XXIII International Symposium on Nuclear Electronics and Computing (NEC 2011), 12-19 September 2011, Varna, Bulgaria

## 3D simulations of low-mass, low-noise analog readout cables for the CBM Silicon Tracking System

*M. Singla<sup>1</sup>, S. Chatterji<sup>2</sup>, W. F. J. Mueller<sup>2</sup>, V. Kleipa<sup>2</sup>, and J. M. Heuser<sup>2</sup>*

<sup>1</sup>Goethe-Universität, Frankfurt, Germany; <sup>2</sup>GSI, Darmstadt, Germany

In the CBM Silicon Tracking System, Kapton cables are used to transfer signals from the sensors to the front-end electronics which is mounted outside the fiducial region. Simulations of these Kapton cables were performed with Raphael, a subpackage of Synopsys TCAD. The purpose of these simulations is to optimize the cables so as to reduce the capacitive and resistive load from these cables on the front-end electronics. For the validation of Raphael, Kapton cables from the D0 experiment were simulated and compared to ANSYS simulations reported in [1]. A good agreement between the two simulations (within several percent) was found.

For the equivalent noise charge (ENC) calculations [2], it is important to determine the contribution of the cables since their lengths could reach up to 50 cm for the inner modules of the CBM tracking system. Keeping various factors in mind including low radiation length, we explored several designs with aluminum and copper traces. An optimum was found with copper traces having a cross-section of  $16 \mu\text{m} \times 8 \mu\text{m}$ . As shown in Fig. 1, the ENC of the optimized design is about 25% less than the current prototype, while maintaining the same material budget. Its capacitance is 0.6 pF/cm, to be compared to 0.95 pF/cm for the present design.

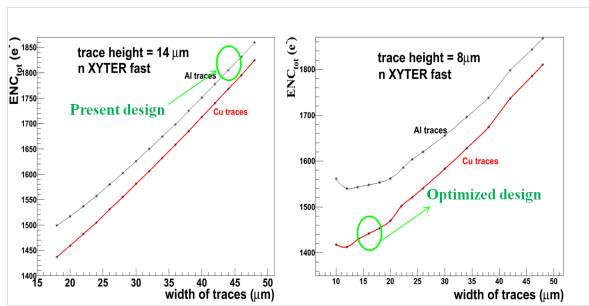


Figure 1: Total ENC as function of trace width for the CBM Kapton cables with a trace height of  $14 \mu\text{m}$  (left) and  $8 \mu\text{m}$  (right)

A SPICE model was implemented in the TCAD package Sentaurus Device to study the transmission losses in the cable. Figure 2 shows the input and output pulses at 81 MHz and 320 MHz. For higher frequencies, the signal amplitude decreases and the pulse broadens at the input of the front-end electronics which may lead to charge loss depending on the RC time constant of the shaper. Figure 3 (left panel) shows the schematics of the cable trans-

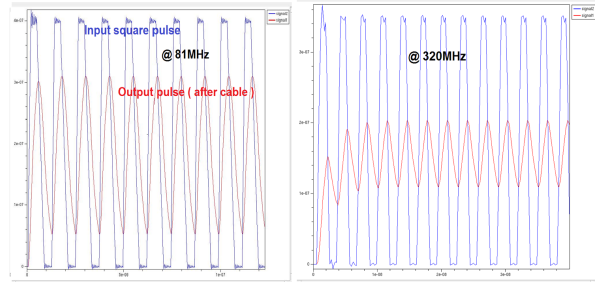


Figure 2: Transmission losses in the cable at a frequency of 81 MHz (left) and 320 MHz (right)

mission line connected to the silicon detector and (right panel) the transmission losses versus frequency in the optimized design of a copper cable. The losses in the expected frequency range of the CBM front-end electronics (20 ns shaping time, 25 MHz), would result in a transmission of about 85%.

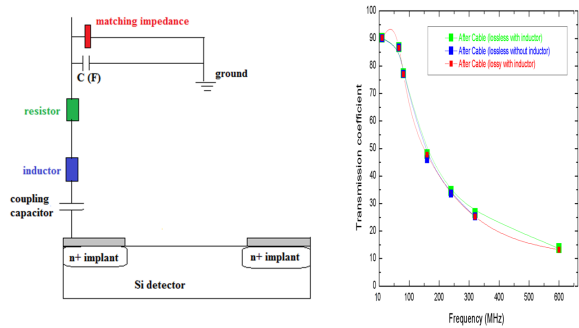


Figure 3: Schematics of cable transmission line (left) and transmission as function of frequency in the optimized cable design with Cu traces (right)

### References

- [1] K. Hanagaki, Nucl. Instrum. Methods A **511** (2003) 121
- [2] <http://pdg.lbl.gov/2010/reviews/rpp2010-rev-particle-detectors-accel.pdf>

## Calibration of the n-XYTER front-end chip

*T. Balog<sup>1,2</sup> and A. Lymanets<sup>3,4</sup>*

<sup>1</sup>GSI, Darmstadt, Germany; <sup>2</sup>Comenius University, Bratislava, Slovakia; <sup>3</sup>Goethe-Universität, Frankfurt, Germany; <sup>4</sup>Kiev Institute for Nuclear Research, Kiev, Ukraine

The self-triggering n-XYTER chip was developed for neutron physics experiments and is used also for early prototyping of several CBM detectors [1]. For a detailed understanding of the performance of the detectors, a calibration of the charge conversion is needed. In the following we describe a calibration with externally pulsed signals as a general means of characterizing the behaviour of the front-end electronics.

Charge injected into the front-end electronics can be realized through a known voltage step  $\Delta V$  over a known capacitance  $C$ . The input charge is then

$$\Delta Q = C \cdot \Delta V. \quad (1)$$

As a pulse generator, the model Philips PM 5786 was used. This allowed to create input pulses with a rise time of 10 ns and a duration of 1  $\mu$ s, as expected from silicon microstrip detectors. In the electronics a short rise time is needed to create a signal that can be easily measured by the fast shaper of each channel, having a shaping time of 19 ns. The pulse length is needed for the measurement of the proper signal amplitude in the slow shaper of each channel, with a shaping time of about 200 ns.

The output voltage of the generator can be adjusted between 128 mV and 5 V. Attenuators were used to reduce the signal amplitude into the dynamic range of the chip. With different combinations of 20 dB and 10 dB attenuators, the signal amplitude was reduced by factors of 105, 330 and 1090, respectively.

For the voltage-to-charge conversion, a capacitance of 1 pF was used. This value is not the effective one, since one has to consider also parasitic capacitances. The total capacitance was determined with an LCR meter as  $C = (2.3 \pm 0.2)$  pF.

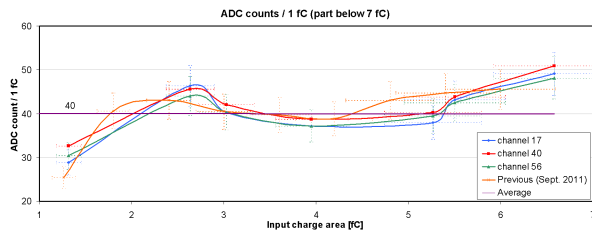


Figure 1: Energy calibration: ADC counts per 1 fC

The calibration was performed in September 2011 and in December 2011 for different n-XYTER front-end boards. No significant change between the measurements was observed. The ADC energy calibration is shown in Figs. 1

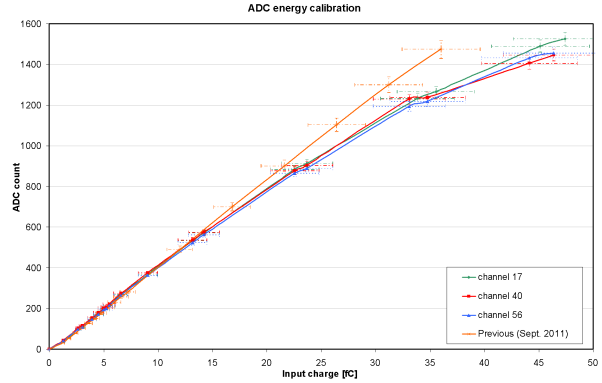


Figure 2: Energy calibration: ADC counts vs. charge

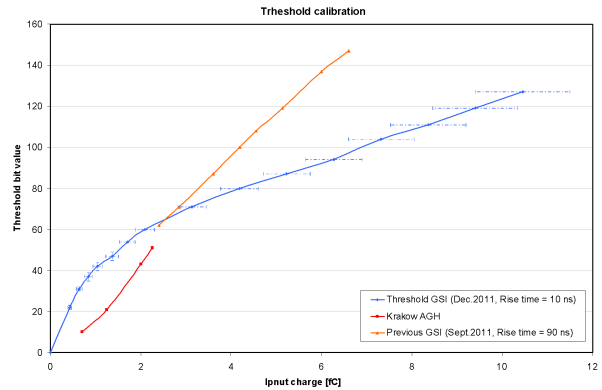


Figure 3: Threshold calibration of the n-XYTER chip

and 2, the threshold calibration in Fig. 3.

For one minimum ionizing particle (charge equal to 3.8 fC), an average ADC value of 145 was observed. Applied to the data from double-sided silicon microstrip detectors of the beam test of December 2010 [2], this leads to a charge collection efficiency of approximately 95%.

## References

- [1] J. M. Heuser *et al.*, CBM Progress Report 2009, Darmstadt 2010, p. 8
- [2] J. M. Heuser *et al.*, CBM Progress Report 2010, Darmstadt 2011, p. 19



## Performance of the n-XYTER chip with external triggering

*J. Heuser<sup>1</sup>, V. Kyva<sup>2</sup>, H. Malygina<sup>2,3</sup>, V. Militsiya<sup>2</sup>, Y. Panasenko<sup>2</sup>, V. Pugatch<sup>2</sup>, and I. Sorokin<sup>2,3</sup>*

<sup>1</sup>GSI, Darmstadt, Germany; <sup>2</sup>KINR, Kyiv, Ukraine; <sup>3</sup>Goethe-Universität, Frankfurt, Germany

A double-sided prototype microstrip detector *CBM02-B2* and the n-XYTER-chip were used for this study. The n-XYTER [1] is a front-end detector readout ASIC that integrates 128 channels, each of them consisting of a low-noise preamplifier and two shapers, a fast one (19 ns) and a slow one (139 ns). The n-XYTER has two operation modes: a self-triggering mode and an external triggering mode.

We used a radioactive  $\beta$ -source  $^{90}\text{Sr}$ - $^{90}\text{Y}$ , which has a continuous spectrum up to 2.2 MeV. After passing through the thin silicon sensor, the electrons were registered by a plastic scintillator. This scintillator triggered the n-XYTER processing of the signal from the silicon sensor. In the given experimental setup, we had a trigger time delay of less than 50 ns, excluding the ROC (read-out controller) delay. The scheme allowed us simulating the detection of minimum ionizing particles (MIPs) by selecting only high-energy electrons with  $E \geq 1$  MeV. Since the peaking time of the n-XYTER's slow shaper is 139 ns, a 50 ns delay (Fig. 1, filled histogram) is appropriate for the external trigger. In this case a Landau-like spectrum is obtained from the MIPs. However, when the delay time is increased to 133 ns, no distinct-shape spectrum can be seen (Fig. 1, black histogram). Further increase up to 200 ns leads to the noise spectrum (Fig. 1, dashed histogram).

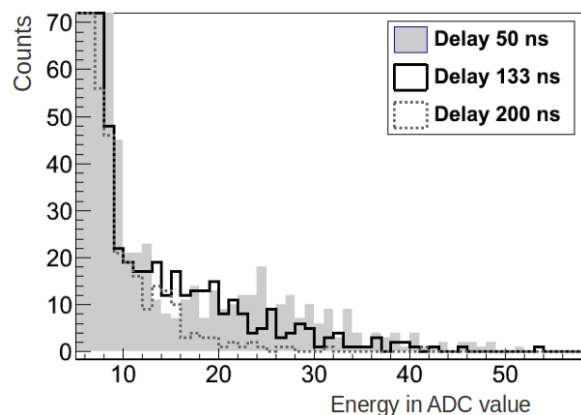


Figure 1: Energy spectrum of electrons with  $E \geq 1$  MeV from one of the detector strips for different delays

Even in the case of 50 ns delay, the spectrum is not a pure Landau-distribution. This is because each MIP deposits the charge onto more than one strip. Thus, one needs to search for the distributed charge among several adjacent strips — a cluster. However, it is difficult to precisely de-

fine clusters. This is due to the fact that in our test set-up, every second readout channel has a higher noise than its neighbour channels. Such an unexpected noise behaviour was concealed in the design of the microcable [2] that connects the silicon sensor with the n-XYTER. The cable has a specific two-layer structure, which leads thereafter to the higher noise in half of the strips and complicates clusters finding. This was corrected in a later cable design.

We investigated the dependence of the signal amplitude on the trigger delay time. A pulser generated both a square signal (near 200 mV) and a trigger signal (1.5 V) simultaneously. The square signal was then transferred through the attenuator to one of the channels of the n-XYTER. For the trigger signal we were able to change its delay time. For each new value of this delay we measured the amplitude of the measured resulting signal delivered by the n-XYTER chip. To achieve zero trigger delay we used an additional delay of the square signal with effectively no trailing edge. As it can be clearly seen from Fig. 2, a 10 ns trigger delay does not affect the resulting signal amplitude.

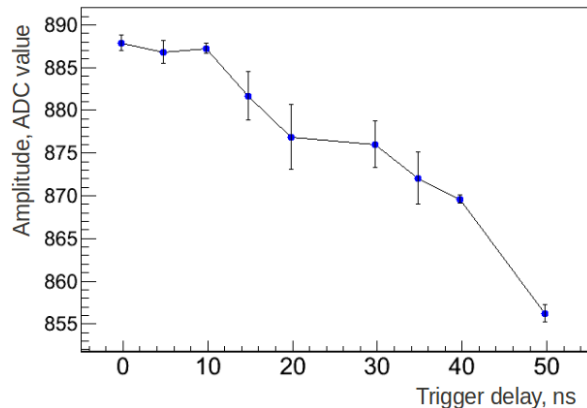


Figure 2: The resulting signal amplitude as function of the trigger delay (not including the delay inside the read-out controller). The displayed errors are statistical.

## References

- [1] A. S. Bronga *et al.*, Nucl. Instrum. Methods **A 568** (2006) 301
- [2] V. M. Borshchov *et al.*, CBM Progress Report 2009, Darmstadt 2010, p. 15

# Rice formula applicability for noise rate estimation in the CBM and other experiments with self-triggered electronics: comparing the calculation to a measurement on example of the n-XYTER chip

I. Sorokin<sup>1,2</sup>, W. F. J. Müller<sup>3</sup>, and C. J. Schmidt<sup>3</sup>

<sup>1</sup>Goethe-Universität, Frankfurt, Germany; <sup>2</sup>KINR, Kiev, Ukraine; <sup>3</sup>GSI, Darmstadt, Germany

Self-triggered electronics is a natural solution for high-rate experiments with Poisson-like distributed events. One of the problems which arise when using self-triggered electronics is fake hits due to noise. In a self-triggered system a noise hit is generated as soon as the instantaneous noise amplitude exceeds the threshold. This is in contrast to conventionally triggered systems, where a noise hit is generated only when a noise fluctuation coincides with the trigger. A triggered system is therefore inherently protected against fake hits.

When designing a self-triggered system, the expected noise rate has to be estimated and taken into account. Underestimating the noise rate may result in overloading the data acquisition system and excessive background, whereas overestimating it may lower the efficiency.

Assuming a Gaussian noise with dispersion  $\sigma$ , the noise rate can be estimated with the Rice formula [1]

$$f_t = \frac{f_0}{2} \exp\left(-\frac{\nu_t^2}{2\sigma^2}\right), \quad (1)$$

where  $\nu_t$  is the threshold,  $f_t$  the threshold crossing rate, which the noise rate equals to provided the dead time is small, and  $f_0$  the zero crossing rate, which depends on the system bandwidth. For a simple CR-(RC)<sup>3</sup> shaper with rise time  $\tau$ , the zero crossing rate is given by [1]

$$f_0 = \frac{1}{\pi\tau}. \quad (2)$$

The applicability of the Rice formula to real systems was tested on example of the n-XYTER chip [2]. A large and stable-in-time noise was induced on a single n-XYTER channel by loading the input with 10 pF capacitance in series with 15.4 k $\Omega$  resistance. The noise rate was measured as a function of the `vth` threshold register. In order to compare the measurement to the Rice formula, the induced noise needed to be known in units of `vth`, and it was measured in the following way: the n-XYTER internal test pulse generator was enabled and the pulse detection efficiency was measured as a function of `vth`; the dependence was fitted with an error function, and the  $\sigma$  parameter of the error function was taken as noise. In addition, the threshold offset (i. e. the physical threshold in units of `vth` at `vth`=0) had to be determined. For this, the latter procedure was repeated with various pulse amplitudes  $A$ , but now we extracted the *mean* parameter of the error function, which is the pulse amplitude  $A_{vth}$  in units of `vth`. The threshold offset was evaluated by extrapolating  $A_{vth}(A)$  to  $A = 0$ . For

a rough estimate of the  $f_0$  parameter, eq. (2) was applied (even though the fast shaper of the n-XYTER is in fact a CR-RC type with a rise time of  $\tau_{fast} = 19$  ns), obtaining  $f_0 = 16.8$  MHz.

Figure 1 compares the measured noise rate to the expectation obtained from the RICE formula (1). Taking into account the simplicity of the model and the fact that no model parameters were fit to the measurement, the observed agreement over six orders of magnitude in rate is considered to be surprisingly good. We conclude that the Rice formula can be used for noise rate estimates in designing self-triggered readout systems for future experiments.

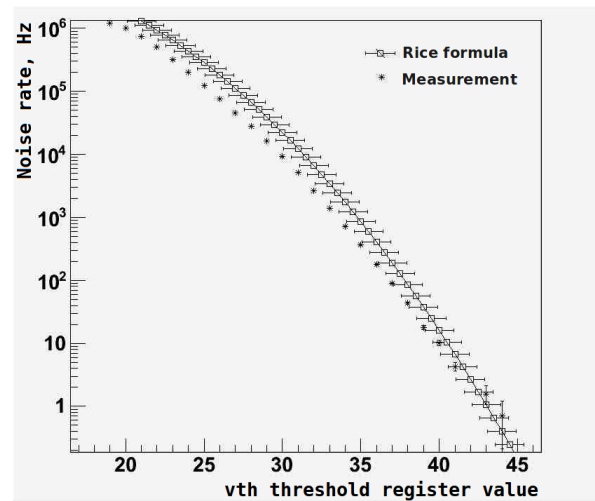


Figure 1: Comparison of the Rice formula calculation to the measurement

## References

- [1] S. O. Rice, Bell Syst. Tech. J. **23** (1944) 282
- [2] A S. Brogna *et al.*, Nucl. Instrum. Methods **A 568** (2006) 301

## Development of a 512-channel front-end board with 4 n-XYTER2 chips

*O. Torheim, V. Kleipa, C. J. Schmidt, and J. Heuser*

GSI, Darmstadt, Germany

Towards obtaining a sufficiently compact layout for the front end boards (FEB) of the CBM Silicon Tracking System, a prototype FEB with 512 input channels equipped with 4 n-XYTER2 readout chips has been developed. The goal of the FEB development effort is to arrive with a design suitable for placing 1024 readout channels, contained in 8 forthcoming CBM-STs readout chips, on a board of about 6 cm width and a similar, minimum height, respecting reasonable constraints on manufacturing (cable and chip bonding), power consumption and data transmission. Compared to existing n-XYTER chips, the CBM-STs chips will be an improvement in terms of reduced power consumption and more compact bonding area. With the CBM-STs chip still to be designed, the current work with compacting the FEBs is based on the last n-XYTER chip, the n-XYTER2, and on conventional PCB design constraints (0.1 mm minimum pitch and microvias of 0.1 mm diameter).

The planned FEB interfaces the STS with a microcable of 120  $\mu\text{m}$  pitch. To arrive with bonding at a much more relaxed pitch, a contact scheme was developed where the cable attaches the PCB in a slanted manner. As a first step of proofing the principle, the cable bonding is to be separately tested. The test board comprises 128 signal lines that in the receiving end interfaces the microcable and in the transmitting end uses conventional connectors of small foot print to interface to already existing n-XYTER FEBs in order to enable the signal integrity test. The microcable connects to a CBM02 prototype microstrip detector.

On the FEB, the n-XYTER chips are mounted into a hole to profit from wire bonding towards two PCB layers, thus realizing a dense layout. We adopt to this scheme also on the test board by routing the first cable layer directly to the first wire row at the PCB top layer, while the second layer of the cable is taken down to the second PCB layer using microvias, and then routed to the second row of landing pads. This is illustrated in Fig. 1.

Our PCB layout software allows routing through scripting. With footprint arrangement and routing performed through C++ generated scripts, one has full freedom to experiment with compactifying the layout and optimizing width and spacing to preferred design rules.

The new n-XYTER2 based FEBs interface the data acquisition system through two VHDCI connectors. The height of two stacked VHDCI connectors was assumed as a board height constraint for the new 4-chip board. Using this constraint, the layout was fulfilled with excellent margins (Fig. 2).

The analog power supply splits into separate domains

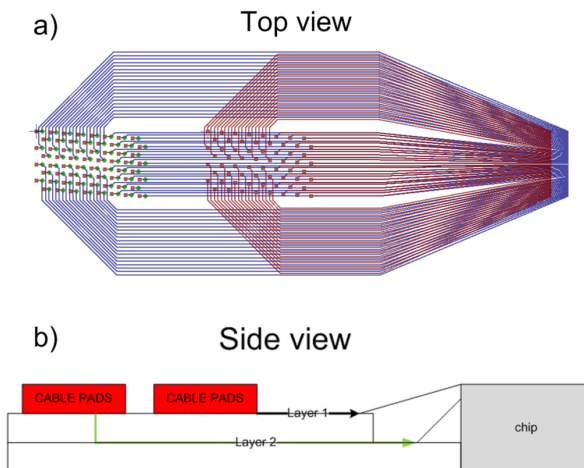


Figure 1: Routing from cable landing pads to chip pads

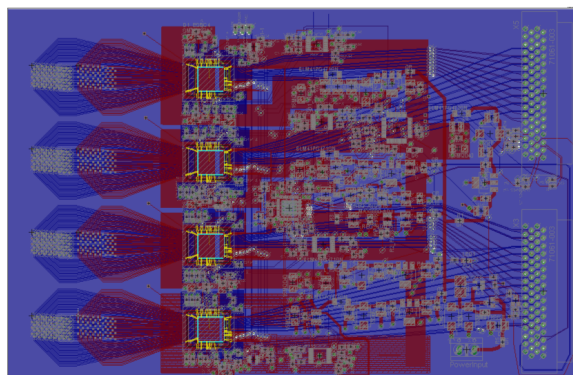


Figure 2: Board layout

for the ADC and each of the n-XYTER chips, minimizing noise and crosstalk, while a common power supply is used for digital signals. The digital power enters the chip with separate fingers which at the same time separates the analog plane shapes from each others. Hence, only two layers are used for power and ground distribution.

An Atmel AVR microcontroller controls and configures the four n-XYTER2 chips and other auxiliary units through I<sup>2</sup>C and SPI interfaces. For the conversion of the sampled data, the four chips share one common ADC.

## Comparison of the SPADIC and n-XYTER self-triggered front-end chips

T. Balog<sup>1,2</sup>, W. F. J. Müller<sup>1</sup>, and C. J. Schmidt<sup>1</sup>

<sup>1</sup>GSI, Darmstadt, Germany; <sup>2</sup>Comenius University, Bratislava, Slovakia

For the detectors of the CBM experiment, high-rate, low-power and low-noise readout ASICs are needed. Since the Poisson-distributed collisions between the nuclei are not correlated to a global trigger signal, the readout ASICs for both the detectors as well as the data acquisition system itself must be self-triggered.

The n-XYTER chip was developed for neutron experiments and nowadays it is also used for early prototyping of the CBM detectors [1]. The performance of such a self-triggered front-end electronics was studied in the last year [2]. The SPADIC chip [3] was designed for the readout of the CBM transition radiation detectors.

The main difference between the chips is in the data storing and ordering mechanism. The n-XYTER chip applies a Token Ring while the SPADIC chip uses an ordering FIFO to aggregate data from all channels into a single output. The Token Ring loops over all channels and if there is any data in a channel FIFO, it reads it in and continues in the next period from the next channel. Data do not come out time ordered and time re-sorting is needed at a later stage. This disadvantage is supposed to be eliminated by an ordering FIFO in the SPADIC chip. When a channel carries a signal, it is (if possible) stored in the channel FIFO and at the same moment there is an input information sent to the ordering FIFO. The FIFO is checked at each time period and the channels are read-out according to the information from this particular FIFO. Such a reading can lead to unexpected higher losses in the SPADIC chip and its performance has to be simulated therefore.

The study of data loss was performed in the SystemC description language which is built on the C++ standard. Both the n-XYTER and the SPADIC chips were simulated with the same amount of channels and the same channel FIFO depth (in this case 7), with the same clock. The proper size of the ordering FIFO and the comparison of the performance of both chips under the same conditions was studied. The results are shown in Figs. 1 and 2.

For a proper performance of the SPADIC chip even at low data input frequencies, the size of the ordering FIFO has to be at least 80% of all cells in all channel FIFOs. The ordering FIFO and Token Ring reading mechanisms do not show any significant change in performance at different frequencies. The key advantage of the ordering FIFO approach is that data are sent time ordered by the front-end chip, which eliminates the need for resorting in later DAQ stages.

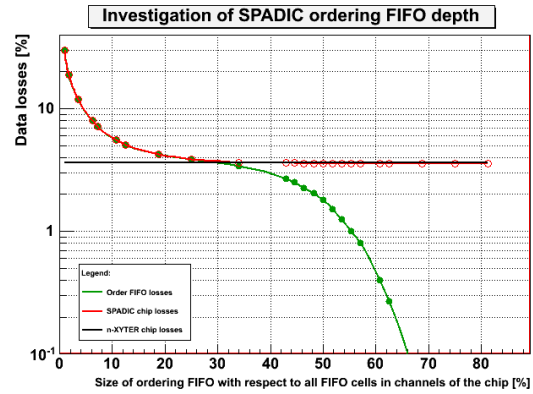


Figure 1: Comparison of the data loss in SPADIC and n-XYTER as function of the size of the ordering FIFO for a data input-to-output frequency ratio of 1.032 (to obtain data loss). The n-XYTER losses are taken as reference.

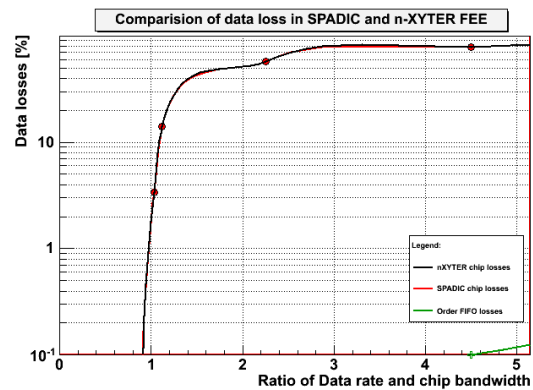


Figure 2: Comparison of SPADIC and n-XYTER data loss at different input frequencies. The size of the SPADIC's ordering FIFO is 80%.

## References

- [1] J. M. Heuser *et al.*, CBM Progress Report 2009, Darmstadt 2010, p. 8
- [2] T. Balog *et al.*, CBM Progress Report 2010, Darmstadt 2011, p. 21
- [3] T. Armbruster, P. Fischer and I. Peric, *SPADIC – A Self-Triggered Pulse Amplification and Digitization ASIC*, NSS Conference Record, 2010 IEEE, Knoxville, USA, November 2010, p. 1358

## Radiation-tolerant operation of a commercial micro controller for applications in front-end electronics

*V. Kleipa*

GSI, Darmstadt, Germany

The next version of front-end electronics boards to be utilized for the prototype detector development of e. g. the CBM experiment will comprise a micro controller (MCU) for the slow controls of the system. The selected micro controller is a state-of-the-art MCU without any specific radiation qualifications. It is required to determine the radiation tolerance of this device. Moreover, a new concept of runtime software needs to be verified. The idea is to reinitialize the MCU just before any slow control command is sent to the MCU and then executed. Single event upsets (SEUs) that might have occurred will thus be removed before a new command request is executed. A RISC micro controller - Atmel ATtiny88 [1] - with Harvard architecture was selected. The program ROM is based on a flash memory. A RISC instruction set supports single cycle executions at 8 MHz clock frequency.

A printed circuit board was designed and assembled comprising an ATtiny chip. The MCU is placed in the middle of the board as shown in Fig. 1. The PCB features a cut-out just below the position of the MCU, and only very few decoupling capacitors are located in its vicinity. This was done to reduce the radiation length and to minimize a possible activation of material in the beam. The MCU is connected via an SPI bus and a reset line to a standard PC

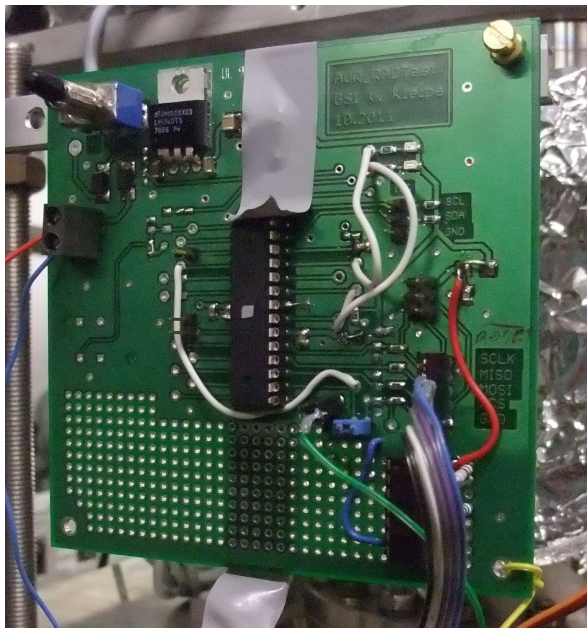


Figure 1: MCU board prepared for the beam test software

printer port. For the beam adjustment, X-ray pictures of the MCU were taken to determine the die position.

The task of the micro controller's software is to receive and to acknowledge the commands sent from the control PC. The reception of the commands and the returned results are checked with additional CRC bytes. A RAM area of 256 bytes is used as a sensor for SEUs and can be filled with bit patterns. During irradiation, this buffer is read out continuously with SPI commands and compared in the PC with the default contents. Communication and RAM content are thus simultaneously checked. SEUs in the RAM or communication errors are recorded in the PC. According to the requirements, the PC can initiate a reboot on the micro controller. The SPI clock is 10  $\mu$ s per bit cycle and the commands to be serviced consist of 2-6 bytes. The MCU rebooting/reset time was reduced from initially 200  $\mu$ s to 15  $\mu$ s. This requires the C compiler pre-initialising the variables to be turned off.

In case of the short reset time, it is straightforward to execute a complete MCU reset before a slow control command is sent. The advantage is a high probability of a SEU-cleaned micro controller.

The micro controller and the software will be tested in beam in order to determine its radiation tolerance. Observables will be for instance SEUs and single-event latches (SELs). The runtime software itself, with fast reboot, will also be tested under real conditions.

### References

- [1] [http://www.atmel.com/dyn/resources/prod\\_documents/doc8008.pdf](http://www.atmel.com/dyn/resources/prod_documents/doc8008.pdf)

## Database development for the CBM Silicon Tracking System

R. Nath<sup>1</sup>, S. Chatterji<sup>2</sup>, and J. M. Heuser<sup>2</sup>

<sup>1</sup>Mody Institute of Technology and Sciences, Lakshmanagarh, India; <sup>2</sup>GSI, Darmstadt, Germany

The purpose of this project is to develop a client-server application for storing quality-assurance data from the production of silicon microstrip detectors for the CBM Silicon Tracking System. For the client side, *php* was used, while for the server side *MySQL* was deployed to design the database. To create the user interface, some forms were designed in *php*, and a connection of the forms to the database was established. In this way, the users just have to choose from a given list of options, and their choice sends a request to the server which in turn searches the database for the most appropriate result to be sent back to the user through the client. The application is also authenticated, and the user has to login or register to get access. Figure 1 shows the welcome page and the registration form.

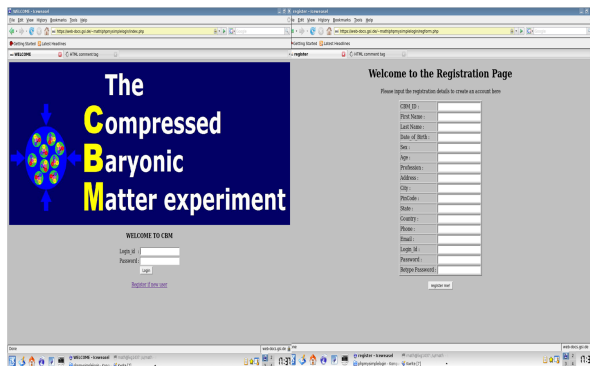


Figure 1: Welcome/Login page of the CBM STS Database

A MySQL server was used to create the database. It is a relational database management system (RDBMS) that runs as a server providing multi-user access to a number of databases. All data are stored in tables, and there are different tables for different types of data. Figure 2 shows such a table written in *MySQL*. One can notice that there are tables for many parameters like current-voltage (I-V), capacitance-voltage (C-V), full depletion, user details and so on. In the bottom of the figure, one can see how the details of the user are entered in *MySQL*.

On the client side *php* was used for designing the user interface. The interface is then connected to the *MySQL* database. Hence, the users cannot see the database directly. They have to request data from the client side, which in this case is the interface designed using *php*. Figure 3 shows how the measured I-V and C-V data can be stored by the user on the client side. One can also extract the stored data from the database by putting some search criterion. As an example, Figure 4 shows how a user can search for stored

```
mysql> show tables;
+-----+
| Tables_in_CBM |
+-----+
| cv           |
| iv           |
| n_cint_v     |
| n_noise      |
| p_cint_v     |
| p_noise      |
| p_rint_v     |
| user         |
| vp           |
+-----+
11 rows in set (0.00 sec)

mysql> desc user;
+-----+-----+-----+-----+-----+-----+
| Field | Type | Null | Key | Default | Extra |
+-----+-----+-----+-----+-----+-----+
| cbm_id | varchar(20) | YES | | NULL | |
| fname | char(20) | YES | | NULL | |
| lname | char(20) | YES | | NULL | |
| DOB | date | YES | | NULL | |
| sex | char(10) | YES | | NULL | |
| age | int(11) | YES | | NULL | |
| profession | char(20) | YES | | NULL | |
| address | varchar(40) | YES | | NULL | |
| city | varchar(20) | YES | | NULL | |
| pincode | double | YES | | NULL | |
| state | varchar(20) | YES | | NULL | |
| country | varchar(30) | YES | | NULL | |
| phone_no | varchar(20) | YES | | NULL | |
| email | varchar(40) | YES | | NULL | |
| login_id | varchar(30) | YES | | NULL | |
| password | varchar(30) | YES | | NULL | |
+-----+-----+-----+-----+-----+-----+
```

Figure 2: A sample *MySQL* table on the server

I-V measured data for measurements done at temperature exceeding  $10^0$  C. The output displays the details of the sensors measured above  $10^0$  C along with other details like full depletion voltage, humidity, date of measurement, fluence and the file path where the data are stored. For collaborative access to the database, a user-friendly web interface was created.

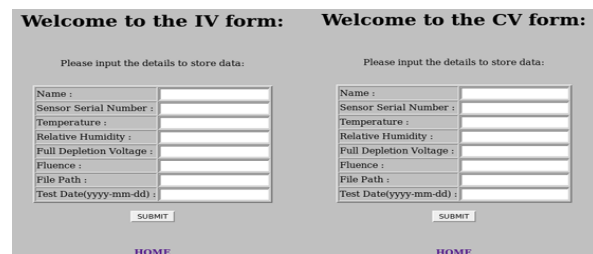


Figure 3: I-V and C-V forms for storing the data of leakage current and backplane capacitance

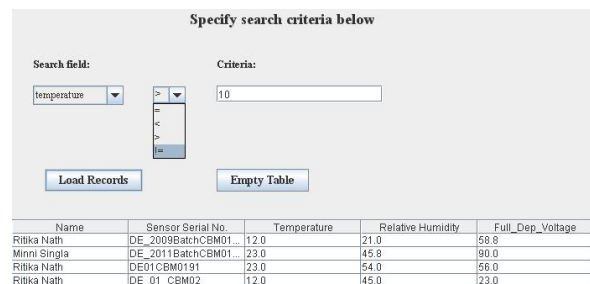


Figure 4: A sample search option in the STS database

## Fiber hodoscopes for beam diagnostic and particle tracking

C. Pauly, K.-H. Kampert, J. Kopfer, J. Pouryamout, J. Rautenberg, and S. Reinecke

Bergische Universität Wuppertal, Germany

Precise knowledge of the beam position and -size as well as single-particle track reconstruction are important prerequisites for accomplishing successful test beam measurements of prototype detectors at CERN-PS, COSY or elsewhere. Scintillating Fiber Hodoscopes (“SciFi hodoscopes”) provide a robust and easy-to-handle solution, with excellent timing properties ( $< 1$  ns), good spatial resolution ( $< 1$  mm), and high rate capabilities ( $> 10^6$  particles/s). Two such compact SciFi hodoscopes were built and successfully tested at CERN and COSY, and are now available for future CBM prototype beam tests.

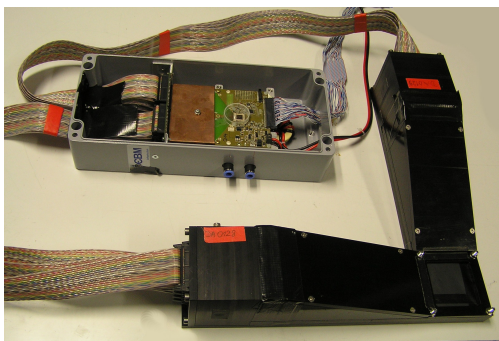


Figure 1: Picture of a complete SciFi hodoscope including electronic box with n-XYTER FEB readout and (copper shielded) attenuator board

Each hodoscope consists of two rectangular arms (see Fig. 1), each of which containing a  $4 \times 64$  fiber ribbon with Bicon BCF-12 single-cladded 1 mm scintillating fibers. The fibers in each ribbon are arranged in 4 interleaved layers of 64 fibers each, each “column” of four fibers forming one readout channel, which results in an effective thickness of  $\approx 3$  mm plastic per layer. The active area of crossing fibers for one hodoscope is roughly  $65 \times 65$  mm<sup>2</sup>.

Each fiber ribbon is read out by a Hamamatsu H8500 MAPMT with 64 channels each and a pixel size of  $5.8 \times 5.8$  mm<sup>2</sup>. The choice of MAPMT is motivated by the CBM-RICH photon detector development [1], which is based on the same type of MAPMT. Good optical coupling to the fibers (glued into a machined and polished PVC matrix) is achieved by using optical grease.

The electronic readout is based on the n-XYTER FEB module, providing 128 channels of amplitude and time information. One such FEB module is sufficient to read out one complete SciFi hodoscope. A modified version of the 128 channels charge attenuator board used in the CBM-RICH photon detector [1], based on the design described in Ref. [2], with an approximate attenuation factor of 500 instead of 50 is used to match the dynamic range of the

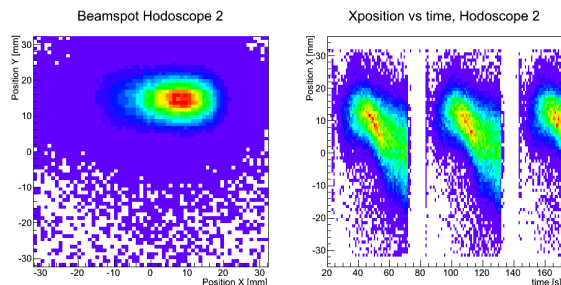


Figure 2: Beam spot as measured with the second Fiber Hodoscope during the COSY beam test in January 2012 (left); variation of the horizontal beam position as function of time during two and a half consecutive COSY cycles (right)

MAPMT signal to the n-XYTER input stage.

On average we expect 15 registered photons per minimum-ionizing particle, corresponding to a charge pulse of 3.5 pC. Custom PCB adapter boards on both ends of the readout chain are used to couple the hodoscope to the FEB module using standard twisted-pair ribbon cables. In addition, the dynode sum signal of each MAPMT is available via a LEMO connector. This allows to easily set up a simple trigger coincidence logic based on the sum signal of each hodoscope arm.

The analysis of the hodoscope data is implemented as a dedicated module within the standard Go4 beamtime analysis framework [3]. After clustering of neighbouring hits in each layer (amplitude splitting between neighbouring fibers is caused by the interleaving ribbon geometry), the hit position per layer is obtained as ADC-weighted mean of all hits in a cluster. This further improves the spatial resolution beyond the fiber spacing of 1 mm.

As an example of the obtained information, Figure 2 (left) shows the integrated beam spot size as measured during a beam test at COSY in January 2012. The larger beam spread in horizontal direction is explained by a shift of beam  $x$  position as function of cycle time as can be also seen from Fig. 2 (right).

## References

- [1] C. Pauly *et al.*, *The photon detection system of the CBM-RICH prototype detector*, this report
- [2] P. Koczon *et al.*, *Readout of the Hamamatsu H8500-03 MAPMT with the n-XYTER chip*, CBM Progress Report 2009, Darmstadt 2010, p. 20
- [3] J. Adamczewski-Musch and S. Linev, *A Go4-based online-analysis framework for CBM beam tests*, this report

## In-beam test of a real-size CBM-RICH prototype at the CERN PS

*J. Kopfer<sup>1</sup>, V. Dobyryn<sup>5</sup>, C. Dritsa<sup>4</sup>, M. Dürr<sup>3</sup>, J. Eschke<sup>2</sup>, I. Galm<sup>3</sup>, C. Höhne<sup>4</sup>, K.-H. Kampert<sup>1</sup>, L. Kochenda<sup>5</sup>, P. Kravtsov<sup>5</sup>, D. Kresan<sup>4</sup>, S. Lebedev<sup>4</sup>, E. Lebedeva<sup>2</sup>, T. Mahmoud<sup>4</sup>, C. Pauly<sup>1</sup>, J. Pouryamout<sup>1</sup>, J. Rautenberg<sup>1</sup>, S. Reinecke<sup>1</sup>, E. Roshchin<sup>5</sup>, V. Samsonov<sup>5</sup>, J. Song<sup>6</sup>, E. Vznuzdaev<sup>5</sup>, M. Vznuzdaev<sup>5</sup>, J. Yi<sup>6</sup>, and I.-K. Yoo<sup>6</sup>*

<sup>1</sup>Bergische Universität, Wuppertal, Germany; <sup>2</sup>GSI, Darmstadt, Germany; <sup>3</sup>Hochschule Esslingen, Esslingen, Germany; <sup>4</sup>Justus-Liebig-Universität, Gießen, Germany; <sup>5</sup>Petersburg Nuclear Physics Institute, St. Petersburg, Russia; <sup>6</sup>Pusan National University, Pusan, Korea

A CBM-RICH prototype, of real size in beam direction, was constructed and tested in a common beam time together with other CBM groups using a secondary beam of negatively charged particles at the CERN PS T9 beamline in October 2011 [1]. Cherenkov rings from electrons, pions and muons could be seen, and valuable data for the evaluation of the gas-, mirror-, and photodetector-system could be collected. The prototype design and first beamtime results will be presented.

As intended for the final CBM-RICH detector, the prototype consists of a gaseous CO<sub>2</sub> radiator volume, VUV mirrors, and a photodetector built from Hamamatsu H8500 multi-anode photomultiplier tubes (MAPMTs). Figure 1 shows a sketch of the detector box. The radiator length is 1.7 m. A computer-controlled gas system keeps the volume of 3.5 m<sup>3</sup> CO<sub>2</sub> clean and dry. During the beamtime O<sub>2</sub> and H<sub>2</sub>O could be kept at 50 ppm and 200 ppm respectively. The detector was operated at 2 mbar over normal pressure, resulting in a pion threshold of 4.65 GeV/c. The four spherical mirrors consist of an Al+MgF<sub>2</sub> coating on a 6 mm thick glass substrate. They have a size of 40 × 40 cm<sup>2</sup> each and radii of 3 m. Every mirror is mounted on three actuators which can be adjusted for alignment. All together they are fixed on a remote-controlled rotatable frame allowing the ring image to be moved to different parts of the photodetector. The photodetector itself consists of 16 H8500 MAPMTs of different type with 1024 channels covering 20 × 20 cm<sup>2</sup> (Fig. 2). The size of the MAPMTs is such that one Cherenkov ring fits on four MAPMTs. Four MAPMTs are covered by a wavelength shifting film (WLS) which absorbs deep UV photons and shifts them to longer wavelengths where the transparency of the MAPMT window and the quantum efficiency of the photocathode is higher. The photodetector is read out via charge-attenuator boards by eight n-XYTER [2] Frontend Boards (FEBs). Online monitoring and online ring fitting is done using the GSI online analysis framework Go4 [3].

During two weeks of beamtime, parameters like particle momentum, position of the ring on the photodetector, position of the Cherenkov cone on the mirrors, gas parameters, and settings of thresholds and HV were varied. From these measurements important quantities regarding the detector performance can be deduced.

Figure 3 displays event-integrated ring images from electrons, muons and pions as well as an electron ring from

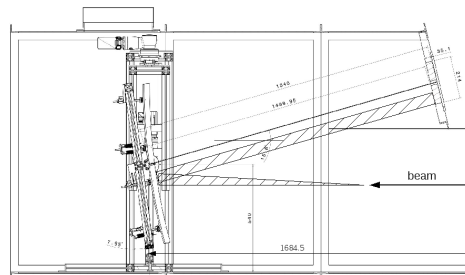


Figure 1: Sketch of the CBM-RICH prototype box with mirrors on a rotatable frame. The photodetector is mounted on the upper right. The hatched area visualizes the Cherenkov cone and its reflection onto the photodetector. The gas system is assembled in a separate rack.

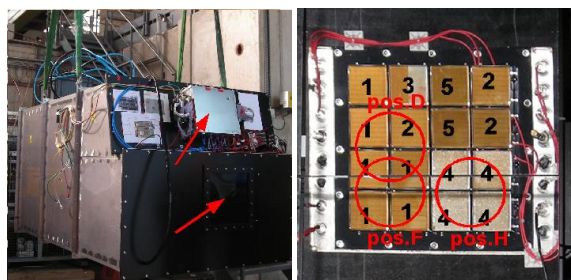


Figure 2: CBM-RICH prototype from the front. The quadractic beam entrance window and the photodetector housing are marked with arrows (left). Photodetector with 16 MAPMTs (right). The numbers refer to five different types of MAPMTs: 1. H8500-03 D, no WLS; 2. H8500-03 C, no WLS; 3. H8500-03 C, 1/2 WLS; 4. H8500-03 D with WLS; 5. H10966, 8 stage, SBA. The WLS film can be recognized by its frosted surface which is seen like this only in the photograph.

a typical single event. The extremely low background noise is due to a very low noise rate of the order of 10 kHz for the whole photodetector, i. e. 10 Hz per channel, and a (still rather wide) timing cut of 500 ns for event selection. In order to quantify the ring size, a ring and ellipse finding algorithm based on a Hough Transform and a ring and ellipse fitting algorithm are applied [5].

In a RICH detector the number of registered photons per



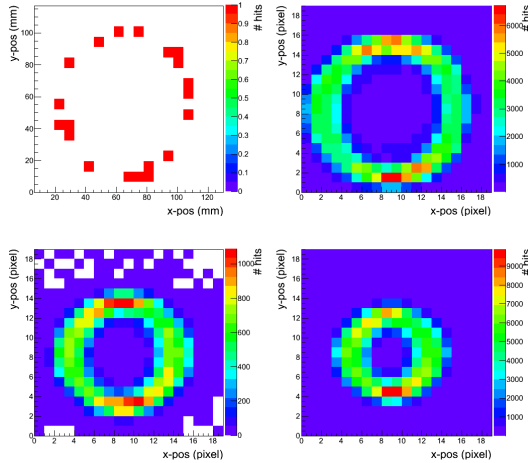


Figure 3: Single-event display of a Cherenkov ring from one electron and accumulated rings from several thousand electrons, muons, and pions at 6 GeV/c (from top left to bottom right)

Cherenkov ring (hit multiplicity) is important for the efficiency of ring finding and the quality of ring fitting. By simply counting the hits per ring, one gets hit multiplicities between 19 and 22 photoelectrons per electron ring depending on the quantum efficiency of the MAPMTs (see Fig. 4, pos.F and pos.D). This is compatible with the expected number of 21 photoelectrons from GEANT simulation [6]. Additional hits in neighbouring pixels due to crosstalk have to be subtracted from the measured numbers. According to an analysis of all 16 MAPMTs with a different data set,  $\approx 12\%$  of the hits are caused by crosstalk. Hence, the crosstalk-corrected hit multiplicities vary between 16.7 and 19.4.

The WLS-coated MAPMTs show enhanced hit multiplicities (Fig. 4, pos.H) when compared to the reference MAPMTs (pos.F). Other MAPMTs with the same characteristics as the reference, however, also show a higher hit multiplicity (pos.D). In order to quantify the effect of the WLS film, the efficiency of every MAPMT will be measured and considered in the analysis.

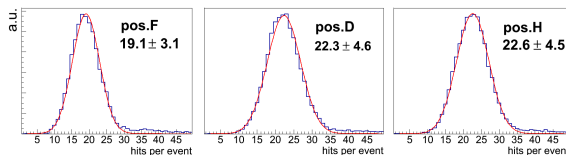


Figure 4: Hit multiplicity for different positions of the ring on the photodetector (cf. Fig. 2)

The momentum of electrons and pions was varied between 2 and 10 GeV/c in steps of 1 GeV/c. Figure 5 shows the simulated and the measured ring radius for electrons and pions as function of particle momentum. A very good agreement between simulation and data is seen. Below the

pion (and muon) threshold only electron rings can be seen. As electrons are ultrarelativistic over the whole momentum range, the electron ring radius is constant with a value of  $\approx 45.5$  mm. Small variations are caused by fluctuations of the refractive index of the radiator due to temperature and pressure variations during the measurement. The data for different momenta were collected over a period of several days and nights. Projecting on the radius one can see that for particles with momenta of 8 GeV/c the separation of electrons and pions is  $> 7\sigma_\pi$  (Fig. 6).

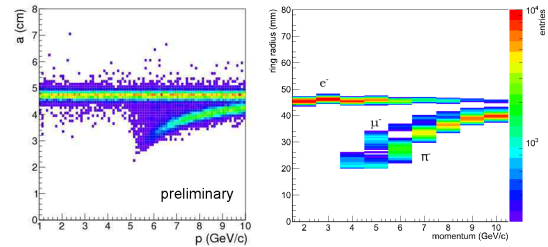


Figure 5: Ring radius for electrons and pions as function of momentum in simulation (left) [4] and data (right). In the data also some muons are visible.

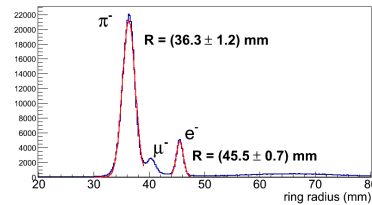


Figure 6: Fitted ring radius for electrons and pions at 8 GeV/c

The authors would like to thank Jörn Adamczewski-Musch and Sergey Linev for setup and operation of the impeccably working DAQ system, Thomas Wasem and Wolfgang Niebur for technical support, Tanya Torres de Heidenreich and Burkhard Kolb for support with the mirror control system and slow control, and Volker Kleipa for help with the electronics.

## References

- [1] C. Bergmann *et al.*, *Common CBM beam test of the RICH, TRD and TOF subsystems at the CERN PS T9 beamline*, this report
- [2] A. S. Brogna *et al.*, *Nucl. Instrum. Methods A* **568** (2006) 301
- [3] J. Adamczewski-Musch and S. Linev, *A Go4-based online-analysis framework for CBM beam tests*, this report
- [4] D. Kresan and C. Höhne, *CBM Progress Report 2010*, Darmstadt 2011, p. 30
- [5] S. Lebedev *et al.*, *J. Phys. Conf. Ser.* **219** (2010) 032015
- [6] C. Höhne *et al.*, *Nucl. Instrum. Methods A* **639** (2011) 294

## Construction of the CBM-RICH prototype detector

T. Mahmoud<sup>1</sup>, W. Niebur<sup>2</sup>, J. Eschke<sup>2</sup>, C. Dritsa<sup>1</sup>, and C. Höhne<sup>1</sup>

<sup>1</sup>Justus-Liebig-Universität, Gießen, Germany; <sup>2</sup>GSI, Darmstadt, Germany

To verify the concept of the CBM-RICH detector [1] and to validate its simulation software, a real-dimension prototype was built and tested at the CERN-PS in fall 2011. The prototype consists mainly of a  $240 \times 120 \times 140 \text{ cm}^3$  body, a mirror system of  $2 \times 2$  mirror segments [2], and a photcamera of  $4 \times 4$  multi-anode photomultipliers (MAPMT) [3]. The relevant dimension of the prototype, i. e. its length, is the same as for the CBM-RICH. The size of the modules is chosen large enough to already study first integration issues for the later full detector. The gas system can later be extended to serve for the CBM-RICH [4].

For simplicity in construction and transportation, the body is divided into three segments (compare Fig. 1 and Fig. 1 in Ref. [5]). Each segment is made of 2 mm thick steal sheets reinforced by 8 mm thick steal beams on the sides. The front and back end covers are made of 15 mm and 10 mm thick plastic sheets, respectively. They enclose the beam entrance and outlet windows, which are made of 2 mm thick plastic sheets. All feedthroughs are located on the back end. The gas in- and outlets go through the front and back ends allowing rapid purging of the gas volume. The front segment holds the camera on a tilted service with an angle of  $74^\circ$  with regard to the  $z$  axis. To ensure gas tightness, self-adhesive cellular rubber strips are placed at the boundaries between the body modules. The inner surface of the prototype body is covered with a black foil to ensure light tightness and absorb photons at the walls. This choice warrants very low outgasing.

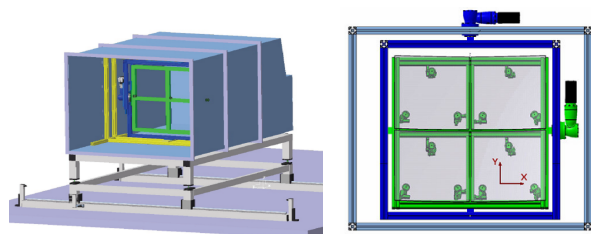


Figure 1: 3D model of the RICH prototype (left); tiltable mirror system (right)

The camera is located at a distance of 1540 mm from the mirror surface although the focal point of the spherical mirrors is  $R/2 = 1500 \text{ mm}$ , with  $R$  being their radius of curvature<sup>1</sup>. The camera [3] consists of different types of MAPMTs, four of which are covered with wavelength-shifting films [6]. With a systematic camera scan enabled by the tiltable mirror frames, the different MAPMTs were tested. The mirror system is located at  $z = 1684 \text{ mm}$

<sup>1</sup>Because of modifications during the construction procedure some dimensions differ slightly from the anticipated values.

from the beam entrance window. It consists of four real-dimension square mirrors with an area of  $40 \times 40 \text{ cm}^2$  each. To enable the camera scan, the mirrors are mounted in two tiltable frames (see Fig. 1) which allow mirror rotations around the  $x$  and  $y$  axes. The rotation is performed with two *Servo Drive A5000* motors with high precision.

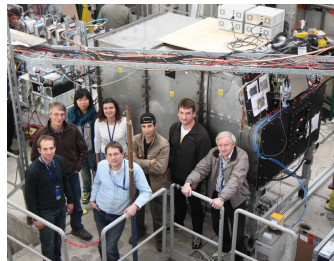


Figure 2: RICH prototype and crew at CERN

The whole prototype is placed on a table which is movable in the  $x$  and  $y$  directions in order to be able to direct the Cherenkov light onto different parts of the mirror assembly. This mirror scan aims at studying the influence of mirror spacing on the number of reflected Cherenkov photons and the influence of mirror displacements and misalignment on the ring quality. In addition to the camera and mirror scans, many other aspects and systematic studies could be addressed with the prototype such as effects of gas purity and gas parameters, trigger thresholds in the electronics and HV for operating the MAPMTs.

Overall, the RICH prototype could be operated very smoothly in the CERN beamtest in October 2011 (Fig. 2), and a large set of systematic studies could be made for which the analysis is still ongoing.

The authors want to thank Mr. R. Weiß, Mr. T. Wasem and the team of the mechanical workshop at the University of Gießen for the excellent construction of the prototype.

### References

- [1] C. Höhne *et al.*, Nucl. Instrum. Methods **A 639** (2011) 294
- [2] V. Dobyryn *et al.*, *Development of a mirror mount system for the CBM-RICH prototype detector*, this report
- [3] C. Pauly *et al.*, *The photon detection system of the CBM-RICH prototype detector*, this report
- [4] L. Kochenda *et al.*, *Beamtest results of the RICH prototype gas system*, this report
- [5] J. Kopfer *et al.*, *In-beam test of a real-size CBM-RICH prototype at the CERN PS*, this report
- [6] I. Galm *et al.*, *Wavelength-shifting films for use on MAPMTs with UV-extended windows*, this report

## The photon detection system of the CBM-RICH prototype detector

C. Pauly, K.-H. Kampert, J. Kopfer, J. Pouryamout, J. Rautenberg, and S. Reinecke

Bergische Universität, Wuppertal, Germany

A major goal of the CBM-RICH prototype test at CERN in October 2011 [1] was to test the Cherenkov photon detection capabilities of the H8500 MAPMT under “realistic conditions”, and the development and test of a design strategy for the full photon detector later to be built. For this purpose, the photon detector of the RICH prototype is based on 16 Hamamatsu H8500 MAPMTs of different types. They are arranged in a 4x4 matrix with 2 mm spacing between the individual tubes. This results in a total active area coverage of 82% (compared to 89% for a single MAPMT). Figure 1 shows a view of the fully equipped photon detector. Some of the MAPMTs (lower right corner) were coated with a wavelength shifter to quantify the effect of WLS usage for real Cherenkov photons.

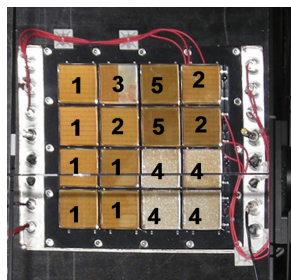


Figure 1: Camera view with 16 MAPMTs installed. The numbers correspond to different versions of H8500 MAPMTs; 4 MAPMTs in the lower right corner were covered with WLS coating.

All MAPMTs were plugged on a custom 4x4 carrier PCB board, which also serves as a gas-tight seal of the radiator gas volume (Figure 2, right). “Plugged vias” were used to assure a gas-tight closing of the PCB vias. Only the MAPMT itself with its (integrated) active voltage divider (ca 0.15 W heat dissipation per MAPMT) is placed inside the radiator volume in this approach, while all readout electronics are kept outside. For H8500D-type MAPMTs even the HV supply was provided via the PCB, avoiding any cable connections inside the radiator vessel. This approach will later be well scalable to larger detector areas.

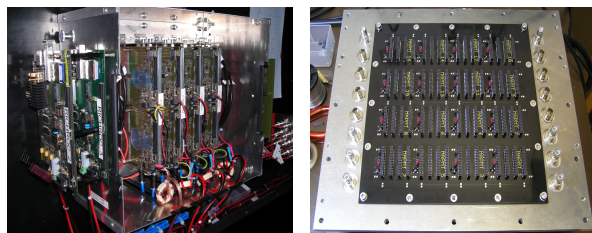


Figure 2: Picture of the photon detector with 4 n-XYTER FEB modules (left) attached to the backside of the PCB carrier board which is shown on the right side.

The signal readout was realized using eight standard n-XYTER FEB modules with 128 channels each together

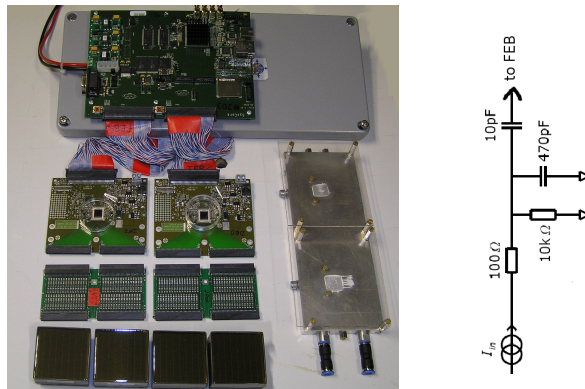


Figure 3: Overview of the complete readout chain consisting of four MAPMTs, two attenuator boards, two n-XYTER FEB modules, water cooling plate, and SysCore ROC. The right side shows a schematic of the charge-attenuator board.

with a special charge-attenuator board to match the dynamic range of the n-XYTER to the H8500 MAPMT (the typical gain is  $1.5 \times 10^6$ ; charge attenuation by a factor of  $\approx 50$  is needed). This technical solution was already tested during previous beam tests, but for the first time the readout electronics could be plugged directly to the back side of the carrier PCB without need for any analog cable connections between MAPMT and FEB. Together with additional copper shields of the sensitive attenuator boards, this resulted in an exceptionally good noise performance: the n-XYTER could be operated at a threshold value as low as 28 (a.u.), and still the overall noise hit rate (including PMT darknoise) was of the order of a few kHz per FEB, corresponding to some 10-30 Hz/channel.

Figure 3 shows a summary of the complete electronic readout chain. Each pair of n-XYTER FEB modules was installed on an aluminum water-cooling heat sink, which also provided mechanical fixation and provided readout of four MAPMTs. An overview of the fully equipped detector box is shown in Fig. 2 (left). The corresponding 4 SysCore ROCs were mounted outside of the box for shielding reasons.

First results of the data analysis are summarized in [2].

### References

- [1] C. Bergmann *et al.*, *Common CBM beam test of the RICH, TRD and TOF subsystems at the CERN PS T9 beamline*, this report
- [2] J. Kopfer *et al.*, *In-beam test of a real-size CBM-RICH prototype at CERN PS*, this report

## Wavelength-shifting films for use on MAPMTs with UV-extended windows

*I. Galm<sup>1</sup>, Th. Schweizer<sup>1</sup>, J. Kopfer<sup>2</sup>, C. Pauly<sup>2</sup>, K.-H. Kampert<sup>2</sup>, and M. Dürr<sup>1</sup>*

<sup>1</sup>Hochschule Esslingen, Esslingen, Germany; <sup>2</sup>Bergische Universität, Wuppertal, Germany

In order to increase the efficiency of photomultiplier tubes (PMT) of Ring Imaging Cherenkov (RICH) detectors, the use of wavelength shifting (WLS) films on top of the PMT windows is an established method [1, 2, 3, 4, 5]. These WLS films typically consist of organic molecules, e. g. p-terphenyl (PT), which absorb light in the UV region and re-emit fluorescence photons at a longer wavelength, ideally at maximum spectral sensitivity of common photocathodes.

So far, the use of WLS films is reported only for PMTs with standard glass windows; furthermore, no data are available for multi-anode photomultiplier tubes (MAPMT) which necessitate different application schemes because of their larger window to be coated when compared with standard PMTs. Here we present first experiments with PT films applied on MAPMTs with windows of which the transmittance is extended to the UV region (UV-extended window).

In Fig. 1, quantum efficiency (QE) measurements of a Hamamatsu H8500-03 MAPMT with an evaporated PT film of approx.  $1 \mu\text{m}$  thickness are compared to the QE of the bare MAPMT. Whereas a significant increase of QE for  $\lambda \leq 250 \text{ nm}$  is observed, the QE is reduced in the wavelength range  $270 \leq \lambda \leq 350 \text{ nm}$ , in contrast to experiments with WLS films on PMTs with standard glass windows, for which such a strong effect was not observed [6].

In order to get a qualitative understanding of this be-

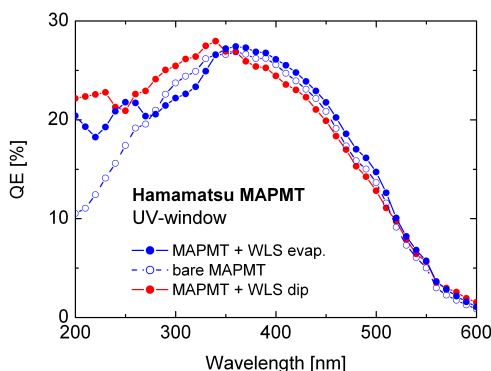


Figure 1: QE curves of a H8500-03 MAPMT with one half coated with an evaporated WLS film (approx.  $1 \mu\text{m}$  thick, blue dots) and one half uncoated (blue circles). The QE measurements of a different H8500-03 MAPMT dip coated with a thin PT/paraloid film (approx.  $0.2 \mu\text{m}$ ) is shown by red dots.

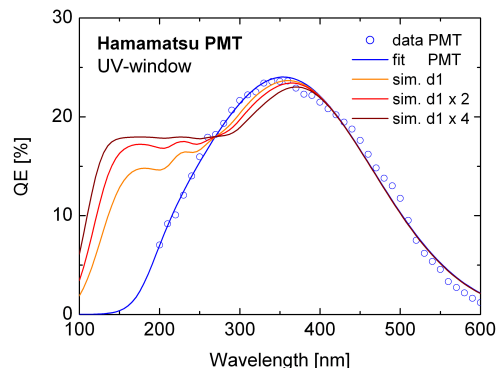


Figure 2: Simulations of QE as a function of wavelength for a PMT with UV-extended window without and with PT coating. The relative layer thickness scales as 1:2:4 with  $d1 \approx 0.1 \mu\text{m}$  of the PT/paraloid film.

havior, the QE on PMTs with UV-extended windows was simulated for different layer thickness based on absorption measurements of PT films as shown in Fig. 2. From these simulations, which do not take scattering effects into account, one can deduce that in the case of PMTs with UV-extended window the absorption of PT leads to a reduction of QE for  $270 \leq \lambda \leq 370 \text{ nm}$ , depending on the thickness of the WLS film. On the other hand, the QE is increasing with increasing layer thickness for  $\lambda \leq 270 \text{ nm}$ . Thus an overall optimized layer thickness is expected for WLS films on PMTs with UV-extended window.

Based on these results, layers of  $\approx 0.2 \mu\text{m}$  thickness were applied on MAPMTs with UV-extended window by means of dip coating from a PT/paraloid/dichloromethane solution. In Fig. 1, QE as a function of wavelength is shown for such a PMT; relatively high QE is observed for  $200 \leq \lambda \leq 350 \text{ nm}$ .

## References

- [1] E. L. Garwin, Y. Tomkiewicz and D. Trines, Nucl. Instrum. Methods **107** (1973) 365
- [2] M. A. F. Alves *et al.*, Nucl. Instrum. Methods **119** (1974) 405
- [3] P. Baillon *et al.*, Nucl. Instrum. Methods **126** (1975) 13
- [4] G. Eigen and E. Lorenz, Nucl. Instrum. Methods **166** (1979) 165
- [5] V. Körstgens *et al.*, Appl. Phys. Lett. **93** (2008) 041916
- [6] C. Höhne *et al.*, Nucl. Instrum. Methods **A 639** (2011) 294

## Measurements of the surface homogeneity for the prototype mirrors of the CBM-RICH detector

*E. Lebedeva<sup>1</sup>, T. Mahmoud<sup>2</sup>, C. Höhne<sup>2</sup>, and M. Dürr<sup>3</sup>*

<sup>1</sup>Goethe-Universität, Frankfurt, Germany; <sup>2</sup>Justus-Liebig-Universität, Gießen, Germany; <sup>3</sup>Hochschule Esslingen, Esslingen, Germany

The CBM RICH detector is designed to provide electron identification in the momentum range of up to 8 GeV/c. It will be operated with CO<sub>2</sub> radiator gas, MAPMTs (Multi-Anode Photo Multiplier) as photodetector and spherical glass mirrors as imaging elements to project the Cherenkov cones as rings on the photodetector. Two properties of the mirrors are of special importance: reflectivity and surface homogeneity. In this article we report about measurements of the latter. Results on reflectivity measurements can be found in Ref. [1].

Figure 1 shows a sketch of the experimental setup for a quantitative measurement of surface homogeneity. It contains a mirror holder with the spherical mirror (a), a laser point source (b), and a CCD camera (c). The Source-Camera (SC) unit is located at a distance which equals the radius of curvature  $R$  of the mirror. The SC is installed on a stepper motor (50 mm range) allowing movement along the optical axis of the mirror. We use an Andor iKon CCD camera with  $1024 \times 1024$  pixels ( $13.3 \times 13.3$  mm<sup>2</sup>) and a laser point source with wavelength 650 nm. Four mirror prototypes ( $40 \times 40$  cm<sup>2</sup>) from SLO Olomouc were tested. They have a (nominal) radius of curvature of  $R = 3$  m and a thickness of 6 mm.

The mirror is illuminated with light from the point source. Ideally the image of the reflected light on the camera chip is pointlike. In reality the image is a non homogeneous spot because of surface inhomogeneities caused by the manufacturing processes. To quantify this surface non-homogeneity, the measure  $D_0$  is used. It is defined as the diameter of the circle which contains 95% of the total light intensity reflected by the mirror.  $D_0$  is expected to be the smallest at a distance of the radius of curvature of the mirror. Two different measurements were done for each mirror: at the nominal radius of 3 m and for the smallest spot of reflected light,  $D_{0,min}$ . Ideally both measurements give the same results. However, in the process of cutting the mirrors to rectangular shape, they can lose some of their concavity leading to a larger radius  $R'$ .

Figure 2 shows the spots of reflected light on the camera chip. The left (right) panel shows the spot with SC at  $R = 3$  m (SC at  $R'$ ). The results for all four mirrors are summarized in Table 1.

All mirrors show very good surface homogeneity ( $D_{0,min} < 1.5$  mm) and have radii slightly larger than 3 m,  $\Delta R$  ranging between 5 and 13 mm. These differences can be taken care of in the mirror mount system. However, at the nominal radius,  $D_0$  is still smaller than 3 mm, which is within the specifications. The tested four mirrors were used for the beam test at CERN in October 2011 [2].

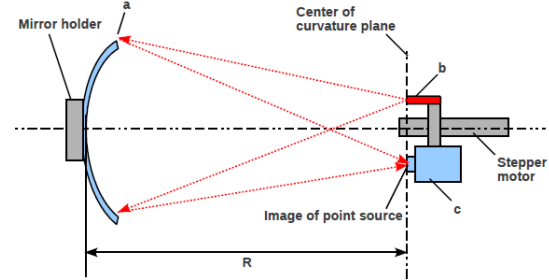


Figure 1: Experimental setup for  $D_0$  measurements

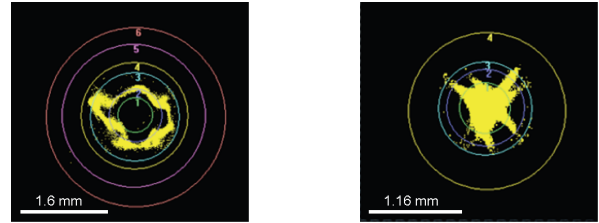


Figure 2: CCD camera view (SP01). Left: for  $R = 3$  m. Right: for the smallest spot.

$D_0$  measurements were also done for a mirror that has been glued to mirror mounts as described in [3]. The corresponding results, also presented in Table 1, demonstrate that the mounting scheme does not cause any significant distortions to the mirror tiles.

Table 1: Summary table of the results of  $D_0$  and mirror radius of curvature measurements ( $\Delta R = R' - R_{\text{nominal}}$ )

Mirror	$D_{0,min}$ [mm]	$\Delta R$ [mm]	$D_0(R = 3 \text{ m})$ [mm]
SP01	1.16	+5	1.60
SP02	1.42	+12	2.58
SP03	0.88	+5	1.81
SP04	1.3	+13	2.89
Mounted	0.98	+3	1.4

## References

- [1] S. Reinecke *et al.*, *Reflectivity measurements of various prototype mirrors for the RICH detector*, this report
- [2] J. Kopfer *et al.*, *In-beam test of a real-size CBM-RICH prototype at the CERN PS*, this report
- [3] V. Dobyryn *et al.*, *Development of a mirror mount system for the CBM-RICH detector*, this report

## Reflectivity measurements of various prototype mirrors for the RICH detector

*S. Reinecke, K.-H. Kampert, J. Kopfer, C. Pauly, J. Pouryamout, and J. Rautenberg*

Bergische Universität, Wuppertal, Germany

After first measurements in 2008 [1], three different prototype mirrors from Compass, Flabeg and SLO Olomouc were finally characterised to determine the optimal candidate for the CBM-RICH detector [2]. Two important parts of this characterisation are the absolute measurement of reflectivity (i. e. comparison of the light spectrum with and without the mirror) in the spectral range from 200 nm to 800 nm and the spatially-resolved measurement of reflectivity using a reflection probe, which allows to efficiently measure the reflectivity as function of the position on the mirror.

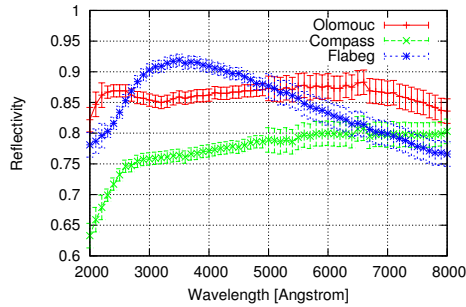


Figure 1: Reflectivities of the three mirror prototypes

The absolute measurements show different results for the three mirrors (Fig. 1). Obviously, the Compass mirror shows the worst reflectivity. For quantitative evaluation the results are folded with the Cherenkov spectrum

$$\frac{dN}{d\lambda} = -\frac{2\pi\alpha z^2}{\lambda^2} \cdot \left[1 - \frac{1}{\beta^2 \cdot n^2(\lambda)}\right] \cdot L \quad (1)$$

Here  $\alpha$  denotes Sommerfeld's fine-structure constant,  $z$  the charge number,  $\beta$  the velocity,  $n$  the refractive index of the Cherenkov radiator and  $L$  the length of the radiator. For simplification we assume  $z = 1$ ,  $\beta = 1$ ,  $n(\text{CO}_2) = 1.00043$  and  $L = 1.5$  m. With these values, we estimate  $\approx 225$  generated photons, out of which  $171 \pm 3$  (only systematic error) would be reflected by the Compass mirror,  $196 \pm 3$  by the Flabeg mirror and  $198 \pm 3$  by the Olomouc mirror. Absorption by the gas and detector efficiency are not considered.

Based on these results, as well as on measurements of  $D_0$  to judge the surface homogeneity [3], additional mirrors were ordered from SLO and tested. According to these tests, all SLO mirrors are of similar quality (Fig. 2).

With the usage of a reflection probe, the reflectivity on 25 dedicated positions of the mirror was measured relative to a calibration mirror of known reflectivity. From this the homogeneity of the reflective coating can be estimated.

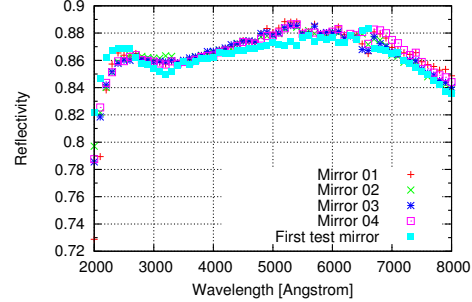


Figure 2: Reflectivities of the Olomouc mirrors

Figure 3 shows the position-dependent reflectivity measurement of one Olomouc mirror at 2000 Å. We observe only small variations in reflectivity of up to 3%. The variations become little larger at short wavelengths ( $< 2500$  Å), but are still small. The mirrors provided by Compass and Flabeg perform worse in this test compared to the mirror from Olomouc.

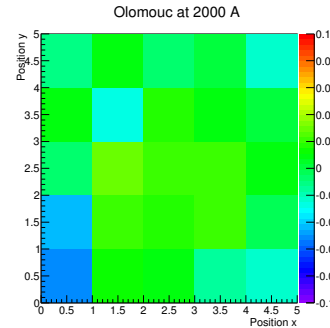


Figure 3: Position-dependent reflectivity of one Olomouc mirror at 2000 Å, relative to the mean value

All results demonstrate that the mirrors from Olomouc are best suited regarding the requirements for the CBM-RICH detector.

### References

- [1] M. Dürr *et al.*, CBM Progress Report 2008, Darmstadt 2009, p. 21
- [2] S. Reinecke, *Charakterisierung von Spiegeln für den RICH-Detektor von CBM*, Diploma thesis, Bergische Universität Wuppertal, October 2011
- [3] E. Lebedeva *et al.*, *Measurements on the surface homogeneity for the prototype mirrors of the CBM-RICH detector*, this report

## Development of a mirror mount system for the CBM-RICH prototype detector

V. Dobyryn, V. Evseev, N. Miftakhov, V. Polyakov, E. Rostchin, G. Rybakov, V. Samsonov,  
O. Tarasenkova, V. Tolchin, E. Vznuzdaev, and M. Vznuzdaev

PNPI, Gatchina, Russia

For the segmented RICH mirror, a mounting system for the mirror tiles has to be developed which does not add any deformation but allows an independent adjustment of each segment to a common spherical surface. First design ideas could be tested in the RICH prototype. The developed and implemented mount system is based on a triangular layout shown in Fig. 1 (left). Each point of attachment has several degrees of freedom as indicated in the figure. This layout differs slightly from the original proposal [1], however presents a more symmetric design. According to calculations this geometry provides at maximum 4-5  $\mu\text{m}$  deviation along the radius of the mirror tile, which would correspond to a contribution of 500  $\mu\text{m}$  only to the  $D_0$  value [2].

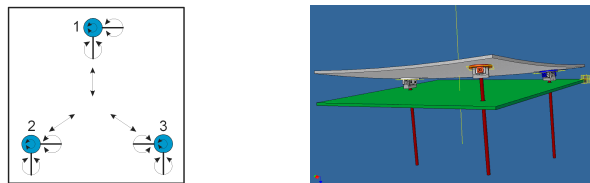


Figure 1: Kinematical scheme of the mirror mount (left) and kinematical model of the mount system (right)

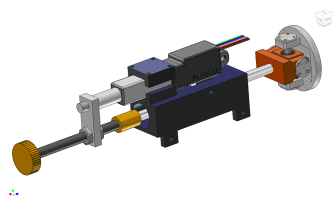


Figure 2: CAD model of the mirror mount

The mount design itself consists of a double cardan shaft connected to the mirror tile through a ring plate which is glued on the mirror tiles (see Fig. 2). A rotatable rod connects the mount support and the cardan shaft. This rod is movable by either the manual screw or a linear actuator of Fircelli (L12 type) which is fixed on a support in parallel to this screw. The actuator is controlled remotely and requires a power supply of +6 V and a control voltage of (0 – 5) V. The Fircelli L12 type linear actuator [3] was chosen because of offering moderate backlash and sufficient retentivity at a reasonable price. Remote operation of the actuators was provided using a test control system on the base of NI-USB 6008 DAQ devices [5]. The usage of remotely controlled actuators will allow for mirror (mis-)alignment during the RICH prototype operation in order to develop specifications for the alignment of the final RICH mirrors.

Attaching three of those mounts to a mirror tile is a complex mechanism with implicit kinematical properties. A movement of any mount along its axis calls the response of the other two mounts. A 3-D kinematical model for the mount system using simplified but adequate kinematics with the real hardware design was built in Autodesk Inventor 2009 in order to verify that no stress arises in this system (Fig. 1 (right)).

First, only one prototype mirror was tested with this mounting scheme. The  $D_0$  measurement showed no deviation from the unmounted mirror indicating that indeed these mirror mounts cause no deviations to the tiles [2]. Testing the full range of movements of the screws ( $\pm 15$  mm), no mechanical problems occurred. Based on these results an assembly of four mirrors was mounted for the RICH prototype in an aluminum frame [4]. Fig. 3 shows the final assembly. Gaps of approximately 6 mm were left between the mirror tiles in order to prevent them from touching during actuator movements. For the RICH prototype operation, the four mirrors could be aligned successfully on a common sphere. Light from a point source illuminating all mirror tiles was reflected back into a circle of 5 mm only. In future the mount system will be further optimized and simplified for the usage for the CBM RICH.



Figure 3: Prototype mirror assembly; the mirrors are already glued to the holders.

### References

- [1] E. Vznuzdaev *et al.*, CBM Progress Report 2010, Darmstadt 2011, p. 33
- [2] E. Lebedeva *et al.*, *Measurements of the surface homogeneity for the prototype mirrors of the CBM-RICH detector*, this report
- [3] Fircelli Technologies Inc., <http://www.fircelli.com>
- [4] T. Mahmoud *et al.*, *Construction of the CBM-RICH prototype detector*, this report
- [5] National Instruments Corporation, <http://www.ni.com>

## Beamtest results of the RICH prototype gas system

L. Kochenda<sup>1</sup>, P. Kravtsov<sup>1</sup>, T. Mahmoud<sup>3</sup>, J. Eschke<sup>2</sup>, C. Drita<sup>3</sup>, and C. Höhne<sup>3</sup>

<sup>1</sup>PNPI, Gatchina, Russia; <sup>2</sup>GSI, Darmstadt, Germany; <sup>3</sup>Justus-Liebig-Universität, Gießen, Germany

The CBM RICH prototype gas system [1] was built to provide pure CO<sub>2</sub> gas to the RICH prototype at a constant differential pressure of about 2 mbar. During the beamtest in October 2011 at CERN we had a good opportunity to test the gas system. The major task was to check the differential pressure stability of the RICH prototype during the recirculation mode in stable operation. To stabilize the differential pressure in the RICH vessel (PT4) we used our slow control system [2] instead of a dedicated Tescom PID controller which is used in the recirculation gas systems for the STAR and PHENIX detectors [3, 4, 5]. It proved reasonable to use this slow control system which is operating the mass controller to stabilize the internal detector pressure by adding more or less fresh pure gas (carbon dioxide). Figure 1 features the results of our pressure regulation. Obviously the differential pressure of the RICH prototype was stable at  $2.0 \pm 0.1$  mbar although the barometric pressure PTB varied in a range of 22 mbar. We see the same result for the STAR and PHENIX gas systems, in spite of the different control technique. For the STAR and PHENIX gas systems mass controllers were used to prepare the fresh mixture with a very stable content. The fresh mixture was added to the gas systems at a constant flow, and therefore the pressure of the detector was stabilized using a dedicated PID-controller in the recirculation mode.

The efficiency of the gas system dryer and purifier was also checked. These units remove moisture and oxygen from the recirculation flow. The dryer was filled with Zeolite NaX and the purifier with pure copper.

The test results are shown in Fig. 2. It should be mentioned that the inner RICH prototype surface was not passed through a special cleaning process, and we had a lot of water and oxygen adsorbed by the walls of the RICH vessel and inner structure elements. Even at these conditions, both the dryer and the purifier had enough efficiency to remove moisture and oxygen to the required level. The gas system was also used to add a certain amount of oxygen in order to check the detector operation at higher oxygen content (spikes in oxygen line in Fig. 2 at day 4). Oscillations of the moisture content are caused by the daily temperature change in the hall.

In general, the gas system provided stable operation with stabilization of all required gas parameters in the RICH prototype. It was reliably controlled by the control system, providing all system parameters to the central slow control system. The RICH prototype vessel (3.5 m<sup>3</sup>) was checked for leaks prior to the beamtime. Measuring this by the pressure decrease in the vessel, the leak rate was below the sensitivity of the gas system ( $\leq 50$  sccm<sup>1</sup>).

<sup>1</sup>sccm=standard cubic centimeter per minute

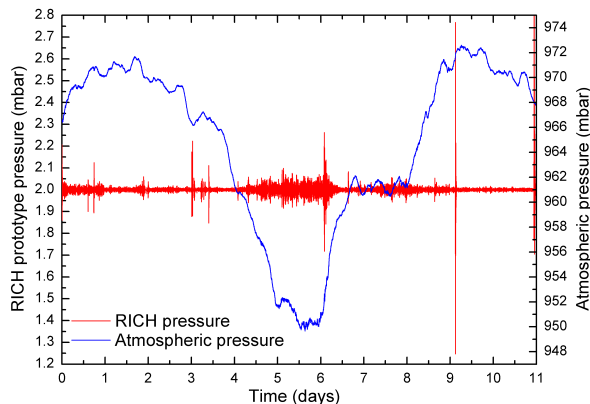


Figure 1: Differential detector pressure (red line) and atmospheric pressure (blue line)

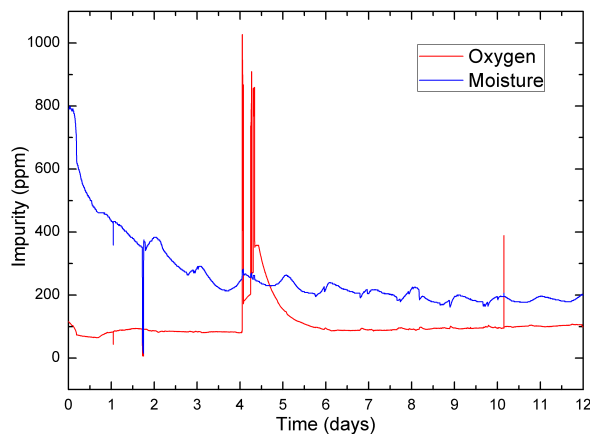


Figure 2: Oxygen (red line) and moisture (blue line) content

## References

- [1] L. Kochenda *et al.*, CBM Progress report 2010, Darmstadt 2010, p. 31
- [2] P. Kravtsov *et al.*, CBM Progress report 2010, Darmstadt 2010, p. 32
- [3] L. Kochenda *et al.*, Nucl. Instrum. Methods A **578** (2007) 172
- [4] L. Kochenda *et al.*, Preprint PNPI **2712**, 2007
- [5] L. Kochenda *et al.*, Nucl. Instrum. Methods A **499** (2003) 703



## Detector control system for the RICH Prototype

*J. Song, C. Son, and I.-K. Yoo*

Pusan National University, Pusan, Korea

For monitoring and control of its detector system, CBM is designing a detector control system using EPICS (Experimental Physics and Industrial Control System). Therefore, EPICS has already been used to develop and integrate control systems for the CBM-RICH prototype: a mirror-positioning control system with TwinCAT (The Window Control Automation Technology), and a HV (high voltage) control system with SNMP (Simple Network Management Protocol).

### Mirror positioning system

In the CBM-RICH prototype the mirror assembly is mounted in two aluminum frames which allow rotation around the  $x$ - and  $y$  axes in order to scan the whole photodetector plane [1]. The rotations of these frames are controlled by two servo motors (AM3021-0C41-0000) which are exclusively intended for speed- and/or torque-controlled operation via digital servo drives from the manufacturer [2]. Each motor has a gear head for slow rotations to prevent breaking the mirrors. The servo motors are connected to a servo drive (AX5203-0000), which is controlled by an Industrial PC (IPC: C6915-0000) using EtherCAT. The TwinCAT program was installed in the IPC based on a window CE operating system. Finally, the TwinCAT program in IPC is linked to EPICS on a linux machine via a Modbus/TCP protocol. This scheme of the hardware components for the mirror positioning control system is shown in Figure 1.

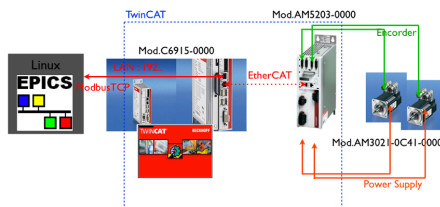


Figure 1: Hardware : IPC, servo drive and servo motors

TwinCAT (The Window Control Automation Technology) consists of the TwinCAT System Manager and the TwinCAT PLC control. The TwinCAT System Manager is the main configuration tool for in- and output of the software tasks [2]. In the main screen of the TwinCAT system manager, there are three parts:

- I/O configuration: hardware components of the system;
- NC configuration: axis configuration;
- PLC configuration: control software.

The I/O configuration communicates with the hardware, and their in-/outputs are linked to the NC (numerical control) configuration, which allows to make the first operations of the system. Finally, the in-/output of the NC configuration are linked to the PLC configuration. In the TwinCAT PLC control, there are code and function blocks for the mirror positioning control. The TwinCAT PLC control provides its own local GUI (Graphic User Interface), which enables us to operate the motors. Nevertheless, the TwinCAT PLC control is integrated into EPICS for common operations of the overall detector system.

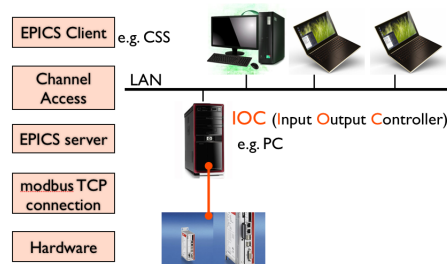


Figure 2: EPICS architecture for the mirror-positioning control system

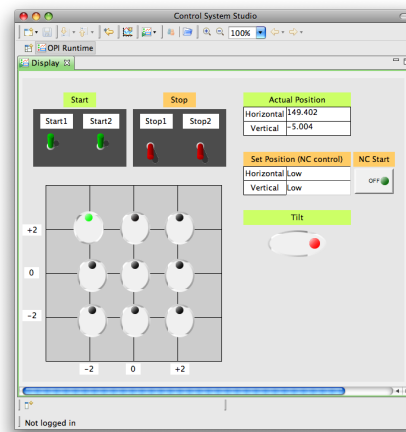


Figure 3: Control panel with CSS

Figure 2 shows the EPICS architecture. The IPC communicates to the IOC (input-output controller) via a modbus TCP. The IOC provides information and service as an EPICS server. An EPICS client accesses the service or asks for informations via a channel access protocol. A CSS

(Control System Studio) is one of the EPICS client GUI tools as shown in Figure 3.

The two start and stop buttons control the power supply of the two motors. The nine circles represent the positions of the ring image on the 16 MAPMT (multi-anode photo-multiplier tube) plane. When switching the circle of the position, the mirrors are moved and the Cherenkov rings will be focused on the envisaged position. In this control system, it is not allowed to activate more than one button at the same time. On the right side of Figure 3 one can read the feedback of the real position and also switch the NC (numerical control). In case of numerical control, one can use numerical input to set any position. The program is developed using a modulo function to prevent 360 degree rotation of the mirror.

### High-voltage control system

In order to supply high voltage to the MAPMTs, an Mpod crate from Wiener and Mpod high voltage modules manufactured by ISEG are used. They are controlled using SNMP integrated in EPICS. The Simple Network Management Protocol (SNMP) is an internet-standard protocol for managing devices on IP networks. In typical SNMP usages, one or more administrative computers called managers have the task of monitoring or managing a group of hosts or devices on a computer network. Each managed system executes, at all times, a software component called an agent which reports information via SNMP to the managers. Essentially, SNMP agents expose management data on the managed systems as variables. The variables accessible via SNMP are organized in hierarchies. These hierarchies, and other metadata (such as type and description of the variable), are described in Management Information Bases (MIBs). SNMP itself does not define which information (which variables) a managed system should offer. Rather, SNMP uses an extensible design, where the available information is defined by management information bases (MIBs). MIBs describe the structure of the management data of a device subsystem [3]. SNMP itself has simple client-server interaction with a few operations to access information. A certain hardware can be controlled by the following commands:

- `snmpwalk` : returns groups of parameters / items;
- `snmpget` : returns a specific parameter (read);
- `snmpset` : sets a specific parameter (write).

In an interactive command mode of the SNMP, the status of the main switch can be checked with `snmpget`, and then the main switch can be turned on using `snmpset`. `snmpwalk` retrieves a block of information and shows the list of all existing output channels.

The EPICS architecture for the high voltage control system is shown in Figure 4. The high voltage modules communicate with the EPICS server via SNMP. This server provides information and service. The client uses the service or asks for information via the CA (channel access)

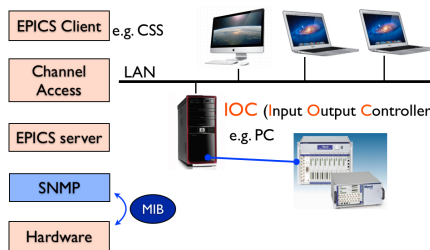


Figure 4: EPICS architecture for the high-voltage control system

protocol.

A graphical user interface for high-voltage control was made also using CSS and is shown in Figure 5. The control panel has buttons for main switches and can control 160 channels at the same time (10 slots with 16 channels each). Voltages and currents can be set and checked from this control panel. It also checks the temperatures of each channel and controls the speed of the fan for keeping stable operation of the crate.

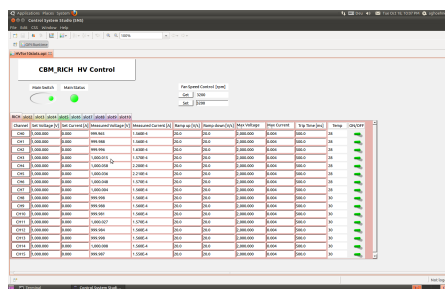


Figure 5: Control panel for the high-voltage control system

### Summary & Outlook

In order to control the positioning of mirrors in the RICH prototype with servo motors, an online control system was developed and successfully installed using TwinCAT and EPICS. A high-voltage control system for the MAPMTs of the RICH prototype was developed and successfully used in the test experiment at CERN in October 2011.

The authors would like to thank Tanya Torres de Heidenreich and Burkhard Kolb from GSI for strong support with the mirror control system and EPICS, and Jürgen Eschke from GSI and Tariq Mahmoud from University Gießen for help with installing and operating the slow control.

### References

- [1] T. Mahmoud *et al.*, *Construction of the CBM-RICH prototype detector*, this report
- [2] [http://infosys.beckhoff.com/index\\_en.htm](http://infosys.beckhoff.com/index_en.htm)
- [3] [http://en.wikipedia.org/wiki/Simple\\_Network\\_Management\\_Protocol](http://en.wikipedia.org/wiki/Simple_Network_Management_Protocol)

## Sector layout of Muon Chambers (MUCH): First results

*S. Chattopadhyay<sup>1</sup>, P. P. Bhaduri<sup>1</sup>, Z. Ahammed<sup>1</sup>, and A. Prakash<sup>2</sup>*

<sup>1</sup>Variable Energy Cyclotron Centre, Kolkata, India; <sup>2</sup>Banaras Hindu University, Varanasi, India

The physics program of the CBM experiment includes the measurement of di-muons originating from the decay of low-mass vector mesons ( $\rho$  and  $\omega$ ) and charmonia. An optimized version of the muon detection system has already been designed through simulations. For the inclusion of a realistic scenario, a modular structure was implemented for the simulations. Each detector layer is divided into several modules of size  $30\text{ cm} \times 30\text{ cm}$  (limited by the GEM foil production technology) and filled with an argon-based gas mixture as the active medium.

One practical disadvantage of this modular design is the non-availability of large-size GEM modules, which results in a complex detector design and a large number of dead zones. A possible solution to this problem is to divide the detector planes into trapezoidal sectors instead of rectangular modules. For such a design, large GEM foils of up to 60 cm in width and without limitation in length are available, and prototypes are being made by CMS and other experiments. These GEMs are produced using single-mask technology, which gives a significantly larger yield of good foils compared to the conventional double-mask GEM. In this paper we report the first results of our feasibility studies with a sectorized MUCH geometry.

Fig. 1 shows the sectorized design of the muon detection system. Each detector layer is divided into 6 or 10 uniform trapezoidal sectors, the number of sectors being a tunable parameter. To accommodate detector electronics, cooling systems etc., half of the sectors are placed on the front side, the other half on the back side. The muon chambers are segmented into different annular regions filled with square pad, with the pad size (a tunable parameter) increasing with radius. This segmentation scheme helps to keep the occu-

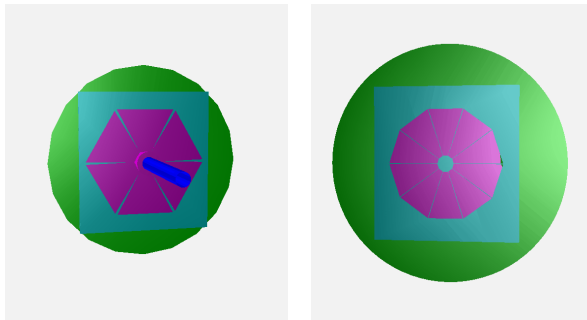


Figure 1: Schematic view of the sector design of the muon detection system. A chamber plane is divided into six sectors (left) or ten sectors (right).

pancy close to constant, which in turn helps to avoid a radial dependence of the detector response. The total number of pads in all the six stations amounts to 550,800, which is much less compared to the modular design ( $\approx 18 \times 10^5$ ). This drastically reduces the overall costs.

We simulated central Au+Au collisions at beam energies of  $E_{\text{lab}} = 8A, 25A$  and  $35A$  GeV. As signal particle we considered the  $\omega$  meson generated by the PLUTO event generator [2]. The background was simulated using the UrQMD event generator [3]. Full event reconstruction was performed in the `cbmroot` framework [4]. A basic digitization was used; detailed digitization with signal generation in the gas is under development and not implemented yet. Comparisons were done for two similar configurations in modular (M) and sector (S) geometries. The reconstruction efficiency and the signal-to-background ratio (S/B) for  $\omega$  mesons calculated in a  $\pm 2\sigma$  window around the signal peak are presented in Tab. 1.

Table 1: Reconstruction efficiency and signal-to-background ratio for  $\omega$  mesons in central Au+Au collision at  $8A, 25A$  and  $35A$  GeV, obtained for the modular (M) and the sectorized (S) segmentations. The results were calculated from 10k UrQMD + PLUTO events.

Energy [ $A$ GeV]	Efficiency [%]		S/B	
	M	S	M	S
8	1.21	1.42	1.41	2.57
25	2.90	2.48	0.49	0.36
35	3.31	2.79	0.34	0.35

As it appears, even with significantly lower pad multiplicity, efficiency and S/B do not deteriorate for the sector geometry compared to the modular one. From the practical point of view, a sector layout is much easier to implement compared to the modular detector design. It also helps to significantly decrease the pad multiplicity and thus reduce the costs.

### References

- [1] A. Kiseleva *et al.*, Indian J. Phys. **85** (2011) 211
- [2] <http://www-hades.gsi.de/computing/pluto>
- [3] S. A. Bass *et al.*, Prog. Part. Nucl. Phys. **41** (1998) 255
- [4] <http://fairroot.gsi.de>

## Study of the characteristics of GEM for the FAIR experiment CBM

S. Biswas<sup>1</sup>, A. Abuhoza<sup>1</sup>, U. Frankenfeld<sup>1</sup>, J. Hehner<sup>1</sup>, C. J. Schmidt<sup>1</sup>, H. R. Schmidt<sup>2</sup>, M. Träger<sup>1</sup>, S. Colafranceschi<sup>3</sup>, A. Marinov<sup>3</sup>, and A. Sharma<sup>3</sup>

<sup>1</sup>GSI, Darmstadt, Germany; <sup>2</sup>Eberhard-Karls-Universität, Tübingen, Germany; <sup>3</sup>CERN, Switzerland

Gas Electron multipliers (GEM) will be used in the CBM Muon Chamber system (MUCH) located downstream of the Silicon Tracking System (STS) along with other sophisticated detectors. In the GSI detector laboratory an R&D effort is launched to study the characteristics of GEM detectors for the CBM experiment. The primary goals of this R&D program are (a) to verify the stability and integrity of the GEM detectors over a period of time, during which a charge density of the order of several C/cm<sup>2</sup> is accumulated in the detector; (b) to establish the functioning of a triple GEM as a precise tracking detector under the extreme conditions of the CBM experiment; (c) to study characteristic parameters like efficiency, rate capability, long-term stability, spark probability by varying conditions like temperature, gas composition or radiation dose.

One triple, double-mask GEM detector obtained from CERN with 3 mm drift gap, 2 mm transfer gap and 2 mm induction gap was studied systematically. The voltage to the drift plane and individual GEM plates was applied through a voltage-divider chain. Although there is a segmented pad readout, the signal in this study was obtained from all pads summed by a add-up board, and a single input was fed to a charge-sensitive preamplifier. A LabView based data acquisition system was used. The variation of the effective gain and the resolution of this detector with the applied high voltage was measured with a Fe<sup>55</sup> X-ray source for different gas mixtures and with different gas flow rates. The fraction of large signal (probable spark) relative to average signal was also measured by setting different threshold values.

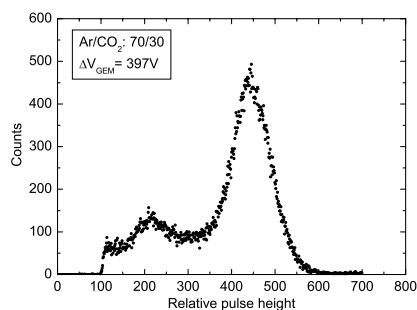


Figure 1: Pulse height distribution for a 5.9 keV Fe<sup>55</sup> source obtained with the triple GEM detector

The detector was operated with Argon and CO<sub>2</sub> with different ratios such as 70:30, 80:20 and also with different flow rates (e. g. 50 ml/min, 100 ml/min and 200 ml/min). Figure 1 shows an example of the pulse height distribution for a Fe<sup>55</sup> X-ray source with Argon and CO<sub>2</sub> in 70:30 ratio

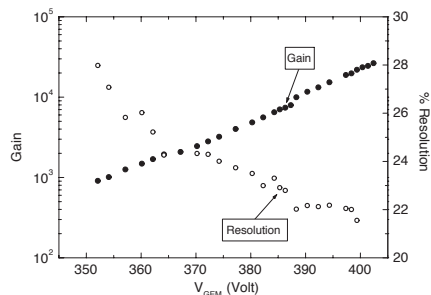


Figure 2: Effective gain curve and energy resolution of the triple GEM, operated in Ar/CO<sub>2</sub> (70:30) as a function of  $\Delta V_{GEM}$

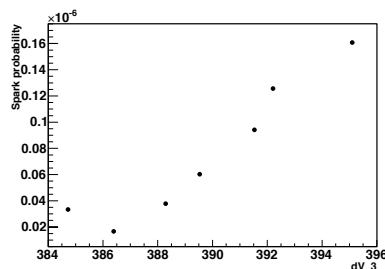


Figure 3: Spark probability as a function of  $\Delta V_{GEM}$

at  $\Delta V_{GEM} = 397$  V. The variation of effective gain and energy resolution (FWHM) with  $\Delta V_{GEM}$  are shown in Fig. 2. As expected, the gain increases exponentially and the energy resolution improves with increasing  $\Delta V_{GEM}$  [1].

The fabrication of a new, 10 cm × 10 cm GEM detector with newly designed box and its characterisation were also accomplished. Testing of GEMs without voltage-divider chain and using a seven channel high-voltage module, dedicated for triple GEMs, was performed as well. Both double-mask and single-mask triple GEM detectors were tested at high rates at the CERN SPS/H4 beam line. In this test the hadronic shower detection and the spark probability was measured with a  $\approx 150$  GeV pion beam. The spark probability for a double-mask, triple GEM with Fe block as a function of  $\Delta V_{GEM}$  is shown in Fig. 3. Building and testing of large-area, single mask GEM is a future plan.

### References

- [1] S. Biswas *et al.*, Proceedings of DAE Symposium on Nuclear Physics **56** (2011) 1068

## Update of the TRD geometry to version v12a

*D. Emschermann and C. Bergmann*

Westfälische Wilhelms-Universität, Münster, Germany

The geometry of the Transition Radiation Detector (TRD) was further developed in CbmRoot, the CBM Simulation and Analysis Framework. The latest geometry version v12a was optimised to match the acceptance of the upstream RICH and the downstream TOF detector (Fig. 1).

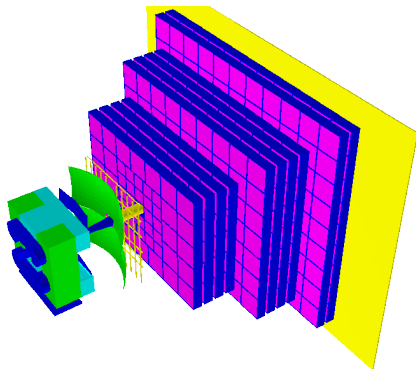


Figure 1: The TRD v12a geometry, consisting of 10 layers

Taking into account the latest results on pion efficiencies from the CERN beam test 2011 [1], the number of layers could be reduced to 10. As compared to [2], the layout of the detector was redesigned, such that the whole TRD can now be assembled from modules of only two different dimensions: While the inner region of the first 8 layers is made of  $60 \times 60 \text{ cm}^2$  sized modules, the outer part of the layers is built by modules of  $100 \times 100 \text{ cm}^2$  size (Fig. 3). The v12a geometry is composed of 708 detector modules covering an area of  $585 \text{ m}^2$  and results in 737.408 readout channels.

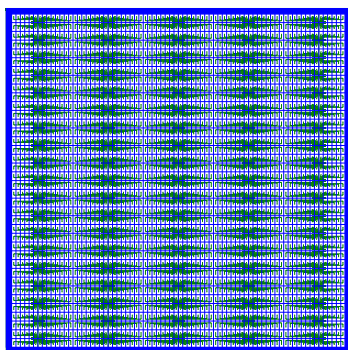


Figure 2: Pad plane for the innermost module of layer 1. 2888 pads of  $1.125 \text{ cm}^2$  size are interfaced to 19 front-end boards, each holding 5 SPADICs with 32 channels.

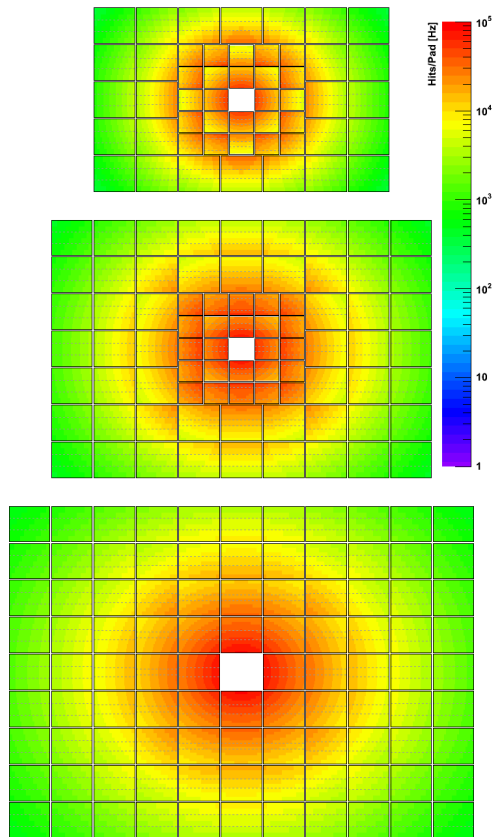


Figure 3: Distribution of the hit rate per pad for the first layer of station 1, 2, and 3 (from top to bottom)

The pad size increases in radial direction from module to module starting from  $1 \text{ cm}^2$  up to  $12 \text{ cm}^2$ . The size of the pads is chosen in a way that the expected hit rate per channel does not exceed  $10^5 \text{ Hz}$  per channel (Fig. 3). Within a layer the hit rate still varies over 2.5 orders of magnitude. The pad plane of the innermost detector of layer 1, holding the smallest pad size, is illustrated in Fig. 2. Such a prototype will be built in 2012.

### References

- [1] C. Bergmann *et al.*, *Test of Münster CBM TRD prototypes at the CERN PS/T9 beam line*, this report
- [2] D. Emschermann *et al.*, *CBM Progress Report 2009*, Darmstadt 2010, p. 35

## Single sided TRD prototype

M. Petriș<sup>1</sup>, M. Târziă<sup>1</sup>, M. Petrovici<sup>1</sup>, V. Simion<sup>1</sup>, D. Bartoș<sup>1</sup>, I. Berceanu<sup>1</sup>, G. Caragheorghopol<sup>1</sup>, V. Cătănescu<sup>1</sup>, F. Constantin<sup>1</sup>, L. Rădulescu<sup>1</sup>, C. Bergmann<sup>2</sup>, D. Emschermann<sup>2</sup>, S. Linev<sup>3</sup>, W. F. J. Müller<sup>3</sup>, and J. P. Wessels<sup>2</sup>

<sup>1</sup>NIPNE, Bucharest, Romania; <sup>2</sup>Westfälische Wilhelms-Universität, Münster, Germany; <sup>3</sup>GSI, Darmstadt, Germany

Although it provides an excellent  $e/\pi$  discrimination in a high counting rate environment, the size of a double sided TRD is limited by the topology of the signal routing. In order to overcome this problem we propose a standard TRD architecture of  $2 \times 4$  mm amplification region coupled with a 4 mm drift zone with a gas thickness identical with the  $4 \times 3$  mm double sided prototype [1]. The drift zone size was chosen such to minimize the drift time ( $< 250$  ns for the 80%Xe+20%CO<sub>2</sub> gas mixture, 2000 V anode voltage and 500 V drift voltage [2]), while keeping the TR conversion efficiency as large as possible. Details on this architecture are presented in Fig. 1. The detector is closed on one side by the drift electrode made from an aluminized kapton foil of 25  $\mu\text{m}$  thickness stretched on a 8 mm Rohacell plate and on the other side by the readout electrode made from a 300  $\mu\text{m}$  thickness PCB. The anode wire plane made from Au coated W wires of 20  $\mu\text{m}$  diameter (3 mm pitch) is situated in the middle of the amplification region.

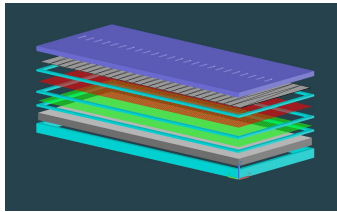


Figure 1: Sketch of the chamber configuration

The cathode wire plane made from 75  $\mu\text{m}$  diameter Cu/Be alloy (1.5 mm pitch) separates the amplification region from the drift zone. Rectangular pads ( $10 \times 80$  mm<sup>2</sup>) split on diagonal define a triangular shape for readout cell, each triangle being readout separately. The pad signals were processed using 8 channel FASP front-end electronics [3].

The detector was flushed with an 80%Ar+20%CO<sub>2</sub> gas mixture and tested with the 5.9 keV X-ray <sup>55</sup>Fe source measuring both anode and pad signals. The obtained energy resolutions were 8% for the anode signal and 9.7% for the pad signals.

The in-beam tests were performed at the PS accelerator at CERN [4]. It was operated with a 80%Xe+20%CO<sub>2</sub> gas mixture, 1900 V anode voltage, 400 V drift voltage and a regular radiator of 20/500/120 (20  $\mu\text{m}$  foil thickness, 500  $\mu\text{m}$  gap, 120 foils).

Electrons and pions were identified using the correlation of the signals from a Cherenkov detector and a lead-glass calorimeter and their pulse height distributions at 2 GeV/c beam momentum were obtained (Fig. 2).

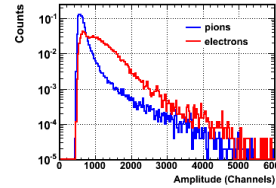


Figure 2: Pulse height distributions for pions (blue line) and electrons (red line)

Using the pulse height distributions as input in a Monte Carlo simulation an electron misidentification probability of 1.1% is reached for a 6 layer configuration, as can be seen in Fig.3.

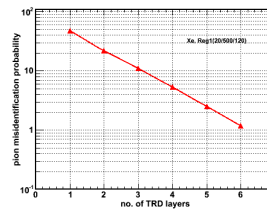


Figure 3: Pion misidentification probability as a function of the number of layers

The position reconstruction and position resolution determination in both coordinates that defines the plane of the readout electrode were obtained following the procedure described in [1]. Position resolutions of about 320  $\mu\text{m}$  across the pads (Fig. 4, left panel) and of 6.3 mm along the pads (Fig. 4, right panel) were obtained.

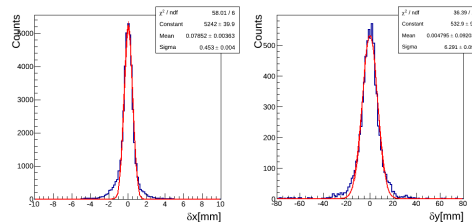


Figure 4: Distribution of the difference between the positions reconstructed with the SSTRD and DSTRD-V1[1]:  $x$  coordinate (left),  $y$  coordinate (right)

## References

- [1] M.Petriș *et al.*,  $e/\pi$  identification and position resolution of double sided TRD, this report
- [2] M. Petrovici *et al.*, CBM Collab. Meeting, Beijing, 2011
- [3] A Caragheorghopol *et al.*, CBM Progress Report 2010, p. 46
- [4] D. Emschermann *et al.*, CBM Progress Report 2010, p. 42

## High granularity single sided TRD prototype

*M. Petriş<sup>1</sup>, M. Târziă<sup>1</sup>, M. Petrovici<sup>1</sup>, V. Simion<sup>1</sup>, D. Bartaş<sup>1</sup>, G. Caragheorghopol<sup>1</sup>, V. Cătănescu<sup>1</sup>, F. Constantin<sup>1</sup>, J. Adamczewski-Musch<sup>3</sup>, C. Bergmann<sup>2</sup>, D. Emschermann<sup>2</sup>, S. Linev<sup>3</sup>, W. F. J. Müller<sup>3</sup>, and J. P. Wessels<sup>2</sup>*

<sup>1</sup>NIPNE, Bucharest, Romania; <sup>2</sup>Westfälische Wilhelms-Universität, Münster, Germany; <sup>3</sup>GSI, Darmstadt, Germany

In order to fulfill the high counting rate and high multiplicity requirements specific to the regions of low polar angles in the CBM TRD subdetector, we designed, built and tested a new version [1] of the single-sided TRD prototype [2].

The counter was designed with the same configuration as [2]: a 2 x 4 mm amplification region coupled with a 4 mm drift zone, an anode pitch of 3 mm and a cathode pitch of 1.5 mm. A sketch of the chamber can be seen in Fig. 1.

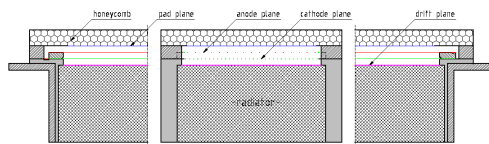


Figure 1: Sketch of the chamber configuration

The readout electrode of the new prototype has a different design. As shown in Fig. 2 it has three pad rows with 74 triangular pads per row. The area of a triangular pad of

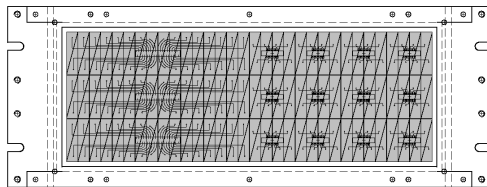


Figure 2: Sketch of the readout electrode

$\sim 1 \text{ cm}^2$  (2.7 cm height x 0.7 cm width) corresponds to the requirements of the innermost zone of the first TRD station. The readout electrode was equipped with two types of connectors: a first type (right side of Fig. 2) can be read-out by 8 channel FASP front-end electronics [3] and second type (left side of Fig. 2) could be operated by 32 channels SPADIC [4] front end electronics. The two identical chambers were tested with an  $^{55}\text{Fe}$  source and in-beam. The chambers were flushed by 80%Xe + 20%CO<sub>2</sub> gas mixture.

For the  $^{55}\text{Fe}$  source and in beam tests the signal delivered by 16 triangular pads (8 consecutive triangular pads from two neighboring rows) were processed by FASP using the flat-top output. A 32 channels peak sense Mesytec ADC (MADC-32) was used for digitization.

The  $^{55}\text{Fe}$  X-ray spectrum recorded with one of the two identical chambers are presented in Fig. 3 for 2000 V anode voltage and 800 V drift voltage. A clear  $^{55}\text{Fe}$  spectrum with

the photopeak corresponding to the full energy absorption (5.9 keV), well separated by the escape peak (1.76keV), is seen.

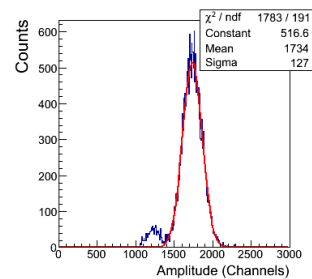


Figure 3: The  $^{55}\text{Fe}$  source spectrum measured with the Xe,CO<sub>2</sub>(20%) gas mixture for one of the two tested chambers

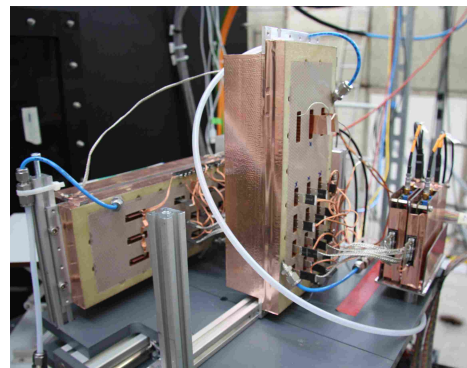


Figure 4: The two chambers in the in-beam tests

The detectors (Fig. 4) were tested with a mixed electron and pion beam of 2 - 10 GeV/c momenta performed at the T9 beam line of the CERN PS accelerator in October 2011 [5]. A detailed analysis is in progress.

## References

- [1] M. Petrovici *et al.*, CBM Collab. Meeting, Beijing, 2011
- [2] M. Petriş *et al.*, *Single sided TRD prototyp*, this report
- [3] A Caragheorghopol *et al.*, CBM Progress Report 2010, p. 46
- [4] T. Armbruster *et al.*, CBM Progress Report 2010, p. 45
- [5] C. Bergmann *et al.*, *Common CBM beam test of the RICH, TRD and TOF subsystems at the CERN PS T9 beamline*, this report

## $e/\pi$ Identification and position resolution of double sided TRDs

M. Petriș<sup>1</sup>, M. Târziă<sup>1</sup>, M. Petrovici<sup>1</sup>, V. Simion<sup>1</sup>, D. Bartoș<sup>1</sup>, I. Berceanu<sup>1</sup>, G. Caragheorghopol<sup>1</sup>, V. Cătănescu<sup>1</sup>, F. Constantin<sup>1</sup>, C. Bergmann<sup>2</sup>, D. Emschermann<sup>2</sup>, S. Linev<sup>3</sup>, W. F. J. Müller<sup>3</sup>, and J. P. Wessels<sup>2</sup>

<sup>1</sup>NIPNE, Bucharest, Romania; <sup>2</sup>Westfälische Wilhelms-Universität, Münster, Germany; <sup>3</sup>GSI, Darmstadt, Germany

Details on the architecture, the energy resolution obtained for <sup>55</sup>Fe X-ray source, and preliminary results of in-beam tests of double sided TRD prototypes with triangular read-out pads using FASP front-end electronics were already reported [1, 2]. Therefore, the present contribution is focused on the  $e/\pi$  identification and position resolution of the two versions with 3 mm (DSTRD-V1) and 4 mm (DSTRD-V2) anode-cathode distance, respectively. The in-beam tests were performed using a mixture of electrons and pions of 1 - 5 GeV/c momentum at the T10 beam line of the PS accelerator at CERN [3]. The electrons and pions were selected using the information from a Cherenkov detector and Pb glass calorimeter positioned in front and in the end of the beam line. The detectors were flushed with a 80%Xe+20%CO<sub>2</sub> gas mixture. The pulse height distributions of electrons and pions at 2 GeV/c are presented in Fig. 1 for DSTRD-V1 (left panel) and for DSTRD-V2 (right panel).

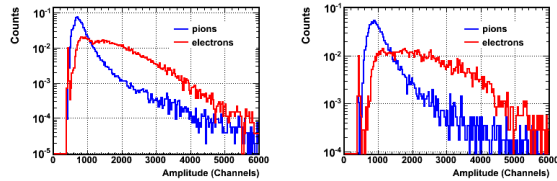


Figure 1: Pulse height distributions for pions (blue line) and electrons (red line): DSTRD-V1 (left) and DSTRD-V2 (right)

Distributions of electrons and pions at 2 GeV/c are presented in Fig. 1 for DSTRD-V1 (left panel) and for DSTRD-V2 (right panel).

DSTRD-V1 was operated at 1700 V with a regular radiator of the type 20/250/220 (i.e. 20  $\mu$ m foil thickness, 250  $\mu$ m gap, 220 foils), while DSTRD-V2 was operated at 2000 V with a regular radiator of the type 20/500/120. These distributions were used as input for a Monte Carlo

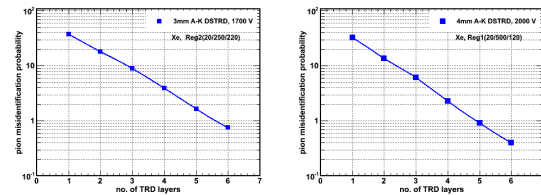


Figure 2: The pion misidentification probability as a function of number of layers: DSTRD-V1 (left), DSTRD-V2 (right)

simulation of the pion misidentification probability as a function of number of layers. The results are presented in Fig.2: an electron misidentification probability of 0.74% (left panel) for a 6 layer configuration based on DSTRD-

V1 is obtained, while using a 6 layers configuration based on DSTRD-V2 improves the electron misidentification by a factor of 2, i.e. 0.38% (right panel).

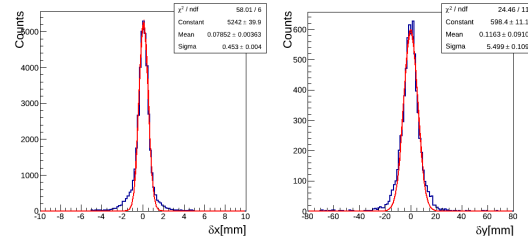


Figure 3: Distribution of the difference between the reconstructed positions of DSTRD-V1 and DSTRD-V2:  $x$  coordinate (left),  $y$  coordinate (right)

In order to estimate the position resolution, we used the position informations from both detectors. The following procedure was used: across the split pads we reconstructed the  $x$  coordinate in a system of coordinates  $(x, y)$  parallel with the cathetus of the right triangle. For the position reconstruction along the pad  $y$  coordinate a second  $x'$  position was calculated in a coordinate system  $(x', y')$ , which is tilted by the hypotenuse angle. From the crossings of lines parallel to the  $y$  and  $y'$  axes with the reconstructed  $x$  and  $x'$  coordinates, we obtained the  $y$  coordinate of the event. The position resolution was obtained from the standard deviation of a Gaussian fitted to the difference between the reconstructed position with the two prototypes. With the assumption that the two prototypes have an equal contribution, a position resolution across the pads of about 320  $\mu$ m was obtained for both,  $x$  (Fig. 3, left panel) and  $x'$  coordinates. The 5.5 mm position resolution (Fig. 3, right panel) along the pads ( $y$  coordinate) was obtained using as reference the information from the DSTRD-V1 rotated by 90° relative to the DSTRD-V2.

These results combined with the ones obtained in previous tests of smaller size prototypes of similar architecture in high counting rate environment [4] show the high performance of such an architecture and associated FEE in terms of  $e/\pi$  discrimination and position resolution in counting rate environment up to  $2 \times 10^5$  particles·cm<sup>-2</sup>·s<sup>-1</sup>.

## References

- [1] M. Petriș *et al.*, GSI Report 2011-1, p. 38
- [2] A. Caragheorghopol *et al.*, GSI Report 2011-1, p. 35
- [3] D. Emschermann *et al.*, GSI Report 2011-1, p. 34
- [4] M. Petrovici *et al.*, Nucl. Instrum. Methods **A 579** (2007) 961



## Development of an EPICS controlled, Mpod based, mixed HV and LV system for the Münster CBM TRD prototypes

*D. Emschermann<sup>1</sup>, J. Adamczewski-Musch<sup>2</sup>, and B. W. Kolb<sup>2</sup>*

<sup>1</sup>Westfälische Wilhelms-Universität, Münster, Germany; <sup>2</sup>GSI, Darmstadt, Germany

A common CBM RICH / TRD / TOF beam test was performed at the CERN PS T9 beam line in October 2011 [1]. The low and high voltages of the Münster TRD prototypes [2], as well as the HV for the beam monitoring detectors and the high voltage of the RICH camera system [3], were managed by a slow control system based on the Experimental Physics and Industrial Control System (EPICS) [4]. The power for the Münster TRDs (Figure 1) was provided by a Mpod mini crate [5] equipped with the following list of modules [6]:

module	channels	function
EHQ 8630n	8 ch	beam monitor HV
EDS 20 025p	4 ch	TRD anode HV
EDS 20 025n	4 ch	TRD drift HV
MPV 8008LD	8 ch	TRD low voltage

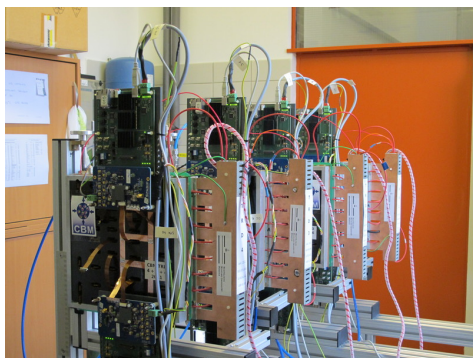


Figure 1: The four Münster CBM TRD prototypes 2011, equipped with eight SPADIC / Susibo front-end units

The 8 SPADIC / Susibo front-end units on the TRDs were supplied by the MPV LV module. Only 8 HV channels of two polarities were required for the four TRDs. The communication between the controller in the Mpod crate and the EPICS IOC was handled through SNMP.

We made use of the EPICS data input to the Data Acquisition Backbone Core (DABC), as described in [7]. Using the Easy Channel Access (EZCA) extension [8], a set of slow control variables were transmitted to the DABC system every 5 seconds. As part of the DAQ stream, it was possible to visualise those EPICS variables in the attached Go4 [9] online monitoring analysis, which was helpful for the fine-tuning of the TRD detector settings during data taking.

For 2012 we plan to test the behaviour of a large MPod



Figure 2: The TRD services infrastructure with the Mpod mini crate visible in the middle left part of the picture

crate, offering 10 slots, each equipped with a 32 channel EDS HV Module. Such a system with 320 HV channels per crate could be used as high voltage power source for the final CBM TRD. It remains to be tested under which conditions the crate controller can handle the data traffic generated by the EPICS IOC. The CBM TRD, consisting of some 700 modules, would require 1400 HV channels, which could be provided by 5 of the above crates.

### References

- [1] C. Bergmann *et al.*, *Common CBM beam test of the RICH, TRD and TOF subsystems at the CERN PS T9 beamline*, this report
- [2] C. Bergmann *et al.*, *Test of Münster CBM TRD prototypes at the CERN PS/T9 beam line*, this report
- [3] J. Kopfer *et al.*, *In-beam test of a real-size CBM-RICH prototype at CERN PS*, this report
- [4] <http://www.aps.anl.gov/epics>
- [5] WIENER, Plein & Baus GmbH, <http://www.wiener-d.com>
- [6] ISEG Spezialelektronik GmbH, <http://www.iseg-hv.com>
- [7] J. Adamczewski-Musch, B. W. Kolb and S. Linev, CBM Progress Report 2010, Darmstadt 2011, p. 61
- [8] <http://www.aps.anl.gov/epics/extensions/ezca>
- [9] <http://go4.gsi.de>

## Test of Münster CBM TRD prototypes at the CERN PS/T9 beam line

C. Bergmann, A. Andronic, D. Emschermann, and J. P. Wessel

Westfälische Wilhelms-Universität, Münster, Germany

The Münster CBM TRD prototypes are derived from the design of the ALICE TRD modules. An amplification region of 3+3 mm or 4+4 mm is combined with a short drift section to obtain an active gas volume with thickness of 12 mm in total, referred to as MS336 and MS444, respectively. Signals are induced on rectangular pads of 5 mm or 8 mm width to allow for charge collection on 3 adjacent pads. This design is scalable to 1m<sup>2</sup>-size, required for the final CBM TRD modules.

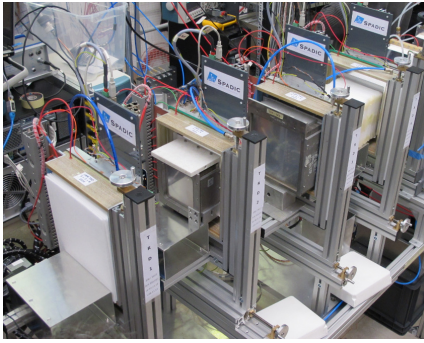


Figure 1: Münster TRD prototypes in the CBM beam test

Various radiator types were investigated on the four Münster prototypes (Fig. 1) during the common CBM beam test [1] in October 2011. The read-out was performed with the SPADIC/Susibo front-end [2]. The setup was entirely EPICS controlled, allowing for online monitoring of the HV settings and inclusion of these values in the DAQ stream, as described in [3]. First results of the ongoing analysis are shown in Figs. 2 and 3.

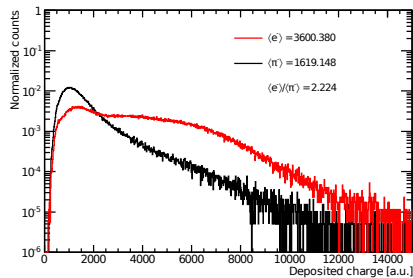


Figure 2: Integrated ADC spectra for electrons (red) and pions (black) on one of the MS336 prototypes operated with Xe/CO<sub>2</sub> (80:20) gas in combination with 30 cm polyethylene-foam radiator (H) at p=3 GeV/c

One important aspect of radiator choice is the requirement to match the TR-emission spectrum to the absorption

spectrum of the detector. For a detailed investigation, we have built different radiator types: regular foil (B, C, D, E, F) and irregular foam (H and H++), fiber (G) and sandwiches (A, I(p) and I(u)). Ideally, a radiator should yield an optimal TR-performance while keeping the material budget as low as possible. While this consideration favors regular foil radiators, they usually require a significant external support frame to keep the foils stretched and in position.

First results (Fig. 3) using self-supporting, irregular foam materials are promising (H and H++). Owing to space constraints during the test beam, foam radiators could only be tested on the upstream TRD prototype. Results from this detector are labelled MS336/10 in Fig. 3. They represent only upper limits, because of intermittent problems with the readout.

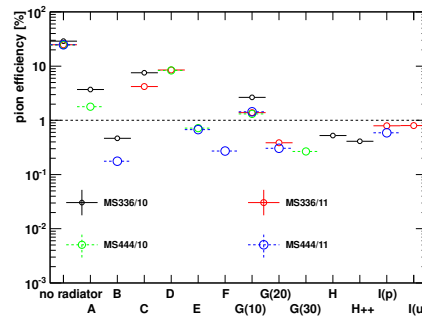


Figure 3: Pion efficiencies, extrapolated to a TRD consisting of 10 layers, for different radiator types studied on the 4 different TRD prototypes at a beam momentum of 3 GeV/c. The dashed line indicates the design goal of 1% pion efficiency, at 90% electron efficiency, achieved by radiators below this line.

Further tests with foam radiators are planned for 2012. In addition, a self-supporting, micro-structured foil radiator with negligible frame material is currently under development.

### References

- [1] C. Bergmann, D. Emschermann and J. P. Wessels, *Common CBM beam test of the RICH, TRD and TOF subsystems at the CERN PS*, this report
- [2] T. Armbruster, P. Fischer and I. Perić, CBM Progress Report 2010, Darmstadt 2011, p. 45
- [3] D. Emschermann, J. Adamczewski-Musch and B. W. Kolb, *Development of an EPICS controlled, MPOD based, mixed HV and LV system for the Münster CBM TRD prototypes*, this report

## Test of the Frankfurt CBM TRD prototypes at the CERN-PS

A. Arend, H. Appelshäuser, T. Bel, P. Dillenseger, and M. Hartig

Goethe-Universität, Frankfurt am Main, Germany

The Transition Radiation Detector (TRD) for the Compressed Baryonic Matter (CBM) experiment aims to provide charged particle tracking and  $e/\pi$  separation in an environment of unprecedented high particle flux. To achieve the physics goal of CBM, a hadron misidentification probability of less than 1% (e.g. “pion efficiency”) is required at 90% detection efficiency for electrons. Based on simulations [1] and results of previous test beams [2], thin MultiWire Proportional Chambers (MWPC) without additional drift region are considered to fulfill this requirement. Symmetric MWPCs with equal distances between entrance window, anode wires and read out plane resulting in a total thickness of 8 mm, 10 mm and 12 mm have been built. The anode wires have a diameter of  $20\ \mu\text{m}$  and a pitch of 2.5 mm. Three different types of TR-radiators have been attached to these MWPCs: a fiber radiator as used in the ALICE TRD, a polypropylene foam radiator, and regular radiators made of  $20\ \mu\text{m}$  thick polypropylene foils. The foil radiators have been constructed in modules of 50 foils each with a spacing of 0.5 mm. The different configurations attached to one MWPC consisted of altogether 150, 200, and 350 layers of foil. The SPADIC chip [3] has been used for data read out. The prototypes have been tested during the common test beam time at the CERN-PS in October 2011 together with other CBM subsystems including the TRD prototypes from Münster, Bucharest and Dubna [4]. In the experimental area T9 a mixed  $e/\pi$ -beam with momenta of 2 to 10 GeV/c has been provided. The combined signals of two Cherenkov detectors and a lead glass calorimeter have been used as reference for particle identification.

Figure 1 shows the distribution of the integrated ADC signal for electrons and pions with a momentum of 3 GeV/c measured with the 8 mm thick MWPC using the foil radiator with 350 layers and a Xe/CO<sub>2</sub> (80:20) gas mixture. Based on these distributions, electron and pion efficiencies can be calculated using a likelihood method and extrapolated to multiple detector stations using a simple Monte Carlo. The remaining pion efficiencies are shown in Fig. 2 for the different radiator types for a required 90% electron efficiency. According to this preliminary result one can assume that a regular foil radiator as well as a foam radiator can fulfill and even significantly exceed the requirements in  $e/\pi$  separation for a detector setup with nine stations.

The present preliminary analysis of the test beam data will be further improved and extended. Based on the available results the developments in the Frankfurt CBM TRD group will be focused on the construction of regular foil radiators combined with the existing thin read out chamber

geometry. These improvements will lead to a large scale prototype which will be tested in the upcoming beam times.

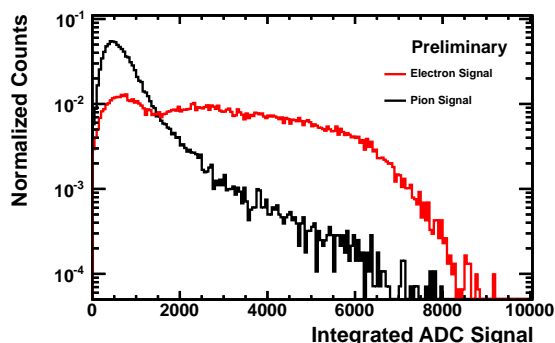


Figure 1: Integrated signal of electrons (red) and pions (black) for the 8 mm thick MWPC using the foil stack radiator with 350 layers

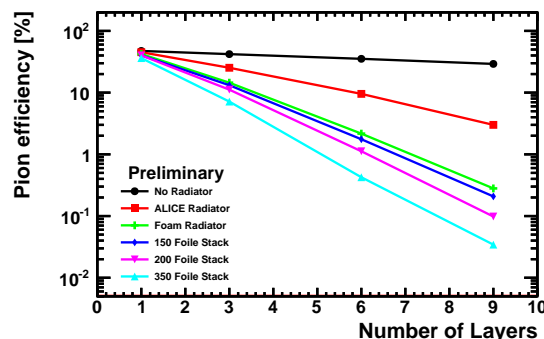


Figure 2: Extrapolated remaining pion efficiency at a beam momentum of 3 GeV/c for multiple layers of the 8 mm thick MWPC when applying 90% electron efficiency for the used radiators

## References

- [1] P. Reichelt, M. Hartig and H. Appelshäuser, CBM Progress Report 2010, Darmstadt 2011, p. 39
- [2] W. Yu *et al.*, CBM Progress Report 2010, Darmstadt 2011, p. 44
- [3] T. Armbruster, P. Fischer and I. Perić, CBM Progress Report 2010, Darmstadt 2011, p. 45
- [4] C. Bergmann, D. Emschermann and J. P. Wessels, *Common CBM beam test of the RICH, TRD and TOF subsystems at the CERN PS*, this report

## Optimization of a setup for ageing studies of gaseous detectors

A. Abuhoza<sup>1,3,4</sup>, H. R. Schmidt<sup>2</sup>, S. Biswas<sup>1</sup>, U. Frankenfeld<sup>1</sup>, J. Hehner<sup>1</sup>, and C. J. Schmidt<sup>1</sup>

<sup>1</sup>GSI, Darmstadt, Germany; <sup>2</sup>Eberhard-Karls-Universität, Tübingen, Germany; <sup>3</sup>KACST, Riyadh, Saudi Arabia; <sup>4</sup>Goethe-Universität, Frankfurt, Germany

High luminosity experiments like Compressed Baryonic Matter (CBM) need several gas detectors with long term ( $\sim 10$  years) stable operation at high rates. Consequently, the construction materials for series production of the detectors have to be chosen carefully in order to ensure the operation of these detectors over the projected lifetime of the experiment. A facility has been established at the GSI detector laboratory to study the ageing properties of construction materials of gaseous detectors.

A standard Multi Wire Proportional Chamber (MWPC) is continuously purged by counting gas at a given flow rate, which is routed through an out-gassing box. The box contains the construction material under investigation, e.g. glues. A second MWPC is connected to the same gas line upstream of the out-gassing box. This chamber serves as a reference to monitor non-ageing related changes due to environmental conditions (temperature, pressure, gas mixture, oxygen content). The normalized gain of the peak of a 5.9 keV  $^{55}\text{Fe}$  x-ray source will be sensitive to any effect of ageing.

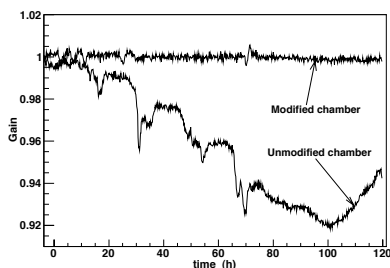


Figure 1:  $p/T$  corrected gain of modified and unmodified chambers, normalized to the gain at the beginning of the measurement period

It is of utmost importance to obtain a stable apparatus which allows distinguishing any permanent gain degradation with a precision of less than 1% peak-to-peak of the normalized gain variation. The main reason is that the irradiation intensity in the test setup should be comparable to the one in the CBM environment, i.e. we have to be sensitive to already small ageing effects in order to carry out the tests on a reasonable time scale.

Consequently, several improvements of the setup have been implemented to obtain the mandatory precision:

1) *Cathodes and gas tightening windows*: At the beginning, the windows of the MWPC have been used as cathodes as well as gas sealing. As a result, the pressure variation was changing the electric field, hence affecting the gain differently in the two chambers. The residual instability of the normalized gain, without any ageing material in the out-gassing box, was about 7% peak-to-peak as shown in fig. 1

for the unmodified chamber.

2) *Outer and inner windows*: Two additional outer windows have been added to act as gas tightening windows whilst the two inner foils function only as cathodes and should thus provide a stable field. A significantly better performance has been obtained after modification of the chamber design as compared to the unmodified chamber as shown in fig. 1 [1].

3) *Mass flow controller (MFC)*: The effect of temperature variations on the behavior of the MFCs has been studied. Fig. 2 indicates a correlation between the rapid variation of the surrounding temperature, which causes a change in the gas concentration, and therefore changes in the normalized gain.

4) *Premixed gas bottle*: As a remedy for the previous observation, a premixed gas bottle Ar/CO<sub>2</sub>(80/20) has been used. Again, the stability of the normalized gain has been improved to a value better than 0.6% peak-to-peak variation as shown in fig. 3.

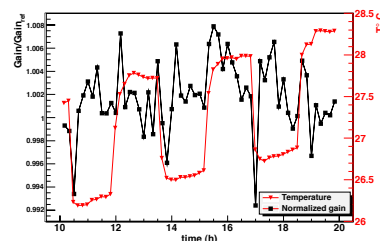


Figure 2: Fluctuation of the normalized gain (black) together with the variation of the environmental temperature in the vicinity of the MFCs (red)

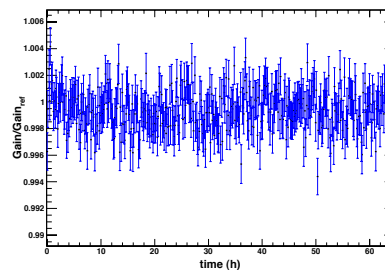


Figure 3: Variation of the normalized gain during 60 hours

In summary, we have optimized our setup such that we will be able to carry out ageing test on a reasonable time scale at still moderate irradiation intensities.

## References

- [1] A. Abuhoza *et al.*, *Study of the ageing properties of construction materials for High Rate Gas Detectors*, in: Proceedings of TIPP 2011, Chicago, USA, to appear in Phys. Proc.

## Free running mode acquisition for a high counting rate TRD

*F. Constantin and M. Petcu*

“Horia Hulube” National Institute for Physics and Nuclear Engineering, Romania

In order to continue the work started with the Fast Analog Signal Processor FASP-0.1 [1, 2] and having in mind the CBM experiment at FAIR we developed an free running mode acquisition device for in-beam tests of our TRD prototypes. The global architecture includes [3]:

- Two MAX1434 Evaluation kits [4].
- PIC32 Ethernet Starter Kit [5].
- A dedicated board.
- Software for PIC32 acquisition, PIC32 data transfer through Ethernet to a PC and a visual user interface.

The MAX1434, a 10-bit analog-to-digital converter (ADC), features fully differential inputs, a pipelined architecture, and digital error correction incorporating a fully differential signal path. The MAX1434 offers a maximum sample rate of 50 MHz. The MAX1434 evaluation kits (EV kits) are fully assembled and tested circuit boards that contain all the components necessary to evaluate the performance of this family of octal 10-/12-bit analog-to-digital converters (ADCs). These ADCs accept differential analog input signals. The EV kits digital outputs can be easily sampled with a user-provided high-speed logic analyzer or data acquisition system. The EV kits also feature an on-board deserializer to simplify integration with standard logic analysis systems. The PIC32 ethernet starter kit provides a easy and cost effective method to perform 10/100 Ethernet development with PIC32. In combination with Microchip’s free TCP/IP software projects can be started very fast.

A dedicated board was designed and implemented in order to:

- provide the clock to the Maxim EV kit,
- provide the different power supplies for each Maxim EV kit,
- transfer data from the EV kit to the Microchip micro controller,
- provide the data transfer handshake.

The two software applications were written in C++ for PIC32 and PC. The full assembly was tested in beam at CERN in October 2011 - see Fig. 1.



Figure 1: Free running mode acquisition for a high counting rate TRD device

### References

- [1] V. Catanescu, *Specific requirements for analog electronics of high counting rate TRD*, CBM Collaboration Meeting, Sept. 2007, Dresden, <https://www.gsi.de/documents/DOC-2007-Oct-79.html>
- [2] V. Catanescu *et al.*, presentation given at the DPG Spring Meeting, March 18, 2009, Bochum
- [3] F. Constantin, *FEE based on FASP for next in-beam tests of Bucharest-Muenster TRD prototypes*, CBM Collaboration Meeting, April 5, 2011, Dresden
- [4] <http://www.maxim-ic.com/datasheet/index.mvp/id/4906>
- [5] <http://www.microchip.com/>

## Development of ceramics RPC for high rate capability timing detector application

*B. Kämpfer, M. Kaspar, R. Kotte, A. Laso Garcia, L. Naumann, R. Peschke, D. Stach, C. Wendisch, and J. Wüstenfeld*

Helmholtz-Zentrum Dresden-Rossendorf, Germany

The installation of timing Resistive Plate Chambers (RPC) is under consideration for the Compressed Baryonic Matter (CBM) experiment [1]. For that purpose prototype timing RPC have been developed at Helmholtz-Zentrum Dresden-Rossendorf (HZDR). Electrodes with a volume resistivity of about  $10^9 \Omega\text{cm}$  [2, 3] are considered for detectors to cope with high fluxes of  $\leq 2 \cdot 10^4 \text{ s}^{-1}\text{cm}^{-2}$ . Special ceramics composites have been developed and processed.

Two new ceramic prototypes have been built and tested in 2011. One small ( $10 \times 10 \text{ cm}^2$ ) prototype with  $300 \mu\text{m}$  gas gaps and one larger detector ( $20 \times 20 \text{ cm}^2$ ) with  $250 \mu\text{m}$  gas gaps. Both detectors are dual-two gap type, where the gaps are obtained by means of mylar separators in the small RPC and by fishing line in the large one.

These two detectors were exposed to 30 MeV electrons at the electron accelerator ELBE@HZDR, and to 2.5 GeV/c protons at COSY, FZ-Jülich. With the electron beam, the beam spot amounts to  $10\text{-}20 \text{ cm}^2$ , while for the proton beam the beam spot was in the order of  $\text{mm}^2$ . In both tests, efficiency and time resolution have been measured at the most central part of the detectors (Figure 1 and 2), and the rate capabilities (defined as a 5 % efficiency drop) of these RPCs have been extracted from the data. Thus the larger detector has a rate capability of  $\sim 8 \cdot 10^4 \text{ cm}^{-2} \text{ s}^{-1}$  and the small detector of  $\sim 10^5 \text{ cm}^{-2} \text{ s}^{-1}$ .

The efficiency is estimated as the number of hits in the RPC, with valid time signals, divided by the number of coincidence signals in the trigger scintillators. For the time of flight a gauss fit to the meantime spectra between both ends of the same strip is obtained. The contribution of the reference time is quadratically subtracted. For the proton beam, due to the small size of the beam spot, only the strip with the most hits is taken into account for the time of flight determination.

Due to the small charge corresponding to the signal collected by the detector no walk-correction was performed. Also the contribution of the electronics was not subtracted.

All these values are obtained with high voltages such that the apparent field in the gas gap would amount to  $\approx 100\text{-}115 \text{ kV/cm}$  (Figure 3).

### References

- [1] I. Deppner *et al.*, Nucl. Instrum. Methods **A 661** (2012) 121
- [2] L. Naumann *et al.*, Nucl. Instrum. Methods **A 628** (2011) 138
- [3] L. Naumann *et al.*, Nucl. Instrum. Methods **A 635** (2011) 113

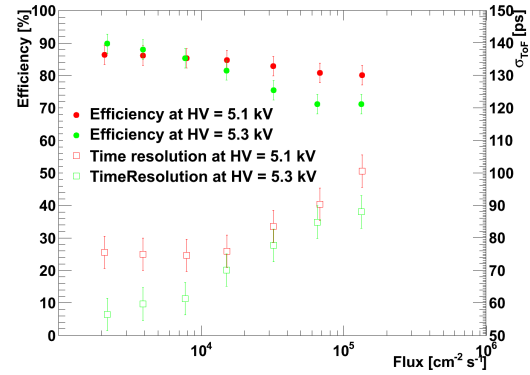


Figure 1: Efficiency and time resolution of the  $20 \times 20 \text{ cm}^2$  RPC as a function of the average electron flux

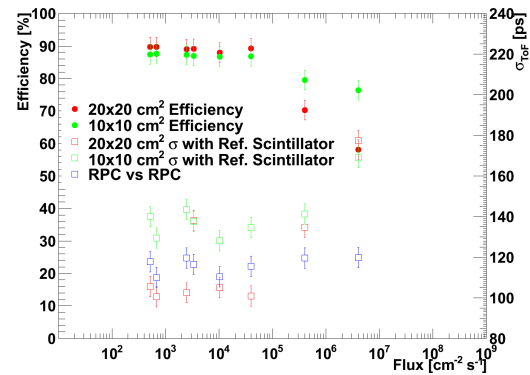


Figure 2: Efficiency and time resolution for both large and small detectors as a function of the average proton flux

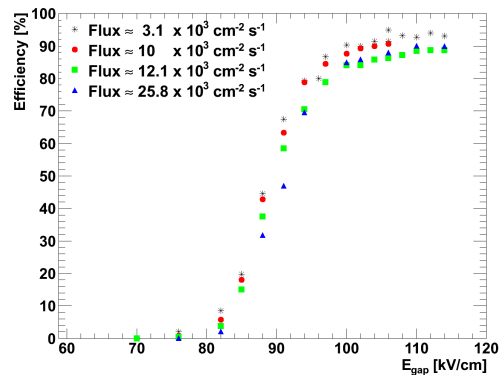


Figure 3: Working curves as a function of the electric field in the gap for the  $20 \times 20 \text{ cm}^2$  RPC

## Time and position resolution for high granularity, multigap, symmetric, differential readout - timing RPC

M. Petriş<sup>1</sup>, M. Petrovici<sup>1</sup>, V. Simion<sup>1</sup>, D. Bartoş<sup>1</sup>, G. Caragheorgheopol<sup>1</sup>, F. Constantin<sup>1</sup>, I. Deppner<sup>2</sup>, N. Herrmann<sup>2</sup>, P. Loizeau<sup>2</sup>, K. Doroud<sup>3</sup>, and M.C.S. Williams<sup>4</sup>

<sup>1</sup>NIPNE, Bucharest, Romania; <sup>2</sup>Physikalisches Institut der Universität Heidelberg, Germany; <sup>3</sup>CERN, Geneva, Switzerland; <sup>4</sup>INFN, Bologna, Italy

As it was previously shown [1, 2], the differential strip read out RPC based on low resistivity glass preserve the good time resolution at high rates (up to  $1.6 \times 10^4$  part. $\cdot$ s $^{-1}$ cm $^{-2}$ ). In order to cope with the high multiplicity environment of the CBM experiment at low polar angles, a new high granularity design has been proposed. Details on the architecture and preliminary results from in-beam tests were already presented in [3]. Here we report on time and position resolution obtained in a beam test performed at the T10 beam line of the CERN PS with 6 GeV/c pions.

Three RPCs of similar design have been tested; two of them are based on float glass resistive electrodes, with a 2 x 7 gaps (140  $\mu$ m each) configuration. The third one was built with 2 x 5 gaps using a special low resistivity glass [4]. The readout electrodes have a strip structure (2.5 mm pitch, 1.1 mm width) with a strip length of 46 mm, 72 strips for each counter. The counters were operated with a 95% C<sub>2</sub>F<sub>4</sub>H<sub>2</sub> + 5% SF<sub>6</sub> gas mixture and 2,086 V/gap high voltage.

The anode and cathode signals were transported via twisted pair cables to a differential FEE card based on the NINO chip [5]. The LVDS NINO outputs were fed into a V1290A VME TDC. We recorded the time information at both ends of each strip ( $t_{left}$ ,  $t_{right}$ ). In order to eliminate the position dependence in the estimation of the time resolution, the mean  $t_{mean} = (t_{left} + t_{right})/2$  was used. The time

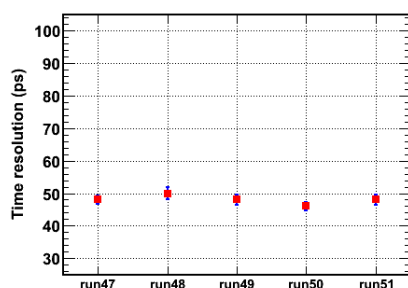


Figure 1: Time resolution for different runs

distribution is the difference between  $t_{mean}$  measured by each chamber. The time resolution for different runs, after walk correction and quadratical subtraction of the electronic contribution (measured in a separate run using pulser signals injected at the level of NINO cards,  $\sigma_{electronics} = 63$  ps), can be followed in Fig.1. As can be seen, the intrinsic time resolution at the level of  $\sigma = 50$  ps is stable over many runs.

The position resolution along the strips is given by the standard deviation of the distribution of the time difference; i.e.  $t_{diff} = (t_{left} - t_{right})$ . The position calibration was performed using the runs in which one RPC was rotated by 90° relativ to the other. Selecting the tracks within a strip pitch in the reference counter, the position distribution along a given strip in the studied counter was obtained. The obtained position resolution ( $\sim 4.5$  mm) for two measured strips conditioned by 5 strips in the reference counter is represented in Fig. 2. The position reconstruction across the

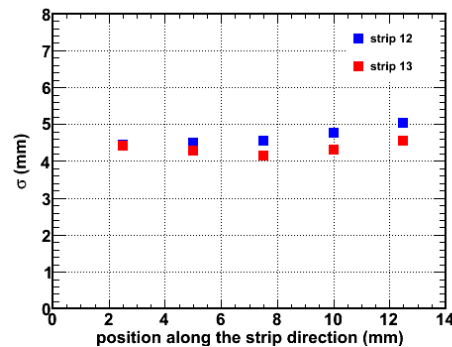


Figure 2: Position resolution along the strip

strips was obtained based on the center of gravity method using time-over-threshold information. The position resolution across the strips ( $\sim 170$   $\mu$ m) was extracted from the Gaussian fit of the residual distribution (obtained as the difference of the hit position in one counter relativ to the track defined by the other two counters).

Based on the results reported in this contribution and previous measurements with low resistivity glass [1], such an architecture is strongly recommended to be used for the most inner region of the CBM-TOF subdetector.

## References

- [1] D. Bartoş *et al.*, IEEE Nuclear Science Symposium Conf. Rec. (2008) 1933
- [2] M. Petriş *et al.*, Rom. Journ. Phys. **56** (2011) 349
- [3] M. Petriş *et al.*, CBM Progress Report 2010, Darmstadt 2011, p. 48
- [4] Yi Wang *et al.*, CBM Progress Report 2010, Darmstadt 2011, p. 50
- [5] F. Anghinolfi *et al.*, Nucl. Instrum. Methods A **533** (2004) 183

## Towards a real size RPC cell for CBM RPC-TOF

M. Petriş<sup>1</sup>, M. Petrovici<sup>1</sup>, V. Simion<sup>1</sup>, D. Bartoş<sup>1</sup>, G. Carageorgheopol<sup>1</sup>, F. Constantin<sup>1</sup>,  
L. Rădulescu<sup>1</sup>, J. Adamczewski-Musch<sup>3</sup>, I. Deppner<sup>2</sup>, N. Herrmann<sup>2</sup>, S. Linev<sup>3</sup>, P. Loizeau<sup>2</sup>, and  
M. C. S. Williams<sup>4</sup>

<sup>1</sup>NIPNE, Bucharest, Romania; <sup>2</sup>Ruprecht-Karls-Universität, Heidelberg, Germany; <sup>3</sup>GSI, Darmstadt, Germany;  
<sup>4</sup>INFN, Bologna, Italy

We proposed as the basic unit for the inner zone of the TOF wall the high granularity, differential strip readout, high counting rate MRPC prototype described in [1]. The MRPC has a differential, strip structure (46 mm strip length x 2.5 mm pitch) readout, a time resolution of  $\sim 50$  ps at an efficiency plateau of 97 - 98 %.

Considering the measured cluster size of about 3 strips [2], the requirement for the readout cell area ( $5.6 \text{ cm}^2$ ) of the most inner zone of the CBM-TOF wall [3] and the cost which is proportional with the number of read-out channels, we propose a new MRPC architecture with the read-out electrodes at 7.1 mm strip pitch (5.6 mm width) and 96 mm strip length (Fig. 1).

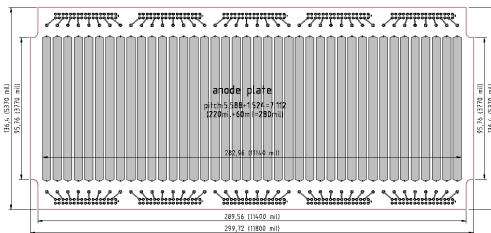


Figure 1: Sketch of the anode electrode

This new design has the advantage of reduced number of the readout channels relative to the MRPC prototype with 2.5 mm pitch, therefore less expensive construction of this particular zone of the CBM TOF wall.

The chamber is a completely symmetric two stack structure with high voltage electrodes for both positive and negative polarities. The high voltage electrodes have a strip structure identical with the readout electrodes. Each stack has 6 resistive electrodes from a special low resistivity glass ( $\sim 10^{10} \Omega\text{cm}$ ) [4] defining 5 gaps of  $140 \mu\text{m}$  each. The central anode has a double sided strip structure. The outermost electrodes are the cathodes. The corresponding strips of the two sides of the central anode and of the outer cathodes, respectively, are connected together. The anode and cathode signals are connected by twisted pair cables of  $50 \Omega$  impedance and sent to the differential FEE based on the NINO chip [5] followed by a V1290A VME TDC.

Two identical chambers are housed by a gas tight stainless steel box. They are mounted one behind the other, with an overlap of 6 mm (Fig. 2). The chambers were tested at T9 beam line of CERN PS accelerator with a mixed electron and pion beam of 2 - 10 GeV/c momenta and in high counting rate at COSY, FZ-Jülich, with 2.5 GeV/c protons.

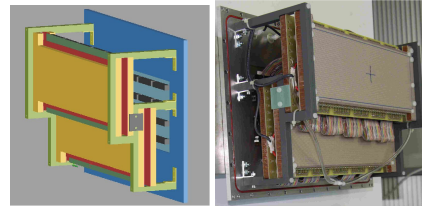


Figure 2: Sketch (left side) and photo (right side) of chamber overlap

The counters were operated with  $90\% \text{C}_2\text{F}_4\text{H}_2 + 5\% \text{SF}_6 + 5\% \text{iso-C}_4\text{H}_{10}$  gas mixture. We recorded the time information at both ends of each strip ( $t_{\text{left}}, t_{\text{right}}$ ). The mean  $t_{\text{mean}} = (t_{\text{left}} + t_{\text{right}})/2$  was used in order to estimate the time resolution. The time difference between  $t_{\text{mean}}$  measured by each chamber is represented in Fig. 3.

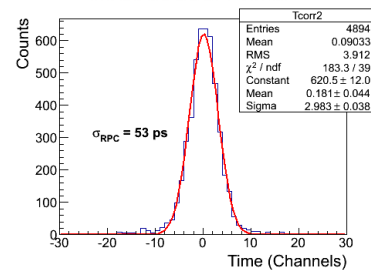


Figure 3: The time of flight spectrum

For an applied high voltage of 2.32 kV/gap, an efficiency of 96% is reached for a counting rate of 1 - 2 kHz/cm<sup>2</sup>. For this electric field and beam rate the single chamber time resolution measured for the overlapping zone of the two MRPCs, after walk correction, including the electronics contribution, is  $\sigma = 53$  ps (Fig. 3). A detailed analysis of the data for efficiency, time and position resolution as a function of high voltage and counting rate is in progress.

## References

- [1] M Petriş *et al.*, CBM Progress Report 2010, p. 48
- [2] M. Petriş *et al.*, CBM Collaboration Meeting, Beijing, 2011
- [3] *Compressed Baryonic Matter Experiment - Technical Status Report*, Darmstadt 2005
- [4] Yi Wang *et al.*, CBM Progress Report 2010, p. 50
- [5] F. Anghinolfi *et al.*, Nucl. Instrum. Methods **A 533** (2004) 183



## Performance of large area MMRPC prototype

I. Deppner<sup>1</sup>, N. Herrmann<sup>1</sup>, P.-A. Loizeau<sup>1</sup>, K. Wisniewski<sup>1</sup>, C. Xiang<sup>1,2</sup>, Y. Zhang<sup>1</sup>, M. Ciobanu<sup>3</sup>, J. Frühauf<sup>3</sup>, M. Petriş<sup>4</sup>, and M. Petrovici<sup>4</sup>

<sup>1</sup>Ruprecht-Karls-Universität, Heidelberg, Germany; <sup>2</sup>Central China Normal University, Wuhan, China; <sup>3</sup>GSI, Darmstadt, Germany; <sup>4</sup>NIPNE, Bucharest, Romania

For the low rate region ( $< 1 \text{ kHz/cm}^2$ ) of the CBM Time-of-Flight wall the setup of Multi-strip Multi-gap Resistive Plate Chambers (MMRPC) equipped with thin standard float glass is considered to be a proper solution which allows to fulfill the PID capability requirements [1]. Making use of the knowledge gained from the previous prototype (see [2]) we developed a new fully differential large area MMRPC prototype at Physikalisches Institut in Heidelberg. Here we report on the design of this counter and present first results obtained during test experiments at GSI.

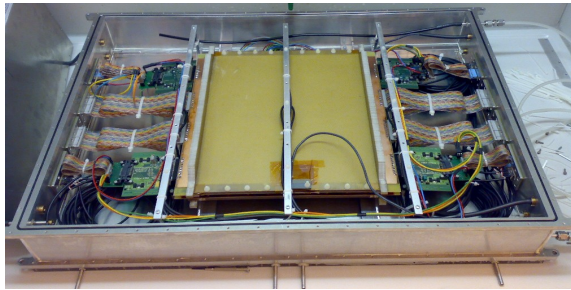


Figure 1: MMRPC mounted in a aluminum box. 16 out of 32 readout strips were equipped with FEE-boards directly on the counter

In order to approach a real size demonstrator we enlarged the active area of the new counter to  $32 \times 27 \text{ cm}^2$ . Consequently the number of strips was increased to 32. For mechanical stiffness 6mm thick honeycomb structured layers were introduced. Fig. 1 illustrates the MMRPC embedded in the gas-tight aluminum box. The inner structure of the counter (gap size, number of gaps, strip width, glass thickness and glass type) is identical to the previous prototype [2]. Modifications were done on the signal pickup electrodes by improving the impedance matching to the front end electronics (FEE) which is now in the order of  $93 \Omega$  and in particular on the signal transmission between strip and FEE. Alternatively it is possible now to connect the FEE-cards carrying the PADI-discriminator directly on the RPC pickup electrode. Therefore RPC signals which are in the order of 20 mV can be discriminated immediately without quality loss due to propagation in the cable. During the test beam time some of the strips were equipped with FEE-boards on the counter. Fig. 2 shows the obtained dependence of the efficiency on the applied RPC high voltage (RPC-HV). The red squares symbolize the measured efficiency with the electronics attached directly

on the RPC inside the box. The threshold of PADI which is applied after the amplification (Gain  $\approx 8$ ) of the analog signal was set remotely to 27 mV. The black data points are related to the results obtained with the electronics located outside the chamber. The threshold in this cases was set to 30 mV (square) and to 50 mV (diamond). This plot illustrates that the demanded efficiency of 95% is reachable for thresholds up to 30 mV at the nominal working voltage of about 11.3 kV. Efficiency measurements done with the electronics mounted inside show slightly better results even if one scales them to the same threshold. The best efficiency (above 97%) was achieved at a threshold of 23 mV. The mean cluster size which is defined as the average number of neighboring strips which fire simultaneously is strongly connected with RPC-HV and therefore with efficiency as well. At nominal working voltage it is in the order of 1.3 and is not reducible without efficiency loss.

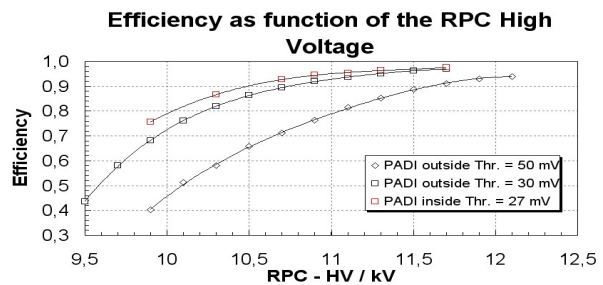


Figure 2: Efficiency vs. applied RPC high voltage for various thresholds

As a reference for time resolution measurements a high granularity MRPC prototype from Bucharest with electrodes made of low resistive glass [3] was used. Including walk correction a full system time resolution of about 70 ps - 75 ps was achieved. Under the assumption that both RPCs have similar resolution a single counter time resolution between 50 ps and 55 ps including the contribution from its FEE is obtained.

## References

- [1] I. Deppner *et al.*, Nucl. Instrum. Methods **A661** (2012) S121
- [2] I. Deppner *et al.*, CBM Progress Report 2009, Darmstadt 2010, p. 40
- [3] M. Petriş *et al.*, CBM Progress Report 2010, Darmstadt 2011, p. 48

## Aging Test of High Rate MRPC

Y. Wang, X. Fan, J. Wang, H. Chen, Y. Li, and J. Cheng

Tsinghua University, Beijing, China

The TOF wall of CBM, used for hadron identification, is proposed to be constructed with MRPCs [1]. In the center area, MRPCs have to be assembled with low resistivity glass to sustain the high hadron flux rate up to  $20 \text{ kHz/cm}^2$ . A kind of low resistivity silicate glass with bulk resistivity in the order of  $10^{10} \Omega \cdot \text{cm}$  was produced in Tsinghua University [2]. Two kinds of MRPCs (Pad readout and strip readout) were developed with this low resistivity glass. The beam test results show that the detectors have a very promising rate capability: time resolutions below  $70 \text{ ps}$  and efficiencies larger than 90% were obtained for particle fluxes up to  $30 \text{ kHz/cm}^2$ . The low resistivity glass is a new material, the goal of the test is to know if the performance of the detector is deteriorated by the large irradiation dose expected in the experiment in several years of operation.

The experiment was operated with the pad MRPC[3] assembled with low resistivity glass. The dimension of readout pad is  $2 \text{ cm} \times 2 \text{ cm}$ . The detector consists of ten gaps and the width of gap is  $220 \mu\text{m}$ . The working gas consists of 90% Freon, 5% isobutane and 5%  $\text{SF}_6$ . The working voltage is  $12 \text{ kV}$ . An X-ray machine is used to do the radiation experiment. In order to monitor the performance, two digital rate meters were used to record the current and signal rate per minute. This is shown in Fig.1. The dose

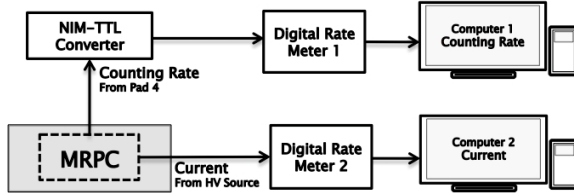


Figure 1: The schematic diagram of monitoring system

rate is about  $2.16 \times 10^{-3} \text{ Gy/h}$ , which is equal to be irradiated with  $30 \text{ MeV}$  electron with flux rate of  $10 \text{ kHz/cm}^2$ . The irradiation is separated into three phase and the total time is  $300 \text{ hours}$ . Fig.2 shows the change of current and counting rate under X-ray with test time. It can be seen that the current fluctuate near  $200 \text{ nA}$  and the counting rate is about  $35 \text{ kHz/pad}$ . Both are very stable during the irradiation. To protect the X-ray supplier, the machine has to be switched off for  $30 \text{ minutes}$  between every  $8 \text{ hours}$  of irradiation. It can be seen from Fig.2 when the X-ray is switched on or off, the current and counting rate change very fast. Fig.2 and 3 shows the comparison between high rate MRPC and common glass MRPC. When the X-ray supplier turns on, current takes very few seconds for high rate MRPC to reach stable state, but for common

glass MRPC, this process will last about two hours.

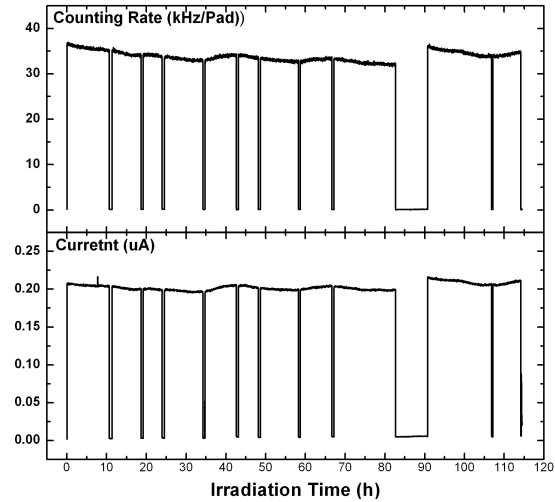


Figure 2: Current and counting rate change with test time (low resistivity glass)

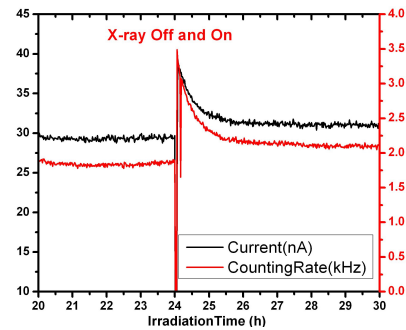


Figure 3: Transient response of common glass MRPC

Between each phase, the MRPC has to be tested with cosmic ray. Efficiency, time resolution and other performances were tested. For example, the time resolution of the  $4^{\text{th}}$  pad is  $90 \text{ ps}$  before irradiation, it becomes  $95 \text{ ps}$  after  $100 \text{ hours}$  irradiation and it is about  $90 \text{ ps}$  after  $300 \text{ hours}$  irradiation. In conclusion, we do not observe any significant performance degradation.

## References

- [1] I. Deppner *et al.*, Nucl. Instrum. Methods **A 661** (2012) S121
- [2] J. Wang *et al.*, Nucl. Instrum. Methods **A 621** (2010) 151
- [3] Y. Wang *et al.*, Nucl. Instrum. Methods **A 661** (2012) S134

## In beam test of CBM-TOF electronics chain

P.-A. Loizeau<sup>1</sup>, N. Herrmann<sup>1</sup>, I. Deppner<sup>1</sup>, K. Wisniewski<sup>1</sup>, C. Xiang<sup>1,2</sup>, J. Adamczewski-Musch<sup>3</sup>, M. Ciobanu<sup>3</sup>, H. Deppe<sup>3</sup>, H. Flemming<sup>3</sup>, J. Frühau<sup>3</sup>, K. Koch<sup>3</sup>, S. Linev<sup>3</sup>, and S. Manz<sup>1</sup>

<sup>1</sup>Ruprecht-Karls-Universität, Heidelberg, Germany; <sup>2</sup>Huazhong Normal University, Wuhan, China; <sup>3</sup>GSI, Darmstadt, Germany

The data acquisition of the CBM experiment will be mostly free-streaming. We develop a prototype for the CBM-Time Of Flight wall electronic chain, specifically adapted for Resistive Plate Chambers (RPC), and present here in-beam test results. The free-streaming data were acquired in November 2011 at COSY, Jülich, with an hybrid DAQ combining and synchronizing them with triggered data.

The self-triggered chain hardware was the same as in 2010[1], while the RPC was the full size prototype tested in June 2011 at GSI with triggered electronics[2]. Modifications were done to the Readout Controller (ROC) and DABC DAQ to reset all GET4 chips automatically if their buffer get stuck. The signals used as time reference in this test are produced by 3 plastic scintillators, 2 in front of the setup and 1 in the back, equipped on both ends with Photomultipliers (PMT). We readout these signals in a triggered CAEN VME TDC board, to decouple the readout system test from the triggered detectors test. For this reason we need the hybrid system. The trigger was built from coincidences of 1 front and 1 back scintillator signal. Detector signals are measured with the GET4 free-streaming TDC.

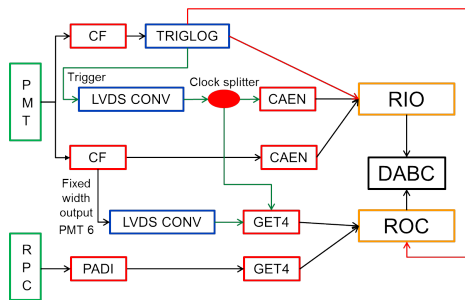


Figure 1: Synchronization in the hybrid system, green lines are time synchronization signals and red ones are event synchronization. CF = Constant Fraction Discriminator.

The synchronization between the two systems proceeds with two levels of accuracy: first at the event level, using already existing possibilities of the DABC DAQ and the TRIGLOG trigger board, then at the timing resolution level, using signals measured in both systems. The first one allows to match free-streaming hits with a defined triggered event. It is done by injecting in both the MBS event and all ROC data streams an event number generated by the TRIGLOG. This number is timestamped by each ROC on reception. The second level is achieved by generating a common point for each event in both the free streaming time frame and the triggered TDC time frame. This is needed to compare the reference time to the detector time

and evaluate the system performances, as they run on different clocks. The synchronization is realised by converting the NIM trigger signal from the triggered system to a LVDS signal accepted by both systems, splitting it with a low jitter clock splitter and re-injecting it in the input of the GET4 TDC and the CAEN TDC, see Fig.1. One PMT signal (PMT 6) signal is also measured in the GET4 system, allowing for an independent cross check of the time offset.

The time resolution is obtained from the width of the time difference distribution  $\Delta t_{ref} = (t_{f1} + t_{f2})/2 - (t_{f3} + t_{f4})/2$  of the front scintillators. It amounts to  $\sigma_{\Delta t_{ref}} = 45ps$ . The contribution of the time synchronization part of the setup can be estimated by calculating the time difference between the PMT6 signal in the triggered system and its signal in the free-streaming system, re-aligned using the offset obtained with the trigger signal:  $\Delta t_{PMT6} = t_{PMT6,CAEN} - t_{PMT6,GET4} - Offset$  with  $Offset = t_{trigger,CAEN} - t_{trigger,GET4}$ . The contribution is given by the width of the difference between those two quantities (Fig. 2), which gives  $\sigma_{\Delta t_{PMT6}} = 80ps$ .

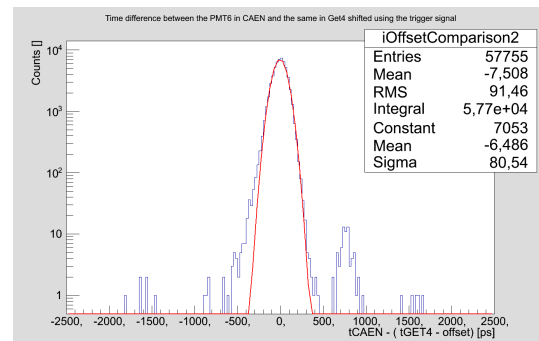


Figure 2: Difference between the time of PMT6 measured in the triggered system and the same recorded in the free-streaming system corrected using the trigger signal

Next steps for the estimation of the free-streaming system performances are extracting both time resolution and efficiency for the RPC + electronic part and comparing to the triggered system to extract the electronics contribution. This comparison will be based on data with a maximum rate of around 100Hz, up to which the current free-streaming system runs stably.

## References

- [1] P.-A. Loizeau *et al.*, CBM Progress Report 2010, Darmstadt 2011, p. 55
- [2] I. Deppner *et al.*, *Performance of large area MMRPC prototype*, this report

## FPGA based control and monitor for CBM-TOF readout

C. Xiang<sup>1,2</sup>, N. Herrmann<sup>2</sup>, I. Deppner<sup>2</sup>, P.-A. Loizeau<sup>2</sup>, K. Wisniewski<sup>2</sup>, Y. Zhang<sup>2</sup>, J. Frühauf<sup>3</sup>, S. Linev<sup>3</sup>, and S. Manz<sup>1</sup>

<sup>1</sup>Central China Normal University, Wuhan, China; <sup>2</sup>Ruprecht-Karls-Universität, Heidelberg, Germany; <sup>3</sup>GSI, Darmstadt, Germany

As the CBM experiment will apply a free streaming data acquisition system, the system will be exposed to a potentially very high data rate like in the case of noisy channels. In order to suppress useless data as soon as possible and to prevent bottle-necks in this readout bandwidth, we design a data preprocessing module in the readout chain [1]. In order to control the proper functioning of the system one needs in addition a monitor module. A third task that could be integrated in the readout controller is a control module that could be used e.g. to automatically modify thresholds. The system is sketched in Fig. 1.

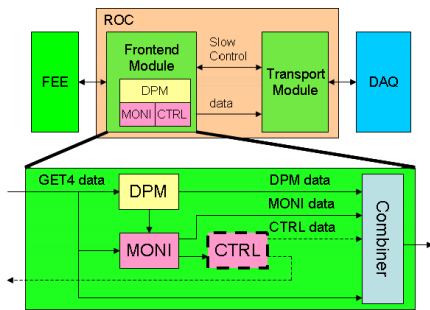


Figure 1: ROC firmware (Frontend module)

The data preprocessing module (DPM) reads in data from the GET4-ASIC [2], inspects the data and sends the results by the transport module to the DAQ system. Several functions are implemented in the DPM like time ordering, hit building and checking the validity of the time-over-threshold (TOT) determination. The main task of the monitor module is to assure the synchronization of the system. This is done by checking the validity of the epoch marks that are part of the GET4 data output stream. When any of these status goes wrong, a message will be sent to DAQ and possibly to the control module. After the control module gets these messages, it will decide what to do and send the control information to DAQ at same time. The monitor module also reads the PADI thresholds and the status of the DPM. To control the full TOF system different ways to implement a control tasks are possible ranging from manual control to fully automatic self-control. While the best control strategy is still under evaluation, for the test experiments, that are performed with prototype components, the manual control initialized by the user via the DAQ interface is fully sufficient.

As the logic resources in the FPGA of the ROC board are limited, the DPM is only implemented from channel 0 to channel 7 out of 56 channels. The ROC firmware

was tested at COSY with proton beam. First results on the performance of the DPM/Monitor are presented here. The left panel of Fig. 2 shows the examples of TOT spectra registered for different channels. The red line is the TOT of channel 9. Comparing with other channels, it has larger number of hits than others, and the TOT spectrum extends to very large unphysical values. This is because of the threshold of channel 9 is too low, which requires an increase of the PADI discrimination threshold. After reconfiguring its threshold, the problem was solved. The right panel shows the total number of hits and the number of valid hit. The black line shows the number of valid hits obtained by the offline analysis, the red line the total number of hits obtained by the offline analysis, the green line the total number of hits obtained by the DPM in ROC, the blue line the number of valid hits obtained by the DPM in ROC. For the first 8 channel, only blue line can be seen, as the other three colored lines are overwritten. This shows that the DPM in ROC gives the same results as offline analysis. There is a large difference between the total number of hits and the number of valid hits registered on channel 13, the reason is its rising edges and leading edges were separated in two epochs. The only way to resolve this problem is to reset the GET4 chip.

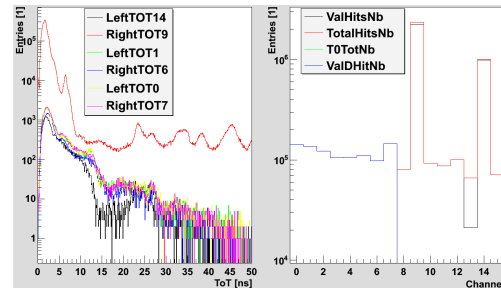


Figure 2: Left: Channel TOT spectrum; Right: the number of hits

The offline analysis result shows the DPM and the monitor module function properly. Next step is adding new features in the DPM, like cluster finding, and implementing self-control.

## References

- [1] S. Manz, "GET4 Read-Out Development", CBM FEE/DAQ Workshop, 22-23 February 2010, Darmstadt, Germany
- [2] H. Flemming and H. Deppe, IEEE Nuclear Science Symposium Conf. Rec. (2009) 295

# The adapted CBM network structure design and CBMnet V2.0 implementation

F. Lemke, S. Schenk, and U. Brüning

Ruprecht-Karls-Universität Heidelberg, Mannheim, Germany

The CBMnet V1 was intensively tested within the CBM DAQ system network structure showing excellent results [1]. Due to some new requirements CBMnet V2.0 has been designed and implemented. The most important new features are link based retransmission, perfectly fitting into the new flow control scheme, and a support for unbalanced communication delivering more lanes (higher bandwidth) in FLES direction than for FEE control towards the detector. In addition, developments have been done to support new SPARTAN 6 FPGAs. This guarantees the usability for new planned ROC versions. Hardware has been assembled and tested to build-up larger test beam read-outs at the beginning of 2012 using up to 5 DCBs. One of them is used as control system and 4 DCBs, which are connected to ABBs, support up to  $4 \times 4 = 16$  ROCs running in parallel supporting different kinds and amounts of FEBs. The implementation of the CBMnet V2.0 that is used as final version for the CBM DAQ network led to the development of a generic module block, which can be used for different FEE ASICs. The generic module structure with CBMnet V2.0 as built-in block for FEE ASICs is shown in Figure 1. This generic module has already been integrated into a first FEE ASIC chip. Additionally to CBMnet V2.0 it delivers a register file with control modules for user defined and global control and configuration of the ASIC, I2C modules for test and bring up, and automatic link bring-up and configuration support.

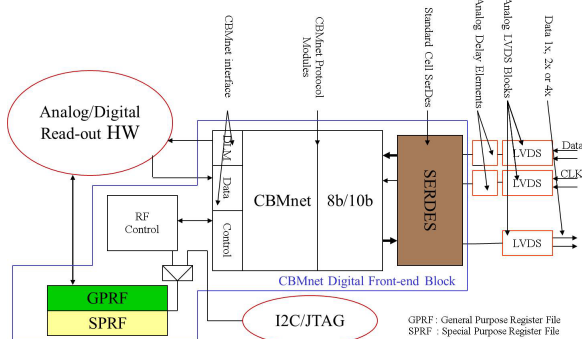


Figure 1: Generic CBMnet Module Structure

The Silicon Tracking System (STS) poses the most demanding requirements for bandwidth and density of all CBM detectors. In STS a total of 17000 ASICs, producing 300-500 GB/sec data, must be read-out in the very confined space available for electronics, calling for a much denser and also more radiation tolerant solution than the

FPGA based ROCs currently used in early prototyping setups. The MUCH and TRD detectors also feature a high data density. The proposed DAQ chain for these detectors is based on a HUB ASIC, responsible for data aggregation, synchronization and rate conversion. An overview of the planned HUB ASIC structure is presented in Figure 2. It mediates between the front-end ASICs, which can be connected with 1,2 or 4 LVDS lanes operated at 500 Mbps, and the optical links operated with at least 5 Gbps. The number of links per HUB is yet to be optimized to meet the density and total cost targets. A plausible value is four 5 Gbps links per HUB, which would allow to support 10 to 40 FEE ASICs per HUB. To achieve the required density for the electrical to optical conversion the usage of active optical cables (AOC) technology with 12 lanes seems to be most promising solution. This allows to use COTS components at this stage. Analysis and research concerning the AOCs [2] has been done, but further analysis for the opto-converter board is required. For the next year first prototyping steps and radiation tests for AOCs are planned.

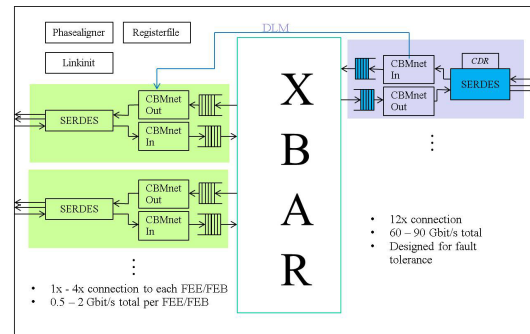


Figure 2: HUB ASIC Structure

## References

- [1] F. Lemke, S. Schenk, U. Brüning, *Experiences and results using the CBMnet protocol including precise time synchronization and clock distribution*, Frühjahrstagung der Deutsche Physikalische Gesellschaft, March 21-25, Muenster 2011, Germany
- [2] D. Wohlfeld, F. Lemke, H. Froening, S. Schenk, U. Brüning, *High Density Active Optical Cable: from a Concept to a Prototype*, SPIE Photonics West, Optoelectronic Interconnects and Component Integration XI, January 22-27, San Francisco 2011, California

## Radiation tolerant 2.5GHz clock multiplier unit in UMC 0.18 $\mu$ m technology

T. K. Bhattacharyya, D. Mandal, T. P. Chand, V. Tantri, P. Kumar, A. Panigrahi, and P. Banerjee

Indian Institute of Technology, Kharagpur, India

In the CBM experiments Hub ASICs are responsible for the data aggregation from several readout-ASICs into a single output link. Each ASIC hub contains many serializers and deserializers along with clock multiplier unit (CMU) and clock and data recovery blocks. Clock multiplier unit will be responsible for the generation of 2.5GHz clock for the multiplexer in the SERDES. Along with the desired functionality it needs to be radiation tolerant. Radiation on the silicon ICs have 2 kinds of effects. The properties of silicon devices will drift over a prolonged duration of exposure which is termed as Total Ionization Dose effects. The other effect of data flipping at memory is called as Single Event Effect. The clock multiplier unit has to be designed keeping these considerations in context.

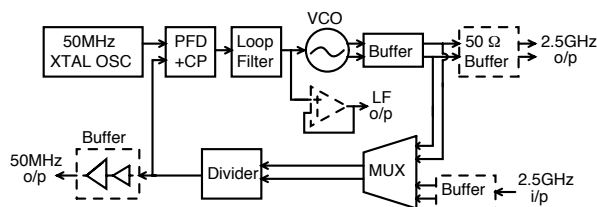


Figure 1: Block diagram of CMU

Figure 1 depicts the overall block diagram of the clock multiplier unit. VCO designed is LC oscillator with operating frequency of 2.5GHz. The reference frequency is 50MHz and the division ratio is 50 for the frequency divider. Differential buffers are used to drive the output buffer and the MUX associated with the divider. A buffer with MUX is designed so that the divider can be tested separately by an external signal and from the VCO output. A single ended to differential signal buffer will generate differential signals from a single ended 2.5GHz signal. The output of the divider will be driven to the output pads through a tapered inverter buffer. The PFD will estimate the phase difference between the reference signal and the divider output and the phase information is converted to voltage domain by the combination of the charge pump and loop filter. A unity gain buffer is associated with the loop filter to observe the output of the loop filter.

Design features of the CMU are:

- 1.) The CMU can work in 5 modes of operation. This has been enabled for better testability of individual blocks against radiation. a) VCO standalone mode, b) divider standalone mode, c) VCO-divider pair, d) divider-PFD-CP-LF, e) normal CMU operation.
- 2.) VCO tail currents can be varied from 1.75mA to 4.5mA

from the bandgap reference.

- 3.) VCO frequencies are tunable with binary weighted switched capacitor arrays to accommodate process variations. With 5 switches the tuning range obtained is from 2.1GHz to 2.85GHz.

- 4.) The divider is designed using 2 logic families. CML is used at the front end for high frequency blocks and CMOS in later stage to reduce static power dissipation. Critical charge at nodes in CML blocks are increased to make it more radiation tolerant.

The schematic of the full block has been designed and simulated. Operation of VCO, divider, buffers and bandgap reference have been verified at all the PVT corners. Layouts of VCO, divider, buffers, bandgap reference have been completed and integrated together. Guard rings have been used in layout to enhance the radiation tolerance. Post layout extraction of these blocks have been done and functionality of the blocks have been verified with post layout simulations. Figure 2 depicts the completed layout of these blocks along with the signal and power routing.

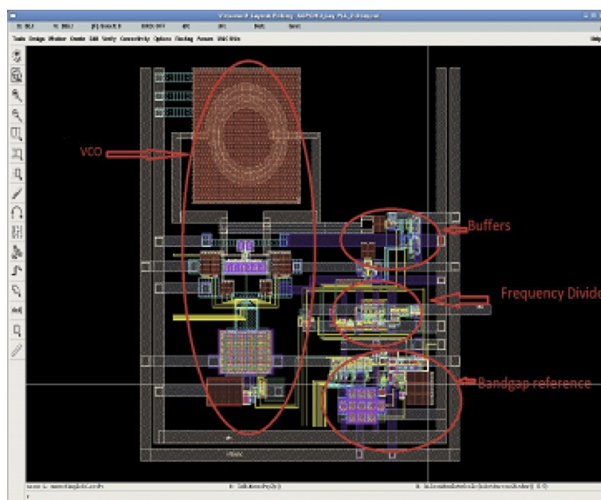


Figure 2: Layout of VCO, divider, BGR and buffers

### References

- [1] R. C. H. van de Beek *et al.*, Solid-State Circuits Conference 2003, IEE-ISSCC (2003) 178
- [2] P. Moreira *et al.*, A Radiation Tolerant Gigabit Serializer for LHC data transmission, Proc. of 7th Workshop on Electronics for LHC Experiments, Stockholm 2001

## SysCore3 — a new board for the Universal ROC

*N. Abel, C. Garcia, J. Gebelein, S. Manz, and U. Kebschull*

Goethe-Universität, Frankfurt/Main, Germany

Since 2007 our contribution focused the Silicon Tracker's FEE (Front End Electronic). Since 2009 we are also designing and implementing readout logic for the GET4 chip. To keep the re-usability as high as possible, we split the ROC into two fully independent modules: the readout logic and the transport logic. This modularization of the ROC and the consequential separation of the control software into different layers, enabled us to provide a Universal ROC, which offers quick access to a long-run tested transport logic and allows us to easily add new readout logic for further FEE setups [1]. The Universal ROC is currently based on the SysCore2 board. In 2011 we focused on the further support of the GET4 chip, the development of a Feature-Extraction for TRD [2] and the design of the new SysCore3 board, which will become the new basis of the Universal ROC in 2012. The design of the SysCore3 board is the logical next step in the development of a platform which shall be as flexible as possible. Based on its flexibility SysCore3 is planned to be used as prototyping platform in a number of subsystems. Examples are the development of read-out ASICs using FEELink interfaces, the development of read-out controllers for nXYTER and GET4, CBMnet HUB chip development and DPB development. Furthermore the SysCore3 will serve as fault tolerant read-out controller for ToF [3].

The SysCore3 board is based on a Spartan-6 LX150T (while SysCore2 is based on a Virtex-4). This change is motivated by the high difference in cost between the Virtex-Series and the Spartan-Series. It is enabled by the fact that, starting with Version 6, the Spartan-Series supports high speed optical links, high speed interfaces (like DDR3) and dynamic reconfiguration which is essential for fault tolerance [4].

If two or more boards are used to reconstruct a physical event, such as the motion of a particle, one of the most important features is time synchronization. The CBMnet provides a very flexible synchronization approach which does not depend on cable lengths [5]. If a board shall not only be able to receive an external clock via an optical port, but shall also be able to respond with a determined latency on the same port, it needs a special connection between the FPGA and this optical port. To put it in a nutshell, the optical port needs different reference clocks for its receiver and its sender part. The SysCore3 board implements this special connection on a particular port (called "uplink"). Furthermore it provides a jitter cleaner which takes the recovered clock from the FPGA, cleans the jitter and thus

enables the usage of the recovered clock as reference clock for optical transceivers. This board-based feature is essential to be able to fully support the CBMnet functionality.

The heart of most ROCs is a SRAM based FPGA, since these FPGAs provide the best combination of performance and long-term flexibility. However, there is a crucial problem regarding FPGAs: the radiation which is inevitable in high energy physics experiments can cause the FPGA's doped silicon to change its electrical properties, depending on its linear energy transfer. This physical separation of electron-hole pairs results in spontaneous Single Event Effects (SEE). This becomes extremely critical for flip-flops at clock signal setup/hold times, which can lead to erroneous data and in the worst case to a total system halt (SEFI). Thus, the usability of FPGAs in radiation environments highly depends on the usage of mitigation technologies such as scrubbing (based on dynamic reconfiguration). This has a strong influence on the board design: the SysCore3 board provides an external FLASH memory and an additional radiation hard flash-based FPGA — both are essential to be able to realize scrubbing. In 2011, example designs have been practically tested under experimental conditions within different particle accelerator beams. Test boards have been directly placed into the center of the particle beam line to get comprehensible results at a maximum ionization impact. Current results are very encouraging and show that the usage of scrubbing in combination with double or triple module redundancy significantly reduces the number of radiation based functional interrupts [6].

### References

- [1] N. Abel *et al.*, CBM Progress Report 2009, Darmstadt 2010, p. 53
- [2] C. Garcia, *First steps towards feature extraction in TRD*, CBM Collaboration Meeting 2011, Beijing, China
- [3] W. Müller, *SysCore V3 - Hardware Concept and Use Cases*, CBM Collaboration Meeting 2011, Beijing, China
- [4] N. Abel, *SysCore V3 - Firmware Aspects*, CBM Collaboration Meeting 2011, Beijing, China
- [5] F. Lemke *et al.*, Real Time Conference 2009, IEEE-NPSS (2009) 506
- [6] J. Gebelein *et al.*, *FPGA fault tolerance in radiation susceptible environments*, this report

## FPGA fault tolerance in radiation susceptible environments

*J. Gebelein and U. Kebschull*

Goethe-Universität, Frankfurt/Main, Germany

Continuous research and development in the field of particle accelerator detector electronics focusing on Static Random Access Memory (SRAM) Field Programmable Gate Arrays (FPGA) confirmed that the use of fault tolerance techniques is inevitably required for safe operation in radiation susceptible environments [1, 2, 3]. (Not even ASICs are spared from it [4].) Therefore, several formerly presented research results dealt with the well-known partial configuration scrubbing, especially Blind Scrubbing, supported by a subset of such devices as well as the creation of standardized components to be used within a Programmable System-on-Chip (PSoC) [5]. Current approaches mainly address techniques on Register-Transfer-Level (RTL), for example the use of Hamming-based Finite State Machines (FSM) in combination with Global Triple Modular Redundancy (GTMR). Due to the fact that commercially available tools like Mentor Precision Rad-Tolerant Tool, BYU Partial TMR Tool (BLTmr), Xilinx XTMR Tool and STAR Tool, which apply GTMR to existing hardware designs, are quite expensive and are working on netlists only, manual Hamming FSM designs with surrounding TMR have been created and tested in GeV proton particle beam at the COSY accelerator in Juelich, Germany.

Manual design of fault tolerance on RTL means in the first order to multiply existing resources and to teach synthesis tools to do not remove them when optimizing the circuitry in several stages. Code multiplication itself comprises mainly of signal duplication/triplication and the correspondent use in the entire design. For example, when a concurrent process statement is triplicated, each externally read and written signal within has to be triplicated. Furthermore, each of these new processes has to be adapted to use only one of the triplicated signals. In case of single connected external resources (e.g. I/O pins) are used within the process statement, new signals have to be added, which are provided with voters for output direction or splitters for input direction. Because this manual design is error-prone and mistakes may lead to an overall reduced fault tolerance of the entire design, an automated approach is currently going to be realized. This tool may be the first step for a designer to create a fault-tolerant design on RTL. Afterward, he can decide whether or not to use the provided mechanism or to reduce some parts to a less sensitive fault tolerance method.

Some of these manually created fault-tolerant designs were tested in GeV proton particle beam as seen in figure 1. All of the designs implemented a 2048 states Hamming FSM with a minimum distance of 3 and used Blind Scrubbing to continuously restore static configuration memory. Whereas design C did not use any additional fault toler-

ance and hence showed the worst results, design E added GTMR and FSM dummy transitions and hence returned the fewest output errors. As seen, Scrubbing works perfectly in restoring configuration memory and even better when joined with fault tolerance techniques, but can still be improved by advancing from Blind Scrubbing to Selective Frame Scrubbing, which is going to be implemented within the next project phase. Looking forward to a detector providing maximum fault tolerance, the recommendation is to double/triple all signal paths, including I/O pins.

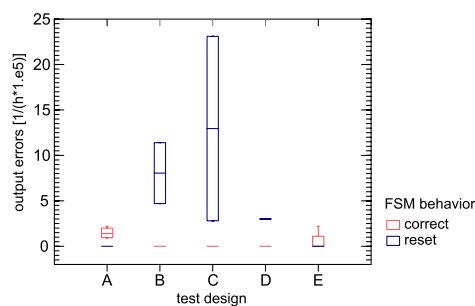


Figure 1: Boxplot (median and quartiles) of the obtained Hamming  $d=3$  FSM beamtest results, normalized to  $1/h$ , 100% chip size and  $1.e5 p+$ . Test designs are using Blind Configuration Scrubbing as well as the following fault tolerance techniques: A: nearly GTMR with FSM dummy transitions, B: nearly GTMR, C: none, D: GTMR, E: GTMR with FSM dummy transitions. I/O pins as well as DCM are single-use in all designs.

### References

- [1] N. Battezzati, L. Sterpone, M. Violante, *Reconfigurable Field Programmable Gate Arrays for Mission-Critical Applications*, 1st Edition, 2011, Springer Verlag, ISBN 978-1-4419-7594-2
- [2] M. Violante, L. Sterpone, *Reconfigurable FPGAs in radioactive environment*, CERN-talk, October 2011, <http://indico.cern.ch/conferenceDisplay.py?confId=152527>
- [3] K. Røed, *Single Event Upsets in SRAM FPGA based readout electronics for the Time Projection Chamber in the ALICE experiment*, University of Bergen, PhD Thesis, 2009
- [4] S. Bonacini, *Redundancy methods in ASICs*, CERN-talk, June 2011, <http://indico.cern.ch/conferenceDisplay.py?confId=131762>
- [5] J. Gebelein, H. Engel, U. Kebschull, *FPGA fault tolerance in radiation susceptible environments*, Proceedings on Radiation Effects on Components and Systems (RADECS) 2010, September 2010



## CBM First-level Event Selector dataflow architecture and microslice concept

*J. de Cuveland, D. Hutter, and V. Lindenstruth*

FIAS Frankfurt Institute for Advanced Studies, Goethe-Universität, Frankfurt am Main, Germany

The First-level Event Selector (FLES) is the central system in the CBM experiment at which all measured data arrives and is analyzed in real time. The detector frontends operate self-triggered, creating a continuous, time-stamped data stream (Fig. 1). The selection of interesting events in the FLES requires sophisticated online analyses including a complete event reconstruction at an incoming data rate exceeding 1 TByte/s.

The FLES system consists of a scalable supercomputer with custom FPGA-based input interface cards and a fast event-building network (Fig. 2). It will be constructed largely from standard components. As a site for the FLES computer system, the new FAIR data center (“Green IT Cube”) has been identified. This location provides an ideal infrastructure for efficient operation of the computer and offers the opportunity to exploit synergies with other FAIR computing systems installed there.

The input interface into the FLES is implemented by add-on cards in the FLES PCs. The FLES Interface Board (FLIB) requires high-speed optical inputs to receive the data from the CBM readout electronics, a high-performance interface to the host PC, and a large buffer memory. A specially developed FPGA-based card with a PCIe interface at the maximum achievable rate will be employed here. A prototype board, realized in cooperation with the ALICE experiment, is currently in an advanced stage of development. It is based on a Xilinx Virtex-6 FPGA and 8x PCIe, and it contains 12 optical links, each at up to 6.6 Gbit/s, and two DDR3 memory module sockets.

The FPGA design implements the DAQ protocol for receiving the data, merges the input links, manages the buffer memory, and controls the PCIe transfer. In addition, it analyzes the incoming time stamp information and builds index tables to facilitate a timestamp-based data access from the host PC.

As the high event rate of 10 MHz prevents a clear a priori assignment of measured particle tracks to events, fundamentally new techniques are necessary regarding the data flow in the system and the reconstruction of events. The employed selection algorithms need the data pertaining to an event of all detectors in a computing node. Instead of event building as in a triggered system, the FLES performs *timeslice building*. The data is first segmented into timeslices containing several events and then distributed appropriately through a network at the full input data rate of 1 TByte/s. The use of InfiniBand QDR for data transfer between the FLES nodes has proven practical.

In order not to require the full bandwidth in case of special selection scenarios and during the phased commissioning of the system, a two-stage selection process has been

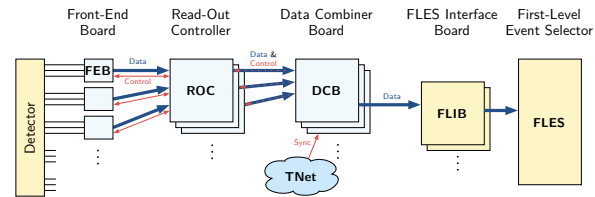


Figure 1: Data flow into the First-level Event Selector

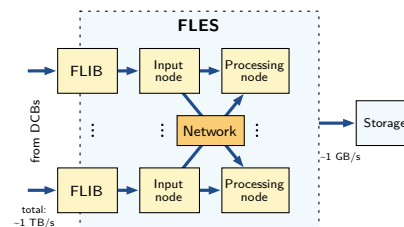


Figure 2: Architecture of the FLES

developed. Data from detectors that do not contribute to the first selection stage is stored in the input nodes and transmitted only on request for selected events to the appropriate computing nodes.

The individual CBM detectors have very different time resolutions and data format requirements. In addition, the data messages sent by the detectors are usually only a few bytes in size. Therefore, the data format of each subsystem is optimized independently for efficient transmission and analysis. However, the FLES system has to collect the data of each timeslice, i. e., an interval of the continuous detector run-time, from all detectors and transmit it to a compute node. Therefore, it needs a way to divide the continuous data streams of the detectors without any loss of information, and it must be able to access the time information in the data stream in a global format. The new concept of *microslices* solves these problems by introducing a special global container format directly at the inputs of the system, where one container comprises the detector data of a globally defined, constant time interval (e. g., 1  $\mu$ s). The lightweight container format generates an overhead of less than 2 percent.

After event selection, the data to be stored it is forwarded for archiving. The resulting data stream of at least 1 GByte/s is sent directly via the FLES network to the mass storage system.

## References

- [1] J. de Cuveland *et al.*, J. Phys. Conf. Ser. **331** (2011) 022006

## ALICE CRORC as CBM FLES interface board prototype

*H. Engel and U. Kebschull*

Goethe-Universität, Frankfurt, Germany

The ALICE Common Read-Out Receiver Card (CRORC) is an FPGA based PCIe read-out card with high density parallel optic connectivity which is currently being developed at CERN. As the requirements for a CBM First Level Event Selector Interface Board (FLIB) prototype are similar to this card, FLIB-specific requirements have already been considered during the planning of the CRORC.

The ALICE Experiment at CERN is using FPGA based Read-Out Receiver Cards (RORCs) at Data Acquisition (DAQ) and High-Level Trigger (HLT) as an interface between the optical Detector Data Link (DDL) and the host machines. The currently used RORCs at DAQ and HLT have similar functionality, but have been developed as independent projects. However, they are now facing the same problem: both cards implement PCI-X as interface to the host machine, which was a state of the art interface standard at the time these cards have been developed, but can now hardly be found in any recent PC mainboard. Furthermore, increased read-out data rates on the optical links are planned, but not possible with the current RORCs.

These facts lead to the development of the CRORC as a common project of DAQ and HLT with recent hardware and interface standards.

The FLES Interface Board serves as an interface between Data Processing Boards and the First Level Event Selector. It is planned to be implemented as an FPGA-based PCI-Express plug-in card with optical interfaces at the FLES input nodes. Streaming data received on the optical interface from the front-end electronics via Read-Out Controllers and Data Processing Boards is received by the FLIB and written into the host machine with Direct Memory Access (DMA). A first prototype board is required as a test platform for FLES hardware and software development as well as a read-out device for testbeams or lab setups.

The full FLES cluster will be fully equipped at a very late stage but all detector components have to be connected at early stages so for the prototype a large number of links is more crucial than a high input rate per link. The FLIB read-out is planned as a two staged process with large on-board buffers to mitigate PCIe bottlenecks and enable partial or on-demand read-out. A FLIB prototype is therefore required to have plenty of DDR memory with a high bandwidth.

The CRORC currently developed for ALICE is a Virtex-6 FF1156 based board with twelve optical links, a PCIe interface and two DDR3 SO-DIMM sockets. A sketch of the board is shown in Fig. 1.

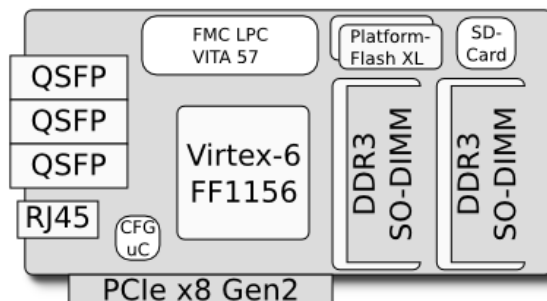


Figure 1: Schematic sketch of the CRORC

The FPGA-internal PCIe hard block is used as interface to the host machine which enables the use of up to eight PCIe Gen2 lanes with an overall bandwidth of up to 32 Gbps. The twelve optical links are realized with three QSFP sockets connected to the Virtex-6 GTX transceivers. A configurable transceiver reference clocks allows link speeds over the whole range of the GTX capabilities of up to 6.5 Gbps per link.

The two DDR3 SO-DIMM sockets can be equipped with standard DDR3 memory modules and can be operated independently with up to 1066 Mbps per data line. The second socket has specifically been added for FLIB prototype purposes.

An FPGA Mezzanine Connector (FMC) allows the connection of custom interface modules or external transceiver reference clocks to the FPGA in order to run the CBMnet protocol.

The FPGA configurations can be stored in on-board flash memories for automatic configuration. Configuration management and monitoring can be done with the FPGA and a microcontroller. An SD-Card slot provides additional non-volatile memory and the RJ45 socket can be used for LVDS IO.

The schematic design of the CRORC is completed and the PCB layout is mostly done. Component purchase and prototype production are currently being prepared. First prototypes are expected for 2012.

## Status of data acquisition software DABC

*S. Linev, J. Adamczewski-Musch, and P. Zumbbruch*

GSI, Darmstadt, Germany

The Data Acquisition Backbone Core (DABC) has been established as DAQ and event building software for CBM test beams [1]. Development of the future version 2 of the DABC framework has been started within 2011. A prototype of DABC v2 was applied in fall 2011 for the test beams at CERN and COSY. For the first time DABC nodes were monitored and controlled by an EPICS-based operator GUI.

Several changes in the DABC core classes were done to increase thread safety of the system. A main problem in a multithreaded environment is that objects created and used by one thread can potentially be destroyed by another thread. To provide a convenient solution for the developers, the special Reference class was introduced to the framework, implementing a thread-safe pointer to any DABC object. Another important change in the framework was the introduction of a ConnectionManager to establish and maintain the data connections between DABC nodes. Such component is crucial in multi-node setups where the probability of a single-node failure is increasing. The task of the Connection-Manager in such case is to renew all connections when a crashed node is restarted. A new interface to the slow control system was introduced to DABC. In contrast to the first version, the control system is fully decoupled from the core functionality of the DABC framework. An implementation for the previous DIM based control protocol was done. The new interface allows to implement and use several control systems simultaneously.

Already DABC v1 had provided a monitoring and control interface by means of the DIM protocol. To integrate the DAQ to the EPICS slow control system [2] that is common for CBM experiment, a separate DIM-EPICS interface application has been used. During the testbeams, this was run as a component of the main EPICS IOC, together with the other detector control system modules. The DABC records as exported via DIM are subscribed by the EPICS IOC and converted to related EPICS process variables. Hence they can be observed and controlled by a regular EPICS GUI, such as the CSS/BOY environment [3]. Figure 1 shows the dedicated GUI as developed for the CERN testbeam in October 2011.

The version 2 prototype of the DABC framework has been used in production for different test setups of the CBM collaboration. A beamtime for TRD and RICH prototypes was performed at CERN/PS T9 in October 2011 [4]. Here a complex heterogeneous setup was implemented: two MBS systems in two VME crates; 12 Susibo/SPADICs boards; 5 ROC/nXYTERs; EPICS readout. Data from all these components were read out and

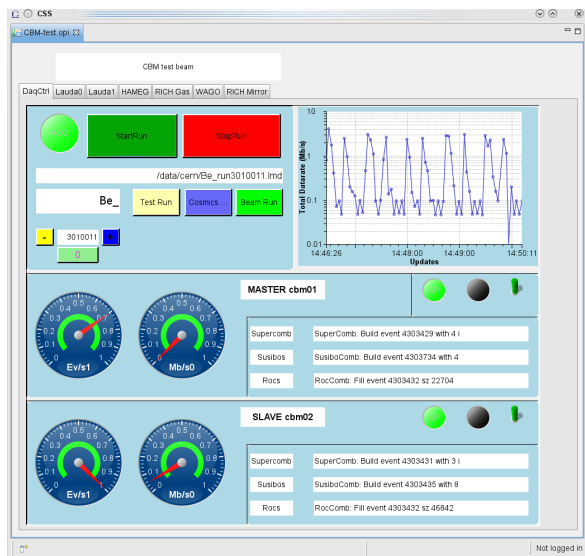


Figure 1: DABC operator GUI at CERN testbeam

combined together by three DABC nodes. Another test beam for TOF/RPC components was done at COSY in November 2011. Here the ROC/GET4 frontend combination was read out via optical fibre connection and PCIe board. A special code in the DABC application was implemented to cope with some readout problems of the GET4 chip.

Version 2 of DABC is under development and has already been used successfully at different detectors tests by the CBM collaboration. DABC version 2 will be released in 2012 and will provide new functionalities not only for CBM test beams, but also for InfiniBand performance tests.

### References

- [1] S. Linev, J. Adamczewski-Musch and J. Frühauf, CBM Progress Report 2010, Darmstadt 2011, p. 64
- [2] <http://www.aps.anl.gov/epics>
- [3] <http://cs-studio.sourceforge.net>
- [4] C. Bergmann *et al.*, *Common CBM beam test of the RICH, TRD and TOF subsystems at the CERN PS T9 beam line*, this report

## A Go4-based online-analysis framework for CBM beam tests

*J. Adamczewski-Musch and S. Linev*

GSI, Darmstadt, Germany

The GSI analysis system *Go4* (<http://go4.gsi.de>) is a standard tool for online and offline analysis, based on the *ROOT* framework. Since 2008 the CBM collaboration has used *Go4* at several detector test beamtimes. To match the requirements for increasing complexity of such tests, the CBM online monitoring software was newly organized as a modular application framework on top of the *Go4* framework.

The basic *Go4* framework allows to split subsequent stages of the analysis into analysis steps, with each step producing intermediate data which is used by the following step. So the first analysis step would unpack the raw data from DAQ. The second analysis step would map such DAQ channels into a detector display and perform a specific analysis. Each analysis step is defined by an event processor class which produces an event element structure as resulting output. However, to cover the use case of various readout systems for different test detectors, each of these analysis steps still needs to be divided up in structurally parallel processing entities and their resulting data structures. Hence the CBM beamtime framework introduces a composite event processor class that can register and run a number of regular *Go4* event processors together within each analysis step. Additionally, the resulting data structures of these software processors are aggregated as a common *Go4* composite event, reflecting the hierarchy of the DAQ and detector set up. An advanced offline analysis could be implemented in a third analysis step, or could be based on the *Go4* output events stored to *ROOT Ttrees*. Figure 1 illustrates the structure of a typical implementation.

By means of shared libraries, the analysis set up for a specific beam time can re-use existing classes of various standard readout components that are acquired and combined by the DAQ system *DABC* [1]. Their data is delivered to *Go4* in generic containers (MBS events): either via TCP sockets, or as listmode data file. So most components of the first *Go4* analysis step were just configured by macro scripts for the actual runtime setup. The source code for each beamtime is also organized in a modular way: each detector subgroup can develop and run their individual code as standalone *Go4* analysis. The combination of several or all subgroup codes can run as advanced or full analysis.

In October 2011, a two week test of TRD and RICH detectors was done at CERN PS beam line T9 [2]. Online monitoring and initial offline analysis were implemented with the new *Go4* based framework. In the first analysis step, generic software modules were used, such as for the *ROC/nXYTER* readout, for the *SPADIC* readout [1], and for EPICS slow control variables [3]. The unpacking of two *MBS* crates data was treated with specific classes. The components of the second analysis step were developed by various institutes. It has different processor modules for beam monitoring scintillators (Uni Frankfurt,GSI), a fiber hodoscope (Uni Wuppertal), a RICH prototype (Uni Wuppertal, Uni Giessen, GSI), and several TRD stations (Uni Frankfurt, Uni Mnster, NIPNE Bucharest and JINR Dubna). The results of such subdetector analysis are combined in this step and can e.g. be used for particle identification. For another beamtime at COSY in November 2011, the online monitoring was organized similarly. The first analysis step consisted of modules for a generic *ROC/Get4* and *ROC/NXYTERr* readout, the *MBS* system, and the EPICS input. The second analysis step contained code for different TOF/RPC prototypes (Uni Heidelberg, HZDR Rossendorf, NIPNE Bucharest), a diamond detector (GSI), and the fiber hodoscope.

### References

- [1] S. Linev, J Adamczewski-Musch and J. Frühauf, CBM Progress Report 2010, Darmstadt 2011, p. 64
- [2] C. Bergmann *et al.*, *Common CBM beam test of the RICH, TRD and TOF subsystems at the CERN PS T9 beam line*, this report
- [3] J. Adamczewski-Musch, B. W. Kolb and S. Linev, CBM Progress Report 2010, Darmstadt 2011, p. 61

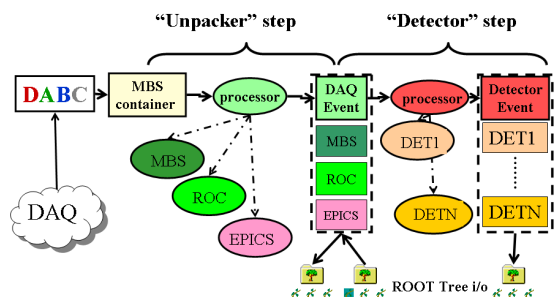


Figure 1: Composite Go4 analysis with two steps

## Study of clustering algorithms for detectors with a pad structure

G. Kozlov

LIT JINR, Dubna, Russia

Clustering algorithms are an important part of the event reconstruction in high energy physics, in particular in the CBM experiment. These algorithms translate fired strips and pads into space coordinates – hits, which are later used in the tracking algorithms. High interaction rate and complex event topology lead to high requirements of the clustering algorithms, which have to perform fast and efficient and be able to deal with high track multiplicity and density. The development of such an algorithm is described in this report.

We reviewed several standard clustering methods and selected two of them. The choice was made by taking into account specific features of the algorithms and their applicability to our problem. The first one is the Ward's method [1]. It has a high efficiency but a low calculation speed, because it calculates a distance matrix. The second one is the single linkage method [2]. This method is simple and fast, but it has a low efficiency for data with a complex topology.

Both of these methods have disadvantages that make it difficult to apply them to our problem. Thus, we developed a specialized clustering algorithm. The basis of this algorithm is the following rule: every pad with local maximum of amplitude forms a separate cluster. Pads not having a local amplitude maximum are attached to the neighbour with the highest amplitudes. This approach allows to define clearly separated clusters (with their own local maximum of amplitude) and does not require complex calculations.

The developed clustering algorithm iterates over all pads with nonzero amplitude. If the amplitude of the pad is greater than the amplitudes of all its neighbours, no action is taken. Otherwise, this pad is attached to the neighbour with the largest amplitude. After all pads are examined, new clusters are formed based on the obtained connections.

For testing we developed a toy model that allows us to identify the main characteristics of the implemented algorithms: accuracy, efficiency and operating speed. We used a field of  $200 \times 200$  mm with pads of  $4 \times 4$  mm<sup>2</sup>. Cluster centers were generated randomly. The amplitudes of the pads surrounding the cluster center were generated with normal distribution. 100 datasets were simulated and processed by each algorithm. The efficiency was defined as the ratio of the number of detected clusters to the number of generated clusters. The time needed for processing 100 datasets we called the operating time of the algorithm. The test was carried out with a different number of generated clusters (from 1 to 20) to determine efficiency and speed of the algorithms in dependence on data complexity.

The results are shown in Fig. 1. As expected, the Ward's method showed the best efficiency (85% for high data com-

plexity). However, its speed strongly decreases with increasing number of clusters. The single linkage method shows a better calculation speed, but the efficiency of this method strongly decreases with increasing data complexity. At high cluster density, this method cannot cope with the task. The developed algorithm shows the speed of the single linkage method and the efficiency of the Ward's method. It thus combines the main advantages of these methods while avoiding their weaknesses.

The new clustering algorithm showed good performance for toy model data. For a detailed comparison of the implemented algorithms, they have to be integrated into the CBMROOT framework and tested with realistic data samples simulated therein. Further developments will also concentrate on the parallel implementation of these methods.

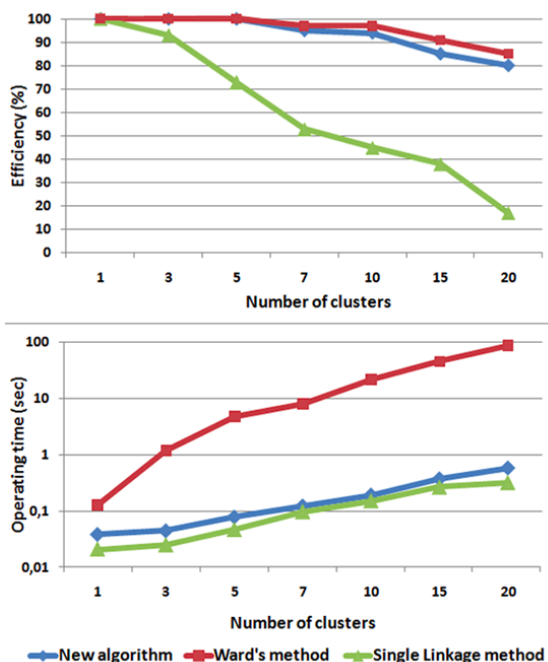


Figure 1: Comparison results for the three implemented clustering algorithms. The top panel shows the efficiency, the bottom panel the calculation speed, both in dependence on the number of clusters. The test was performed on a PC with an Intel Xeon x3210 processor.

### References

- [1] J. H. Ward, J. Amer. Statist. Assoc. **58** (1963) 236
- [2] R. Sibson, The Computer Journal **16** (1973) 30

## Numerical stability of the KF track fit in single precision

I. Kisel<sup>1,2</sup>, I. Kulakov<sup>1,3</sup>, and H. Pabst<sup>4</sup>

<sup>1</sup>Goethe-Universität, Frankfurt, Germany; <sup>2</sup>GSI, Darmstadt, Germany; <sup>3</sup>University of Kyiv, Kyiv, Ukraine; <sup>4</sup>Intel, Germany

The Kalman Filter (KF) track fit is the core of the event reconstruction in the CBM experiment; its optimization with respect to speed and precision is therefore crucial. The KF track fit [1] has recently been implemented in single precision in order to use the full power of modern many-core processors. However, the conventional KF algorithm becomes numerically unstable in single precision, opposite to the widely used double precision. In order to improve the numerical stability, an accurate initial approximation of the track parameters and stabilization of the covariance matrix computation at the measurement update step were used [1].

Further improved numerical stability can be obtained using a square root KF approach [2]. It operates with a square root  $S$  of the covariance matrix  $C = SS^T$ . Since the logarithm of the condition number of the square root matrix is smaller by a factor of two, the precision of calculations is doubled.

In the square root KF algorithm, the track parameters are propagated and updated at each measurement. The propagation step was implemented by constructing an orthogonal matrix  $T$  and a lower triangular matrix  $S_k^-$  such that

$$T \begin{bmatrix} (S_{k-1}^+)^T F_{k-1}^T \\ Q_{k-1}^{T/2} \end{bmatrix} \mathbf{r}_k^- = \begin{bmatrix} F_k \mathbf{r}_{k-1}^+ \\ 0 \end{bmatrix}. \quad (1)$$

Here,  $\mathbf{r}_k^-$  and  $\mathbf{r}_k^+$  are the track parameters vectors before and after the  $k$ -th measurement update,  $S_k^-$  and  $S_k^+$  the corresponding square roots of the covariance matrix,  $F_k$  the propagation matrix and  $Q_k^{T/2}$  the transported square root of the process noise matrix. The measurement update was implemented according to

$$\begin{aligned} \varphi &= S_k^- H_k^T, & S_k^+ &= S_k^- (I - a\gamma\varphi\varphi^T), \\ a &= \frac{1}{\varphi^T \varphi + V_k}, & K_k &= a S_k^- \varphi, \\ \gamma &= \frac{1}{1 + \sqrt{a R_k}}, & \zeta_k &= m_k - H_k \mathbf{r}_k^-, \\ & & \mathbf{r}_k^+ &= \mathbf{r}_k^- + K_k \zeta_k, \\ & & \chi_k^2 &= \chi_{k-1}^2 + \zeta_k^T a \zeta_k, \end{aligned} \quad (2)$$

assuming that the measurement  $m_k$  is a scalar, with the measurement model  $H_k$ , the covariance of the  $k$ -th measurement  $V_k$  and the total  $\chi^2$ -deviation  $\chi_k^2$ .

In the implementation we use for vectorization headers with overloaded operators, Vector classes (Vc) [3] and Intel Array Building Blocks (ArBB) [4]. Intel Threading Building Blocks (ITBB) [4] and ArBB are also used for task level parallelization. Two methods for extrapolation are imple-

mented: a 4-th order Runge-Kutta propagation and an analytic formula, which uses the Taylor expansion [1].

Table 1: Track fit quality (resolutions and pulls) and time per track per core of the square root KF approach

	Resolution ( $\mu\text{m}$ , mrad, %)			Pull			Time, $\mu\text{s}$
	$x$	$t_x$	$p$	$x$	$t_x$	$q/p$	
Header	43.0	0.30	0.94	1.1	1.2	1.3	0.93
Vc	43.0	0.30	0.94	1.1	1.2	1.3	0.92
ArBB	43.1	0.31	0.94	1.1	1.2	1.3	0.92

Tests of the time and track fit quality were performed on the computer lxir075 with 4 Xeon E7-4860 processors, which gives 80 logical cores in total. The results are shown in Tab. 1. The widths of the residual and pull distributions are similar to those obtained with the conventional KF approach in double precision. In Fig. 1 the scalabilities using ITBB are shown, demonstrating good linear scalability for both propagation methods.

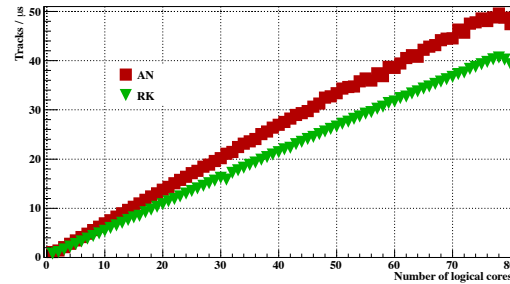


Figure 1: Scalability of the square root KF track fitter using headers with the 4-th order Runge-Kutta propagation (RK) and the analytic formula (AN)

In conclusion, the square root KF approach shows good numerical stability, timing and many-core scalability.

## References

- [1] S. Gorbunov *et al.*, *Comp. Phys. Comm.* **178** (2008) 374
- [2] P. G. Kaminski, *Discrete Square Root Filtering: A Survey of Current Techniques*, *IEEE Trans. Automatic Control* **16** (1971) 727
- [3] Vector Classes, <http://gitorious.org/vc>
- [4] Intel software, <http://www.intel.com>

# Study of the L1 CA track finder efficiency in the STS for $\Lambda^0$ , $K_s^0$ and $\phi$ signals

I. Rostovtseva<sup>1</sup>, D. Golubkov<sup>1</sup>, I. Kisel<sup>2</sup>, and Yu. Zaitsev<sup>1</sup>

<sup>1</sup>Institute for Theoretical and Experimental Physics (ITEP), Moscow, Russia; <sup>2</sup>Goethe-Universität, Frankfurt, Germany

For the optimization of the L1 reconstruction software, it is useful to have an estimate for the upper bound of the efficiency for real physical signals achievable in a given configuration. In this study we concentrate on the two-prong decays of  $\Lambda^0$ ,  $K_s^0$  and  $\phi$  because of their large production cross-sections and ease of reconstruction via two-body decay modes starting from the first data, and because of the interest in measuring their differential cross sections for QCD physics studies. Yet, the chosen signals have slightly different kinematics, and their daughter tracks belong to different track classes: *RefSec* and *ExtraSec* for  $\Lambda^0$  and  $K_s^0$ , and *RefPrim* for  $\phi$ .

In this analysis we use only the STS (without MVD). The study was performed for central Au+Au events at 25A GeV from UrQMD, without taking into account  $\delta$ -electrons. The used version of the TrackFinder algorithm had been adapted to STS inefficiency and was able to extrapolate tracks through stations without found hits [1]. We consider a particle to be reconstructed if both its MC daughters are matched to reconstructed tracks. Effects like mass resolution or background suppression cuts will only reduce the overall efficiency.

The loss of *reconstructable* tracks (i. e. tracks having hits in more than three STS stations), was evaluated for two values of single-strip inefficiency (see Tab. 1). We observe that even for an STS inefficiency of 0.3%, a significant fraction of negative pions from  $\Lambda^0$  (11.7%) and positive pions from  $K_s^0$  (11.0%) is lost already before track reconstruction.

We further distinguish between two classes of tracks which remain *reconstructable* after digitization and clusterization: *undamaged* tracks with hits in all crossed stations, and *damaged* tracks with no hits in some of the crossed station(s). Using these classes of tracks, the efficiency due to the reconstruction algorithm itself was evaluated (see Fig. 1). A detailed presentation of the study can be found in [2].

Table 1: Efficiency loss before track finding for different single-strip inefficiencies

Daughter particle	STS inefficiency	STS inefficiency	
		0.3%	10%
$\pi^-$ from $\Lambda^0$		11.7%	18.6%
$p$ from $\Lambda^0$		1.7%	7.8%
$\pi^-$ from $K_s^0$		6.6%	11.0%
$\pi^+$ from $K_s^0$		11.0%	15.6%
$K^-$ from $\phi$		1.0%	3.8%
$K^+$ from $\phi$		2.9%	5.3%

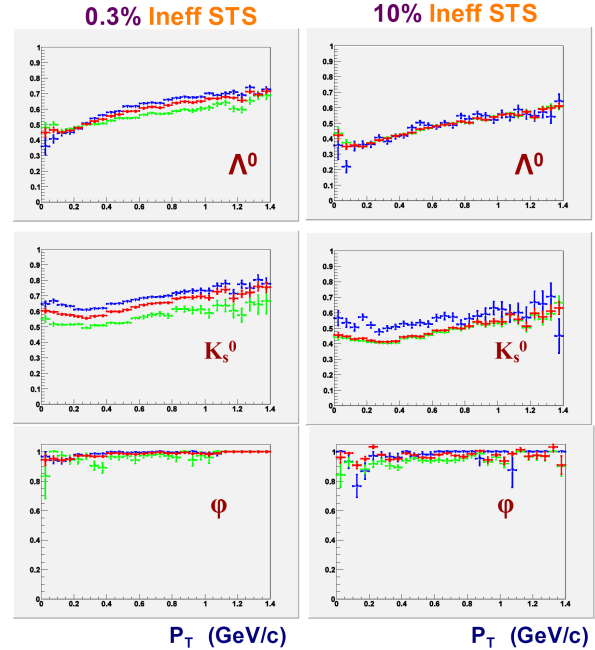


Figure 1: Efficiency of the TrackFinder *per se* depending on transverse momentum, for a single-strip inefficiency of 0.3% (left) and 10% (right). The results for “undamaged” tracks are shown in blue, those for “damaged tracks” in green, the combined efficiency in red.

We observe that the adaptation of the L1 CA TF [1] significantly improves the reconstruction of the “damaged” tracks, reaching practically the same efficiency as for “undamaged” tracks. We also found a significant loss of  $\pi^-$  from  $\Lambda^0$  and  $\pi^+$  from  $K_s^0$ , which introduces charge-asymmetry in the track reconstruction efficiency at the digitization / clusterization level (Tab. 1).

As this study was performed using STS-only reconstruction, we plan to extend it to global tracking, which is especially important for the kaon identification in case of  $\phi$  reconstruction.

## References

- [1] I. Kisel *et al.*, CBM Progress Report 2010, Darmstadt 2011, p. 67
- [2] I. Rostovtseva *et al.*, *Study of L1 Track Finder efficiency using Phi, K0S, Lambda signals*, 17th CBM collaboration meeting, Dresden, 4-8 April 2011

## Optimization of the CA-based track finder for CBM

S. Jarp<sup>1</sup>, I. Kisel<sup>2,3</sup>, I. Kulakov<sup>2,4</sup>, J. Leduc<sup>1</sup>, and M. Zyzak<sup>2,4</sup>

<sup>1</sup>CERN, Geneva, Switzerland; <sup>2</sup>Goethe-Universität, Frankfurt, Germany; <sup>3</sup>GSI, Darmstadt, Germany; <sup>4</sup>University of Kyiv, Kyiv, Ukraine

The main tracking challenges of the CBM experiment are: up to  $10^7$  collisions per second, about 1000 particles per central collision, non-homogeneous magnetic field, double-sided strip detectors. The Cellular Automaton (CA) algorithm is used for track reconstruction [1] in the Silicon Tracking System (STS). Since it is the most sophisticated and time-consuming part of the event reconstruction, it should be fast and should have a good scalability with respect to the number of cores. The speed of the CA algorithm is especially important, since the full event reconstruction and selection are required at the First Level Event Selection (FLES) stage.

The CA algorithm creates short track segments (triplets) in each three neighboring stations, then links them into track candidates and selects them according to the maximum length and minimum  $\chi^2$  criteria. The algorithm is already optimized with respect to time, fully implemented in single precision [2] and robust with respect to the detector geometry and inefficiency. The algorithm was further optimized with respect to time: additional information (acceptance,  $\chi^2$ ) is taken into account, input data are re-sorted, computations are simplified, data copying and the number of finding iteration are reduced. A speed-up by a factor of 5 was achieved with the same track reconstruction quality.

For testing, 1000 minimum bias Au+Au UrQMD events at 25A GeV with a realistic STS setup were simulated. Tests of time and efficiency were performed on the server lxir075 with 4 Xeon E7-4860 processors, which gives 80 logical cores in total. The results are given in Tab. 1 and in Fig. 1. The efficiencies for reference tracks, which include tracks of particular physics interest, are high. The efficiencies for extra and secondary tracks are lower, since such tracks are shorter and more complicated for reconstruction. The levels of clone and ghost tracks are negligible.

Table 1: Track reconstruction quality for minimum bias events: efficiencies (%) for different sets of tracks, clone and ghost levels (%) and time on a single core

Reference primary set efficiency	97.7
Extra primary set efficiency	90.5
Reference secondary set efficiency	81.9
Extra secondary set efficiency	50.9
All set efficiency	88.9
Clone level	0.1
Ghost level	0.3
Number of reconstructed tracks per event	121
Time per event, ms	11

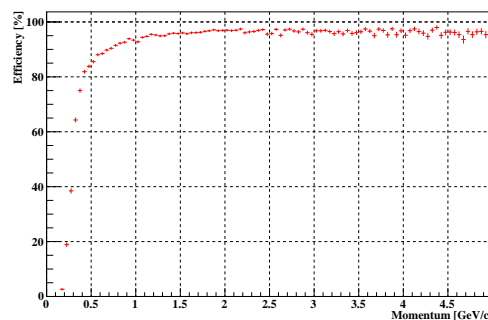


Figure 1: Track reconstruction efficiency versus momentum

For scalability tests, also FIAS and CERN openlab servers were used. Figure 2 demonstrates good linear scalabilities using Intel Threading Building Blocks [3] for all tested many-core systems.

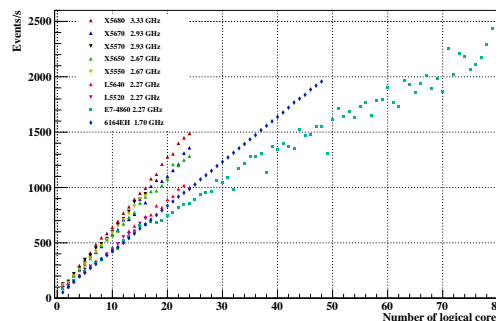


Figure 2: Scalability of the CA track finder on many-core systems at GSI, FIAS and CERN.

In conclusion, running on a computer with 80 cores the CA track finder demonstrates a maximum throughput of 2500 mbias events per second and track reconstruction efficiency of 97.7% for fast primary tracks. The algorithm shows a linear scalability with the number of cores.

### References

- [1] I. Kisel, Nucl. Instrum. Methods **A 566** (2006) 85
- [2] I. Kisel, I. Kulakov and H. Pabst, *Numerical Stability of the KF track fit in single precision*, this report
- [3] Intel software, <http://www.intel.com>



## Status of event reconstruction for the RICH detector in the CBM experiment

S. Lebedev<sup>1,2</sup>, C. Höhne<sup>1</sup>, A. Lebedev<sup>2,3</sup>, G. Ososkov<sup>2</sup>, and I. Rostovtseva<sup>4</sup>

<sup>1</sup>Justus-Liebig-Universität, Gießen, Germany; <sup>2</sup>LIT JINR, Dubna, Russia; <sup>3</sup>GSI, Darmstadt, Germany; <sup>4</sup>ITEP, Moscow, Russia

In this report the status of developments regarding RICH detector simulation is presented.

Systematic studies of the ring finder [1] were performed in order to improve ring reconstruction and understand losses in the efficiency. In these studies the algorithm was tested using events with one primary  $e^+$  or  $e^-$ ; thus, only one electron ring was registered in the RICH detector per event. For this ideal case, the ring reconstruction efficiency was lower than 100% and dropped down significantly for rings with less than 15 hits. The investigation of this efficiency losses yielded two main reasons. The first one is the division of hits into two groups while performing the Hough transform [1]. In this case the peak in Hough space was not high enough, and therefore many rings were rejected at this step. The second reason are very strong cuts in the ring finding algorithm in order to reject fake rings, tuned for events with high ring multiplicity. For single-ring events, these cuts can be relaxed. After these modifications, a ring reconstruction efficiency of 99.4% was obtained for rings with more than 7 hits, and 100% for reference rings with 15 or more hits (see Fig. 1).

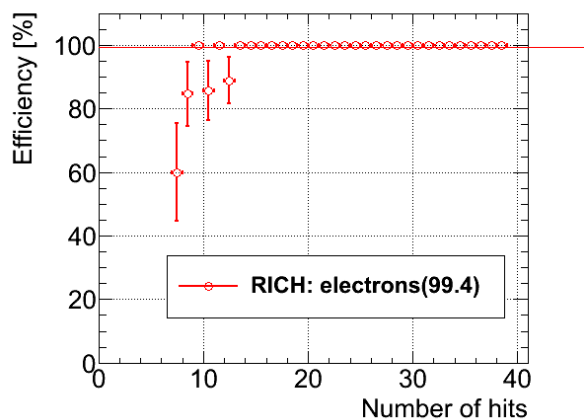


Figure 1: Ring reconstruction efficiency as function of the number of hits in the ring for events with one ring

The ring finder was also tested with different hit producer parameters. For example, noise hits and additional hit errors due to the mirror inhomogeneities were eliminated. It was found that these parameters do not influence the ring finding efficiency.

It was observed that many rings with 7 – 9 hits are not reconstructable as their hits are distributed non-uniformly, being concentrated on one half of a ring. Most of such

rings are located on the edges of photodetector or even on both photodetectors. They cannot be properly fitted. The remaining 0.6% of not reconstructed rings belong to this category and have to be eliminated from the RICH detector acceptance calculation.

The *CbmRichGeoTest* class was significantly improved, and many new features were implemented in order to allow a better understanding of the RICH detector performance. The detector acceptance is calculated as function of transverse momentum, rapidity, momentum and number of hits in the ring. A new display for the visualization of the RICH ring fitting was implemented, which draws MC points, hits, fitted circles and ellipses.

Our current simulation does not provide pure Monte-Carlo information about the RICH ring parameters. The RICH Monte-Carlo points are fitted by the circle and ellipse fitters, and the obtained parameters are assumed to be Monte-Carlo RICH ring parameters. We found the mean ring radius for the circle fit using MC points to be 4.88 cm, with an RMS of 0.29 cm. Using reconstructed hits, the circle fit gives about the same mean value (4.80 cm), but the RMS is larger by a factor of two (0.59 cm).

The difference between MC point and hit fitting is interpreted as error of the ring parameters arising from the digitization in the photodetector. These errors depend on the number of hits in the ring; they are larger for rings with a smaller number of hits. The integrated RMS of the errors for the circle fit are  $R - 0.13$  cm,  $X_c - 0.13$  cm and  $Y_c - 0.16$  cm. For the ellipse fit, we obtained  $A - 0.19$  cm,  $B - 0.17$  cm,  $X_c - 0.15$  cm and  $Y_c - 0.19$  cm ( $A$  and  $B$  being the semi-axes of the ellipse).

The fitting efficiency is the number correctly fitted rings divided by the number of accepted rings, where a correctly fitted ring is a ring with parameters in a range  $\pm 3$  RMS around the mean value. The mean integrated efficiency of circle fitting is 97.4%, dropping down to less than 60% for rings with 10 hits. For the ellipse fit, we obtain a mean integrated efficiency of 92.6%, which drops down to less than 60% for rings with 15 hits.

The calculation of ring parameter errors for the circle fit as described above was implemented for the circle fit. In order to test the fitting algorithms, a toy model of the ring simulation was used. The residuals and pulls of the circle fit were calculated. The RMS values of the pull distributions of all parameters are close to unity as it should be.

### References

- [1] S. Lebedev et al., CBM Progress Report 2008, Darmstadt 2009, p. 84

## Status of global track reconstruction in the CBM experiment

A. Lebedev<sup>1,2</sup>, S. Lebedev<sup>1,3</sup>, and G. Ososkov<sup>2</sup>

<sup>1</sup>GSI, Darmstadt, Germany; <sup>2</sup>LIT JINR, Dubna, Russia; <sup>3</sup>Justus-Liebig-Universität, Gießen, Germany

Global track reconstruction, i. e. tracking in the TRD and MUCH, track merging between STS, TRD and MUCH, TOF hit merging and construction of global tracks are performed by the `littrack` package in the CBMROOT framework. In this report the status of developments in the `littrack` package is presented.

The structure of the package was significantly reorganized. For convenience and in order to decrease the dependencies between different parts of `littrack`, the package was decomposed into four main parts: 1) `cbm` - interface of the tracking software to CBMROOT, quality monitoring etc. 2) `std` - scalar implementation of the tracking using the full magnetic field map and TGeo for geometry navigation. It depends on ROOT and does not depend on CBMROOT. 3) `parallel` - SIMDized and multithreaded implementation of the tracking. It depends only on the compiler and can be used in standalone mode for performance testing. 4) `cuda` - test implementation using CUDA.

The quality assurance routines for track reconstruction were considerably improved.

In the performed studies the algorithms were tested using central Au+Au collisions at 25A GeV beam energy from UrQMD. In addition, to check the reconstruction of signal tracks, 5  $J/\psi$  decayed into  $e^+e^-$  pairs in case of the electron setup or  $\mu^+\mu^-$  pairs in case of the muon setup were embedded in each event. A realistic detector description as implemented in the STS, TRD and MUCH detectors was used. It includes advanced digitization and clustering procedures.

The global tracking efficiency as function of momentum for the electron setup is shown in Fig. 1. Its average value for signal tracks ( $e^+e^-$  or  $\mu^+\mu^-$ ) is 76.1% for the electron setup and 92.1% for the muon setup. The mean TRD track finding efficiency for all tracks is 94.5% and 89% for signal electrons. The lower value for electrons is attributed to their energy loss through Bremsstrahlung. The mean tracking efficiency for the MUCH detector is 95.1%.

A study was done in order to investigate the STS tracking performance. It was shown that the observed drop of the STS tracking efficiency with increasing momentum is due to the lower acceptance of the new STS geometries (v11a and v11b) compared to the previous one (v09a).

A comparison of the STS and global tracking efficiencies for two new STS geometries (v11a and v11b) using different strip stereo angles ( $\pm 7^\circ$ ,  $0^\circ - 4^\circ$ ,  $0^\circ - 6^\circ$ ,  $0^\circ - 8^\circ$ ) was performed. It was shown that the STS and global reconstruction efficiencies stay the same for both STS geometries. The tracking efficiency starts to drop down and the ghost rate increases only for the smallest stereo angle investigated ( $0^\circ - 4^\circ$ ).

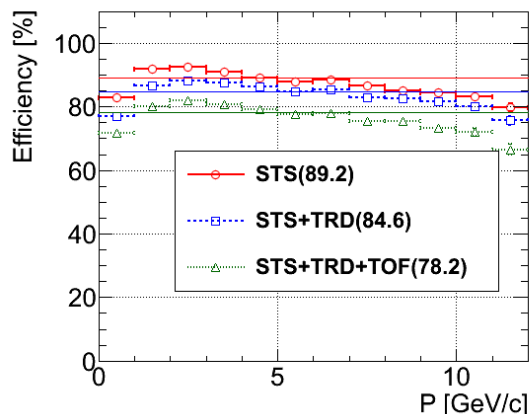


Figure 1: Global track finding efficiency as function of momentum for the electron CBM setup. The average efficiency numbers in % are shown in brackets.

A fast parallel tracking algorithm was further investigated. To avoid the use of the main memory and to implement a SIMDized algorithm, we use a polynomial approximation of the magnetic field map. However, detailed studies of such an approach showed that in the stray magnetic field after the STS detector, the polynomial approximation is not accurate enough. A new algorithm for field approximation was thus implemented. It builds a grid, similar to that of field map, but only on predefined  $x - y$  slices perpendicular to the  $z$  position. The drawback of such an approach is that access to this grid cannot be effectively SIMDized. On the other hand, the algorithm is as accurate as the field map, has low memory consumption and is fast. The algorithm was tested with track propagation and track fit. Its implementation into the `littrack` package is ongoing.

Software documentation is an important part of the development process. The Doxygen-based documentation of the `littrack` package was thus improved. It can be accessed through <http://www-linux.gsi.de/~andrey/littrack-docs/html>.

In summary, the global track reconstruction algorithms for the CBM experiment are well advanced now. The developed `littrack` package is the default global track reconstruction software in CBM. It provides good tracking efficiency for both the electron and the muon setup of CBM and is suitable for detector optimization studies of different CBM setups.

## A SIMDized particle finder for the CBM experiment

*I. Kisel<sup>1,2</sup>, I. Vassiliev<sup>1,2</sup>, and M. Zyzak<sup>1,3</sup>*

<sup>1</sup>Goethe-Universität, Frankfurt, Germany; <sup>2</sup>GSI, Darmstadt, Germany; <sup>3</sup>University of Kyiv, Kyiv, Ukraine

One of the most challenging tasks of the CBM experiment is a full event reconstruction with an event rate of up to  $10^7$  collisions per second. For on-line selection purposes, a fast and efficient reconstruction of short-lived particles is required. Since modern CPUs are many-core systems and have SIMD units, parallelization and vectorization of the algorithms are necessary for utilization of the full power of the CPU. In order to achieve the maximal speed, a particle finding procedure based on SIMDized algorithms for track and particle fitting is being developed.

Our investigations were started with the reconstruction of  $K_s^0$ , which decays into  $\pi^+\pi^-$  with a branching ratio of 69.2%, and  $\Lambda$ , which decays into  $p\pi^-$  with a branching ratio of 64%. Containing strangeness they are of interest for the CBM experiment. These particles were chosen as a first step because of the simplicity of their reconstruction algorithm.

The particle finder is based on the Kalman filter track fitter [1] and the KFPARTICLE package [2]. The entire reconstruction procedure is implemented in single precision and is SIMDized. The reconstruction algorithm is similar to that used in the off-line reconstruction of  $K_s^0$  and  $\Lambda$ .

The algorithm consists of several steps. First, the primary vertex of an event is reconstructed. Then, secondary tracks are selected according to two criteria: the tracks should be well displaced from the primary vertex, since  $c\tau$  of  $K_s^0$  is 2.68 cm and 7.89 cm for  $\Lambda$ , and the parameters and covariance matrices of the tracks should be well defined. In order to reject tracks originating from the primary vertex, only tracks with  $\chi_{\text{prim}} > 3$  are selected, where  $\chi_{\text{prim}}$  is the distance between the primary vertex and the track position at the target plane normalized to the total error of the track and the primary vertex coordinates. From the selected secondary tracks, particle candidates for  $K_s^0$  and  $\Lambda$  are constructed assuming pion masses of the tracks. Tracks contributing to particle candidates with a good quality (i. e. the parameters of the particle candidate are well defined and its  $\chi^2/\text{NDF} < 3$ ) are selected for the further analysis. As a final step, the particles are constructed from the tracks satisfying all cuts, assuming corresponding masses for the daughters: for  $K_s^0$  the pion mass is assumed for both daughters, while for  $\Lambda$  the proton mass is assumed for the positively charged daughter and the pion mass for the negatively charged one.

The algorithm was tested with 1000 central Au+Au UrQMD events at 25 AGeV. Only the STS detector was used for these studies. The test was performed on the lxir039 server with Xeon X5550 processors. The developed SIMDized  $K_s^0$  and  $\Lambda$  particle finder shows practically the same results as the off-line algorithm (see Fig. 1 and

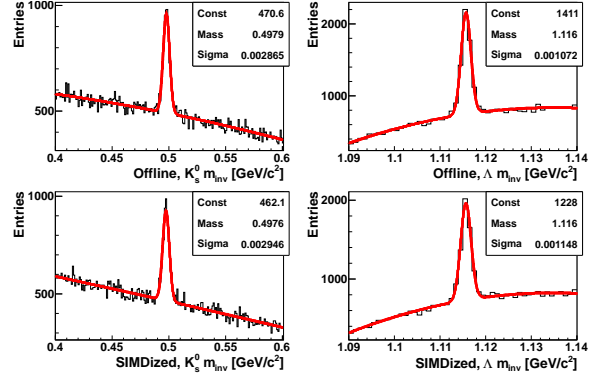


Figure 1: Invariant-mass spectra for the offline (top) and the SIMDized algorithm (bottom)

Tab. 1). The efficiencies of the SIMDized particle finder for all particles in  $4\pi$  are 13.9% for  $K_s^0$  and 12.1% for  $\Lambda$ . The efficiencies for particles which have both daughter tracks reconstructed are 68% and 57.8%, respectively. The execution time of the SIMDized particle finder per event is 0.7 s, distributed between the reconstruction of the primary vertex (65.2%), the selection of tracks (26.2%), the reconstruction of  $K_s^0$  (4.3%) and the reconstruction of  $\Lambda$  (4.3%).

Table 1: Comparison of the off-line and SIMDized algorithms. S is the signal (the number of reconstructed particles), S/B the signal-to-background ratio, and  $M$  and  $\sigma_M$  the reconstructed mass and its error in  $\text{MeV}/c^2$ .

		S	S/B	$M$	$\sigma_M$
$K_s^0$	Offline	3225	0.57	497.9	2.9
	SIMDized	3258	0.60	497.6	2.9
$\Lambda$	Offline	3619	1.14	1115.7	1.1
	SIMDized	3373	1.01	1115.7	1.1

As a next step, more particles of particular interest, such as  $D$ -mesons and strange hyperons, will be included to the particle finder, and parallelization between cores will be investigated.

## References

- [1] S. Gorbunov *et al.*, *Comp. Phys. Comm.* **178** (2008) 374
- [2] S. Gorbunov and I. Kisel, *Reconstruction of decayed particles based on the Kalman filter*, CBM-SOFT-note-2007-003 (2007), <https://www.gsi.de/documents/DOC-2007-May-14-1.pdf>

## Towards automatization of software quality monitoring in CBM

*A. Lebedev<sup>1,2</sup>, S. Lebedev<sup>2,3</sup>, and G. Ososkov<sup>2</sup>*

<sup>1</sup>GSI, Darmstadt, Germany; <sup>2</sup>LIT JINR, Dubna, Russia; <sup>3</sup>Justus-Liebig-Universität, Gießen, Germany

Automatization of regularly performed tasks is an important component of a well-organized software development process. One of such important tasks is software testing. A good and automatized testing procedure can considerably improve the development process, since the developers can be sure that changes made in the code are correct and do not lead to program crashes. It can also considerably reduce the development cycles.

In the development of physics experiment software like CBMROOT, it is important to have a reliable and unified tool which provides a set of quality assurance tests and gives a global picture of results of all software packages, namely, Monte-Carlo simulation, detector simulation, event reconstruction and physics analysis. In this report we discuss a prototype of quality monitoring tool which is being developed for CBMROOT.

The main goal of this development is to run the standard simulation, reconstruction and analysis chains automatically on a regular basis, check the results and publish them on a web site for common access. The tool consists of two main components. The first one is a "performance calculator" which creates histograms and performs the actual calculation of results. The second component is responsible for the representation of the results to the users: it extracts useful numbers from histograms, draws them and generates reports.

As a first step, we started our developments with the event reconstruction software. The developed routines allow to calculate a set of important quality assurance numbers and histograms like detector acceptance, track and ring reconstruction, electron identification and pion suppression efficiencies. They calculate local reconstruction efficiencies for each detector (STS, RICH, TRD, MUCH, TOF) as well as for different combinations of detectors and normalizations (MC, STS-RICH, STS-TRD etc.). All efficiencies are evaluated in dependence on momentum, transverse momentum, rapidity and number of hits. For a specific detector, this list can be extended.

For better and quicker understanding of the obtained simulation results, it is important to have a good representation of it which contains main useful numbers, tables and figures in an easy-to-read format. This report is generated in two steps. First, all necessary numbers are extracted from histograms and saved in JSON format. Figures are created and saved in PNG files. Second, the report is generated out of the JSON and image files in HTML, Latex or plain text format (for console output).

An automatic check of the results for correctness was also implemented. It allows to inspect the results based on

predefined limits for each value. In the report each value can be marked with a certain color which indicates whether it is correct, not correct or not checked.

The combination of the described tools allowed to automatize the quality monitoring of the event reconstruction. Nightly tests for the electron and muon setups of CBM are performed. Simulation and reconstruction are run using the standard CBMROOT dashboard which is based on CDASH. Then, the tracking performance is calculated. The results are automatically checked, and a HTML report is generated and copied to the web server.

Simulation of the experiment requires to perform a lot of systematic detector optimization studies, in which many different simulations have to be compared. The interpretation and analysis of the results obtained in such studies are hard as a large variety of numbers have to be checked. In order to improve and speed-up such studies, a new feature was implemented which allows to produce an easy-to-read summary report out of many different simulations.

The developed QA routines allow to improve the testing of the software within the CBMROOT framework. It does not require any additional efforts from the developers since testing is done automatically. The developed prototype of the event reconstruction quality monitoring can be found in <http://www-linux.gsi.de/andrey/api/index.php>. Further development will concentrate on the extension of the test suit in order to obtain a higher code coverage, and on improvements of the web site.

## Identification of high-momentum pions with RICH

V. P. Ladygin, A. I. Malakhov, and T. A. Vasiliev

LHEP-JINR, Dubna, Russia

In CBM hadrons will be identified by measuring the particle momentum with STS in the magnetic field and its time of flight using a wall of RPCs. Assuming a RPC time resolution of 80 ps, pions and kaons can be separated by  $2\sigma$  in the squared mass distribution for  $p < 3.5$  GeV/c [1, 2].

In order to perform measurements of high- $p_T$  pion production, the implementation of the RICH detector into the high-momentum pion identification procedure was proposed [3]. The independent identification of high-momentum pions ( $p > 7$  GeV/c) in STS+RICH with almost 100% purity can be concurrent with the identification of pions with  $p_T > 2.5$  GeV/c based on STS+TOF in the energy domain of SIS-100. The use of the RICH detector can significantly extend the high- $p_T$  measurements at SIS-300 energies [4].

Simulations were performed for 10k Au+Au UrQMD 2.3 central events at 10A and 25A GeV using the standard STS geometry and the magnetic field map for the electron version of CBM, release JUN11. The standard RICH configuration for JUN11 was used.

The dependence of the number of hits in the RICH photodetectors on the pion momentum is shown in Fig. 1. The threshold ( $N_{tr} \geq 7$ ) for the number of hits of the ring finding algorithm is shown by the dashed line. The average number of hits for pions ( $N \approx 12$ ) is significantly less than for electrons ( $N \approx 21$ ).

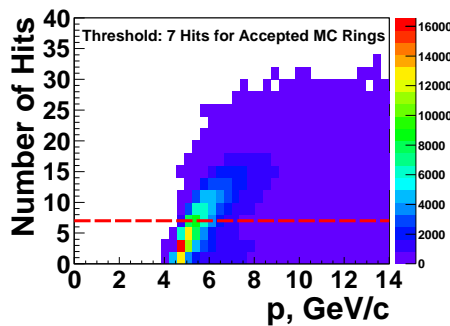


Figure 1: Dependence of the number of hits in the RICH on the pion momentum at 10A GeV

Figure 2 shows the reconstructed RICH ring radius as function of momentum. The pion identification is indicated by the contour. Pions with  $p < 5.5$  GeV/c are not visible in RICH. For  $5.5 < p < 7$  GeV/c the ring efficiency is not uniform. For  $p > 7$  GeV/c the number of hits for pions ( $N \geq 7$ ) is sufficient for ring finding. In this region the efficiency defined as the ratio of the number of identified pions in RICH to the number of accepted pions in

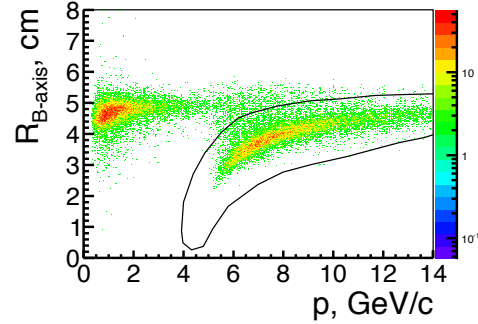


Figure 2: Ring radius versus momentum for central Au+Au events at 25A GeV

STS is 0.53 (0.35) at 10A (25A) GeV. The efficiency of pion identification by the RICH at 25A GeV is lower than at 10A GeV because of the higher hit density (see Fig. 3).

In summary, the CBM setup at SIS-100 allows to obtain high- $p_T$  data at mid- and forward rapidity unreachable at AGS. The implementation of the RICH detector for the pion ID at SIS-300 can significantly extend the high- $p_T$  measurements [4].

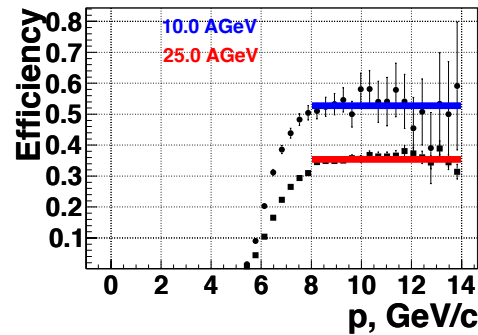


Figure 3: Efficiency of pion identification for central Au+Au collisions at 10A (circles) and 25A GeV (boxes)

## References

- [1] D. Kresan and C. Höhne, CBM Progress Report 2008, Darmstadt 2009, p. 63
- [2] V. P. Ladygin, A. I. Malakhov and T. A. Vasiliev, CBM Progress Report 2010, Darmstadt 2011, p. 58
- [3] C. Höhne, *Particle identification with the RICH detector*, CBM Tracking Week, January 2005, <https://www.gsi.de/documents/DOC-2005-Jan-52-1.ppt>
- [4] V. P. Ladygin, A. I. Malakhov and T. A. Vasiliev, CBM Progress Report 2010, Darmstadt 2011, p. 76

# $K_s^0$ , $\Lambda$ and $\Xi^-$ reconstruction in Au+Au collisions at NICA energies

I. Vassiliev<sup>1,2</sup> and V. Akishina<sup>1,3</sup>

<sup>1</sup>Goethe-Universität, Frankfurt am Main, Germany; <sup>2</sup>GSI, Darmstadt, Germany; <sup>3</sup>LIT, JINR, Dubna

The main goal of the CBM experiment is to study the behaviour of nuclear matter under the condition of high baryonic density, in which the transition to a deconfined quark gluon plasma phase is expected. One of the potential signatures of this phase transition is the enhanced production of strange particles.

In the CBM experiment hyperons will be identified by their decay into charged hadrons, which are detected in the Silicon Tracking System (STS). To study the feasibility of  $\Xi^-$ ,  $\Lambda$  and  $K_s^0$  reconstruction with CBM, a set of 10k central Au+Au UrQMD events at 4.85A GeV were simulated. These collisions contain on average 5  $K_s^0$ , 7  $\Lambda$  and 0.029  $\Xi^-$ . The  $\Xi^-$  decays into  $\Lambda + \pi^-$  with a branching ratio of 99.9% and  $c\tau = 4.91$  cm. The STS geometry with 8 double-sided segmented strip detectors was used for tracking. No kaon, pion or proton identification is applied. In order to reconstruct the  $\Lambda \rightarrow p\pi^-$  decay, the proton mass was assumed for all positively charged tracks as well as the pion mass for all negatively charged tracks.  $K_s^0$  is reconstructed assuming the pion mass for tracks of both polarities. The combination of the single track cut ( $\chi_{prim}^2 > 3\sigma$ ) and the geometrical vertex cut ( $\chi_{geo}^2 < 3\sigma$ ) allows to identify a clear signal. For  $K_s^0$  the invariant mass resolution is  $1.2 \text{ MeV}/c^2$ , and the signal-to-background ratio within the  $2\sigma$  peak region results to 2.44. For  $\Lambda$  the invariant mass resolution value is  $2.7 \text{ MeV}/c^2$  and the signal-to-background ratio within the  $2\sigma$  peak region is about 10 (see Figs. 1 and 2).

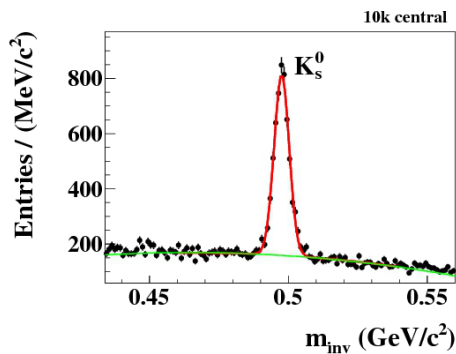


Figure 1:  $\pi^+\pi^-$  invariant mass spectrum. The red line results from a Gaussian fit to the signal, the green line from a polynomial fit to the background.

The  $\Xi^-$  reconstruction includes several steps: fast on-line track finding and fitting [1, 2], where all tracks are found; tracks with  $\chi_{prim}^2 > 8$  and  $5\sigma$  (positively and negatively charged, respectively) are selected for a  $\Lambda$  search,

where positively charged tracks were combined with  $\pi^-$  tracks to construct a  $\Lambda$  KFParticle; a geometrical vertex ( $\chi_{geo}^2 < 3\sigma$ ) was required to suppress the combinatorial background.

Table 1: Results for hyperon reconstruction at 4.85A GeV

Particle:	$K_s^0$	$\Lambda$	$\Xi^-$
Multiplicity (HSD):	5	7,2	0,029
Decay channel:	$\pi^+\pi^-$	$\pi^-p$	$\pi^+\pi^-p$
Branching ratio:	69,2 %	63,9 %	63,8 %
Rec. efficiency	8,5 %	13,9 %	2,8 %
Acceptance	24,9 %	28,9 %	20 %

The invariant mass of the reconstructed pair is compared with the  $\Lambda$  mass; only pairs in a mass window of  $1.116 \pm 0.016$  ( $6\sigma$ ) are accepted; primary  $\Lambda$  were rejected by requiring  $\chi_{prim}^2 > 5\sigma$  and  $z_{vertex} > 6$  cm. The thus selected  $\Lambda$ s were combined with secondary  $\pi^-$  tracks ( $\chi_{prim}^2 > 8\sigma$ ) to  $\Xi^-$  candidates. A  $\Xi^-$ -candidate was accepted in case of a geometrical and topological detached vertex:  $\chi_{geo}^2 < 3\sigma$ ,  $\chi_{topo}^2 < 3.5\sigma$ ,  $z_{vertex} > 2$  cm.

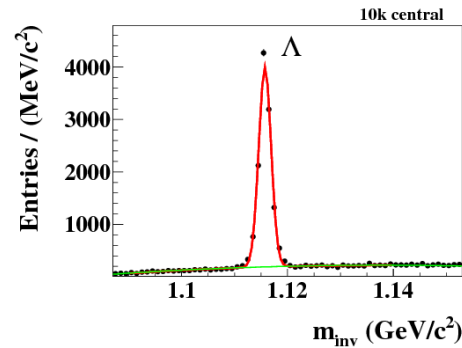


Figure 2:  $p\pi^-$  invariant mass spectrum. The red line results from a Gaussian fit to the signal, the green line from a polynomial fit to the background.

As a result 8  $\Xi^-$  with no background were reconstructed in the invariant mass spectrum of the  $\Lambda\pi^-$  candidates with a signal reconstruction efficiency of about 2.8%. A summary of the results for hyperon reconstruction is given in Tab. 1.

## References

- [1] I. Kisel, Nucl. Instrum. Methods **A 566** (2006) 85
- [2] S. Gorbunov *et al.*, Comp. Phys. Comm. **178** (2008) 374

## On a study of sub-threshold production of heavy hyperons with the CBM STS

Yu. A. Murin<sup>1</sup>, K. K. Gudima<sup>1,2</sup>, E. I. Litvinenko<sup>1</sup>, V. A. Vasendina<sup>1</sup>, and A. I. Zinchenko<sup>1</sup>

<sup>1</sup>JINR, Dubna, Russia; <sup>2</sup>Institute of Applied Physics of Academy of Sciences of Moldova, Chisinau, Moldova

The prospects for an experimental study of the sub-threshold production of  $\Xi^-$  and  $\Omega^-$  hyperons in central gold-gold collisions with the CBM STS were analyzed within the frame of the HYPQGSM event generator [1] and the `cbmroot` framework package [2]. Figure 1 demonstrates the evolution of the partial probabilities for  $\Omega^-$  hyperon production in different combinations of collisions of mesons (M), baryons (B) and hyperons (Y) in central gold-gold collisions at 60A GeV (bottom panel) and 4A GeV (upper panel). The HYPQGSM data shown in the figure demonstrate that the decrease of energy leads to domination of YY-collisions in the cascade of baryons acting as a source of heavy hyperons. This points to the prevalence of multi-step processes in production of heavy hyperons in this energy domain, the yields of heavy hyperons carrying valuable information on the baryon density of the fireball and on the details of the hyperon-hyperon interactions. Hopefully, the contribution of each factor may be determined with a detailed energy scan of the hyperon yields at energies below the hyperon formation thresholds in nucleon-nucleon collisions.

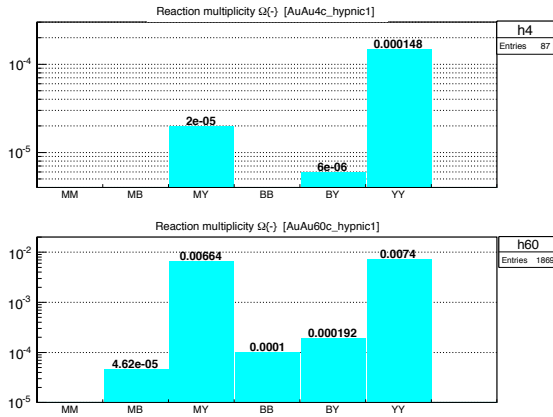


Figure 1: Evolution of the partial probabilities of different collisions of the fireball constituents mesons (M), baryons (B) and hyperons (Y) leading to production of  $\Omega^-$  hyperons in central gold-gold collisions at 60A GeV (bottom panel) and 4A GeV (upper panel)

A study of the identification power of the low cross section, sub-threshold  $\Xi^-$  and  $\Omega^-$  hyperons emitted in central gold-gold collisions at 4A GeV was undertaken with the resulting invariant mass distributions for the tracks corresponding to the products of  $\Xi^-$  and  $\Omega^-$  hyperons shown in

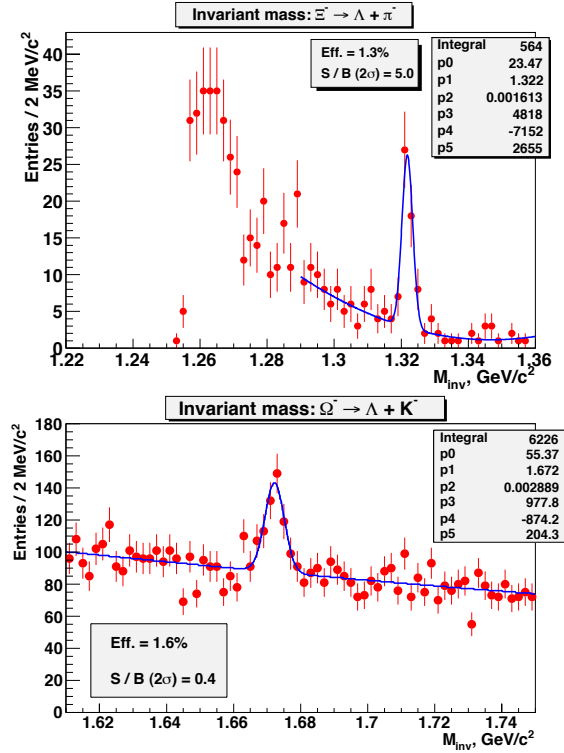


Figure 2: Invariant mass distributions restored from simulated data delivered from the CBM STS for central gold-gold collisions at 4A GeV

Fig. 2. The results were obtained with  $10^5$  and  $1.2 \times 10^8$  central collisions for  $\Xi^-$  and  $\Omega^-$  hyperons, respectively.  $\Omega^-$  reconstruction was done under the assumption of perfect kaon identification. Although the peak corresponding to the chain of products of the weak  $\Omega^-$  decay is rather small, it is still sufficient for the identification of rare hyperon production events with the CBM STS owing to its large aperture. Thus, the computer analysis performed demonstrates the feasibility of the CBM STS setup for the study of sub-threshold production of heavy hyperons.

## References

- [1] K. K. Gudima, Yu. A. Murin and E. I. Litvinenko, *The HYPQGSM event generator for the simulation of hypernuclei production in central collisions of heavy ions for NICA/MPD and FAIR/CBM*, this report
- [2] <http://fairroot.gsi.de>

## Feasibility study of light hypernuclei reconstruction with the CBM detector

A. I. Zinchenko<sup>1</sup>, K. K. Gudima<sup>2</sup>, E. I. Litvinenko<sup>1</sup>, Yu. A. Murin<sup>1</sup>, and V. A. Vasendina<sup>1</sup>

<sup>1</sup>JINR, Dubna, Russia; <sup>2</sup>Institute of Applied Physics, Academy of Science, Chisinau, Moldova

The search for hypernuclei offers a fascinating perspective to explore the third (i.e., strange) axis of the chart of nuclei. Moreover, the investigation of hypernuclei provides information on the hyperon-nucleon and even on the hyperon-hyperon interaction, which play an important role in neutron star models. Here we present results on a feasibility study to reconstruct light hypernuclei with CBM in Au+Au collisions at 10A GeV.

Hypernuclei were produced using the HYPQGSM event generator [1], and their decays were simulated during the particle transport according to the data on hypernuclei decay modes and their branching ratios (see Tabs. 1 and 2 for  ${}^3_{\Lambda}\text{H}$  [2] and  ${}^4_{\Lambda\Lambda}\text{H}$  [3]). Bold marked in table 1 are decay modes which can be observed with the CBM experiment.

Table 1:  ${}^3_{\Lambda}\text{H}$  decays

Decay channel	Branching ratio, %
$\pi^- + {}^3\text{He}$	<b>24.7</b>
$\pi^0 + {}^3\text{H}$	12.4
$\pi^- + \text{p} + \text{d}$	<b>36.7</b>
$\pi^0 + \text{n} + \text{d}$	18.4
$\pi^- + \text{p} + \text{p} + \text{n}$	1.5
$\pi^0 + \text{n} + \text{n} + \text{p}$	0.8
$\text{d} + \text{n}$	0.2
$\text{p} + \text{n} + \text{n}$	1.5

Table 2:  ${}^4_{\Lambda\Lambda}\text{H}$  decay modes

First decay	Branching ratio, %	Second decay	Branching ratio, %
$\pi^- + {}^4_{\Lambda}\text{He}$	16.0	${}^4_{\Lambda}\text{He} \rightarrow {}^3\text{He} + \text{p} + \pi^-$	32.0
$\pi^- + \text{p} + {}^3_{\Lambda}\text{H}$	18.0	${}^3_{\Lambda}\text{H} \rightarrow {}^3\text{He} + \pi^-$	24.7
$\pi^- + \text{p} + {}^3_{\Lambda}\text{H}$	18.0	${}^3_{\Lambda}\text{H} \rightarrow \text{d} + \text{p} + \pi^-$	36.7
$\pi^- + \Lambda + {}^3\text{He}$	2.3	$\Lambda \rightarrow \text{p} + \pi^-$	64.0
$\pi^- + \Lambda + \text{d} + \text{p}$	27.0	$\Lambda \rightarrow \text{p} + \pi^-$	64.0

The single- $\Lambda$  hypernuclei reconstruction procedure was based on the search for relatively long-lived objects (displaced vertices) decaying into two or three charged tracks. The results presented below were obtained with the assumption that positive tracks (protons and heavier particles) were identified in the CBM detector (by STS and / or TOF). Identification of negative tracks (pions) was not required.

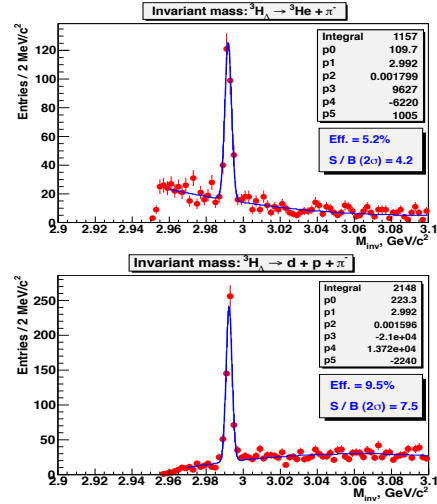


Figure 1: Reconstructed invariant mass for two- and three-prong decays of  ${}^3_{\Lambda}\text{H}$

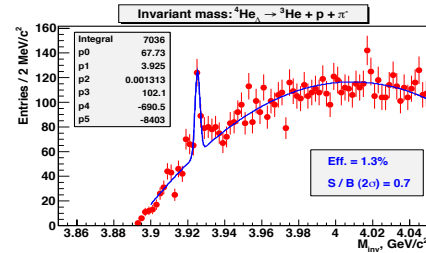


Figure 2: Reconstructed invariant mass of  ${}^4_{\Lambda}\text{He}$

Figure 1 shows that the lightest hypernucleus  ${}^3_{\Lambda}\text{H}$  can be reconstructed with high efficiency and signal-to-background ratio, both for two- and three-prong decay modes. The less abundant species  ${}^4_{\Lambda}\text{He}$  can be identified as well (Fig. 2). These two hypernucleus species (along with  $\Lambda$ -particle) will be further used to look for the double- $\Lambda$  hypernucleus decays in different modes (Tab. 2).

## References

- [1] K. K. Gudima, Yu. A. Murin and E. I. Litvinenko, *The HYPQGSM event generator for the simulation of hypernuclei production in central collisions of heavy ions for NICA/MPD and FAIR/CBM*, this report
- [2] H. Kamada *et al.*, Phys. Rev. **C 57** (1998) 1595
- [3] I. Kumagai-Fuse and Sh. Okabe, Phys. Rev. **C 66** (2002) 014003



## Reconstruction of $\pi^0$ and $\eta$ with a light ECAL

S. M. Kiselev

ITEP, Moscow, Russia

UrQMD head-on ( $b=0$  fm) events ( $10^6$  p+C at 30 GeV,  $10^5$  C+C,  $10^4$  Cu+Cu and  $10^4$  Au+Au at 25A GeV), simulated and reconstructed in the light ECAL by M. Prokudin [1], were analyzed in the frame of the Cbm-Root package (trunk Sep2010, Geant3). The set-up consisted of STS and the light ECAL wall of the size  $5.28 \times 4.32\text{m}^2$  with a beam hole of  $0.24 \times 0.24 \text{m}^2$  at a distance of 6 m from the target. Reconstructed photons with  $p > 0.5 \text{ GeV}/c$  and  $\chi_{cluster}^2 < 25$  were taken for the analysis.

A signal in the  $\pi^0$  range of the invariant mass spectrum is seen for the systems p+C, C+C and Cu+Cu. It was fitted by the sum of a Gaussian and a 2nd order polynomial, obtaining  $\sigma_{\pi^{pC}} \approx 6 \text{ MeV}$ ,  $\sigma_{\pi^{CC}} \approx 6 \text{ MeV}$ ,  $\sigma_{\pi^{CuCu}} \approx 10 \text{ MeV}$ . A signal in the  $\eta$  range is seen only for the p+C system, with  $\sigma_{\eta^{pC}} \approx 18 \text{ MeV}$ . The signal-to-background ratios S/B and significances for different  $p_t$  bins are presented in Tabs. 1 and 2.

Table 1: Signal-to-background ratios (S/B) and significances (in brackets) for  $\pi^0$

$p_t$ (MeV/c)	0.4 - 0.8	0.8 - 1.2	1.2 - 1.6
p+C	4.06 (343)	11.60 (161)	24.89 (73)
C+C	0.65 (184)	2.00 (100)	4.24 (46)
Cu+Cu	0.04 (33)	0.13 (25)	0.24 (12)
Au+Au	0.003 (8)	0.008 (7)	0.02 (5)

Table 2: Signal-to-background ratios, S/B, and significances (in brackets) for  $\eta$

$p_t$ (MeV/c)	0.4 - 0.8	0.8 - 1.2	1.2 - 1.6
p+C	0.13 (31)	0.29 (23)	0.47 (11)
C+C	0.02 (9)	0.03 (6)	0.05 (3)
Cu+Cu	0.001 (1.7)	0.002(1.1)	0.003 (0.6)
Au+Au	0.0001 (0.5)	0.0002 (0.4)	0.0004 (0.3)

The invariant mass spectra of the reconstructed photon pairs from true  $\pi^0$  and  $\eta$  have a Gaussian shape for the low mass systems p+C and C+C with  $\sigma_{\pi^{pC}} \approx 6 \text{ MeV}$ ,  $\sigma_{\eta^{pC}} \approx 18 \text{ MeV}$ ,  $\sigma_{\pi^{CC}} \approx 7 \text{ MeV}$ ,  $\sigma_{\eta^{CC}} \approx 20 \text{ MeV}$ . For the heavier systems Cu+Cu and Au+Au, the true signals have a non-Gaussian shape with a long tail to the right side. The "true signals" were used to estimate the S/B ratios in the cases when the signal was not seen in the invariant mass spectrum

of reconstructed photon pairs. The results are presented in Tabs. 1 and 2. Tables 3 and 4 summarize the main characteristics of the  $\pi^0$  and  $\eta$  analyses. Plots for acceptance and reconstruction efficiencies and the invariant mass distributions for all systems can be found in Ref. [2].

Table 3: Main characteristics of the  $\pi^0 \rightarrow \gamma\gamma$  analysis

	p+C	C+C	Cu+Cu	Au+Au
yield/event	2.5	13.5	107	365
accept. eff.	17%	22%	21%	21%
reconst. eff.	94%	84%	35%	5%
total eff.	16%	18%	7%	1%
$\sigma$ (MeV)	6.1	6.4	10.1	-
S/B	1.65	0.22	0.02	0.002
signif.	509	207	33	8

Table 4: Main characteristics of the  $\eta \rightarrow \gamma\gamma$  analysis

	p+C	C+C	Cu+Cu	Au+Au
yield/event	0.10	0.53	4.22	14.2
accept. eff.	26%	34%	34%	34%
reconst. eff.	96%	87%	46%	9%
total eff.	25%	30%	16%	3%
$\sigma$ (MeV)	18.2	20.8	-	-
S/B	0.11	0.016	0.001	0.0001
signif.	46	15	2.6	0.8

The results for the p+C and the Au+Au system can be compared with those obtained with the large ECAL [3]. Because of the high material budget in front of the large ECAL, its acceptance is lower ( $\sim 12\%$  and  $\sim 9\%$  for  $\pi^0$  and  $\eta$ , respectively). On the other hand, the large ECAL is placed at a twice larger distance from the target, and its reconstruction efficiencies for Au+Au (for p+C they are almost the same) is higher ( $\sim 19\%$  and  $\sim 27\%$  for  $\pi^0$  and  $\eta$ , respectively). As a consequence, the light ECAL does not improve the results for the Au+Au collision system.

## References

- [1] M. Prokudin, *Calorimeter for the CBM light option*, 17th CBM collaboration meeting, April 2011, Dresden, Germany
- [2] S. M. Kiselev, *Reconstruction of  $\pi^0$  and  $\eta$  with light ECAL*, 17th CBM collaboration meeting, April 2011, Dresden
- [3] S. M. Kiselev, *CBM Progress Report 2009*, Darmstadt 2010, p 69

# Reconstruction of $\omega \rightarrow \pi^0\gamma$ with a light ECAL in p+C collisions at SIS-100

S. M. Kiselev

ITEP, Moscow, Russia

The feasibility of  $\omega$  reconstruction by its decay  $\omega \rightarrow \pi^0\gamma$  using the light ECAL was studied on a sample of  $10^6$  p+C ( $b=0$  fm) events from UrQMD at the SIS-100 energy 30 GeV. The detector geometry and software version are described in Ref. [1]. The invariant mass spectrum of  $\gamma\pi^0$  pairs is displayed in Fig. 1.  $\gamma\pi^0$  pairs within the invariant mass interval  $0.77 < M_{\gamma\pi^0} < 0.79$  GeV are taken as "primary"  $\omega$ .

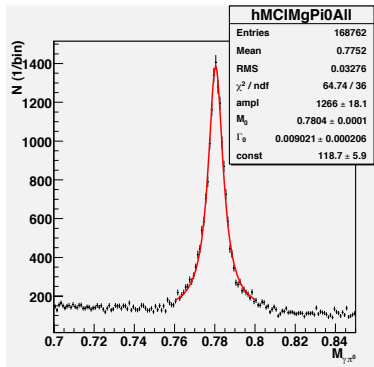


Figure 1: Invariant mass spectra of  $\gamma\pi^0$  pairs for p+C at 30 GeV, fitted by a Breit-Wigner function (red line)

Only about 4% of "vertex" photons are lost before the light ECAL. In case of the  $\omega$  reconstruction, photons with  $p > 1$  GeV/c were used. The resulting  $\gamma\gamma$  invariant mass distribution is shown in Fig. 2. As  $\pi^0$  candidates, pairs with  $m_{\pi^0} - 2\sigma < M_{\gamma\gamma} < m_{\pi^0} + 2\sigma$  were selected, where  $\sigma = 5.3$  MeV.

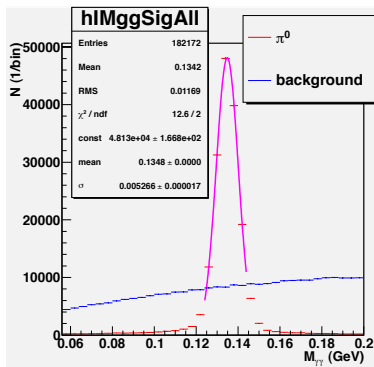


Figure 2: Invariant mass distributions of signal (red) and background (blue)  $\gamma\gamma$  pairs for p+C at 30 GeV

Figure 3 depicts the invariant mass distributions of  $\gamma\pi^0$  pairs. We obtain a signal-to-background ratio (S/B) of about 3.7% with a significance of 5.4. The main charac-

teristics of the analysis are summarized in Tab. 1.

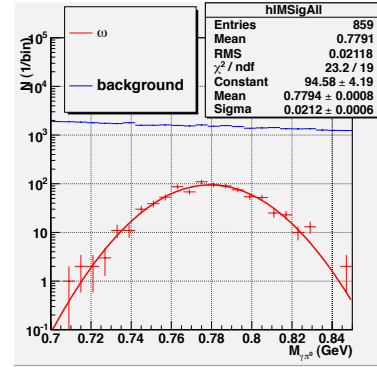


Figure 3: Invariant mass spectra of signal (red) and background (blue)  $\gamma\pi^0$  pairs for p+C at 30 GeV

Table 1: Main characteristics of the  $\omega$  analysis for p+C at 30 GeV

characteristic	value
statistics (events)	$10^6$
yield/event	0.015
acceptance efficiency	22 %
reconstruction efficiency	77 %
cut efficiency	35 %
total efficiency	6 %
$\sigma$ (MeV)	21
S/B $_{2\sigma}$	3.7 %
significance	5.4

In comparison with the large ECAL [2], the S/B is 5 times larger due to mainly because of the larger acceptance. With the current statistics (859 reconstructed signal pairs), it is not possible to study the dependence of the S/B on transverse momentum. The physical motivation for the presented investigation as well as more analysis details can be found in [3].

## References

- [1] S. M. Kiselev, *Reconstruction of  $\pi^0$  and  $\eta$  with light ECAL*, this report
- [2] S. M. Kiselev, CBM Progress Report 2010, GSI Darmstadt, p. 83.
- [3] S.M. Kiselev, *Reconstruction of  $\omega \rightarrow \pi^0\gamma$  with light ECAL in p+C at SIS100*, 18th CBM collaboration meeting, September 2011, Beijing, China

## $D^{*+}$ decay reconstruction in C+C collisions at 25A GeV in the CBM experiment

I. Vassiliev<sup>1,2</sup>, I. Kisel<sup>1,2</sup>, and V. Vovchenko<sup>2,3</sup>

<sup>1</sup>Goethe-Universität, Frankfurt, Germany; <sup>2</sup>GSI, Darmstadt, Germany; <sup>3</sup>T. Shevchenko National Univ., Kyiv, Ukraine

The aim of the nucleus-nucleus collision research program of CBM at FAIR is to study the QCD phase diagram at high baryon densities and moderate temperatures. One of the main observables are D mesons or  $\Lambda_c$  which carry a charm quark and are expected to be created in the early stage of the nucleus-nucleus collision. The D mesons can be detected via their hadronic decay into charged pions and kaons. This task requires fast and efficient track reconstruction algorithms and high-resolution secondary vertex determination. The challenge in recognizing the displaced vertex of the rare Open Charm decays lies (i) in the separation from weak  $K_S^0$  and  $\Lambda$  decays which produce displaced vertices downstream the target, (ii) the very low multiplicity of the open charm production, (iii) its low branching ratios and (iv) in multiple scattering inside the beam pipe and detector materials. To calculate the multiplicity of different D mesons in C+C collisions at 25A GeV, the Hadron String Dynamics (HSD) model (v2.5) was used [1].

To study the feasibility of  $D^0$  and  $D^{*+}$  decay reconstruction with the CBM experiment, a set of  $10^5$  central C+C UrQMD events at 25A GeV was simulated. The decay to  $D^{*+} \rightarrow \pi^+ D^0$  was embedded into each event in order to simulate a signal in the environment of background hadrons. A realistic STS geometry with 2 MVD stations at 5 cm (thickness 300  $\mu\text{m}$ ) and 10 cm (thickness 500  $\mu\text{m}$ ) and 8 double-sided segmented strip detectors (thickness 400  $\mu\text{m}$ ) was used. The primary vertex was reconstructed with high accuracy (6  $\mu\text{m}$  in  $z$  direction, 1  $\mu\text{m}$  in  $x$  and  $y$ ) at a multiplicity of about 450 tracks reconstructed in the STS inside a non-homogeneous magnetic field by the SIMDized Kalman filter procedure described in [2].

The  $D^0$  particle was reconstructed from its  $K^+\pi^-$  daughter particles using the primary vertex as the production point. The  $D^0$   $z_{\text{vertex}}$  resolutions results to 52  $\mu\text{m}$ . By originating from a displaced decay vertex, the  $D^0$  daughter tracks have a non-vanishing impact parameter at the target plane. Since the majority of the primary tracks have a very small impact parameter, a large fraction (99%) of the background tracks was rejected using a cut on their  $\chi^2$  distance to the primary vertex. The combinatorial background is suppressed mainly by the geometrical and topological vertex cuts. The shape of the background in the signal IM region was estimated using the event mixing technique. The resulting spectrum, consisting of background plus the  $D^0$  signal from HSD, is shown in Fig. 1.

$D^{*+}$  decays in the primary vertex; the  $D^{*+}$  daughter tracks must thus originate from this point. Therefore, in order to reconstruct  $D^{*+}$  one needs to combine all identified  $D^0$  in the window of  $1.84 < m_{\text{inv}}(\text{GeV}/c^2) < 1.89$

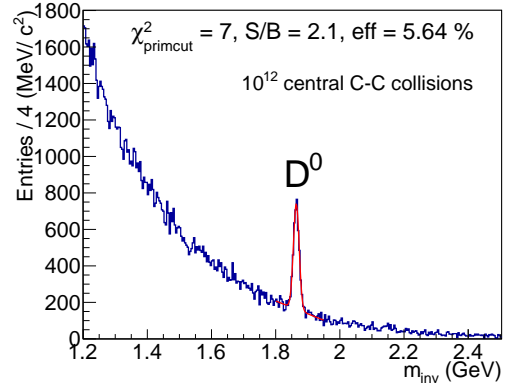


Figure 1: Reconstructed  $D^0$  mesons in  $10^{12}$  central C+C collisions at 25A GeV. The red line shows the  $D^0$  signal, the blue one the combinatorial background.

with all positively charged primary tracks. A  $\chi_{\text{geo}}^2 < 3\sigma$  cut was used to ensure that the daughter tracks come close enough to each other to be considered as daughter products of  $D^{*+}$ . Additionally, a  $\chi_{\text{topo}}^2 < 3\sigma$  cut was used to suppress combinatorial and direct  $D^0$  background. As shown in Fig. 2, the  $D^{*+}$  signal can be clearly distinguished, and the signal-to-background ratio is relatively high. The total number of collected  $D^{*+}$  results to about 740 at a reconstruction efficiency of 3.8%.

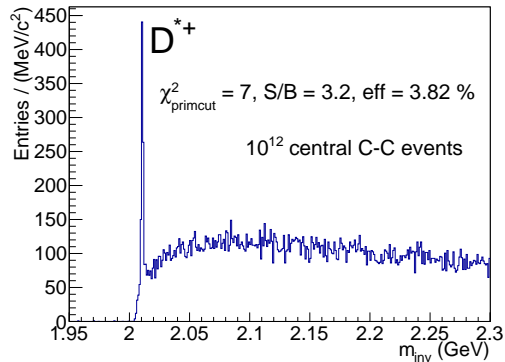


Figure 2: Reconstructed  $D^{*+}$  mesons and combinatorial background in  $10^{12}$  central C+C collisions at 25A GeV

### References

- [1] W. Cassing and E. L. Bratkovskaya, Phys. Rep. **308** (1999) 65
- [2] S. Gorbunov *et al.*, Comp. Phys. Comm. **178** (2008) 374

## Status of low-mass di-electron simulations in the CBM experiment

*E. Lebedeva<sup>1</sup>, T. Galatyuk<sup>1</sup>, C. Höhne<sup>2</sup>, and J. Stroth<sup>1,3</sup>*

<sup>1</sup>Goethe-Universität, Frankfurt, Germany; <sup>2</sup>Justus-Liebig-Universität, Gießen, Germany; <sup>3</sup>GSI, Darmstadt, Germany

Results of systematic studies of the reconstruction performance for low-mass di-electrons in different CBM detector setups are presented in this report. We compare four different simulation setups, namely, 100% and 70% magnetic field scales and setups with and without the MVD detector. In case of presence of the MVD detector, simulations were performed including  $\delta$ -electrons as well. The report thus presents the most realistic simulations performed so far.

The simulations were carried out for central Au+Au collisions at 25 GeV/u beam energy. Low-mass vector mesons ( $\rho^0$ ,  $\omega$ ,  $\phi$ ) were generated using the Pluto event generator.  $\delta$ -electrons are produced in the target by all Au ions crossing the target. They are registered only by the MVD detector as it has a comparatively long readout time; for other detectors this effect can be neglected. According to the used 25  $\mu\text{m}$  thick gold target (0,1% nuclear interaction length), assuming 33 kHz interaction rate and 30  $\mu\text{s}$  readout time of the MVD detector, 1000 Au ions were embedded for each UrQMD event. The mean number of hits in MVD per event is 1100. Including  $\delta$ -electrons gives 3000 hits per event. Using the 70% B-field the number of MVD hits increases further by 30% up to 3900.

The reconstruction performance results for single  $e^\pm$  from  $\rho^0$ -mesons are shown in Tab. 1. The number of reconstructed global tracks per event is 580 – 680 depending on the setup. The detector acceptance of single  $e^\pm$  from  $\rho^0$

Table 1: Reconstruction: summary table of the reconstruction performance of single  $e^\pm$  from  $\rho^0$  for different simulation setups. Analysis: summary table of the analysis of  $\rho^0$ ,  $\omega$  and  $\phi$  mesons after all cuts for different simulation setups.  $S/B_{(0.2-0.6)}$  is S/B for  $0.2 < M_{ee}/(\text{GeV}/c^2) < 0.6$ .

	100% B-field scale		70% B-field scale			
MVD?	no	yes	no	yes		
$\delta$ -electrons?	—	no	yes	—	no	yes
Reconstruction of single $e^\pm$ from $\rho^0$ meson						
global tr./ev.	581	621	677	593	624	674
Acc/MC [%]	50.4	50.0	50.1	54.3	53.9	54.7
rec. eff. [%]	66.2	66.2	63.7	66.4	65.4	63.2
el. id. eff. [%]	55.7	55.6	53.3	55.0	53.9	51.8
pion supp.	7100	8550	6890	9190	9060	7010
dP/P <sub>RMS</sub> [%]	1.14	1.26	1.49	1.50	1.64	1.88
Analysis						
$\omega$ : eff. [%]	5.7	5.9	5.5	6.4	6.4	5.5
$\omega$ : S/BG	0.40	0.32	-	0.3	0.29	0.25
$\rho^0$ : eff. [%]	4.4	4.5	4.0	4.8	4.8	3.9
$\phi$ : eff. [%]	7.5	8.9	8.2	8.6	9.5	8.4
$\phi$ : S/BG	0.49	0.24	-	0.31	0.18	0.17
$S/B_{(0.2-0.6)}$	0.012	0.01	0.006	0.03	0.02	0.02

is 50% for 100% B-field, and 54% for 70% B-field. The global reconstruction efficiency in STS+RICH+TRD+TOF for single  $e^\pm$  from  $\rho^0$  is around 65%. The RICH, TRD and TOF detectors provide a momentum integrated (0 – 10 GeV/c) pion suppression factor of 7000 – 9200 at around 54% electron identification efficiency depending on the setup. The momentum resolution increased from 1.14% to 1.88% when using the MVD detector and 70% B-field.

Several background rejection cuts were used [1]:  $\gamma$  conversion cut, track topology cuts, transverse momentum cut. When the MVD detector is present in simulations, a two-dimensional cut on the distance between the intersection point of an electron track in the MVD station to its nearest neighbor hit versus the electron track momentum is applied.

The invariant mass spectrum of electron pairs including full event reconstruction and electron identification after applying background rejection cuts is shown in Fig. 1.

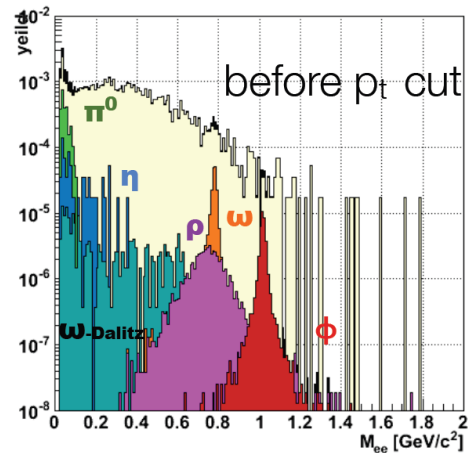


Figure 1: Invariant mass spectra after all cuts (except  $p_t$ ). Setup: MVD, 70% field scale, no  $\delta$ -electrons, 70k events.

Six configurations with the most realistic simulations being available so far were investigated. The results are comparable with those obtained previously [1]: the efficiencies are the same, the S/B ratios differ within a factor of 2. However, the fact that the S/B ratio seems to drop if including the MVD detector is not understood yet and needs more investigations.

### References

- [1] T. Galatyuk *et al.*, CBM Progress Report 2009, Darmstadt 2010, p. 63

## Reconstruction of $J/\psi \rightarrow e^+e^-$ in Au+Au collisions at SIS-300 energies

O. Yu. Derenovskaya<sup>1</sup> and I. O. Vassiliev<sup>2,3</sup>

<sup>1</sup>LIT, JINR, Dubna, Russia; <sup>2</sup>Goethe-Universität, Frankfurt, Germany; <sup>3</sup>GSI, Darmstadt, Germany

The investigation of charmonium production is one of the key goals of the CBM experiment. The main difficulty lies in the extremely low multiplicity expected in Au+Au collisions at 25A GeV, near the  $J/\psi$  production threshold. Hence an efficient event selection based on  $J/\psi$  signatures is necessary in to reduce the data volume to a recordable rate. Here we present results of  $J/\psi$  meson reconstruction in its di-electron decay channel using the KFParticle package with a complete reconstruction chain including the current STS detector as a main tracker. For particle identification the RICH, TRD and TOF detector systems were used.

To study the feasibility of  $J/\psi$  identification, signal as well as background events were simulated. Electrons from  $J/\psi$  decays were simulated by the PLUTO event generator and embedded into background events (central Au+Au at 25A GeV generated with UrQMD). For event reconstruction in the standard CBM detector setup, particles are tracked by the silicon tracking system placed inside a magnetic field, providing the momentum of the tracks. Global tracking provides particle identification information using the RICH, TRD and TOF detector systems. In order to reconstruct  $J/\psi$ , we have used the full electron identification procedure as briefly described in Ref. [1]. Identified electrons and positrons emerging from the target are combined to  $J/\psi$  candidates using the KFParticle package [2]. In order to further suppress the electron background, a transverse momentum cut at 1 GeV/c was applied. Figure 1 shows the  $z$  component of the vertex  $z_{\text{vertex}}$  of reconstructed  $J/\psi$ s. The KFParticle package

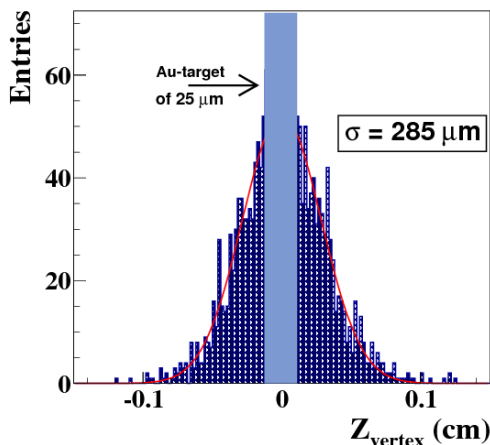


Figure 1: Distribution of  $z_{\text{vertex}}$  of reconstructed  $J/\psi$ . The rectangle shows the target area.

allows to reconstruct  $z_{\text{vertex}}$  for  $J/\psi$  with a resolution of about  $\sigma = 285 \mu\text{m}$ .

In order to study the signal-to-background ratio, the signal mass spectrum was obtained from UrQMD events with one embedded  $J/\psi$  decay, while the combinatorial background was generated from the original central UrQMD events. To increase the statistics and to get the proper shape of the background, the event mixing technique was applied. The signal spectrum was added to the background after scaling, taking into account the assumed multiplicity (HSD transport code), the decay branching ratio and the  $J/\psi$  reconstruction efficiency. The resulting invariant-mass spectrum is displayed in Fig. 2 in the charmonium mass region. The obtained results show a high capability of CBM to reconstruct  $J/\psi$  in Au+Au collisions at SIS-300 energies with good statistics.

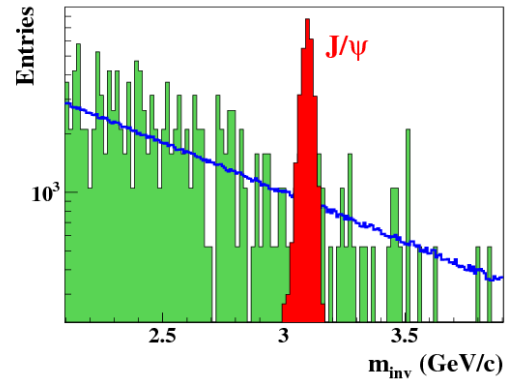


Figure 2: Invariant-mass spectrum of  $J/\psi$  for central Au+Au collisions at 25 AGeV

Table 1: Multiplicity, branching ratio, signal-to-background ratio, reconstruction efficiency and mass resolution for  $J/\psi$  in central Au+Au collisions at 25A GeV

	Mult.	Br.ratio	S/B	Eff.	$\sigma$
$J/\psi$	$1.92 \times 10^{-5}$	0.06	2	0.19	24 MeV

## References

- [1] I. Vassiliev and O. Derenovskaya, *J/psi detection in p + Au collisions at 30 GeV*, this report
- [2] S. Gorbunov and I. Kisel, *Reconstruction of Decayed Particles Based on the Kalman Filter*, CBM-SOFT-note-2007-003

## $J/\psi$ reconstruction in p + Au collisions at 30 GeV

O. Yu. Derenovskaya<sup>1</sup> and I. O. Vassiliev<sup>2,3</sup>

<sup>1</sup>LIT, JINR, Dubna, Russia; <sup>2</sup>Goethe-Universität, Frankfurt, Germany; <sup>3</sup>GSI, Darmstadt, Germany

The investigation of p + Au collisions at 30 GeV beam energy is considered a part of the CBM research program and will be performed in the first phase of FAIR with a start version of the CBM detector at SIS-100. Here we present the results of  $J/\psi \rightarrow e^+e^-$  reconstruction in p+Au collisions. The complete CBM track reconstruction chain includes the STS as a main tracking detector and for particle identification the RICH, TRD and TOF detector systems.

The feasibility study of  $J/\psi$  reconstruction is based on a set of p+Au events ( $b = 0$ ) at 30 GeV generated with UrQMD. One  $J/\psi$  decay into  $e^+e^-$ , generated by PLUTO, was embedded in each UrQMD event in order to simulate a signal within the environment of background tracks. In order to reconstruct  $J/\psi$ , we use the full electron identification procedure including the RICH, TRD and TOF detector systems. To analyze the RICH hits we use the elliptic ring fit procedure and apply ring quality cuts based on a neural network algorithm to separate electrons from pions (Fig. 1).

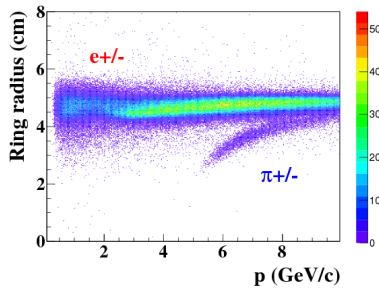


Figure 1: Radius of the reconstructed rings as a function of the particle momentum. Electrons and pions are clearly separated up to  $p = 5.5$  GeV/c.

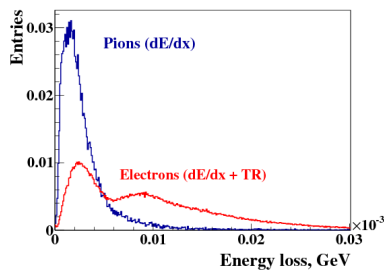


Figure 2: Distribution the energy loss of electrons ( $dE/dx + TR$ ) and pions ( $dE/dx$ ) in the TRD

In addition, the electrons are identified via their transition radiation measured by the TRD. Based on the individ-

ual and total energy loss (see Fig. 2), the neural network algorithm discriminates electrons from pions misidentified by the RICH analysis. The information from the TOF detector system is used to further separate hadrons from electrons (see Fig. 3). A momentum-dependent cut on the squared mass is applied to reject hadrons (mainly pions) from the identified electron sample.

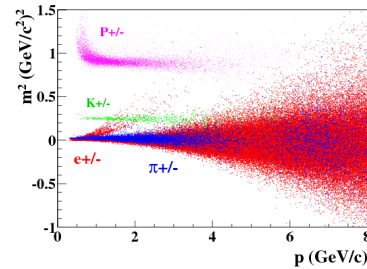


Figure 3: Squared mass of charged particles as a function of the particle momentum in the TOF for RICH-identified electrons and misidentified pions

The  $J/\psi$  reconstruction procedure is described in [1]. A reconstruction efficiency of 68% is achieved by the combined RICH-TRD-TOF analysis. The combined RICH and TRD identification suppresses pions by a factor of about 24,000. The thus obtained invariant-mass spectrum of  $J/\psi$  mesons in p + Au collisions at 30 GeV beam energy is shown in Fig. 4. The total signal reconstruction efficiency is about 27%. For the simulation we assumed a  $J/\psi$  multiplicity of  $6 \times 10^{-8}$  and a branching ratio of 6%. The invariant-mass resolution is 23 MeV and a signal-to-background ratio of 18 is achieved ( $2\sigma$ ).

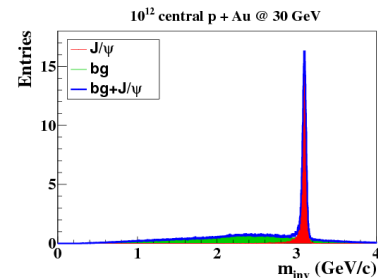


Figure 4: Reconstructed invariant-mass spectrum of  $J/\psi$  mesons for central p+Au collisions at 30 GeV

## References

- [1] I. Vassiliev and O. Derenovskaya, *Reconstruction of  $J/\psi \rightarrow e^+e^-$  in Au+Au collisions at SIS-300 energies*, this report

## High $p_T$ pion production in central Au+Au collisions at SIS-100/300 energies with CBM

V. P. Ladygin<sup>1</sup>, A. I. Malakhov<sup>1</sup>, and T. A. Vasiliev<sup>1</sup>

<sup>1</sup>LHEP-JINR, Dubna, Russia

The suppression of particle production at high transverse momenta  $p_t$  in central heavy-ion collisions is generally interpreted as a sign of parton loss in the strongly interacting matter. Its study can provide information on the partonic phase of strongly interacting matter even in the energy domain of SIS-100 [1].

The rapidity distributions of  $\pi^+$  from central Au+Au events are shown in Fig.1. Open symbols denote the data for one central Au+Au event at 10.7 A·GeV from the UrQMD 2.3, UrQMD 1.3 [3] and HSD 2.5 [4] generators, respectively. The model results for  $\pi^+$  spectra differ significantly. The solid symbols show the rapidity distribution of  $\pi^+$  for central collisions selected by the ZDC in the E866 experiment at AGS [2]. The distribution from AGS is scaled by the factor of 1/10 and corresponds to the  $y - y_{cm} < 0$  region, where  $y_{cm} = 1.6$ . The acceptance of the CBM setup for pions is shown by the vertical line. The CBM setup allows to extend the rapidity region for high  $p_t$  pion production to central and forward rapidities.

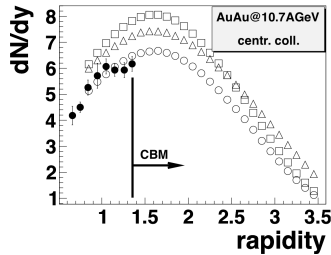


Figure 1: Rapidity spectra for  $\pi^+$  for central Au+Au collisions at 10.7 A GeV from the UrQMD 2.3 (open circles), UrQMD 1.3 (boxes) and HSD 2.5 (triangles) models. AGS data [2] scaled by the factor of 1/10 are shown by filled symbols.

Simulations were performed for 10k central Au+Au events from UrQMD 2.3 at 10A and 25A GeV. Pions were selected using the  $m^2 - p$  correlation, where momentum and time-of-flight were reconstructed from STS and RPC information, respectively. This method unavoidably leads to a contamination by misidentified kaons and protons, especially at high momentum values [1]. To improve the purity of the particle identification procedure, the  $m^2 - p$  selection was modified as described in [1]. The usage of RICH for the pion ID was investigated at 10A and 25A GeV. Figs. 2 and 3 represent the high  $p_t$  data for  $\pi^+$  at 10A and 25A GeV, respectively. The  $p_t$  spectra at 10A GeV show approximately equal fractions of high-

$p_t$  events selected by the STS-TOF and STS-RICH sub-detectors. As shown in Fig. 3, RICH significantly extends the high- $p_t$  pion measurements at 25A GeV. The CBM setup at SIS-100 allows to obtain high- $p_t$  data at mid- and forward rapidities, which were unreachable at AGS. The usage of the RICH detector for pion ID with CBM@SIS-300 can significantly extend the high- $p_t$  measurements.

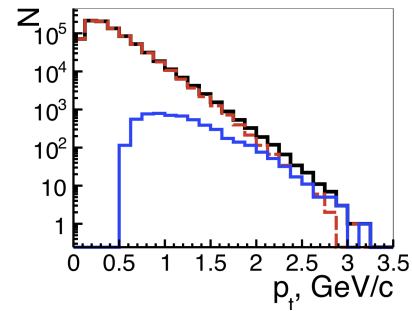


Figure 2:  $p_t$  spectra of  $\pi^+$  for central Au+Au collisions at 10A GeV. The red line shows pions identified by STS and TOF, the blue line those identified by STS and RICH. The black line denotes the sum of both.

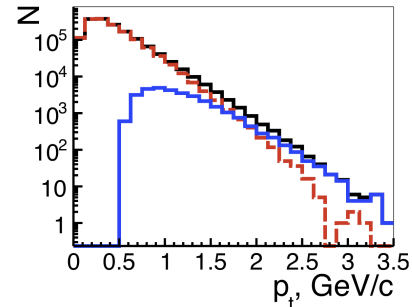


Figure 3: Same as Fig. 2, but for central Au+Au collisions at 25A GeV

### References

- [1] V. P. Ladygin, A. I. Malakhov and T. A. Vasiliev, CBM Progress Report 2010, Darmstadt 2011, p. 58
- [2] L. Ahle *et al.*, Phys. Rev. **C 59** (1999) 2173
- [3] S. A. Bass *et al.*, Prog. Part. Nucl. Phys. **41** (1998) 225  
M. Bleicher *et al.*, J. Phys. **G 25** (1999) 1859
- [4] W. Cassing and E. L. Bratkovskaya, Phys. Rep. **308** (1999) 65

## Performance analysis of the Cellular Automaton algorithm on a many-core server at LIT JINR

*I. S. Kulakov<sup>1,2</sup>, S. A. Baginyan<sup>3</sup>, V. V. Ivanov<sup>3</sup>, and P. I. Kisel<sup>3</sup>*

<sup>1</sup>Goethe-Universität, Frankfurt, Germany; <sup>2</sup>University of Kyiv, Kyiv, Ukraine; <sup>3</sup>LIT JINR, Dubna, Russia

High event multiplicity and an intensive background, as well as a nonhomogeneous magnetic field and the necessity of full on-line track reconstruction in the CBM experiment require not only the development of new approaches to the solution of the problem under consideration [1, 2, 3], but also the maximum usage of the potential of modern many-core CPU/GPU architectures. Results of the performance analysis of the Cellular Automaton and the Kalman filter algorithms for the solution of the track reconstruction problem in the STS detector on a many-core server at LIT JINR are presented here.

The server has two Intel Xeon E5640 CPUs, each having four cores at 2.66 GHz and 12 MB third-level cache memory. A 45 GB RAM is equally partitioned between the CPUs. The availability of the hyper-threading technology enables the usage of each physical core as two logical cores. Thus, the server has 16 logical cores in total, which is quite sufficient for the investigation of the reconstruction algorithm.

Simulated data of minimum bias and central Au+Au collisions at 25A GeV energy were used. The average reconstruction efficiency for all track categories is 88% for minimum bias and 86% for central events. The average reconstruction time for one event on a single core is 25 ms for

minimum bias and 220 ms for central events. The scalability of the Cellular Automaton (CA) algorithm was investigated by running it in parallel on different numbers of CPU cores. The Intel Threading Building Blocks (TBB) library was used for the distribution of the parallel calculations between the cores.

The results of the scalability study are presented in Figs. 1 and 2. Our results show that the algorithm shows a good linear scalability on the many-core server at LIT JINR [4].

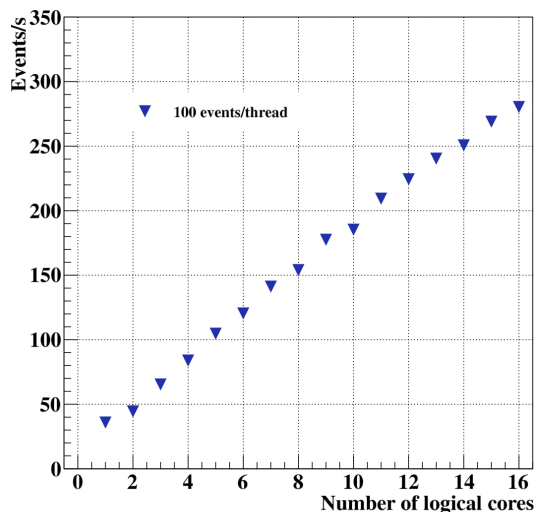


Figure 1: Scalability of the CA track finder for minimum bias events

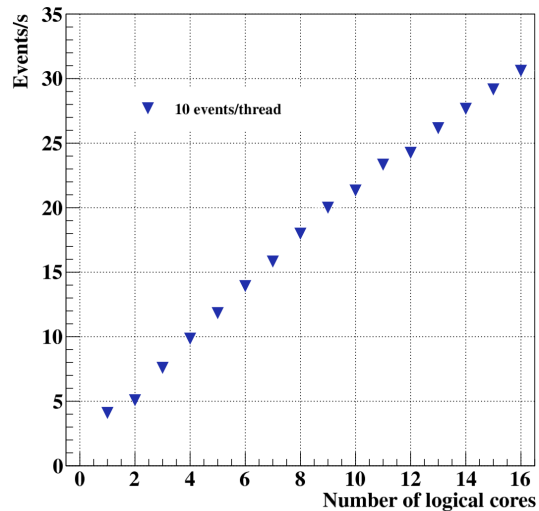


Figure 2: Scalability of the CA track finder for central events

### References

- [1] I. Kisel, Nucl. Instrum. Methods A **566** (2006) 85
- [2] M. P. Bussa *et al.*, Nucl. Instrum. Methods A **389** (1997) 208
- [3] S. Gorbunov *et al.*, Comp. Phys. Comm. **178** (2008) 374
- [4] I. S. Kulakov *et al.*, *Performance analysis of the track recognition algorithm in the STS detector of the CBM experiment on the LIT JINR many-core server*, JINR Rapid Communications P10-2012-1 (2012)



## CBM publications 2011

- S. N. Bazylev *et al.*:  
**A prototype coordinate detector based on granulated thin-walled drift tubes**  
Nucl. Instrum. Methods A **632** (2011) 75  
[doi:10.1016/j.nima.2010.09.073](https://doi.org/10.1016/j.nima.2010.09.073)
- S. Belogurov *et al.*:  
**CATIA-GDML geometry builder**  
J. Phys.: Conf. Ser. A **331** (2011) 032035  
[doi:10.1088/1742-6596/331/3/032035](https://doi.org/10.1088/1742-6596/331/3/032035)
- M. Ciobanu *et al.*:  
**In-Beam Diamond Start Detectors**  
IEEE Trans. Nucl. Sci. **58** (2011) 2073  
[doi:10.1109/TNS.2011.2160282](https://doi.org/10.1109/TNS.2011.2160282)
- V. I. Davkov *et al.*:  
**Spatial resolution of thin-walled high-pressure drift tubes**  
Nucl. Instrum. Methods A **634** (2011) 5  
[doi:10.1016/j.nima.2010.10.045](https://doi.org/10.1016/j.nima.2010.10.045)
- J. de Cuveland and V. Lindenstruth:  
**A First-Level Event Selector for the CBM Experiment at FAIR**  
J. Phys.: Conf. Ser. A **331** (2011) 022006  
[doi:10.1088/1742-6596/331/2/022006](https://doi.org/10.1088/1742-6596/331/2/022006)
- M. Deveaux *et al.*:  
**Radiation tolerance of a column parallel CMOS sensor with high resistivity epitaxial layer**  
JINST **6** (2011) C02004  
[doi:10.1088/1748-0221/6/02/C02004](https://doi.org/10.1088/1748-0221/6/02/C02004)
- D. Doering *et al.*:  
**Annealing studies on X-ray and neutron irradiated CMOS Monolithic Active Pixel Sensors**  
Nucl. Instrum. Methods A **658** (2011) 133  
[doi:10.1016/j.nima.2011.05.079](https://doi.org/10.1016/j.nima.2011.05.079)
- J. Eschke and C. Höhne:  
**Results from first beam tests for the development of a RICH detector for CBM**  
Nucl. Instrum. Methods A **639** (2011) 307  
[doi:10.1016/j.nima.2010.10.104](https://doi.org/10.1016/j.nima.2010.10.104)
- V. Friese:  
**Simulation and Reconstruction of Free-streaming Data in CBM**  
J. Phys.: Conf. Ser. A **331** (2011) 032008  
[doi:10.1088/1742-6596/331/2/022006](https://doi.org/10.1088/1742-6596/331/2/022006)
- J. Gebelein and U. Keschull:  
**A three-dimensional FPGA array beam detector for ionizing radiation experiments**  
Proceedings of 12th European Conference on Radiation and Its Effects on Components and Systems (RADECS 2011) p. 771  
[doi:10.1109/RADECS.2011.6131450](https://doi.org/10.1109/RADECS.2011.6131450)

- J. Heuser:  
**The Compressed Baryonic Matter Experiment at FAIR**  
EPJ Web of Conferences **13** (2011) 03001  
[doi:10.1051/epjconf/20111303001](https://doi.org/10.1051/epjconf/20111303001)
- C. Höhne *et al.*:  
**Development of a RICH detector for electron identification in CBM**  
Nucl. Instrum. Methods **A 639** (2011) 294  
[doi:10.1016/j.nima.2010.10.062](https://doi.org/10.1016/j.nima.2010.10.062)
- L. Naumann *et al.*:  
**Ceramics high rate timing RPC**  
Nucl. Instrum. Methods **A 628** (2011) 138  
[doi:10.1016/j.nima.2010.06.302](https://doi.org/10.1016/j.nima.2010.06.302)
- L. Naumann *et al.*:  
**High-rate timing RPC with ceramics electrodes**  
Nucl. Instrum. Methods **A 635** (2011) S113  
[doi:10.1016/j.nima.2010.09.121](https://doi.org/10.1016/j.nima.2010.09.121)
- F. Uhlig:  
**Software Development Infrastructure for the FAIR Experiments**  
J. Phys.: Conf. Ser. **A 331** (2011) 042024  
[doi:10.1088/1742-6596/331/4/042024](https://doi.org/10.1088/1742-6596/331/4/042024)

## CBM presentations 2011

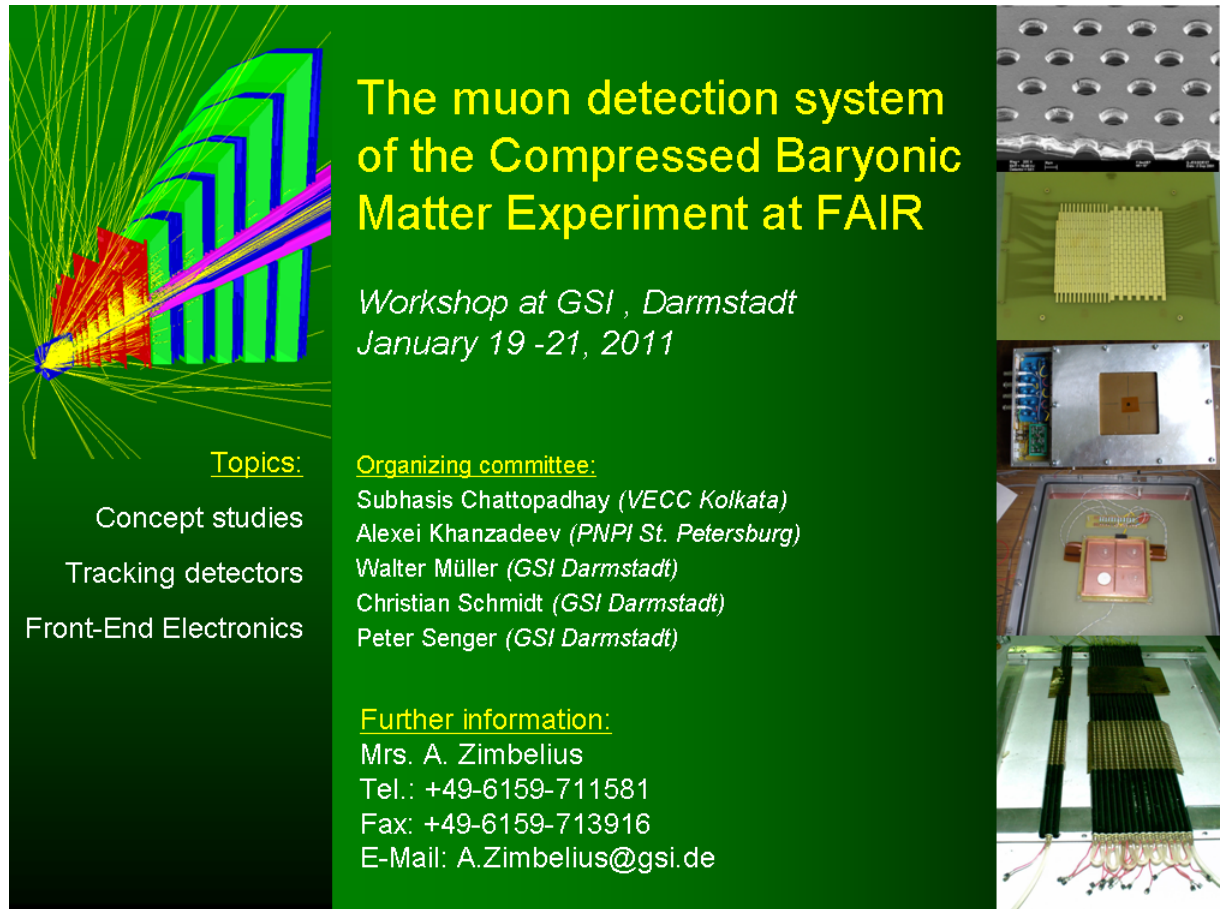
<http://cbm-wiki.gsi.de/cgi-bin/view/Public/PublicPresentations2011>

## Doctoral, diploma, master and bachelor theses 2011

<http://cbm-wiki.gsi.de/cgi-bin/view/Public/Thesis2011>

## CBM Muon Detector Workshop

19 – 21 January 2011, Darmstadt, Germany



**The muon detection system  
of the Compressed Baryonic  
Matter Experiment at FAIR**

*Workshop at GSI , Darmstadt  
January 19 -21, 2011*

Topics:

- Concept studies
- Tracking detectors
- Front-End Electronics

Organizing committee:

- Subhasis Chattopadhyay (VECC Kolkata)
- Alexei Khanzadeev (PNPI St. Petersburg)
- Walter Müller (GSI Darmstadt)
- Christian Schmidt (GSI Darmstadt)
- Peter Senger (GSI Darmstadt)

Further information:

- Mrs. A. Zimbelius
- Tel.: +49-6159-711581
- Fax: +49-6159-713916
- E-Mail: A.Zimbelius@gsi.de

The goal of the workshop was to discuss the main challenges of the CBM muon detection system: track reconstruction at very high hit densities, new technologies for fast, large-area and highly segmented tracking chambers, and free-streaming read-out electronics. In addition to contributions from CBM collaborators, experts from major muon detection experiments at accelerators were invited for presentations. Ruben Shahoyan discussed the design and analysis techniques of the NA60 muon detectors, Stefano Colafranceschi reported on micropattern (GEM) detectors based on large-area single-sided GEM foils for tracking and trigger in CMS, Sebastian Uhl explained the high-rate capable GEM detectors with strip and pixel read-out for COMPASS, and Jörg Wotschack reviewed the development of micromegas for the ATLAS muon system upgrade. In the concluding session of the workshop the discussion was focused on the next steps in the realization of the CBM muon detection system.

<https://indico.gsi.de/conferenceDisplay.py?confId=1120>

# 17<sup>th</sup> CBM Collaboration Meeting and Symposium on Charm, Dileptons and Deconfinement

4 – 8 April 2011, Dresden, Germany

**PHYSICS OF COMPRESSED BARYONIC MATTER**

**HZDR**

HELMHOLTZ  
ZENTRUM DRESDEN  
ROSSENDORF

April 4 – 8, 2011, Dresden, Germany

**17<sup>th</sup> CBM COLLABORATION MEETING**  
and Symposium on Charm, Dileptons and Deconfinement




[www.hzdr.de/cbm2011](http://www.hzdr.de/cbm2011)

**Scientific Committee**  
S. Chattopadhyay (VECC, Kolkatta)  
B. Kämpfer (HZDR, Dresden)  
P. Senger (GSI, Darmstadt)  
Y. Zaitsev (ITEP, Moskau)

**Local Organizers**  
R. Eißmann  
A. Laso Garcia  
R. Kotte  
L. Naumann  
R. Peschke  
C. Wendisch  
J. Wüstenfeld

**Conference Secretary**  
F. Seifert  
Phone: +49 351 260 3293  
E-mail: cbm2011@fzd.de









Forschungszentrum Dresden-Rossendorf | 01.01.2011 | Helmholtz-Zentrum Dresden-Rossendorf | Bautzner Landstr. 400 | 01328 Dresden



<https://www.hzdr.de/workshops/cbm2011>

## **Fifth Work Meeting of the CBM-MPD STS Consortium “Prototyping STS towards Practical Applications”**

16 – 20 May 2011, Alushta, Ukraine

The Consortium was formed in 2008 to develop technical solutions for the silicon tracking detector systems in the CBM experiment at FAIR and the NICA experiment at Nuclotron. It joins different fields of expertise from research institutes in Germany, Russia and Ukraine.

During the fifth work meeting, organized by JINR and GSI from 16-20 May 2011 at Hotel Dubna in Alushta, Crimea, Ukraine, about 30 participants contributed to the discussion and planning of “Prototyping the CBM-STs towards practical applications”. Those include technical in-beam tests of components and a fixed-target set-up at the Nuclotron facility prior to the main experiments. The presentations covered in particular aspects of the production and quality assurance of detector components and questions regarding their integration into the STS structures. The outcome of the meeting is a first description of the work share and the work flow towards the production of CBM silicon detector modules.



<http://sts-crimea11.jinr.ru>

## Workshop on system integration of highly granular and thin vertex detectors

6 – 9 September 2011,  
Mont Saint Odile, France

The design of next generation vertex detectors such as the CBM-MVD imposes numerous technological challenges in terms of the design of highly granular, light and radiation tolerant pixel sensors and their integration into ultra thin ladders. Additional challenges arise in the field of cooling, DAQ and FEE. The HIC4FAIR “Workshop on system integration of highly granular and thin vertex detectors” provided the exchange of experience among the vertex detector experts of different experiments in HEP and heavy ion physics. Among others, we welcomed representatives of CBM, STAR, ALICE, AIDA and the ILC community.

Besides enabling a fruitful information exchange, the workshop helped to identify common interests and synergies in the R&D programmes of the different communities.

Workshop on system integration of highly granular and thin vertex detectors

6th - 9th Sept. 2011,  
Mont Saint Odile, France

Sensor R&D, Integration,  
DAQ & FEE, Cooling,  
Radiation tolerance,  
Device simulation

Organization committee:  
M. Devesaux, I. Fröhlich, J. Stroth, M. Winter  
Conference secretary:  
M. Frey (+49 69 798 47023, frey@atom.uni-frankfurt.de)  
Conference page:  
<https://indico.cern.ch/conferenceDisplay.py?confId=144152>

HIC4FAIR  
Heavy Ion Collider for FAIR  
IPHC  
Institut für Experimentelle Kernphysik  
UNIVERSITÄT GIESSEN  
GOETHE  
UNIVERSITÄT  
FRANKFURT AM MAIN



<https://indico.cern.ch/conferenceDisplay.py?confId=144152>

# 18<sup>th</sup> CBM Collaboration Meeting and Symposium on QCD Phase Structure and High Baryon Density

26 – 30 September 2011, Beijing, China



**PHYSICS OF COMPRESSED BARYONIC MATTER**  
September, 26 - 30, 2011, Beijing, China

18<sup>th</sup> CBM COLLABORATION MEETING  
and Symposium on QCD Phase Structure at High-Baryon Density

 <http://hepd.ep.tsinghua.edu.cn/cbm2011>

**Scientific Committee**  
Kejun Kang (Tsinghua)  
P. Senger (GSI, Darmstadt)  
Nu Xu (CCNU, LBNL)



**Local Organizers**  
Yuanjing Li  
Yi Wang  
Yulan Li  
Jingbo Wang  
Ying Gu



**Conference Secretary**  
Jie Yang  
Phone: +86 01062772428  
E-mail: [cjpl@mail.tsinghua.edu.cn](mailto:cjpl@mail.tsinghua.edu.cn)



Tsinghua University, Beijing, 100084, China



<http://hepd.ep.tsinghua.edu.cn/cbm2011/index.php>

### CBM Software Workshop

8 – 10 November 2011, Ebernburg, Germany

cbmroot, the software framework of the CBM experiment, has been continuously growing over the years and comprises by now about 1.25 million lines of code. The increasing complexity of the software calls for both training of novices and coordinated efforts for maintenance and further development. The CBM Software Workshop was intended to meet both requirements. 39 participants united in the beautiful, yet November-misty location of the Ebernburg castle, a stronghold of the Reformation, overlooking the wine-rich river Nahe.

The medieval environment, forming a nice contrast to the workshop topic, did not derogate a productive working atmosphere featuring lectures and hands-on tutorials as well as technical and strategic discussions. The workshop covered the entire range of CBM software, from transport over detector response simulation to reconstruction and analysis, without skipping infrastructural aspects like efficient programming and software organisation.

The workshop established a basis for further collaborative efforts towards software developments and its usage in simulation and analysis. The positive rating by the participants suggests that it should be followed up by similar events on a regular basis.

Thanks go to the HIC4FAIR programme for the financial support of the workshop.



<https://indico.gsi.de/conferenceDisplay.py?confId=1309>



## The CBM Collaboration

- **Aligarh, India, Department of Physics, Aligarh Muslim University**  
N. Ahmad, M.D. Azmi, M. Irfan, M.M. Khan
- **Beijing, China, Department of Engineering Physics, Tsinghua University**  
Jianping Cheng, Zhi Deng, Jin Li, Yuanjing Li, Yulan Li, Yi Wang, Qian Yue, Xianglei Zhu
- **Bergen, Norway, Department of Physics and Technology, University of Bergen**  
D. Röhrich, K. Ullaland, S. Yang
- **Bhubaneswar, India, Institute of Physics**  
D.P. Mahapatra, P.K. Sahu
- **Bucharest, Romania, Horia Hulubei National Institute of Physics and Nuclear Engineering (IFIN-HH)**  
C. Andrei, D. Bartos, I. Berceanu, F. Constantin, V. Cătănescu, G. Caragheorghopol, A. Herghelegiu, M. Petriș, A. Petrovici, M. Petrovici, A. Pop, C. Schiaua, M. Tarzila
- **Bucharest, Romania, Atomic and Nuclear Physics Department, University of Bucharest**  
D. Argintaru, V. Baban, C. Beșliu, M. Călin, V. Covlea, T. Eșanu, A. Jipa, I. Lazanu, C. Ristea, O. Ristea, A. Scurtu
- **Budapest, Hungary, Eötvös Loránd University**  
B. Bozsogi, M. Csanád, Á. Fülöp, A. Kiss
- **Budapest, Hungary, KFKI Research Institute for Particle and Nuclear Physics (KFKI-RMKI)**  
L. Boldizsar, E. Denes, Z. Fodor, E. Futo, J. Kecskemeti, T. Kiss, A. Laszlo, T. Tolyhi, G. Vesztergombi
- **Chandigarh, India, Department of Physics, Panjab University**  
M.M. Aggarwal, A.K. Bhati, Manjit Kaur
- **Darmstadt, Germany, GSI Helmholtzzentrum für Schwerionenforschung GmbH**  
A. Abuhoza, J. Adamczewski, M. Al-Turany, V. Akishina, A. Andronic, E. Badura, T. Balog, E. Berdermann, D. Bertini, S. Biswas, S. Chatterji, M. Ciobanu (ISS, Bucharest), H. Deppe, J. Eschke, H. Flemming, U. Frankenfeld, J. Frühauf, V. Friese, P. Ghosh, J. Hehner, J. Heuser, R. Holzmann, R. Karabowicz, V. Kleipa, K. Koch, P. Koczoń, B. Kolb, A. Kotynia, D. Kresan, I. Kulakov, J. Kunkel, A. Lebedev, S. Linev, S. Löchner, A. Lymanets (KINR, Kiev), H. Malygina (KINR, Kiev), W.F.J. Müller, W. Niebur, J. Pietraszko, C.J. Schmidt, A. Senger, P. Senger, C. Simons, M. Singla, I. Sorokin (KINR, Kiev), D. Soyk, C. Sturm, O. Torheim, F. Uhlig, P. Zumbruch, M. Zyzak
- **Dresden, Germany, Institut für Strahlenphysik, Helmholtz-Zentrum Dresden-Rossendorf (HZDR)**  
A. Laso Garcia, E. Grosse, K. Heidel, J. Hutsch, B. Kämpfer, R. Kotte, L. Naumann, C. Wendisch J. Wüstenfeld
- **Dubna, Russia, Veksler and Baldin Laboratory of High Energies, Joint Institute for Nuclear Research (JINR-VBLHE)**  
Yu. Anisimov, S. Avdeyev, A. Bychkov, V. Chepurinov, S. Chernenko, S. Dubnichka, A. Dubnichkova, O. Fateev, V. Golovatyuk, Yu. Gusakov, A. Ierusalimov, E.-M. Ilgenfritz, V. Karnaukhov, V. Kirakosyan, V. Ladygin, A. Malakhov, J. Manjavidze, E. Plekhanov, S. Razin, A. Shabunov, I. Tsakov, T. Vasiliev, Yu. Zanevsky, V. Zrjuev
- **Dubna, Russia, Laboratory of Particle Physics, Joint Institute for Nuclear Research (JINR-LPP)**  
K. Davkov, V. Davkov, Ju. Gousakov, G. Kekelidze, V. Lucenko, V. Mialkovski, S. Parzhitski D. Peshekhonov, V. Peshekhonov, A. Zinchenko

- **Dubna, Russia, Laboratory of Information Technologies, Joint Institute for Nuclear Research (JINR-LIT)**  
P. Akishin, E. Akishina, T. Akishina, S. Baginyan, O. Derenovskaya, Victor Ivanov, Valery Ivanov, P. Kisel, G. Kozlov, E. Litvinenko, G. Ososkov, A. Raportirenko, P. Zrelow
- **Frankfurt, Germany, Frankfurt Institute for Advanced Studies, Goethe Universität Frankfurt (FIAS)**  
M. Bach, J. de Cuveland, S. Gorbunov, D. Hutter, S. Kalcher, I. Kisel, M. Kretz, V. Lindenstruth
- **Frankfurt, Germany, Institute for Computer Science, Goethe Universität Frankfurt**  
S. Böttger, T. Breitner, H. Engel, C. Garcia Chavez, J. Gebelein, U. Kebschull, C. Lara, S. Manz, A. Oancea
- **Frankfurt, Germany, Institut für Kernphysik, Goethe Universität Frankfurt**  
S. Amar-Youcef, H. Appelshäuser, A. Arend, T. Bel, C. Blume, M. Deveaux, P. Dillenseger, D. Doering, M. Domachowski, I. Fröhlich, T. Galatyuk, M. Hartig, M. Koziel, Qyian Li (CCNU, Wuhan), B. Neumann, B. Milanovic, C. Müntz, P. Reichelt, C. Schrader, S. Seddiki, J. Stroth, T. Tischler, C. Trageser, I. Vassiliev, B. Wiedemann, Weilin Yu
- **Gatchina, Russia, Petersburg Nuclear Physics Institute, NRC Kurchatov Institute (PNPI)**  
V. Baublis, V. Dobyryn, V. Golovtsov, V. Ivanov, A. Khanzadeev, L. Kochenda, B. Komkov, P. Kravtsov, E. Kryshen, L. Kudin, N. Miftakhov, V. Nikulin, V. Poliakov, E. Rostchin, Y. Riabov, V. Samsonov, O. Tarassenkova, S. Volkov, E. Vznuzdaev, M. Vznuzdaev, M. Zhalov
- **Giessen, Germany, II. Physikalisches Institut, Justus-Liebig-Universität Gießen**  
C. Dritsa, C. Höhne, S. Lebedev, E. Lebedeva, T. Mahmoud
- **Guwahati, India, Department of Physics, Gauhati University**  
B. Bhattacharjee, K. Dey R. Talukdar
- **Hefei, China, Department of Modern Physics, University of Science & Technology of China (USTC)**  
Hongfang Chen, Cheng Li, Haiping Peng, Ming Shao, Yongjie Sun, Zebo Tang, Yifei Zhang
- **Heidelberg, Germany, Physikalisches Institut, Universität Heidelberg**  
I. Deppner, D. Gottschalk, N. Herrmann, Tae Im Kang, P. Loizeau, K. Schweda, C. Simon, K. Wisniewski (Warsaw University), Yapeng Zhang
- **Heidelberg, Germany, Zentrales Institut für Technische Informatik, Universität Heidelberg, Standort Mannheim**  
T. Armbruster, U. Brüning, P. Fischer, C. Kreidl, M. Krieger, F. Lemke, M. Nüsse, I. Peric, D. Wohlfeld
- **Jaipur, India, Physics Department, University of Rajasthan**  
R. Raniwala, S. Raniwala
- **Jammu, India, Department of Physics, University of Jammu**  
P.V.K.S. Baba, A. Bhasin, A. Gupta, S. Mahajan, S.S. Sambyal, M. Sharma
- **Katowice, Poland, Institute of Physics, University of Silesia**  
A. Bubak, A. Grzeszczuk, E. Kaptur, S. Kowalski, E. Stephan, W. Zipper
- **Kharagpur, India, Indian Institute of Technology**  
P. Banerjee, T.K. Bhattacharyya, A. Haldar, A.K. Singh
- **Kolkata, India, High Energy Physics Division, Saha Institute of Nuclear Physics**  
Sukalyan Chattopadhyay, D. Das, I. Das, A.K. Dutt-Mazumdar, L. Pal, S. Pal, P. Roy, T. Sinha
- **Kolkata, India, Department of Physics and Department of Electronic Science, University of Calcutta**  
A. Bhattacharyya, S. Bandyopadhyay, A. Chakrabarti, Sanatan Chattopadhyay, G. Gangopadhyay

- **Kolkata, India, Variable Energy Cyclotron Centre (VECC)**  
Z. Ahmad, P. Bhaduri, Subhasis Chattopadhyay, M. Dey, A. Dubey, S.A. Khan, B. Mohanty, G.S.N. Murthy, T. Nayak, S. Pal, A. Roy, Y. Saini, R.N. Singaraju, V. Singhal, P. Trivedy, Y.P. Viyogi
- **Kraków, Poland, Faculty of Electrical Engineering, Automatics, Computer Science and Electronics, Department of Measurement and Instrumentation, AGH University of Science and Technology**  
J. Gajda, P. Gryboś, K. Kasinski, R. Kłeczek, P. Maj, P. Otfinowski, R. Szczygieł, M. Żołądź
- **Kraków, Poland, Marian Smoluchowski Institute of Physics, Jagiellonian University**  
J. Brzychczyk, Z. Majka, P. Staszal
- **Kyiv, Ukraine, Department of Nuclear Physics, National Taras Shevchenko University of Kyiv**  
O. Bezshyyko, I. Kadenko, Y. Onishchuk, V. Plujko
- **Kyiv, Ukraine, High Energy Physics Department, Kiev Institute for Nuclear Research (KINR)**  
M. Borysova, A. Kovalchuk, V. Kyva, V. Militsija, Ya. Panasenko, V. Pugatch, D. Storozhyk
- **Moscow, Russia, Institute for Nuclear Research (INR)**  
M. Golubeva, F. Guber, A. Ivashkin, O. Karavichev, T. Karavicheva, E. Karpechev, A. Kurepin, A. Maevskaya, V. Marin, I. Peshenichnov, O. Petukhov, A. Reshetin, A. Sadovsky, V. Tiflov, N. Topil'skaya, E. Usenko
- **Moscow, Russia, Alikhanov Institute for Theoretical and Experimental Physics (ITEP)**  
A. Akindinov, A. Arefiev, S. Belogurov, A. Chernogorov, D. Golubkov, A. Golutvin, F. Khasanov, S. Kiselev, I. Korolko, K. Mikhailov, P. Polozov, M. Prokudin, I. Rostovtseva, A. Semennikov, G. Sharkov, A. Stavinskiy, Y. Zaitsev
- **Moscow, Russia, Skobeltsyn Institute of Nuclear Physics, Lomonosov Moscow State University (SINP-MSU)**  
N. Baranova, D. Karmanov, M. Korolev, M. Merkin, V. Popov, A. Voronin
- **Moscow, Russia, Kurchatov Institute**  
D. Blau, A. Kazantsev, V. Manko, I. Yushmanov
- **Moscow, Russia, National Research Nuclear University MEPhI**  
E. Atkin, Y. Bocharov, O. Malyatina, A. Petrovskiy, V. Shumikhin, A. Simakov, M. Strikhanov, Y. Volkov
- **Münster, Germany, Institut für Kernphysik, Westfälische Wilhelms Universität Münster**  
R. Berendes, C. Bergmann, D. Emschermann, N. Heine, Ch. Klein-Bösing, W. Verhoeven, J. Wessels
- **Obninsk, Russia, National Research Nuclear University**  
N. D'Ascenzo, A. Galkin, V. Galkin, D. Ossetski, V. Saveliev
- **Prag, Czech Republic, Czech Technical University (CTU)**  
V. Petráček, V. Pospisil, L. Skoda
- **Protvino, Russia, Institute for High Energy Physics (IHEP)**  
A. Artamonov, V. Gapienko, S. Golovnya, Yu. Kharlov, D. Konstantinov, I. Lobanov, E. Lobanova, V. Rykalin, S. Sadovsky, A. Semak, Y. Sviridov, Yu. Tsyupa, M. Ukhanov, A. Vorobiev
- **Pusan, Korea, Pusan National University (PNU)**  
Kunsu Oh, Jihye Song, Jun-Gyu Yi, In-Kwon Yoo
- **Řež, Czech Republic, Nuclear Physics Institute, Academy of Sciences of the Czech Republic**  
A. Kugler, O. Svoboda, P. Tlustý
- **Seoul, Korea, Department of Physics, Korea University**  
Byungsik Hong, Suhyun Lee, Kwang-Souk Sim

- **Split, Croatia, University of Split**  
I. Carević, M. Anđelić, M. Dželalija
- **Srinagar, India, Department of Physics, University of Kashmir**  
F. Ahmad, S. Ahmad, S. Bashir, M. Farooq Mir, W. Raja
- **St. Petersburg, Russia, Ioffe Physico-Technical Institute, Russian Academy of Sciences**  
V. Eremin, E. Verbitskaya
- **St. Petersburg, Russia, V.G. Khlopin Radium Institute (KRI)**  
O. Batenkov, V. Jakovlev, V. Kalinin, Y. Murin, A. Veshikov
- **St. Petersburg, Russia, St. Petersburg State Polytechnic University (SPbSPU)**  
A. Berdnikov, Y. Berdnikov
- **Strasbourg, France, Institut Pluridisciplinaire Hubert Curien (IPHC), IN2P3-CNRS and Université de Strasbourg**  
G. Claus, A. Dorokhov, W. Dulinski, M. Goffe, A. Himmi, K. Jaaskelainen, F. Rami, I. Valin, M. Winter
- **Tübingen, Germany, Physikalisches Institut, Eberhard Karls Universität Tübingen**  
B. Hess, H.R. Schmidt, J. Wiechula
- **Varanasi, India, Department of Physics, Banaras Hindu University**  
A. Prakash, B.K. Singh, C.P. Singh
- **Warsaw, Poland, Institute of Experimental Physics, Warsaw University**  
M. Kirejczyk, P. Gasik, T. Matulewicz, J. Rozynek (National Centre for Nuclear Research, Warsaw), K. Piasecki, B. Sikora, K. Siwek-Wilczynska
- **Wuhan, China, Institute of Particle Physics, Hua-zhong Normal University**  
Xu Cai, Guangming Huang, Feng Liu, Dong Wang, Yaping Wang, Changzhou Xiang (Heidelberg Univ.), Nu Xu, Zhongbao Yin, Daicui Zhou
- **Wuppertal, Germany, Fachbereich Physik, Bergische Universität Wuppertal**  
K.-H. Becker, K.-H. Kampert, J. M. Kopfer, C. Pauly, J. Pouryamout, S. Querschfeld, J. Rautenberg, S. Reinecke
- **Zagreb, Croatia, Rudjer Bošković Institute**  
Z. Basrak, R. Čaplar, I. Gašparić, M. Kiš

# Contacts

## Chairman of the Collaboration Board

Yogendra P. Viyogi  
[viyogi@veccal.ernet.in](mailto:viyogi@veccal.ernet.in)

## Spokesman

Peter Senger  
[p.senger@gsi.de](mailto:p.senger@gsi.de)

## Deputy Spokesman

Yuri Zaitsev  
[zaitsev@itep.ru](mailto:zaitsev@itep.ru)

## Deputy Spokesman

Subhasis Chattopadhyay  
[sub@veccal.ernet.in](mailto:sub@veccal.ernet.in)

## Technical Coordinator

Walter Müller  
[w.f.j.mueller@gsi.de](mailto:w.f.j.mueller@gsi.de)

## Physics Coordinator

Volker Friese  
[v.friese@gsi.de](mailto:v.friese@gsi.de)

## Ressource Coordinator

Jürgen Eschke  
[j.eschke@gsi.de](mailto:j.eschke@gsi.de)

## Management Board

S. Chattopadhyay, N. Herrmann, F. Rami, M Petrovici, J. Stroth, J. Wessels, Y. Zaitsev

<http://www.gsi.de/fair/experiments/CBM>

